COMPUTER-AIDED DETECTION OF CEREBRAL ANEURYSMS IN ANGIOGRAPHIES

Dissertation
zur Erlangung des akademischen Grads
Doktoringenieur (Dr.-Ing.)

angenommen durch die Fakultät für Informatik
der Otto-von-Guericke Universität Magdeburg

von DIPL.-ING. CLEMENS M. HENTSCHKE
geb. am 29.10.1983 in Stuttgart

Gutachter:
PROF. DR.-ING. KLAUS TÖNNIES
PROF. DR.-ING. BERNHARD PREIM
PROF. DR.-ING. HORST-KARL HAHN

Magdeburg, 24.10.2013

Das Schönste, was wir entdecken können, ist das Geheimnisvolle

— ALBERT EINSTEIN

Eigentlich wollte ich diese Arbeit mir widmen, da ich die meiste Arbeit damit hatte und den größten Teil zu ihrer Fertigstellung beigetragen habe. Das schien mir dann aber etwas vermessen.

Ich widme diese Arbeit Papa.

ABSTRACT

Cerebral aneurysms are pathological dilations in the vasculature of the human brain that are subject to rupture. A rupture can cause permanent disability or death. As unruptured aneurysms can be treated leading to a good patient outcome, early detection of aneurysms is very important. They are commonly detected in angiographic imaging techniques. Angiographic data sets are routinely acquired for diagnosis of vessel related pathologies.

Aneurysm detection by assistance of a computer-aided diagnosis system is desirable. Such a system has the potential to find additional aneurysms that may have been overlooked by physicians.

This thesis presents a system to automatically detect unruptured aneurysms in angiographic data sets. The processing of different angiographic modalities, Reconstructed 3D X-ray Rotation Angiography (3D-RA), Contrast-Enhanced Magnetic Resonance Angiography (CE-MRA), Time of Flight Magnetic Resonance Angiography (TOF-MRA) and CT Angiography (CTA), is supported by the system. A vessel segmentation that could heavily influence the whole detection system is not required.

Initial aneurysm candidates are found by applying a sphere-enhancing filter. Several features are computed on found Region(s) of Interest (ROI) and are combined in a Linear Discriminant Function (LDF) to distinguish between true aneurysms and false positives. The features include shape information, spatial information and probability information. The LDF is parametrized either by domain experts or automatically by training on a database.

The system is evaluated on 197 clinical angiographic data sets of all four relevant angiographic modalities. Evaluation assesses the parameter robustness as well as the contribution of the individual parts of the system to the overall performance. For all modalities, more than 90 % of aneurysms were found at reasonable average false positive rates. The average rates were between 2 and 14 per data set. The expert parametrization yield equal or better results than the trained parametrization. It was shown that the system is able to find aneurysms that were previously overlooked by physicians.

ZUSAMMENFASSUNG

Zerebrale Aneurysmen sind krankhafte Arterienerweiterungen in Hirngefäßen. Eine Ruptur kann zum Tod oder zu schweren Behinderungen führen. Es existieren Behandlungsmethoden, die nicht rupturierten Aneurysmen zu verschließen oder zu entfernen. Dafür ist jedoch eine Erkennung dieser Pathologie notwendig. Zu Erkennung von Aneurysmen werden angiographisch bildgebende Methoden verwendet. Systeme zur computerassistierten Erkennung von Aneurysmen können Ärzte unterstützen, nicht rupturierte Aneurysmen zu finden.

Diese Arbeit stellt ein solches System vor, dass ohne Nutzerinteraktion und ohne Segmentierung diese Aufgabe durchführen kann. Dazu werden verschiedene angiographische Methoden, 3D Rotationsangiographie, kontrastverstärkte Magnetresonanzangiographie, Time-of-Flight Magnetresonanzangiographie und CT Angiographie, verarbeitet.

Das vorgestellte System basiert auf einem multi-skalen Filter, der kugelförmige Objekte in den Datensätzen hervorhebt. Aus dem Filterergebnis werden Regionen von zusammenhängenden Pixeln bestimmt; auf diesen werden Merkmale berechnet. Die Merkmale verwenden räumliche Information sowie Form- und Wahrscheinlichkeitsinformation. Die Merkmale werden in einer linearen Diskriminanzfunktion zur Unterscheidung zwischen tatsächlichen Aneurysmen und falschpositiven Kandidaten verwendet. Die Diskriminanzfunktion kann entweder durch Experten oder durch Training auf vorhandenen Datensätzen parametrisiert werden.

Eine Evaluation wird auf 197 Datensätzen von allen relevanten angiografischen Modalitäten durchgeführt. Sowohl die Robustheit der Parameter, als auch der Anteil jedes Algorithmusschrittes zum Gesamtergebnis wird getestet. In allen Modalitäten können mehr als 90 % der Aneurysmen erfolgreich detektiert werden. Die Anzahl der insgesamt gefundenen Kandidaten schwankt dabei zwischen 2 und 14 im Durchschnitt pro Datensatz. Mit der Expertenparametrisierung werden gleiche bzw. bessere Ergebnisse als mit der trainierten Parametrisierung erzielt. Es kann gezeigt werden, dass das vorgestellte System Aneurysmen erkennt, die von Ärzten übersehen worden sind.

PUBLICATIONS

Some ideas and figures have appeared previously in the following publications:

Clemens M. Hentschke and Klaus Tönnies. Intensity-based Registration of 2D-DSA and 3D-DSA Data Sets for Flow Simulation in Intracranial Aneurysms. In *Vision, Modeling, and Visualization (VMV)*, pages 375–376, Braunschweig, 2009.

Clemens M. Hentschke and Klaus Tönnies. Automatic 2D-3D Registration of Cerebral DSA Data Sets. In *Bildverarbeitung für die Medizin*, pages 162–166, Aachen, 2010.

Clemens M. Hentschke, Steffen Serowy, Gábor Janiga, Georg Rose, and Klaus Tönnies. Estimating Blood Flow by Re-projection of 2D-DSA to 3D-RA Data Sets for Blood Flow Simulations. In *Computer Assisted Radiology and Surgery (CARS)*, pages 342–343, Geneva, 2010.

Clemens M. Hentschke, Steffen Serowy, Gábor Janiga, Georg Rose, and Klaus Tönnies. Estimating blood flow velocity in angiographic image data. In *SPIE Medical Imaging*, pages 7964—1–8, Orlando, 2011.

Clemens M. Hentschke, Oliver Beuing, Rosa Nickl, and Klaus Tönnies. Automatic Cerebral Aneurysm Detection in Multimodal Angiographic Images. In *IEEE Medical Image Conference*, pages 3116–3120, Valencia, 2011.

Clemens M. Hentschke, Oliver Beuing, Rosa Nickl, and Klaus Tönnies. Detection of cerebral aneurysms in MRA, CTA and 3D-RA data sets. In *SPIE Medical Imaging*, pages 8315—1–8, San Diego, 2012.

Clemens M. Hentschke, Klaus Tönnies, Oliver Beuing, and Rosa Nickl. A new feature for automatic aneurysm detection. In *IEEE International Symposium on Biomedical Imaging*, pages 800–803, Barcelona, 2012.

DANKSAGUNG

Mit Freunden die Mensa- oder Kaffeepause zu verbringen war ein wichtiger Teil des Alltags. Solche Pausen haben Abwechslung gebracht und haben mir wieder neue Energie gegeben. Vielen Dank an Thomas, Apo, Robert und Antje.

Ich danke natürlich auch Papa, Mama und ganz besonders meinen Eltern. Und natürlich Victoria. Außerdem danke ich Sigrid und Stefan, ihr habt mich immer wie euren eigenen Sohn behandelt. Zu wissen, dass man eine Familie hat, die einen stets unterstützt, ist sehr kostbar und ich habe diese Unterstützung sehr genossen. Wenn ich nicht mehr an mich geglaubt habe, habt ihr es getan und das hat mich unheimlich motiviert.

Zum Schluss möchte ich Jessi danken. Du bist meine Muse. Ich bin unendlich dankbar dafür, dich gefunden zu haben. Danke für deine fortwährende Unterstützung und Liebe.

CONTENTS

LIST OF TABLES

LIST OF SYMBOLS

a Surface area of an object

acc Accuracy measure for evaluation of classifiers (defined in Section 6.3)

a_{CH} Surface area of the convex hull of an object

A Score value of linear discriminant function (defined in Section 5.8)

AUC Area under curve of a FROC (defined in Section 6.3)

A_t Absolute threshold for a ROI to be in the set of C_f (defined in Section 5.8)

b Blobness (defined in 4.3.1)

bn Bottleneck factor (defined in Section 3.4)

B Blobness image

B_{max} Maximal blobness value in a data set

c_i ROI of proposed system

C_0 Set of ROI before execution of rule-based system

C_1 Set of ROI after execution of rule-based system

C_f Final set of ROI after sorting based on A

C_x Cost matrix of MetaCost (defined in 5.9)

C_{TP}, C_{FP} set of ROI containing true positives/false positives

d_a Aneurysm diameter

d_c Distance of a point to the center of a data set

d_n Neck width of an aneurysm

d_{cmax} Maximal valid value of d_c for inclusion in C_1 (defined in Section 5.7)

d_{CoWmax} Maximal valid value of d_{CoW} for inclusion in C_1 (defined in Section 5.7)

d_{CoW} Distance to the nearest vessel pixel of the Circle of Willis defined by the segmentation in the model data set (defined in Section 5.6)

D Data/Database

DS Data set

e Ellipticity index (defined in Section 3.4)

E Energy

fp_{DS} Average amount of false positives per data set (defined in Section 6.3)

f_{max} Maximum feature value

f_{min} Minimum feature value

F Feature vector

$FP_{0.9}$ fp_{DS} at $se = 0.9$ (defined in Section 6.3)

g_m G-means measure for evaluation of classifiers (defined in Section 6.3)

G Graph

H Hessian matrix

i Intensity

L Class label vector

m Model

m_g Moment-based geometric invariants

m_z Moment-based Zernike invariants

M Modality

ns Nonsphericity index (defined in Section 3.4)

n_p Surface normal of a point p

n_{FN} Number of false negatives

n_{FP} Number of false positives

n_{TN} Number of true negatives

n_{TP} Number of true positives

N Sampling rate for r_i in multi-scale blobness (defined in 4.3.1)

$N(p)$ Local neighborhood of a point

p Position of a voxel/object

ps_p, ps_s Pixel spacing in plane/in slice

p_A Probability of aneurysm occurrence based on atlas

p_g Given aneurysm position

p_m Modes of Variation

p_{FP} Probability of false positive occurrence based on atlas

rk_t Rank order threshold for a ROI to be in the set of C_f (defined in Section 5.8)

r_a Aspect ratio of an aneurysm (defined in Section 3.4)

r_{max} Maximal radius of an object

r_{min} Minimal radius of an object

s Volume of a Region of Interest (defined in Section 5.6)

se Sensitivity (defined in Section 6.3)

se_{10} Average sensitivity at $10\,\mathrm{fp_{DS}} \pm 5\,\mathrm{fp_{DS}}$ (defined in Section 6.3)

sp Specificity (defined in Section 6.3)

s_{CH} Volume of convex hull

s_{min} Minimal volume of a ROI (defined in Section 5.7)

t Threshold in blobness image for ROI definition (defined in Section 5.5)

t_u, t_l Upper/lower threshold for double thresholding

u Undulation index (defined in Section 3.4)

v Vesselness

V Vesselness image

W Weighting vector for LDF (defined in Section 5.8)

Wr Writhe number (defined in Section 4.3.2)

W_e Expert weighting vector for LDF (defined in Section 5.8)

W_t Trained weighting vector for LDF (defined in Section 5.8)

W_{te} Trained weighting vector for LDF with feature selection (defined in Section 5.8)

x_0 Landmark points

$\bar{x}$ Average shape of an object

α, β, γ Parameters of Frangi's blobness definition (defined in 4.3.1)

ϵ Error term for linear regression

η Tolerance value for d_{cmax} computation (defined in Section 5.7)

θ Transformation

κ_1 Primary principal curvature

κ_2 Secondary principal curvature

λ Eigenvalue

μ Between-class ratio of imbalanced data sets (defined in 5.9)

σ Standard deviation of Gaussian kernel

φ Parametrization

Φ Parameter space

χ Similarity function

Ψ Sphericity (defined in Section 4.3.1)

Ω Maximum fp_{DS} value for AUC computation (defined in Section 6.3)

LIST OF ACRONYMS

2D-DSA Intra-arterial Digital Subtraction X-ray Angiography

3D-RA Reconstructed 3D X-ray Rotation Angiography

AAA Abdominal Aortic Aneurysm

AAM Active Appearance Model

ACA Arteria Cerebri Anterior

ACI Arteria Carotis Interna

ACM Arteria Cerebri Media

AComm Arteria Communicans Anterior

ACP Arteria Cerebri Posterior

ANG Cerebral Angiography

ANN Artificial Neural Network

ASM Active Shape Model

AUC Area under Curve

BB-MRA Black-blood Magnetic Resonance Angiography

BSCTA Bone Subtracted Computed Tomography Angiography

CADe Computer-aided Detection

CADq Computer-aided Quantification

CADx   Computer-aided Diagnosis

CAD   Computer-aided Diagnosis

CA   Contrast Agent

CCA   Connected Component Analysis

CE-MRA   Contrast-Enhanced Magnetic Resonance Angiography

CFD   Computational Fluid Dynamics

CTA   CT Angiography

CT   Computed Tomography

DICOM   Digital Imaging and Communications in Medicine

FEM   Finite Element Method

FN   False Negative

FPS   Frames per Second

FP   False Positive

FROC   Free Response-operator Characteristic

FSI   Fluid-structure Interaction

GHT   Generalized Hough Transform

GUI   Graphical User Interface

HEA   Hessian Eigenvalue Analysis

HU   Hounsfield Unit

ISUIA   International Study of Unruptured Intracranial Aneurysms

kNN   k-nearest Neighborhood classifier

LDA   Linear Discriminant Analysis

LDF   Linear Discriminant Function

MAP   Maximum a Posteriori

MIP   Maximum Intensity Projection

MRA   Magnetic Resonance Angiography

MRF   Markov Random Field

MRI   Magnetic Resonance Imaging

MSE   Mean Square Error

MSL   Marginal Space Learning

MSM   Mass-spring Model

OSI   Oscillatory Shear Index

PAO   Parent Artery Occlusion

PC-MRA   Phase-Contrast Magnetic Resonance Angiography

PCA   Principal Component Analysis

PComm   Arteria Communicans Posterior

PR   Prevalence Ratio

QDA   Quadratic Discriminant Analysis

RBS   Rule-based System

ROI   Region(s) of Interest

SAH   Subarachnoid Hemorrhage

SBDI   Shape-based Difference Image

SMOTE   Synthetic Minority Over-sampling Technique

SNR   Signal-to-Noise Ratio

SVM   Support Vector Machine

TCD   Transcranial Doppler Sonography

TM   Template Matching

tMIP   Maximum Intensity Projection over Time

TN   True Negative

TOF-MRA   Time of Flight Magnetic Resonance Angiography

TP   True Positive

WSS   Wall Shear Stress

INTRODUCTION

Cerebral aneurysms are pathological dilations of cerebral blood vessels inside the head that can rupture. This poses a serious threat resulting in a hemorrhage that can lead to death or permanent disability. Currently, a prognosis if and when a rupture occurs is only possible with low accuracy. The treatment of unruptured aneurysms is commonly done to prevent a rupture. Therefore, the early detection of unruptured aneurysms plays an important role in therapy.

Recently, due to the increased use of medical imaging modalities, incidental findings of aneurysms occur more frequently [Gabriel et al., 2010]. Until now, no Computer-aided Diagnosis (CAD) algorithm exists that is able to detect cerebral aneurysms with a sufficient high accuracy in multimodality angiographic image data. Almost all algorithms are developed especially for one modality, Time of Flight Magnetic Resonance Angiography (TOF-MRA), such as [Arimura et al., 2006; Yang et al., 2011]. Moreover, all algorithms depend on vessel segmentation and the evaluation of most algorithms was done with too few data sets.

The overall goal of this thesis is to develop a system to detect unruptured cerebral aneurysms to assist the physician. The relatively low prevalence of aneurysms impairs the detection rate of radiologists. Thus, especially small aneurysms are overlooked. The system should work with angiographic data sets acquired of the head of living humans. Four modalities are relevant in aneurysm detection: Reconstructed 3D X-ray Rotation Angiography (3D-RA), Contrast-Enhanced Magnetic Resonance Angiography (CE-MRA), TOF-MRA and CT Angiography (CTA) [Wanke and Forsting, 2008]. Further requirements of the system are the processing with minimal user interaction and the independence to a vessel segmentation. The vision is that the system can be clinically used to routinely scan acquired image data for aneurysms. If aneurysms are found, the physician is provided with this information to confirm or reject the finding. As no additional images are needed to be acquired, no disadvantage occurs for the patient.

In terms of quality, the algorithm aims for detecting $> 90\,\%$ aneurysms with a preferably small amount of False Positives (FPs). The FP rate varies depending on the modality, an average of ten FP per data set should not be exceeded.

The aneurysm detection has to overcome several challenges:

1. The shape of cerebral aneurysms can hardly be generalized,

2. The feature characteristics for aneurysms are rather variable and depend on the modality,

3. The image quality varies depending on the modality as well as on the acquisition device,

4. CTA has difficult intensity characteristics as the intensity levels of bones and blood overlap and

5. Statistical information should only minimally be used.

1.1 STRUCTURE

This thesis is divided into seven chapters. Chapter 2 introduces the *medical back-ground*. First, an overview about cerebral aneurysms is given and their treatment options are explained. Second, the relevant angiographic imaging modalities are discussed especially by their value and use in aneurysm management. Finally, the chapter is concluded with an overview of the cerebral aneurysm management at the University Hospital of Magdeburg.

In Chapter 3, an overview is given about *computer-aided management of aneurysms*. The different areas of computer assistance are introduced and discussed with respect to their use in a clinical environment.

In Chapter 4, the *State of the Art* of aneurysm detection is given. In a broad-to-fine approach, first, object detection algorithms are outlined, then, an overview about CAD algorithms is given and finally, existing algorithms to detect cerebral aneurysms are discussed in detail.

In Chapter 5, the proposed *method* is explained. Details about all algorithm steps are given and it is illustrated how these steps were found. Furthermore, the different parametrizations are discussed and alternatives to parts of the algorithm are presented.

In Chapter 6, a thorough *evaluation and discussion* of the proposed method is made. Experiments are made to evaluate the robustness of algorithm parameters and to prove the suitability of the chosen algorithm parts. Also variants or alternatives of the different parts are tested. After the discussion of the proposed system, the system is compared with existing methods.

In Chapter 7, a *summary* of the thesis is given. The scientific contributions and the future work are discussed.

Marginal notes are used for summarizing the most important statements of a section.

A list of all symbols and a list of abbreviations can be found after table of contents.

MEDICAL BACKGROUND

In this chapter, a short overview about aneurysms is given with the focus on cerebral aneurysms. Furthermore, the angiographic modalities that are relevant for cerebral aneurysm management are introduced and discussed with respect to their clinical value.

2.1 ANEURYSMS

An aneurysm is a pathological blood vessel dilation. Aneurysms occur on vessels throughout the human body, e.g., in the brain (Figure 2.1a), heart, intestine and aorta. The clinical relevant aneurysms appear at arterious vessels, however also venous aneurysms occur, but they are rare [Gillespie et al., 1997]. The two most relevant types of aneurysms with respect to health risk and possible fatal consequences in case of a rupture are cerebral aneurysms and aortic aneurysms. *Cerebral aneurysms* are located inside the brain and *aortic aneurysms* are located at the aorta. A rupture of a cerebral aneurysm is possible which may lead to a severe hemorrhage causing a stroke. Aortic aneurysms are dilations of the aorta. A rupture leads to massive internal hemorrhage that leads to death unless it is immediately treated. More information about aortic aneurysms are given in [Upchurch and Schaub, 2006; Hirsch et al., 2006].

In Germany, 62 085 people died in 2011 of cerebrovascular diseases, the expenses of the consequences were € 1044 billion [Bundesamt, 2012]. Thus, a rupture of an aneurysm has to be prevented with respect to ethical aspects and economical costs.

2.1.1 *Classification*

Aneurysm can be classified based on *location*, *morphology*, *size* and *etiology*.

Intracranial aneurysms are often used as a synonym for cerebral aneurysms in the literature. However, they are limited in their location within the skull. It has to be differentiated between extradural and intradural aneurysms. Intradural aneurysms are within the dura mater (a thin membrane around the brain) and a rupture of these lead to a Subarachnoid Hemorrhage (SAH). Extradural aneurysms are commonly located at the cavernous section of the Arteria Carotis Interna (ACI) and do not lead to a SAH in case of rupture, but rather lead to a formation of a fistula that is not life-threatening [Fiehler, 2012]. In this thesis only unruptured cerebral aneurysms are considered. If not stated otherwise, unruptured cerebral aneurysms are meant if spoken of aneurysms.

Classification based on location

Cerebral aneurysms can be divided into three types based on their morphology [Wanke and Forsting, 2008]:

- saccular aneurysms (Figure 2.2a) ,

- fusiform aneurysms (Figure 2.2b) and

Classification based on morphology
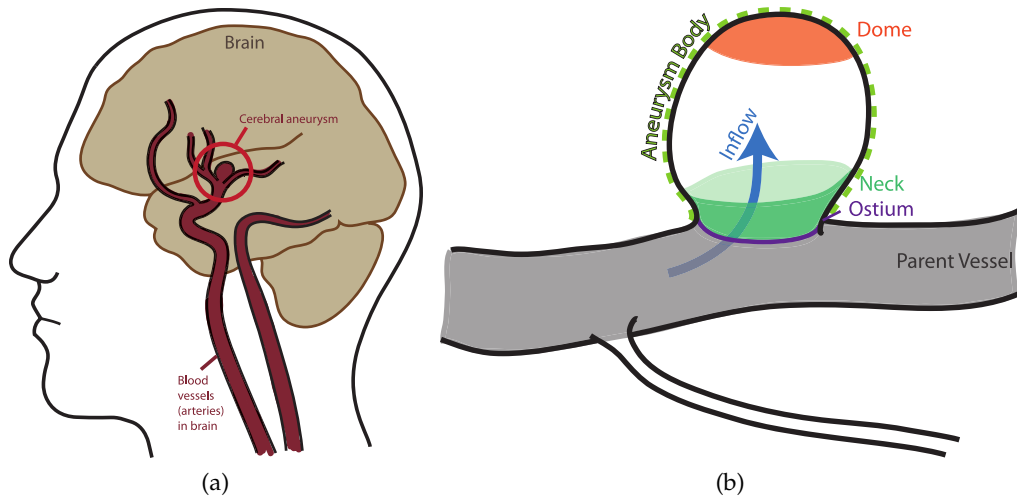
Figure 2.1: (a) Sketch of an aneurysm in the human head. (b) Scheme of a saccular aneurysm adapted from [Neugebauer et al., 2010].
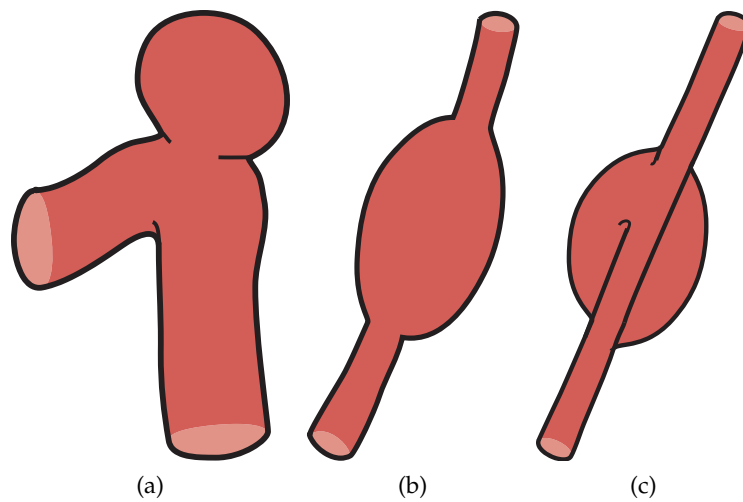
Figure 2.2: Scheme of (a) a saccular, (b) a fusiform and (c) a dissecting aneurysm.

- dissecting aneurysms (Figure 2.2c).

Saccular aneurysms are balloon-shaped vascular eversions (see Figure 2.3). They can be divided into several structural shape parts (see Figure 2.1b). Blood flows through the *parent or feeding vessel* into the aneurysm and leaves it commonly through the same vessel. The structural shape part includes: The *ostium* separates the aneurysm body from the vessel. The aneurysm part furthermost from the neck is called *dome*. In saccular aneurysms, a *neck* exists commonly, as the diameter at the ostium is usually smaller than the largest diameter of the aneurysm sac forming a bottleneck for the inflowing blood. The neck is connected to the feeding vessel. Saccular aneurysms are the most common cerebral aneurysm morphology, as they account for about 91 % of cerebral aneurysms [Inagawa, 1991].

In contrast, *fusiform aneurysms* are dilated, tortuous and elongated vessel segments. They usually appear as an enlargement of the vessel with a peak diameter
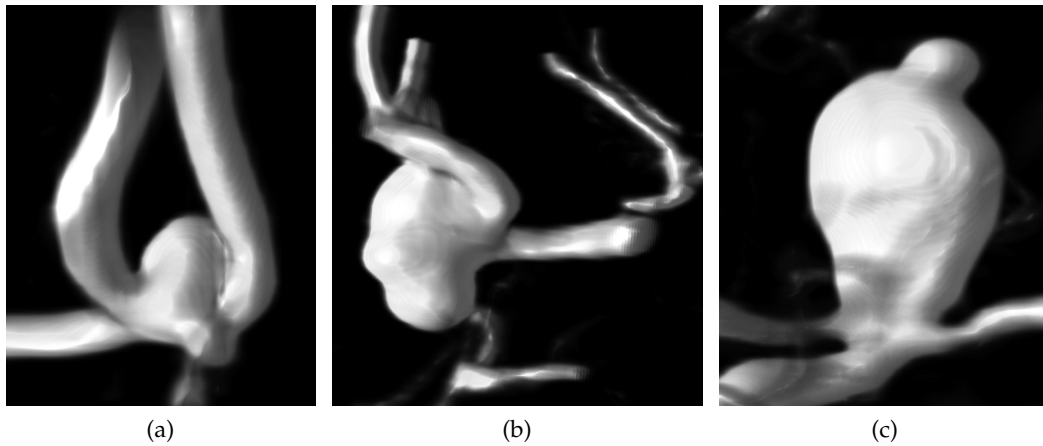
Figure 2.3: Example visualizations of aneurysms with different sizes based on 3D-RA data sets. Only the aneurysms and the surrounding vessels are shown. The data sets are courtesy of Oliver Beuing, department of neuroradiology, University Hospital of Magdeburg. (a) An aneurysm at the AComm with a diameter of 3.9 mm. (b) An aneurysm at the ACM with a diameter of 8.7 mm. (c) An aneurysm at the ACI with a diameter of 16.6 mm.

in the middle decreasing to both sides. A neck is not present. They represent about 6 % of all cerebral aneurysms [Inagawa, 1991].

Dissecting aneurysms are rips in the vessel wall that lead to bleeding within the wall. The occurrence is more seldom than the two other types [Wanke and Forsting, 2008], however, no explicit numbers are provided in the literature. Other aneurysm types that have almost no clinical relevance are infectious aneurysms, traumatic aneurysms and inflammatory aneurysms [Wanke and Forsting, 2008]. This work focuses on saccular and fusiform aneurysms as they represent the vast majority of all cerebral aneurysms.

Aneurysm classification based on size and etiology is discussed in the next section.

2.1.2 *Properties*

It is difficult to estimate the prevalence of cerebral aneurysms in the general population. The most recent meta-analysis of studies suggests a prevalence of 3.2 % in a healthy, age-normalized population consisting of an equal amount of men and women [Vlak et al., 2011]. However, the Prevalence Ratio (PR) for first-degree relatives with a history of intracranial aneurysms of SAH is 3.4 [Vlak et al., 2011] because of genetic factors. Aneurysms occur more often in women than men leading to a PR of 1.6 [Vlak et al., 2011]. Interestingly, the PR for German citizens is higher than for citizens of other countries in the Western world, although the values are not significant [Vlak et al., 2011]. Generally, aneurysm occurrence is linked to the age, but the difference was not significant except for patients older than 80 years and younger than 30 years [Vlak et al., 2011]. The frequency of multiple aneurysms in a patient is 19 % to 27 % [Inagawa, 2009, 1991] in all aneurysm patients. If the gender and the age is given, a patient specific prevalence can be computed.

Aneurysm prevalence

Aneurysm etiology

The majority of aneurysms are not congenital, but they develop during life [Wiebers, 2006]. The cause and pathogenetic criteria for aneurysm development are only partially understood. Endogenous factors like elevated blood pressure and exogenous factors like cigarette smoking have been found to be associated to aneurysm occurrence [Fiehler, 2012; Juvela et al., 2001]. Furthermore, the very seldom autosomal dominant polycystic kidney disease is known to elevate the risk for formation of an aneurysm significantly [Vlak et al., 2011]. Recently, also genetic components are discussed as it was found that specific genes are associated with cerebral aneurysms [Helgadottir et al., 2008]. However, the research in this area is far from being conclusive.

The majority of unruptured aneurysms are asymptomatic. Only in a few cases aneurysms cause symptoms due to their mass, e. g., if pressure is applied on the optic nerve where vision disorders would be the consequence. Most aneurysms remain undetected unless they become symptomatic, i. e., a rupture occurs. Recently, aneurysms are often incidentally found by neurological imaging techniques [Tummala et al., 2005; Gabriel et al., 2010].

Aneurysm location

Most cerebral aneurysms emerge on vessels associated to the Circle of Willis also known as Circulus arteriosus cerebri (see Figure 2.4a). It is located in the midbrain and indicates the major arteries that supply the brain with blood. Furthermore, most aneurysms are located in proximity to a bifurcation of the major arteries. About 85 % of all cerebral aneurysms originate from the anterior circulation [Vlak et al., 2011]. The location, where aneurysms occur, is classified by their feeding vessel. The arteries in the human head are classified as given in Figures 2.4a and 2.4d and can be grouped using the following scheme:

- Anterior circulation system (Figure 2.4c)
    - Arteria Carotis Interna (ACI)
        * Cavernous part of the ACI
        * Non-cavernous part of the ACI
        * PComm
    - Arteria Cerebri Media (ACM)
    - Arteria Cerebri Anterior (ACA) system
        * Arteria Cerebri Anterior (ACA)
        * Arteria Communicans Anterior (AComm)
- Posterior circulation system
    - Arteria basilaris
    - Arteria vertebralis
    - Arteria Cerebri Posterior (ACP)

For each artery group, for the formation of aneurysms a probability can be given. The most common location given in the literature is the AComm or the ACI, depending on the definition and the formed groups. A comparison between three different sources is given in Figure 2.5. Between 38 % and 42 % of aneurysms originate from the ACI. Between 23 % and 35 % of aneurysms emerge at the ACM and between 12 %

(a)

(b)

(c)

(d)
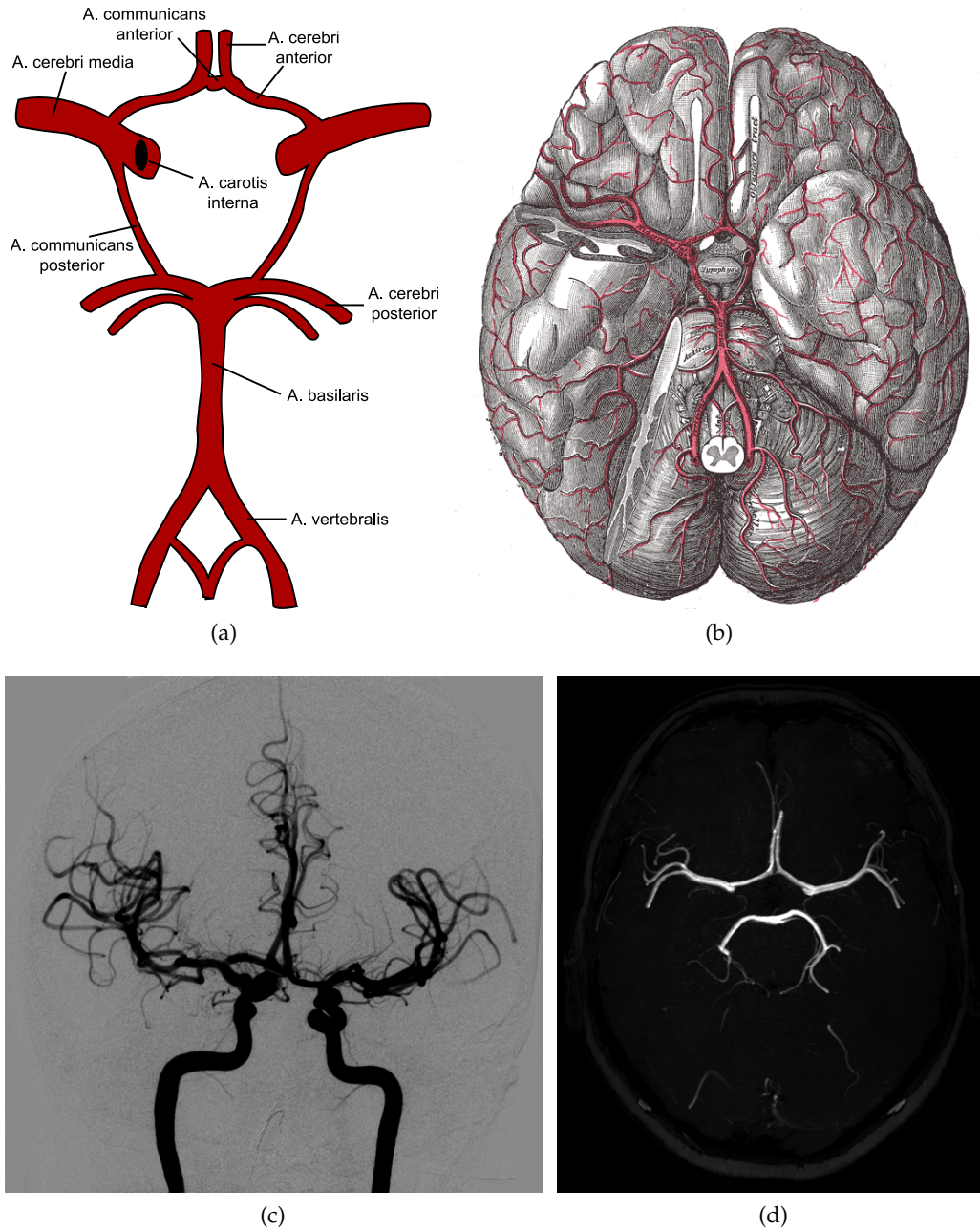
Figure 2.4: The Circle of Willis as a (a) symbolic representation (adapted from `http://commons.wikimedia.org/wiki/File:Circle_of_Willis_la.svg`, public domain, author: Rhcastilhos). (b) The Circle of Willis and the brain in a joint visualization (`http://commons.wikimedia.org/wiki/File:Gray516.png`, public domain, author: Gray's Anatomy). (c) Coronal view of the anterior circulation as two combined 2D-DSA images that are both visualized as a tMIP. (d) Transversal view of the Circle of Willis as seen in TOF-MRA by combining 20 slices. Above left and right, the ACM can be seen. In the center, the AComm is displayed. Below left and right the ACP is seen and in the center the Arteria basilaris is displayed. The PComm is not visible in TOF-MRA although it is located among the slices. The data sets are courtesy of Oliver Beuing, department of neuroradiology, University Hospital Magdeburg.
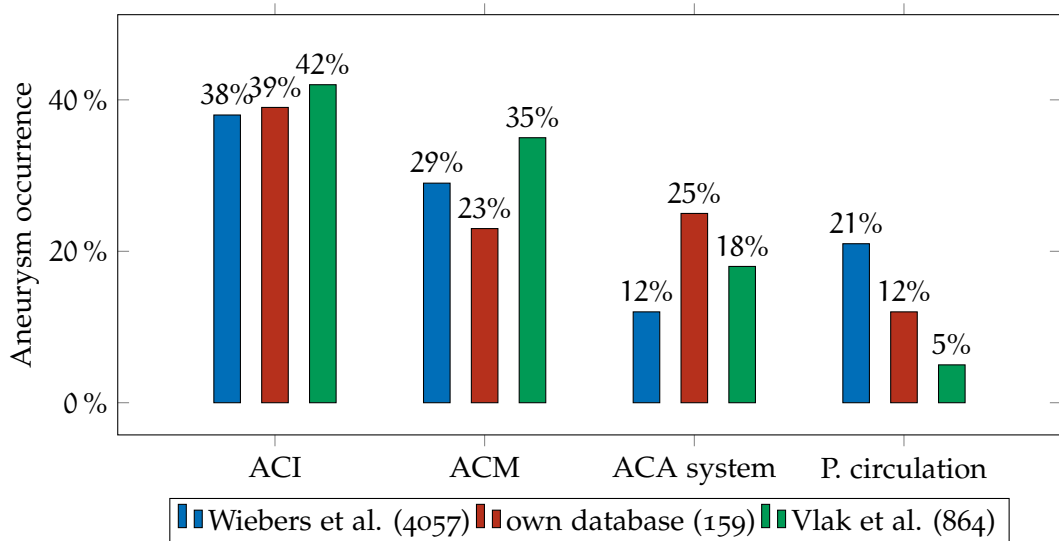
Figure 2.5: Percentage of aneurysm occurrence by feeding vessel. The vessels are divided into Arteria Carotis Interna (ACI), Arteria Cerebri Media (ACM), Arteria Cerebri Anterior (ACA) and Posterior circulation. The data is taken from [Wiebers et al., 2003], [Vlak et al., 2011] and from the own database. The number in brackets represent the number of aneurysms in the respective study. P. circulation = Posterior circulation.

and 25 % appear at the ACA system. The posterior circulation system only plays a minor role as most of the aneurysms in this group occur at the tip of the basilar artery. Despite measuring the occurrence probability based on the feeding vessel, it is possible to connect single bifurcation points with common forming [Edlow et al., 2008]. The most common site for fusiform aneurysms is the ACM [Park et al., 2008].

Aneurysm size The size of aneurysms varies broadly. It is usually measured by taking the largest diameter of the aneurysm body into account. Additionally, height and width is sometimes measured. Height is defined as the maximum length of the line from ostium to the dome and width is defined as the maximum length of the line perpendicular to the height line inside the aneurysm sac. Aneurysms with a size of smaller than 2 mm are hardly visible in medical imaging modalities and are commonly excluded from studies. Aneurysms with size more than 25 mm are called giant aneurysms. The mean of the maximal diameter ranges from 5.7 mm to 11.4 mm, depending on the study [Wiebers et al., 2003; van Rooij and Sluzewski, 2006; Beck et al., 2006].

The International Study of Unruptured Intracranial Aneurysms (ISUIA) was the largest study of unruptured cerebral aneurysms with 4060 patients and 6221 aneurysms assessed from centers in North America and Europe [Wiebers et al., 2003]. It was a prospective non-randomized study. Here, the mean maximum diameter was between 9 mm ± 7.1 mm. 47 % of the patients had an aneurysm with size between 2 mm and 7 mm, in 32 % the size was between 7 mm and 12 mm, in 16 % the size was between 13 mm and 24 mm and 5 % of the aneurysms were greater than

25 mm[1]. A meta-analysis provided the information that 66 % of aneurysms have a size of ⩽ 5 mm, 27 % of aneurysms have a size between 5 mm and 10 mm and only 7 % have a size of ⩾ 10 mm [Vlak et al., 2011]. These numbers question the ISUIA study.

The main threat of aneurysms is their potential to rupture. A rupture leads to an uncontrolled leakage of blood into the subarachnoid region called Subarachnoid Hemorrhage (SAH). The mortality rate for this pathology is about 50 % [van Gijn et al., 2007]. 46 % of survivors have long-term impairment with serious effects on quality of life [Suarez et al., 2006]. Thus, the economical expenses are tremendous and the consequences of a rupture are severe.

Consequences of rupture

Prognosis, if and when a rupture of a cerebral aneurysm emerges is currently only possible with insufficient accuracy. According to the ISUIA, significant predictors of rupture are size and location of aneurysms [Wiebers et al., 2003]. However, the total rupture rate of aneurysms is relatively small. A rupture rate of 0.05 % per year for aneurysms ⩽ 10 mm in diameter was reported. For aneurysms having a diameter ⩾ 10 mm, the rate was 0.5 % per year [Wiebers et al., 2003]. The study was controversially discussed; the low rupture rates have been questioned by the medical community.

Estimation of rupture rate

A review article scrutinizes the validity of ISUIA as they authors of the review article found several methodological difficulties that bias the rupture rate [Raymond et al., 2008]. They further criticized the non-randomized design of the study and the high follow-up loss. A worst-case scenario where these follow-up losses are rated among death from aneurysm rupture leads to a considerably higher rupture rate of 1.2 % per year. A study was proposed that overcomes these difficulties and gives a reliable estimation of the rupture rate [Raymond et al., 2011]. However, this study was stopped after three years because of poor patient recruitment. A possible explanation for the failure of this study is that patients were very anxious and refused to participate in the study as they preferred an interventional treatment over a conservative treatment or randomization [Fiehler, 2012].

These psychological factors have to be taken into account in aneurysm management as the life quality can drastically decrease once the knowledge about an aneurysm is present [Ferns et al., 2011]. Aneurysms are commonly perceived as a ticking bomb in the head once they are found, hence a proper risk assessment about treatment is not possible [Fiehler, 2012]. Thus, the widely used ISUIA results should be cautiously approached although the general tendencies presumably are still valid. Similar to aneurysm formation, there are different risk factors for their rupture. An overview of different endogenous and exogenous risk factors is given in Table 2.1. The most important factors are age, gender, size, location and type (symptomatic vs. asymptomatic) [Wermer et al., 2007].

Other studies report rupture rates of small aneurysms < 5 mm of 0.54 % per year. An interventional treatment is recommended if the patient is younger than 50 years, has hypertension and multiple aneurysms ⩾ 4 mm [Sonobe et al., 2010]. Another review study reports an annual rupture rate of 1.9 % [Rinkel et al., 1998].

---

1 The sizes are grouped disadvantageously. The histogram bins are not equally distributed and it also remains unclear where aneurysms with a size between 12 mm and 13 mm and between 24 mm and 25 mm are grouped.

Table 2.1: Overview of risk factors for aneurysm rupture. The data is taken from [Wermer et al., 2007; Clarke, 2008]. Those numbers marked with * were significant.

	Factor	Relative Risk
Endogenous	Gender: being a woman	1.6*
	Age	2.0 if $\geqslant 60$ years*
	Posterior circulation	2.5*
	Size	Proportional to size (e. g., 2.9* with > 10 mm compared to < 5 mm)
	Ethnicity	3.4* if of Finnish/Japanese descent
	Causes symptoms	4.4*
Exogenous	Hypertension	1.1
	Smoking	1.7
	Heavy alcohol consumption	2.1*
	Body mass index	1.4

Additional hypotheses link features from blood flow simulations such as Computational Fluid Dynamics (CFD) with rupture risk [Cebral et al., 2005]. Hemodynamic factors such as complexity of flow patterns and the size of the inflow jet were investigated with respect to the rupture rate. It is stated that vague trends have been found, but that CFD is still too imprecise and dependent from other parameters to give a clear prognosis of rupture. Also, a shape analysis of aneurysms was proposed as a discriminant for rupture [Lauric et al., 2011]. Further insights are given in Section 3.4 and Section 3.5.

In conclusion, the rupture risk depends on several factors. A rough estimation of the rupture rate of 5 % in 5 years is reasonable [Fiehler, 2012]. Factors like age, size and type of the aneurysm are already influencing the treatment decision of physicians. However, the interference of these factors is still unknown. Whether the type, the size of an aneurysm or hypertension of the patient influences the rupture risk has to be determined. Besides a prediction if an aneurysm ruptures the time of a ruptures is crucial and complicates the topic further. Hence, there are no methods known to accurately predict aneurysm rupture that could support physicians in treatment decision.

2.1.3 *Treatment*

Because of the relatively low rupture rates, the treatment options of unruptured aneurysms have to be considered very carefully. With the increasing use of imaging modalities, the chance to incidentally detect unruptured aneurysms increases [Tummala et al., 2005; Gabriel et al., 2010]. The following treatment options exist:

- Conservative treatment

- Endovascular treatment

    - with coiling (Figure 2.6a)
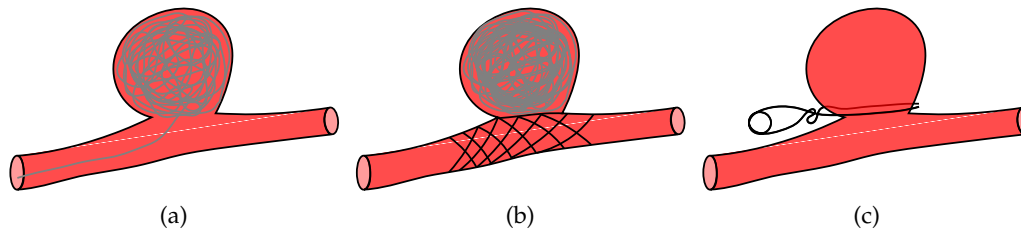
Figure 2.6: The three different treatment options shown as symbolic schemes. (a) Treatment by coiling, (b) treatment by stenting and (c) treatment by clipping.

  – with stenting (Figure 2.6b)

  – with a combination of both techniques

  – Parent Artery Occlusion (PAO)

  – liquid embolization

  • Surgical treatment

  – with clips (Figure 2.6c)

  – using a bypass treatment

Conservative treatment is the first possible treatment option. No intervention is done and the aneurysm growth is screened regularly with angiographical methods. The patient is clarified about risks and chances.

Two active treatment methods are applied routinely: surgical clipping and endovascular coiling. In the first method, a craniotomy is performed and the ostium of the aneurysm is closed with a clip [Solomon et al., 1994]. Endovascular coiling is minimally invasive and was introduced by Guglielmi in 1991 [Guglielmi et al., 1992]. The coil is attached to a delivery wire and mostly passed through the aorta into brain arteries and finally into the aneurysm. The platinum coil is detached electrolytically from the delivery wire to fill most of the aneurysm volume with the coil. The goal is to initiate a thrombotic reaction that occludes the aneurysm.

Active treatment is done via clipping, coiling or stenting

Apart from these two treatment methods, stents are also used [Byrne et al., 2000]. Originally they were used to keep coils confined within the aneurysm, especially in wide neck aneurysms [Piotin et al., 2010]. Recently, so-called flow-diverters have emerged that aim at reducing the blood flow into the aneurysm enforcing a thrombosis [Pierot, 2011]. These stents are very fine-meshed. Furthermore, the stent is used to restore the original vessel by forming a scaffold for fibrocytes. Stents are delivered via a wire to the feeding vessel of the aneurysm. They are expandable and consist of coils that are tortuously arranged to mimic a tube shaped vessel. Stents are very flexible in their shape, they adapt also to gyrose vessels. This treatment option is usually taken into account if the two other methods are impossible due to the morphology of the aneurysm or the vessel topology (e. g., if an aneurysm thrombosis would block the arterial supply of the brain).

Other methods less commonly used are PAO, liquid embolization and a bypass treatment. PAO prevents the blood flow in the whole artery e. g., by using coils [Kallmes and Cloft, 2004]. As most arteries in the Circle of Willis are connected to each other, other arteries can compensate the blood flow of the blocked artery.

However, the consequences of this method have to be well evaluated before. Liquid embolization is similar to coiling in that the aneurysm sac is filled with a liquid that solidifies on blood contact [Mandai et al., 1992]. In case of a bypass treatment, a bridge is build around the aneurysm blocking the blood supply [Ausman et al., 1990].

A lot of effort was made to compare the treatment methods by their mortality, i. e., if patients died because of the treatment and morbidity, i. e., if treatment has led to permanent disability or a poor health. The ISAT study was one of the largest study regarding the comparison of both methods with 2143 patients [Molyneux et al., 2005]. One year after the intervention, the mortality for endovascular treatment was 8.0 %, while for surgical treatment, it was 9.9 %. The morbidity at one year was 15.5 % for endovascular treatment and 21.0 % for neurosurgical treatment. Other studies report mostly lower mortality and morbidity rates for endovascular coiling.

Also, first results have been published regarding the clinical outcome with stents. These report a mortality of 8 % and a morbidity of 4 % in 70 patients [Byrne et al., 2010].

Conservative treatment has the lowest mortality and morbidity rates

Interestingly, the combined mortality and morbidity rate is lower for a conservative treatment (i. e., between 0.5 % and 1.9 % annual rupture rate) than for any sort of interventional treatment (between 8.7 % and 30.9 %). However, these statistical numbers are not yet clinically accepted and unruptured aneurysms are usually actively treated. The chosen treatment option is a complex decision based on several factors like clinical preferences, the experience of the physician and the location of the aneurysm.

Nevertheless, an early detection of unruptured aneurysms is favorable as neuroradiologists and neurosurgeons can individually decide, together with patients, for a therapy option.

2.1.4 *Aneurysm screening*

Screening for aneurysms has been discussed in the scientific medical community. The natural history of aneurysms has to be taken into account, i. e., their prevalence, their rupture rate and their growth. Generally, for being effective, a screening would have to be highly sensitive and specific. Magnetic Resonance Angiography (MRA) or CTA would be the imaging modality of choice. However, for small aneurysms, those modalities have some limitations in terms of sensitivity (see Section 2.2). A general screening for aneurysms similar to screening programs for breast cancer is not reasonable [Wardlaw and White, 2000]. However, a screening is recommended if two or more first-degree relatives have had a SAH or a history of polycystic kidney disease [Rinkel, 2005]. As this standard is very strict, a more individual analysis is suggested since also other risk factors increase the aneurysm prevalence [Fiehler, 2012; Wardlaw and White, 2000]. Also for patients who suffered a SAH, a screening can be taken into account as they are at risk of a recurrence. It has been shown that the risk of recurrences has been halved by screening, however only with a decrease in life quality and increasing costs [Wermer et al., 2008]. The psychological effects of an aneurysm screening should also been taken into account. Screening can lead to anxieties and depressing states [Ferns et al.,

2011]. The patient should be clarified about the consequences of a positive finding [Fiehler, 2012; Rinkel, 2005]. A repetition of screening is advised every 2 to 5 years [Rinkel, 2005].

Although a screening for aneurysms may not be recommended, a CAD system to automatically find aneurysms may be useful as cerebral angiographies are routinely used in the diagnosis and detection of arteriovenous malformations, arteriosclerosis, tumors or a stroke. If the image is routinely acquired or without a specific aneurysm suspicion, the radiologist does not specifically search for aneurysms which can lead to overlooking aneurysms. Also, usually only one radiologist reads the data opposed to screening programs where two radiologists look at the images [Tang et al., 2009]. A CAD system could indicate possible aneurysms that are then evaluated by the radiologist. Additionally, CAD has been proven to be useful as a second opinion [Doi, 2007].

Aneurysm screening is only reasonable in some cases

2.2 ANGIOGRAPHIC MODALITIES

In this section, it is discussed which modalities are suitable for the use in aneurysm management. Each relevant technique is shortly introduced and analyzed for their image quality, radiation, sensitivity to detect aneurysms by physicians and other criteria that influence aneurysm management. Usually, (neuro)radiologists read the images, however also other physicians like neurosurgeons or emergency physicians may read the images.

Non-invasive medical imaging methods form the backbone of modern medicine as they visualize internal structures in the body. Starting from the discovery of the X-radiation by Wilhelm Röntgen in 1885, medical imaging is now routinely used in medical environments for diagnosis and therapy planning. Especially the invention of Magnetic Resonance Imaging (MRI) and Computed Tomography (CT) in the 1970s are the reason for the success of the medical imaging modalities.

Among others, X-ray based methods, magnetic resonance modalities, sonography modalities and nuclear medicine modalities exist to create images of the human body. X-ray based and magnetic resonance methods are used to visualize the three-dimensional morphology, whereas sonography techniques are used to depict a two-dimensional slice[2]. Nuclear medicine modalities and a subtype of MRI are functional imaging techniques that are able to visualize time-resolved processes such as blood-flow or Contrast Agent (CA) concentration.

Generally, CT and MRI methods can be used to evaluate cerebrovascular diseases. CT is commonly deployed if SAH is suspected [Wanke and Forsting, 2008]. SAH can also be detected by MRI using the FLAIR sequence [Fiebach et al., 2004], although this is only rarely used. To detect other, especially subtle vascular diseases like cerebral aneurysms, however, specialized angiographic modalities are by far more suitable. These techniques are used to visualize blood vessels in the human body. Methods including the administration of CA exist, but there are also other methods that do not rely on CA. Of particular interest are the depiction of arteries, veins and the heart chambers. With respect to cerebral aneurysms, the cerebral vasculature morphology is important, i. e., the vessels inside the brain. Additionally, functional angiographic modalities that visualize the time-dependent blood flow exist. In the

---

2 Three-dimensional ultrasound containing multiple slices also exists.

following, angiographic modalities and Transcranial Doppler Sonography (TCD) are analyzed.

To quantitatively compare several imaging method and other factors, objective measures have to be established. Assuming a valid ground truth is provided, sensitivity and specificity can be computed. The sensitivity se is defined as:

$$se = \frac{n_{TP}}{n_{TP} + n_{FN}}, \qquad (2.1)$$

where n_{TP} are the number of true positives, i.e., the correctly found aneurysms and n_{FN} is the number of false negatives, i.e., the aneurysms that were not found. Thus, se gives the percentage of aneurysms that were found. Detection rate is used as a synonym for sensitivity.

Definition of sensitivity and specificity to evaluate the angiographic modalities

The specificity sp is defined as:

$$sp = \frac{n_{TN}}{n_{TN} + n_{FP}}, \qquad (2.2)$$

where n_{TN} is the number of true negatives, i.e., the correctly rejected structures and n_{FP} is the number of false positives, i.e., the incorrectly found aneurysms. This number measures how many aneurysms are erroneously found although no aneurysms are present.

A high sensitivity and a high specificity are simultaneously desirable as it indicates no errors. However, with respect to aneurysm detection or pathological findings in general, a high sensitivity is more important than a high specificity because overlooked aneurysms have a worse consequence than false positive findings.

As gold-standard double-read Intra-arterial Digital Subtraction X-ray Angiography (2D-DSA) is frequently used in publications [Wanke and Forsting, 2008; Sugahara et al., 2002; Suri et al., 2002a]. The double-reading is done commonly by experienced neuroradiologists. The reason is the excellent spatial image resolution and the clear contrast between blood vessels and background. Thus, 2D-DSA has a sensitivity and specificity of 100 % by definition.

2D-DSA is used as gold-standard

The following modalities are relevant for aneurysm management and are therefore discussed in the following sections:

- Cerebral Angiography

- CT Angiography (CTA)

- Magnetic Resonance Angiography (MRA)

- Transcranial Doppler Sonography (TCD)

2.2.1 *Cerebral Angiography*

Two types of the classical cerebral angiography exist: 2D-DSA (see Figure 2.7a) and 3D-RA (see Figures 2.7b and 2.7c). In this work, both types are aggregated by the term Cerebral Angiography (ANG). Both types rely on injecting an iodine-based CA intra-arterially that has a high density. Thus, the X-rays are absorbed

(a)

(b)   (c)
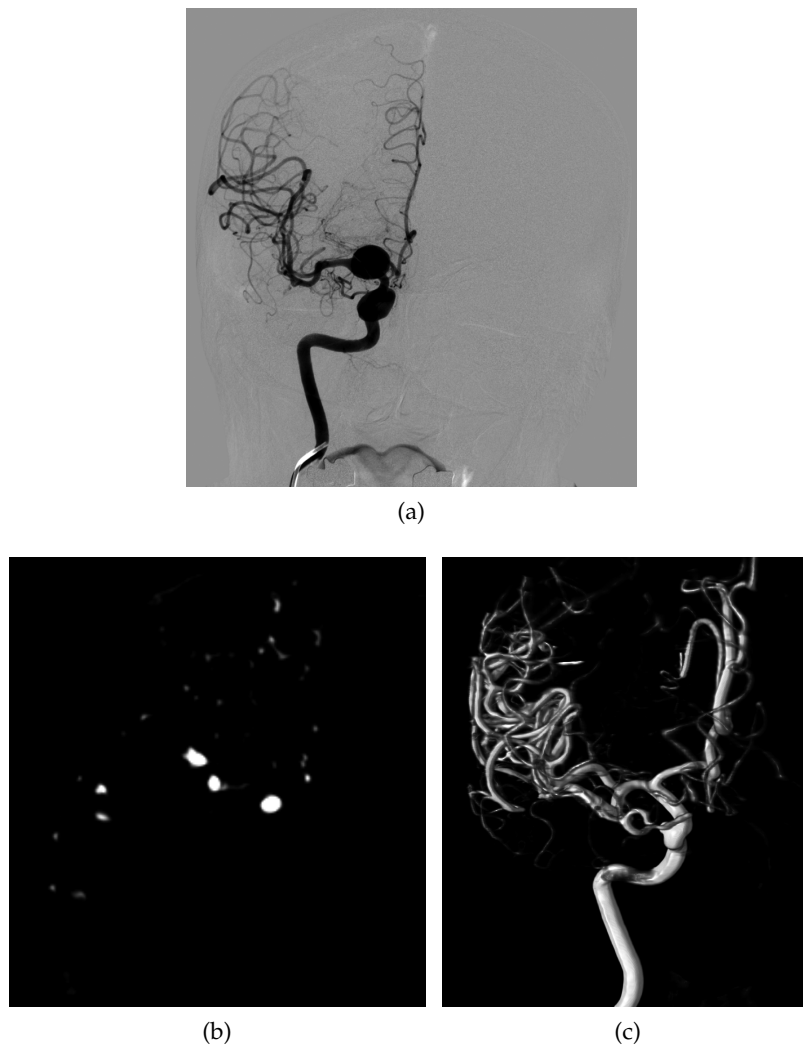
Figure 2.7: Example visualization of (a) 2D-DSA image displayed as a tMIP containing two aneurysms, (b) a transversal slice of a 3D-RA and (c) a volume-rendering of 3D-RA showing the left ACI. The data sets are courtesy of Oliver Beuing, department of neuroradiology, University Hospital Magdeburg.

by the CA. A mask image is acquired prior to the CA injection. The mask image is then subtracted from the contrast-enriched images in real-time leaving only the vessels visible. In 2D-DSA, the propagation of the blood over time is made visible in a two-dimensional image, thus it is a type of fluoroscopy. This modality is used to visualize the hemodynamics of the blood. It is typically acquired with 5 Frames per Second (FPS) to 30 FPS.

In 3D-RA only the morphology of the cerebral vessel system is displayed, no hemodynamics is shown. A X-ray gantry rotates around the head and acquires 2D projections, from which a three-dimensional volume is reconstructed similar to CT. In these projection images, however, the hemodynamics is visible.

As only one CA injection at a time is done at both modalities, only a part of the cerebral vasculature, the contrasted artery and their successors, are visible. If an examination of the whole vasculature is necessary, four consecutive image

sequences have to be acquired as four arteries supply the brain with blood (the left and right ACI and the left and right Arteria vertebralis³).

In case of vascular defects, bi-plane 2D-DSA images are routinely acquired. The images are two-dimensional and time-dependent (2D+t). Based on the two projections, the physician is able to build a mental representation of the current branch of the cerebral vasculature system. The hemodynamics in aneurysms is different than in normal vessels as the velocity is usually smaller and the flow is more turbulent. This flow characteristics and the shape help radiologists to find aneurysms.

In some cases, a selective catheter angiography is performed where a catheter is pushed forward into the aneurysm and the CA injection is then started. The hemodynamics of large aneurysms can be better evaluated by using this technique.

3D-RA is more and more routinely acquired additional to 2D-DSA. However, in the literature it is mostly regarded as helpful additional image source. 3D-RA is a three-dimensional modality providing geometrical information and no flow information. Hence, the physician can only rely on the shape information of aneurysms as a criterion. The precise 3D visualization of the aneurysm neck, the shape, the size and the relationship to nearby vessels are important facts for treatment decisions and planning of endovascular therapy [Anxionnat et al., 2001]. 3D-RA has the potential to replace 2D-DSA as the gold-standard [Shi et al., 2011; van Rooij et al., 2008].

The disadvantages of cerebral angiographies are the invasiveness and the radiation exposure. For 2D-DSA, a mean effective dose of 3.4 mSv per scan was reported. For 3D-RA, a lower mean effective dose of 0.2 mSv was reported [Bridcut et al., 2007]. Due to the radiation and the interventional procedure, the cerebral angiography increasingly substituted by its CT and MRI counterparts [Wanke and Forsting, 2008].

2.2.2 CT Angiography

The CTA (Figure 2.8a and 2.8b) is less invasive than ANG, but also requires the injection of a CA to highlight the blood vessels. The iodine-containing CA is injected in an arm vein; this procedure is more comfortable for the patient than the intra-arterial catheter injection in ANG. CTA is no subtraction-based modality, i. e., additional objects are visible in the scans as the main difference to CT are the contrasted blood vessels. The Hounsfield Unit (HU) of the contrast enriched blood in CTA is in the same range as bones, which leads to problems separating those two structures. Due to research progress, multi-detector CT scanners, flat detector CT scanners and dual-source or dual-energy CT scanners were developed that lead to improved image quality with < 1 mm slice thickness at a shorter scan time and lower radiation exposure [Kalender, 2011].

CTA is more patient friendly as 3D-RA, but the resolution of 3D-RA is superior (see Table 2.2). The disadvantage of radiation exposure still remains. The effective dose for the patient is between 4.7 mSv and 13.7 mSv per scan [Fraioli et al., 2006]. Another study reports a radiation exposure of 1 mSv to 2 mSv for a head CT similar to CTA [Furlow, 2010]. Thus, CTA has a considerably higher radiation exposure than 2D-DSA and 3D-RA. Modern CT scanners offer low-dose protocols with 0.3 mSv to

---

3 Actually, the Arteria carotis externa provides also blood to the brain, but only to the cerebral membrane and to the face, though it is usually neglected.

(a)   (b)
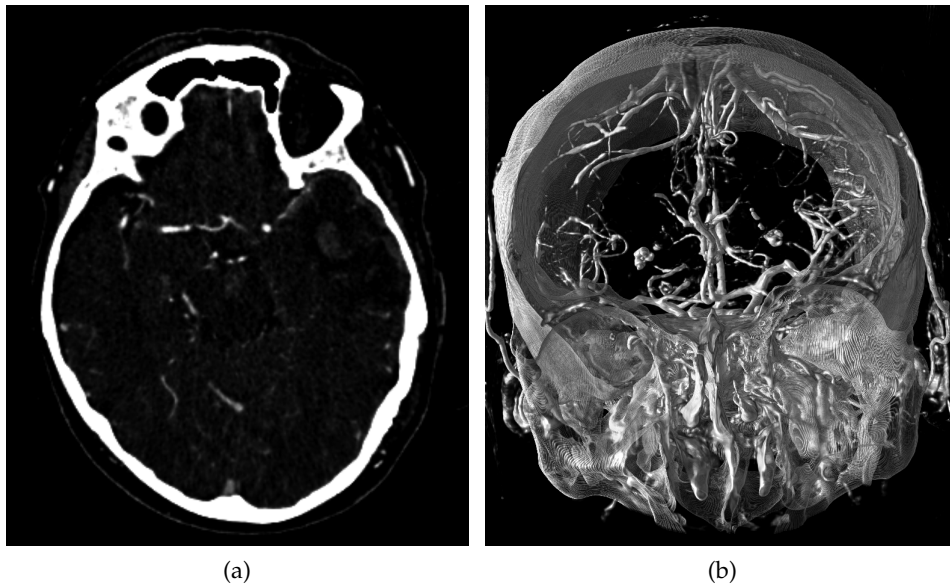
Figure 2.8: Example visualization of (a) a CTA slice and (b) a CTA volume rendering (the volume rendering is clipped in front and the back so that the skull does not occlude the vessels). The data sets are courtesy of Oliver Beuing, department of neuroradiology, University Hospital Magdeburg.

1.4 mSv per scan with a similar quality [Siemens, 2012; Philips, 2012]. In contrast to ANG, CTA depicts the complete cerebral vasculature at once.

CTA has the potential to become the new gold standard

The detection rate of cerebral aneurysms in CTA is 85 % to 98 % [Wardlaw and White, 2000]. Due to the increasing quality of CT technique, the detection numbers are also generally increasing in newer studies [Teng et al., 2006]. A recent meta-study confirms this fact by reporting a sensitivity in 1-row CTA of 91.8 %, in 4-row CTA of 92.8 % and in 64-row CTA of 97.8 % [Menke et al., 2011].

However, the detection rate decreases with aneurysm size. For aneurysms smaller than 3 mm, a detection rate of only 61 % is reported [White et al., 2000]. This detection rate also significantly increases with the amount of detector rows. For aneurysms $\leqslant$ 4 mm, the detection rate is 75 % with 1-row CTA and 94 % for 64-row CTA [Menke et al., 2011].

Furthermore, problems regarding the detection arise if the location of the aneurysm is close to a bone structure like the skull. It was shown that CTA with bone subtraction leads to a better sensitivity, 91.5 %, than without bone subtraction, where 84.4 % of the aneurysms were found [Hwang et al., 2010]. Three techniques exist to suppress bones: Bone Subtracted Computed Tomography Angiography (BSCTA) or digital subtraction CTA, dual-energy CTA and software-based methods.

The use of modern scanners leads to a detection rate of 98 % in CTA data sets

In BSCTA, two scans are acquired: a non-enhanced CT scan and a CTA scan. Bones are extracted in the CT volume and then, the volume is registered to the CTA volume. Finally, bones are subtracted in the CTA scan. BSCTA allows for robust elimination of bony structures and thus is useful for detection and therapy planning of cerebral aneurysms, especially if they are located at the skull base [Tomandl et al., 2006]. Sensitivity regarding aneurysm detection increases significantly [Hwang

et al., 2010]. However, the radiation exposure increases compared to CTA by 20 % to 25 % [Van Straten et al., 2005].

The dual-energy CTA relies on only one scan with two different tube voltages (there are two X-ray sources and detector pairs arranged at 90°) that are simultaneously acquired. The bone removal is then trivial as the bone and contrast-enhanced blood characteristics are different at two different voltages. It was shown that the sensitivity is between 95 % and 96.5 % [Zhang et al., 2010b; Zhou et al., 2012]. For aneurysms $\leqslant 3$ mm, a sensitivity of 91.3 % was reported [Zhou et al., 2012]. It was also shown that the radiation exposure is smaller in dual-energy CTA than in BSCTA [Zhang et al., 2010a].

Software-based approaches for CTA bone removal without acquiring a second scan have also been proposed based on an interactive controlled watershed algorithm [Hahn et al., 2006] and a probabilistic model [Militzer and Vega-Higuera, 2009]. However, these methods have disadvantages due to their challenging task.

CTA is widely regarded as a possible replacement for 2D-DSA and 3D-RA although this modality has a higher radiation exposure [Zhang et al., 2010a; Wanke and Forsting, 2008]. The presence of bones can be circumvented by using dual-energy CTA.

2.2.3 *MR Angiography*

Two different MRA techniques exist to display the cerebral vasculature, one incorporating the injection of CA, the other without CA administration. The latter can be divided into five subtypes according to [Suri et al., 2002a]:

- Contrast-Enhanced Magnetic Resonance Angiography (CE-MRA) (examples displayed in Figures 2.9c and 2.9d)

- non-contrast enhanced MRA

    – Time of Flight Magnetic Resonance Angiography (TOF-MRA) (examples displayed in Figures 2.9a and 2.9b)

    – black-blood MRA

    – Phase-Contrast Magnetic Resonance Angiography (PC-MRA) (an example displayed in Figure 2.10)

    – T_2-weighted MRI

    – T_2^*-weighted MRI

CE-MRA relies on the injection of a CA that is Gadolinium-based and reduces the T_1 value of the blood [Ho et al., 2005]. Similar to CTA, the CA is also injected intravenously. So-called blood-pool agents that remain in the vasculature up to an hour, allow high resolution scans with larger acquisition times. Timing of the CA injection plays an important role in CE-MRA. Improper timing results in artifacts and worse image quality as well as a preferred visualization of veins compared to arteries [Suri et al., 2002a]. A major advantage is the short scan time with good Signal-to-Noise Ratio (SNR) (approximately 20 s) [Weiger et al., 2000].

TOF-MRA relies on the in-flow effect [Lewin et al., 1991]. A short repetition time is used that results in a much stronger signal of the flowing blood compared to the
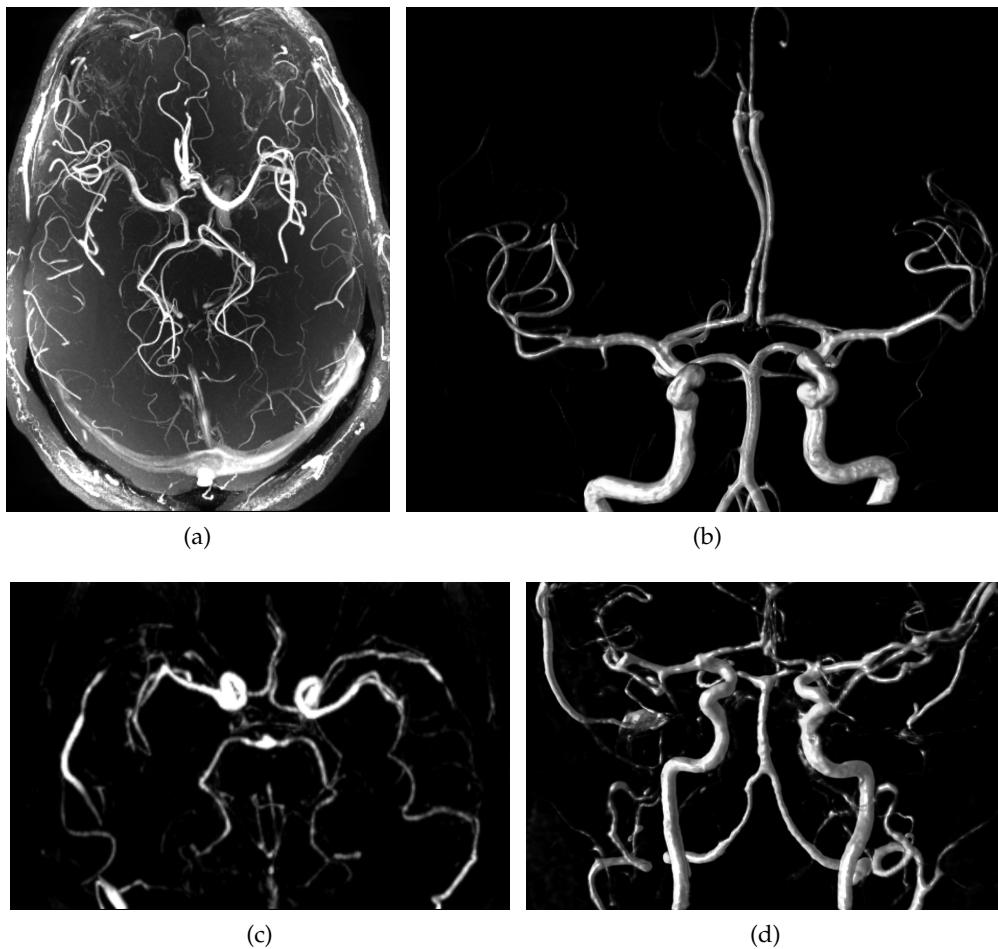
Figure 2.9: Visualizations of example data sets. Displayed are (a) a MIP of a TOF-MRA volume around the Circle of Willis, (b) a volume rendering of a TOF-MRA volume, (c) a MIP of a CE-MRA volume around the Circle of Willis and (d) a volume rendering of a CE-MRA volume. The data sets are courtesy of Oliver Beuing, department of neuroradiology, University Hospital Magdeburg.

non-moving tissue which exhibit low signal intensities [Suri et al., 2002a; Backens and Schmitz, 2005]. The technique is non-invasive as it requires no CA, but rather relies on the flowing properties of blood. A drawback is that slow flowing areas like large aneurysms or turbulent blood do not provide accurate vessel visualization [Suri et al., 2002a]. Also, the scan time is considerably longer than for CE-MRA, namely 4 min to 12 min [Hoogeveen, 2007]. The quality of TOF-MRA particularly relies on the magnetic field strength.

Black-blood Magnetic Resonance Angiography (BB-MRA) aims to minimize flow related-signal in contrast to TOF-MRA. Signal voids exist at flow positions describing the vasculature and leading to its name [Suri et al., 2002a]. This technique enables to visualize the vessel lumen more accurate than TOF-MRA and is less sensitive to slow flowing blood. However, as also other dark or black areas exist in these images, the interpretation is challenging for radiologists. It is rarely used in neuroradiological departments, but it is suggested as useful additional technique as morphological measurements can be done more accurately [Stivaros et al., 2009].

MRA has the advantage of no radiation exposure
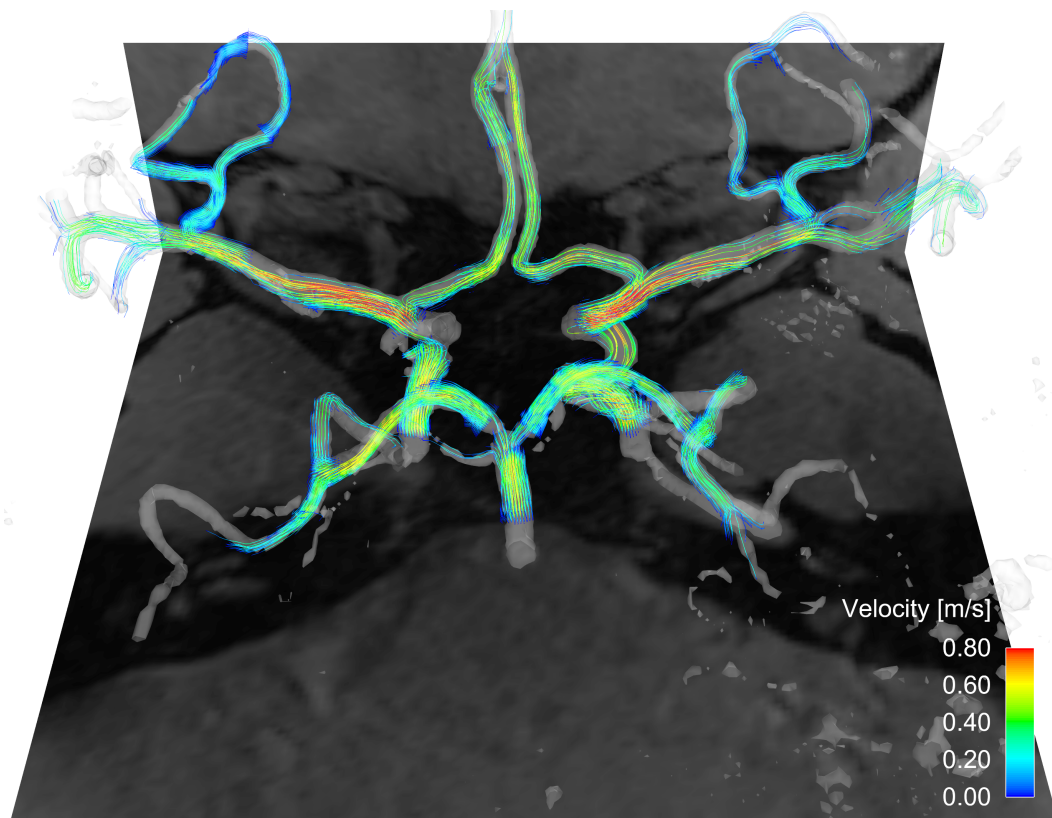
Figure 2.10: Visualization of a PC-MRA volume by employing transparent streamlines and the overlaid vessel morphology. The data sets are courtesy of Daniel Stucht, department of biomedical magnetic resonance, University of Magdeburg and Oliver Beuing, department of neuroradiology, University Hospital Magdeburg.

Opposed to other MRA techniques PC-MRA is a 3D+t functional imaging technique, although also 2D+t images are possible [Dumoulin et al., 1989]. This means, additionally to the morphology, the blood flow direction and velocity is measured. The dislocation of the blood can be estimated by the phase difference that is caused by moving through a bipolar gradient magnetic field [Suri et al., 2002a]. PC-MRA also works without CA. A major disadvantage is the long acquisition time (approximately 10 min for a field of view covering the Circle of Willis and a resolution of 0.8 mm per pixel) as at least four acquisitions are needed to sample all dimensions in 3D (three for all dimensions and one reference frame). Also, the spatial resolution is limited. PC-MRA is a rather exotic technique that has its strength in other areas than imaging, e. g., quantitative flow measurement [Markl et al., 2003].

Additionally, also T_2-weighted MRI and T_2^*-weighted MRI exist, e. g., the FLAIR sequence, but as they are not specialized for the visualization of vessels, the other MRA modalities are clinically preferred.

Further technical details about the MRA imaging modalities can be found in [Suri et al., 2002a].

The technical progress of magnet resonance modalities in the past few years is promising. High field strength in MRI of 3 T or even 7 T have led to higher resolution at the same scan time or a shorter scan time at the same resolution.

Recently, 3 T MRI scanners are available more frequently [Kapsalaki et al., 2012]. Also, parallel imaging methods and compressive sampling lead to better image quality at the same scan time [Trzasko et al., 2011].

The detection rate of MRA is generally lower than the rate of CTA, 79 % to 97 % [Wardlaw and White, 2000]. A recent meta-study reported a sensitivity of 85 % [Zhang et al., 2012]. The rate also decreases with size. Only 38 % of the aneurysms with a size ⩽ 3 mm were detected [White et al., 2000]. Even in a more recent study using 3 T TOF-MRA images, the sensitivity was only 67 % for aneurysms ⩽ 3 mm compared to 89 % overall [Hiratsuka et al., 2008]. Another study reports considerably better detection rates, 99.3 % overall and 98.2 % for aneurysms < 3 mm [Li et al., 2011] with 3 T TOF-MRA images. Initial results of aneurysm detection with 7 T scanners are available, but the results are only preliminary and the statements vague [Mönninghoff et al., 2009]. In conclusion, MRA is only suitable for detection of aneurysms with a size ⩾ 3 mm.

Even if scanners with high Tesla field strength are used, the detection rate in MRA data sets is lower than in CTA data sets

It is difficult to compare the different types of MRA with respect to their sensitivity. The detection rate of TOF-MRA images acquired with field-strength ⩾ 3 T and CE-MRA are comparable. However, different studies report contrary statements whether TOF-MRA or CE-MRA leads to a better detection rate [Gibbs et al., 2005; Nael and Villablanca, 2006]. CE-MRA is more suitable for follow-up investigation after endovascular aneurysm repair [Kaufmann et al., 2010]. Black-blood MRA was assessed comparable to TOF-MRA, however no quantitative study was performed [Stivaros et al., 2009]. In a small study, the sensitivity of PC-MRA was worse than the sensitivity of TOF-MRA [Ikawa et al., 1994].

The visualization type influences the detection rate. An accurate visualization is an axial-based 2D slice view of the images. Also, 3D visualizations are suitable [Li et al., 2012]. In contrast, MIP as a projection-based technique is not suitable as important information are lost [Wardlaw and White, 2000].

Most studies conclude that MRA can be used for detection of aneurysms; however other modalities have to be used to exclude small aneurysms. A more critical study reports different aneurysm findings in MRA and 2D-DSA in 59 % of the cases [Schwab et al., 2008]. False-positives have been found and the MRA findings differed substantially from 2D-DSA in terms of location, number and aneurysm type. The authors criticized that previous studies were done in an academical setting that does not reflect a clinical environment. It was suggested to use MRA techniques neither as screening modality nor as sole basis for a therapeutic decision making.

2.2.4 *Transcranial Doppler sonography*

Transcranial Doppler Sonography (TCD) is also a non-invasive technique to visualize cerebral blood vessels. The method relies on exploiting the Doppler effect to measure blood flow velocity. Ultrasound is blocked by bony structures like the skull. Thus, regions with thinner walls have to be found. In 5 % to 20 % of all patients no such region can be identified [Wanke and Forsting, 2008]. Additionally, TCD is very operator-dependent and it was reported that in 18 % of the cases the quality of the ultrasound was unsatisfactory for evaluation of the aneurysmal site [Cordebar et al., 2004].

TCD is unsuitable for aneurysm detection

An advancement of TCD, Power TCD, was applied for cerebral aneurysm detection. Detection rates of 82 % have been reported [White et al., 2000]. The sensitivity dropped to 35 % for aneurysms $\leqslant 5\,\text{mm}$ [White et al., 2001]. Although the method is quick, safe and inexpensive, TCD cannot be recommended for routine use of aneurysm detection because of the low sensitivity [Wanke and Forsting, 2008]. Even for the use of follow-up after endovascular treatment, the technique cannot be recommended [Cordebar et al., 2004]. From the imaging point of view, TCD has a low SNR with many artifacts which leads to a challenging reading and analysis of the images. Also, the modality is only two-dimensional.

2.2.5 *Clinical detection of aneurysms*

The detection of aneurysms by physicians depends on several factors:

- aneurysm-based
    - size of aneurysm
    - location of aneurysm (i. e., parent vessel)
- image-based
    - contrast vessel-background
    - image resolution
    - image artifacts
- experience of physician
    - with reading angiographic images
    - with aneurysms detection

The aneurysm-based factors have been discussed in Section 2.1.2, the image-based factors have been discussed in Section 2.2 and the last factor is shortly discussed in this section.

From the imaging modality side, there is a trend in clinical institutions to use CTA and MRA instead of ANG. Reasons are the more patient-friendly approach in case of CTA and the non-invasiveness and lack of radiation exposure in case of MRA. Nevertheless, ANG is still the gold standard with regard to resolution and clinical detection rate of aneurysms. Modern CT scanners have an isotropic sub-mm resolution, a high SNR and thus a high sensitivity for aneurysms. Dual-energy CT scanners also circumvent the problem of aneurysm finding close to bones. MRA has a lower sensitivity compared to ANG and CTA, especially for aneurysms $< 3\,\text{mm}$. However, these aneurysms also have a smaller rupture rate than larger aneurysms. Therefore, MRA is an option for the use in screening and as follow-up of endovascular treated aneurysms.

An overview about all discussed modalities with relevant parameters is given in Table 2.2.

Most studies about aneurysm detection in angiographies do not consider the experience and specialization of the physician. The expertise and experience in reading an angiographic image and searching for aneurysms is relevant. A highly

Table 2.2: Comparison of different modalities regarding technical specifications. The data are taken from recent publications [White et al., 2000, 2001; Bridcut et al., 2007; Furlow, 2010; Menke et al., 2011; Hiratsuka et al., 2008; Ikawa et al., 1994] and are valid for modern scanners only. Dim.: Dimension, Voxel size: typical voxel size in plane and out of plane, se: Sensitivity, proj.: projective technique without voxel size.

Modality	Dim.	Voxel size	se (all/$\leqslant 3$ mm)	Radiation	Duration	CA
Unit	-	mm	-	mSv	min	
2D-DSA	2+t	proj.	100 %/100 %[a]	3.4	< 1	x
3D-RA	3	0.5/0.5	~2D-DSA	0.2	< 1	x
CTA	3	0.5/0.5	98 %/94 %	2.0	< 1	x
TOF-MRA	3	0.4/0.4	89 %/67 %	none	~ 8	
CE-MRA	3	0.5/0.6	~TOF-MRA	none	~ 1	x
BB-MRA	3	unknown	~TOF-MRA	none	~ 4	
PC-MRA	3+t	0.8/0.8[b]	70 %/-[c]	none	~ 10	
TCD	2+t	proj.	82 %/35 %[d]	none	real time	

[a] per definition.
[b] PC-MRA has a temporal resolution of 64 ms.
[c] no data was available.
[d] for aneurysms $\leqslant 5$ mm as no information for aneurysms $\leqslant 3$ mm is available.

specialized neuroradiologist found more aneurysms than a neurosurgeon and a general radiologist in MRA volumes [Okahara, 2002]. This statement most likely applies also to other modalities than MRA. Furthermore, the detection rates of aneurysms in clinical studies are dependent on the prevalence of aneurysms in the data: the higher the prevalence, the higher is the detection rate [Wardlaw and White, 2000]. As most clinical studies are performed with more than 75 % aneurysm prevalence, the detection rate is overestimated.

The experience of the physician plays a major role in aneurysm detection

The aim of a Computer-aided Diagnosis (CAD) algorithm is to support radiologists in reading the images by pointing them to possible abnormal structures such as aneurysms. CAD systems are useful as a second opinion for a radiologist. It is especially important that such a system detects small aneurysms, aneurysms at unusual positions and in modalities that have a detection rate < 95 %. It has been shown that CAD is able to significantly improve physician sensitivity [Hirai et al., 2005] and is also able to reduce the mean reading time [Kakeda et al., 2008]. All angiographic three-dimensional modalities have their relevance in aneurysm management and, in general, in vascular imaging. They are used according to the diagnostic question, the availability and preference of the radiologist or the clinical institution.

2.3 ANEURYSM MANAGEMENT AT UNIVERSITY HOSPITAL MAGDEBURG

This research was done in cooperation with the department of neuroradiology at the University Hospital of Magdeburg. Therefore, the current practice is introduced in this section.

A neuroradiological department is relatively rare in Germany and not situated in every major hospital, not even in every University Hospital. Thus, the department has a relatively large draw radius of about 100 km. The next neuroradiological departments are situated in Berlin, Leipzig and Hannover. The department is headed by Prof. Skalej and consists of ten neuroradiologists.

Multiple angiographic images have to be managed in the daily workflow. In case of an emergency admission and symptoms like a severe headache or if a hemorrhage, e. g., a SAH, is suspected, a CTA volume is acquired. The presence of intracerebral blood is then confirmed or excluded by physicians that read the image slice by slice. Additionally, as ruptured cerebral aneurysms are a major causes of SAH, the ruptured aneurysm quickly is found in most cases.

Other suspicions that entail an acquisition of a CTA are stroke and vascular defects. MRA images are acquired if the patient is unable to undergo CTA, e. g., because of radiation protection or if no explicit aneurysm suspicion is present. Additionally, other angiography images from foreign institutions that were referring the patient to the University Hospital are imported into the database.

If a suspicion of a ruptured aneurysm is present because of SAH or other symptoms, the three-dimensional data-sets are carefully evaluated to find the site. If no aneurysm symptom is present, an explicit search for an unruptured aneurysm is not done. Rather, the image is scanned quickly slice-by-slice for the clinical report. Thus, it depends on the skill of the radiologist and the time pressure if a cerebral aneurysm is found. Especially small asymptomatic aneurysms tend to be overlooked.

If an unruptured aneurysm is found, a CTA is done to confirm the aneurysm if it has not been acquired before and ANG images are acquired to exclude a false finding. Quantitative measurements of the found aneurysms are done and the feeding vessel is determined. Additionally, these ANG modalities are used to decide, after consulting the patient, for a treatment. The decision is done by a council of neuroradiologists and neurosurgeons. An endovascular treatment is preferred; however cases where such a treatment is not possible are referred to the neurosurgery department at the University Hospital. A conservative treatment is usually not desired by the patient independent from the recommendation like explained in Section 2.1.3.

2D-DSA, 3D-RA, CTA, TOF-MRA and CE-MRA are used for aneurysm management at the University Hospital of Magdeburg

If an endovascular treatment was chosen, this is done at the neuroradiology department. A coiling procedure is the first choice, a stenting procedure is only considered if the arterial tree ahead of the aneurysm is complicated, if outflow arteries originate from the aneurysm or if a coiling would otherwise inhibit the blood flow. Also, health economic reasons have to be considered as special fine-mesh stents, so-called flow-diverters are very cost-intensive.

Throughout the procedure, 2D-DSA is done to monitor the process of the catheter and the occlusion of the aneurysm. Complications like blood wall perforation by the catheter, coil or aneurysm rupture are immediately detected. The duration of the procedure depends on the difficulty due to the aneurysm location and the aneurysm size.

Regular follow-up is done after the procedure with CE-MRA. This modality is suitable for detection of recurring perfusion of the aneurysm (see Section 2.2.3).

3

COMPUTER-AIDED MANAGEMENT OF CEREBRAL ANEURYSMS

In today's clinical practice, computers are regularly used for image analysis, segmentation, quantification, detection and other purposes for CAD (see also Section 4.2). In this chapter, the potential of CAD algorithms in aneurysm management is discussed and existing algorithms are presented.

Different clinical workflows in the area of aneurysm management have been proposed that incorporate patient-specific data to assist the physician in the analysis and treatment of cerebral aneurysms. A workflow is defined as sequence of concatenated steps that starts with the acquisition of angiographic data sets and ends with an appropriate visualization of annotated or information-enriched image data.

The two research projects @neurIST and Mobestan have been working on this subject. While @aneurIST [Frangi, 2007] is a large intra-European project funded by the European Union, Mobestan [Thévenin, 2008] is a smaller project within the University of Magdeburg funded by the state of Sachsen-Anhalt. The proposed workflow of @aneurIST can be found in [Villa-Uriol et al., 2010, 2011] and an excerpt of the workflow of Mobestan is published in [Janiga et al., 2011, 2013].

The patient-specific concepts to specifically adapt each relevant part to the patient have a major relevance. Therefore, the goal of computer-aided management is to model a workflow to reach the best possible outcome by providing patient-specific clinical decision support.

The following steps are necessary to build a workflow:

- acquisition of angiographic image data and addition of the data sets and other relevant information to the patient entry in the clinical database

- extraction of vessels (Section 3.1)

- detection of aneurysm, either by the physician or automatically (Section 3.2)

- extraction of aneurysm Region(s) of Interest (ROI) (Section 3.3)

- aneurysm segmentation and model generation (Section 3.3)

- aneurysm shape analysis and quantification (Section 3.4)

- performing a blood flow simulation (Section 3.5)

- performing a virtual stenting or coiling (Section 3.6)

- rupture prediction based on shape-based or hemodynamic-based features (Sections 3.4 and 3.7)

- visualization of e. g., the morphology or the blood flow simulation (Section 3.8)
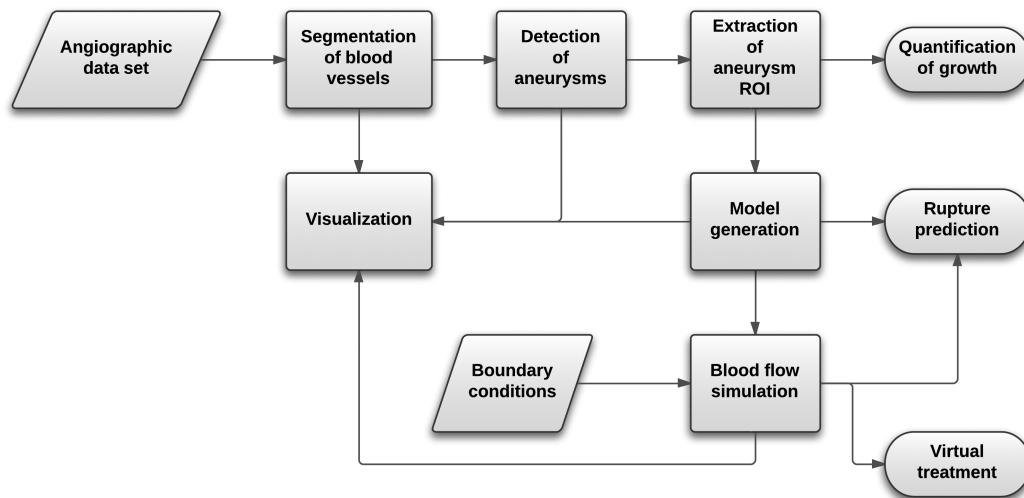
Figure 3.1: Simplified workflow of computer-aided management of cerebral aneurysms.

These steps are interdependent as summarized in Figure 3.1 and will be described in detail in the following sections.

3.1 SEGMENTATION OF BLOOD VESSELS

Angiographic modalities depict the cerebral vascular system. However, also non-vascular objects are visible in the image data. As only the vessels are relevant for analysis, these have to be extracted from the image data by segmentation techniques. The method has to be chosen according to the modality. Trivial methods reach good results for 3D-RA, but sophisticated methods have to be used for the extraction of vascular structures in CTA. The goal of the segmentation is to extract a vessel model of the complete cerebral vessel or arterial system, respectively.

Vessel segmentation is a prerequisite for many of the before mentioned workflow steps, particularly blood-flow simulations, aneurysm quantification and analysis of the aneurysm shape. Vessel segmentation only depends on the image data.

Vessel segmentation forms the basis of most workflow steps

Apart from vessel segmentation, a classification of cerebral arteries has been presented [Uchiyama et al., 2006]. It is based on a cerebral atlas and includes point-based registration at bifurcation points.

Several vessel segmentation techniques have been proposed. Detailed reviews can be found in [Kirbas and Quek, 2004; Suri et al., 2002b; Lesage et al., 2009]. [Lesage et al., 2009] categorize the segmentation methods by three major aspects: models, features and methodology. Models describe the (simplifying) assumptions about the vessels, whereas features aim at describing these models in the image. The methodology then employs a model guided by features to compute the final vessel segmentation. The disadvantage of most algorithms is their unknown multi-modality ability as they are only tested on one modality. The modality-dependence is discussed as last topic of this section.

3.1.1 *Vessel models*

Models can be further subdivided into appearance models, geometric models and hybrid models [Lesage et al., 2009]. Appearance models are based on the expectation of a certain intensity distribution of vessels. In angiographic modalities, vessels usually have a higher intensity than the background. Therefore, intensity-based models have been presented [Chung et al., 2002; Manniesing et al., 2006].

In contrast to appearance models, geometric models use the shape of vessels as driving force. An Active Shape Model (ASM) model was proposed for segmentation of Abdominal Aortic Aneurysm (AAA) [de Bruijne et al., 2003]. Centerlines can be seen as geometrical modeling since they represent the skeleton of a generalized cylinder, e. g., in [Bouix et al., 2005].

By far the most methods employ hybrid information of both models, e. g., by template-based shape spaces to model vessels as generalized ellipsoids [Frangi et al., 1998; Sato et al., 1998].

3.1.2 *Vessel features*

Features can be categorized either as local intensity-based or as local geometry-based [Lesage et al., 2009]. Intensity features can be e. g., the *medialness* operator [Aylward et al., 1996] or the *spherical flux* [Law and Chung, 2009].

An example for geometric features is the *vesselness* feature. It employs second-order intensity derivatives for modeling a feature describing vascular structures. The local intensity variation is analyzed by an eigenanalysis of the Hessian matrix. The implicit similarity to bright elongated ellipsoids is computed. These have the property of two large eigenvalues and one eigenvalue close to 0. The various variants of the feature enjoy a high popularity in the vessel segmentation community [Frangi et al., 1998; Sato et al., 1998; Koller et al., 1995; Li et al., 2003; Forkert et al., 2011]. The vesselness feature is mostly used as multiscale filter employing Gaussian scale-space theory.

The vesselness feature is commonly used as feature to enhance vessels

3.1.3 *Extraction methodology*

The extraction methodology can be divided into *skeleton-based* and *non-skeleton-based* methods [Suri et al., 2002b]. While skeleton-based approaches derive a segmentation based on the detection of the vessel centerline, non-skeleton-based approaches directly compute a segmentation on the image data. Non-skeletal approaches can be categorized in region-growing, threshold-based, active contours and stochastic approaches [Lesage et al., 2009].

Most algorithms require a pre-processing to initialize the segmentation. The initialization can be done either automatically or user-given. Automatic initialization may be based on a priori knowledge, such as a mask of the object of interest or a probabilistic atlas [Passat et al., 2005]. User-based initialization ranges from defining a single point up to drawing a ROI.

Abnormalities like vessel stenoses, aneurysms or calcifications usually interfere with the vessel segmentation algorithms as they change the vessel characteristics.

Some methods are robust against aneurysms, e. g., a centerline-based segmentation of the aorta that is able to handle AAA in the image data [Wink et al., 2000].

A major problem of vessel segmentation algorithms is the restricted image resolution that causes problems to segment small vessels. Also, the kissing vessel effect where two nearby vessels seem to touch [Tomandl et al., 1999] and anomalies cause problems. The quality of an algorithm can be assessed by comparing the results with ground truth data. The crucial question is always what the expert defines as minimal vessel diameter that has still to be included in the segmentation. Common choices are a diameter of 1 mm to 2 mm. In order to find vessels having a smaller diameter, the parametrization can be adapted. However, it is likely that a higher noise level severely influences the segmentation quality then.

Most skeleton-based methods are semi-automatic as they need a user-given seed point at the root of the vascular tree. The local orientation of the vessel can be used in a tracking-like algorithm by, e. g., employing the Hessian matrix [Aylward and Bullitt, 2002]. If the start point and the end point of a vessel is given, an energy-minimizing approach can be used to determine the centerline [Wink et al., 2004; Udupa and Samarasekera, 1996].

Flux-driven automatic centerline extraction methods have been proposed [Bouix et al., 2005] that rely on the outward flux of the gradient vector field of a distance function to the boundary of vessels. Another interactive algorithm is based on a medialness description of the centerline and findings of bifurcation points [Antiga et al., 2008].

Non-skeleton-based approaches incrementally segment objects by iterating over pixels based on a starting pixel. They can be categorized into global and local threshold-based methods and active contours.

Local thresholding methods like *region-growing* has been successfully applied to vessel segmentation [Passat et al., 2005]. Also front propagation techniques are used commonly for vessel extraction [Quek and Kirbas, 2001; Sethian, 2001].

Threshold-based methods rely on a global homogeneity criterion, Region-growing approaches rely on a local criterion. However, for most modalities thresholding methods are not suitable as the intensity distributions of vessels and background overlap partly.

The classic *active contours* have also been used for vessel segmentation. Active contours use internal model-based forces and external image-derived forces to iteratively influence an initialized geometrical model. Parametric models as proposed by [Kass et al., 1988] and extensions like Topology-adaptive snakes [McInerney and Terzopoulos, 1999] have been tested for vessel segmentation. They rely on a Lagrangian formulation for contour evolution. Their advantage is the computational efficiency; a disadvantage is the complex parametrization in 3D.

Level-Sets are frequently used for vessel segmentation

Implicit active contours such as *Level-Sets* are very popular and have been successfully employed for vessel segmentation [Manniesing et al., 2006]. Their computation relies on an Eulerian formulation of contour evolution as partial differential equations are solved. Their parametrization is less complex; however, their algorithmic cost is higher than parametric active contours. Efficient solving methods such as the narrow-band Level-Set method have been proposed [Sethian, 2001; Osher, 2001]. The strength of Level-Sets is their ability to handle topological changes implicitly which is advantageous especially for vessel segmentation. A major dis-

advantage of Level-Sets is their dependence on the initialization as they find only local optimal solutions. An example of Level-Sets used for vessel segmentation can be found e. g., in [Chan and Vese, 2001].

3.1.4 *Image modality*

The quality of a segmentation algorithm especially depends on the image modality and the intensity of vessels. For CTA data sets, intensities correspond to the HU value range of vessels and are known [Wesarg and Firle, 2004]. However, for MRA data sets, the topic is more complicated as the intensity values depend on the acquisition device and the sequence.

The intensity distributions for vessel and background are separable in 3D-RA although in a typical histogram the peak is too small to be seen due to the small number of vessel pixels (see Figure 3.2a). A simple thresholding technique produces good results [Lauric et al., 2010]. The threshold can reliably be determined using threshold estimation techniques such as [Zack et al., 1977; Otsu, 1975].

CE-MRA data sets have a slightly lower image quality than 3D-RA because of the higher noise levels (see Figure 3.2b for a histogram). Vessel segmentation algorithms have been presented, e. g., based on fuzzy connectedness [Saha et al., 2000].

The image quality differs per modality

The extraction of vessels in TOF-MRA data sets is more difficult than in CE-MRA because of the lower contrast between vessels and background (see Figure 3.3a for a histogram). Furthermore, image artifacts play a role, e. g., magnetic field inhomogeneities that occur especially at high field strength $\geqslant 3\,$T. Techniques for vessel segmentation in TOF-MRA have been presented that rely on vesselness filtering [Forkert et al., 2011] or a combination of thresholding and region-growing [Uchiyama et al., 2009].

CTA is the most challenging modality for vessel segmentation because of several reasons. In a histogram of an example data set, it can be seen that no peak at vessel positions exists (Figure 3.3b). Data sets can either include or exclude bones depending on the abilities of the acquisition device. Also software solutions for bone extraction exist (cf. Section 2.2.2). For data sets where bone is already excluded, several segmentation methods have been presented [Manniesing et al., 2006; Kostopoulos et al., 2007].

In [Manniesing et al., 2006], a Level-Set was applied that incorporates user-supplied information about the vessel intensity distribution and the background distribution. In [Kostopoulos et al., 2007], the distributions are trained using a supervised pixel-classification algorithm. Only few algorithms have been presented to segment the cerebral vasculature in CTA images that still contain bones [Behrens, 2012; Straka et al., 2003; Militzer and Vega-Higuera, 2009; Scherl et al., 2007]. The method by [Behrens, 2012] relies on geodetic dilatation preprocessing, double-thresholding segmentation and subsequent Level-Set segmentation. A disadvantage is that not all blood vessels in proximity to bones are segmented. The other methods rely on a probabilistic aspect [Straka et al., 2003; Militzer and Vega-Higuera, 2009] or a semi-automatic initialization of a Level-Set [Scherl et al., 2007].

Software-based methods to remove bones from CTA have limitations

Very few algorithms that are capable to segment vessels in multi-modality data sets have been presented. This ability is important for the use of a segmentation al-
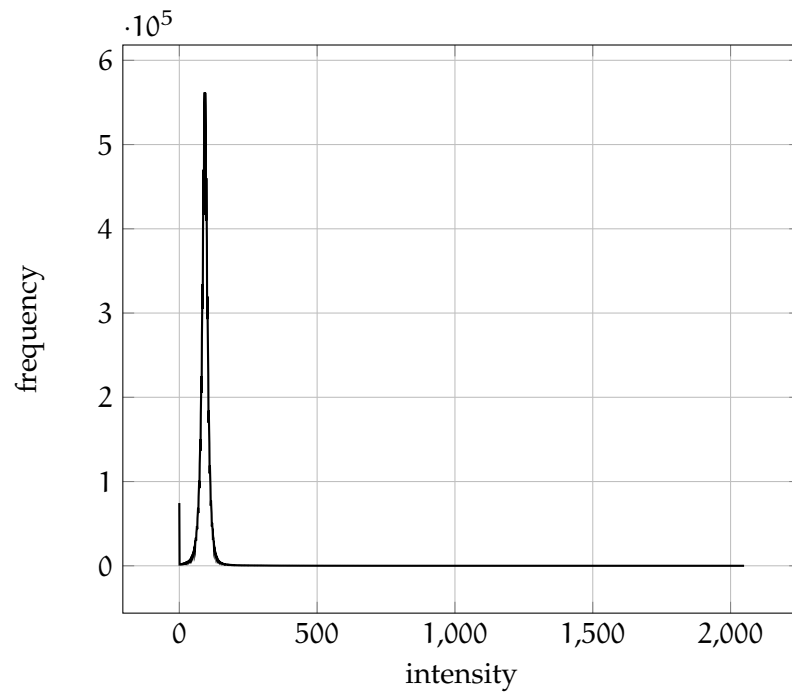
(a)
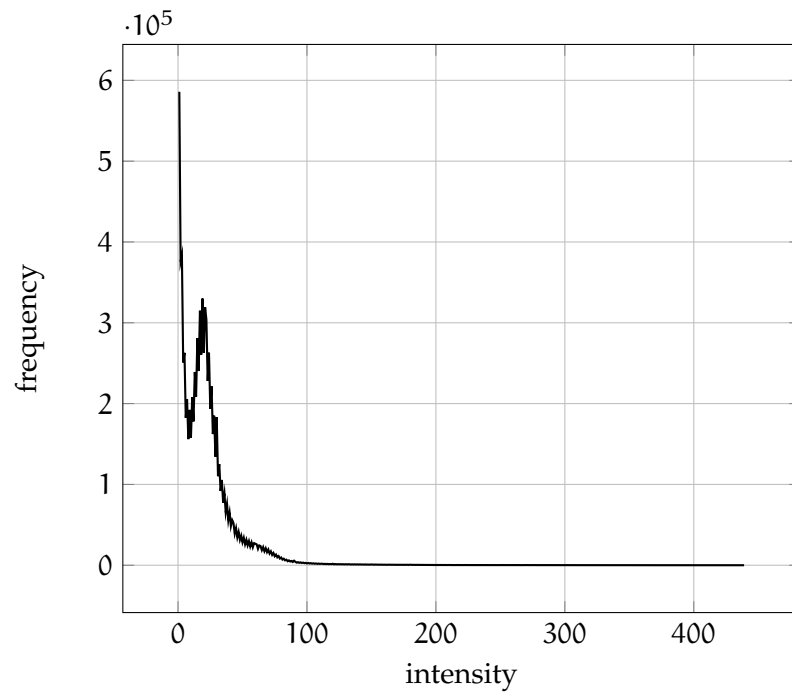
(b)

Figure 3.2: Histogram of (a) a 3D-RA data set and (b) a CE-MRA data set. In both histograms, only one peak at the background can be seen. No peak can be seen at values > 1000 (3D-RA) or > 100 (CE-MRA) representing vessels.

(a)

(b)
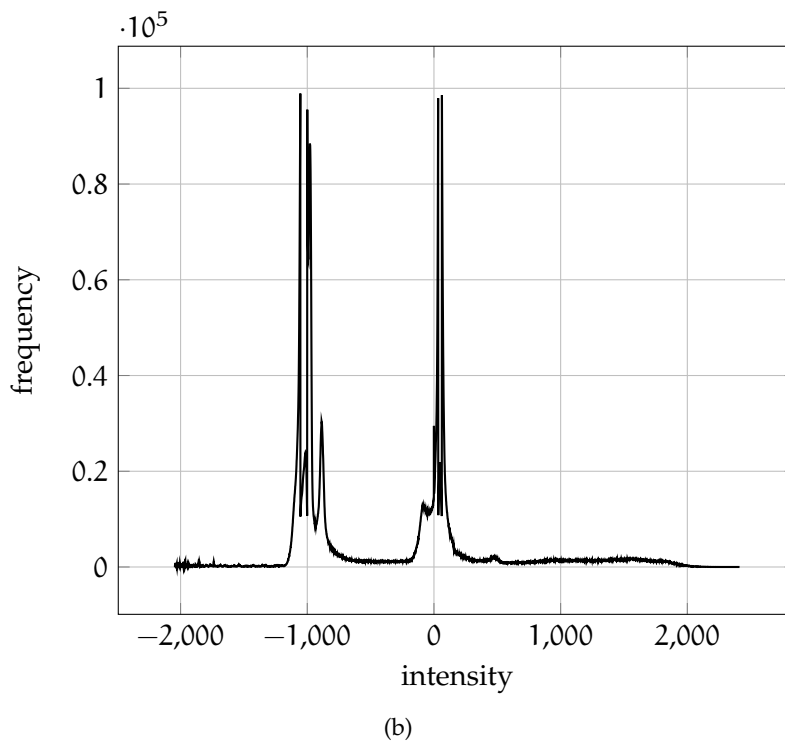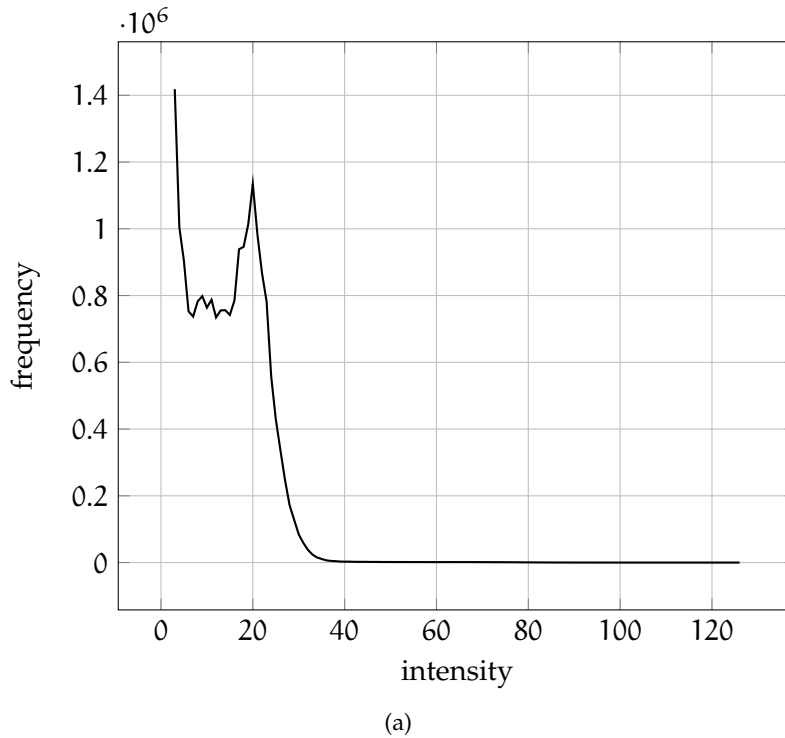
Figure 3.3: Histogram of a (a) a TOF-MRA data set and (b) a CTA data set. In (a), a peak at the background that is either air or brain matter can be seen. Vessels having intensities > 50 form no peak. In (b) the first large peak at −1000 HU represents air, the small peak at −900 HU represents pillows to fixate the head, the small peak at −100 HU is fat tissue and the second large peak at 0 HU represents water. No peak can be seen at vessel HU values between 150 and 300.

gorithm in aneurysm management. A technique to segment vessels in 3D-RA and CTA images was presented by [Hernandez and Frangi, 2007]. A histogram-based intensity-normalization was done as a preprocessing step [Bogunović et al., 2008]. For segmentation, a Level-Set algorithm was used. The speed function guiding the Level-Set expansion depends on intensity gradients and trained intensity distributions. An improved version of the algorithm was also tested with TOF-MRA [Bogunović et al., 2011]. Very good results were achieved on ten data sets with the average surface error being in the pixel-resolution range. Interestingly, the results of the marching cubes algorithm [Lorensen and Cline, 1987] using a manually-chosen threshold were only slightly worse with respect to the given ground truth.

Few segmentation algorithms exist that are able to process multi-modality data sets

3.2 DETECTION OF ANEURYSMS

Aneurysm detection is the next step in computer-aided aneurysm management. The goal is to identify (rectangular) ROI containing aneurysms by determining the center point $(x, y, z)^T$ and the volume s of the region. All further analyses have to be done on these ROI only. This preprocessing of the data is suitable as an analysis of the complete cerebral vasculature would be computationally expensive and lead to more exceptions. Additionally, these pathologic regions are of clinical interest.

Aneurysm detection can be done manually, semi-automatically or automatically. Manual search involves common slice-based scanning of volumes by a domain expert, usually a neuroradiologist. The scanning is done in one to three directions of axial-aligned slices, which usually are orthogonal to each other. Less commonly, multiplanar reconstruction having a manually defined direction is used. All four major arteries are slice-based scanned craniocaudal until small vessels at the skull are reached. The vessels that usually form a circular profile are followed slice-by-slice. Any abnormalities are carefully analyzed employing also other planes. During this manual process, the physician has to develop a mental representation of the major cerebral blood vessels in order to identify suspicious areas. As aneurysms are expected on certain locations, e. g., specific bifurcation points [Edlow et al., 2008], at these locations the visual analysis is performed more thoroughly. 3D volume visualization techniques or MIP are only rarely employed for aneurysm detection, they are rather used for evaluating the aneurysm morphology or for neurosurgical intervention planning.

Manual aneurysm detection relies on the experts experience

If aneurysm-related symptoms exist, the physician examines the data set more thoroughly than if the data set was acquired for another reason. It is possible that there are initial assumptions of the aneurysm site, e. g., due to a known SAH. As most aneurysms are asymptomatic until their rupture, usually no aneurysm is suspected and only a quick routine scanning of the data set is done which increases the probability that aneurysms (or other pathologies) are overlooked.

Automatic algorithms for aneurysm detection have been proposed and will be extensively discussed in Section 4.3. The main advantage is the ability to include such algorithms in a clinical workflow without altering it. Potential aneurysms could be found automatically by scanning the data set without the need for user interaction. Thereby, physicians could evaluate these suspicious regions at a self-chosen point in time. The probability to overlook aneurysms would be decreased, especially in data sets without aneurysm symptoms. If the amount of time should

decrease, the amount of FP must not be too high. If such an algorithm has to be clinically valuable, it should work on multiple angiographic modalities. As pointed out in Section 4.3, only two algorithms exist that fulfill these requirements. However, neither algorithm has been tested with all relevant angiographic modalities. Besides, the evaluation was not sufficient to estimate a reliable quality because of a too small database or an unclear evaluation. Furthermore, all algorithms require a good vessel segmentation. This is not desirable. Thus, only a newly developed algorithm could fulfill all necessary requirements.

The detection of aneurysms is the most important step in the aneurysm management workflow as it has the potential to change the whole clinical aneurysm management. Almost all other steps, except the vessel segmentation, depend directly or indirectly on the knowledge of the positions of aneurysms (see Figure 3.1 and Table 3.2). The manual detection is complex, time-consuming and, even if done by experienced neuroradiologists, error-prone which would greatly benefit from an automatic approach. However, it is important to bear in mind that such an approach is thought as support for physicians in the sense of CAD. Otherwise, it would be part of an automated computer diagnosis system which has proven in the past to be too complex and unsuitable (cf. Section 4.2).

In this thesis, the detection of aneurysms is chosen as major topic of all methods in the domain of computer-aided management of cerebral aneurysms.

Automatic detection of aneurysms is able to increase the detection rate of radiologists

3.3 EXTRACTION OF ANEURYSM REGIONS

After the ROI containing aneurysms were detected, only the inflowing and outflowing vessels and the aneurysm itself are of further interest and therefore, all other background voxels can be excluded from further analysis. This step involves determination of the relevant vessels, of the aneurysm sac and of the aneurysm neck (see Figure 2.1b).

The main problem in algorithms determining the aneurysm neck is that there are various subjective definitions of the aneurysm neck. It would be desirable if an objective definition would exist that is accepted in the medical community. Thus, the used measures lead to a large inter-observer variance.

In [Neugebauer et al., 2012], a discrimination between near-vessel and far-vessel regions is proposed additionally to the aneurysm sac. The discrimination is based on a centerline representation. To locate the ostium, an algorithm was used that computes an ostium plane and thus divides the geometry into aneurysm sac and adjacent vessels [Neugebauer et al., 2010]. The adjacent vessels are then analyzed by an approximation of the vessel cross section shape using an ellipse and a subsequent vessel area profile computation along the centerline. The function of the area of the approximated ellipse is fitted to a Gaussian function and the transition between far and near vessel is defined by a specific point at the approximation function. The decomposition was found to be useful by medical experts and it has been shown to be robust to noise. Disadvantages are that the size of the ROI has to be determined manually and that the centerline detection algorithm is only semi-automatic. Similar to the previous approach, [Shojima et al., 2004] defined near vessel and far vessel domains whereby vessel segments having a distance of

Commonly, the aneurysm ROI is classified into aneurysm and near/far vessel

$< 10\,\text{mm}$ to the ostium surface are defined as near vessel region, the remaining ones as far vessel region.

A simple definition of the relevant vessels was presented by [Millan et al., 2007]. The parent vessel is included in the ROI from the aneurysm neck until the length that equals one diameter of the aneurysm.

[Firouzian et al., 2011] presented an algorithm based on a Level-Set formulation to segment the aneurysm sac in CTA volumes. A user-provided seed point is given. The speed function to find the aneurysm surface is based on intensity, gradient magnitude and local intensity variance. The intensity is assumed to be similar to the neighborhood of the seed point, the gradient magnitude and the local variance are assumed to have high values. The aneurysm and surrounding vessels could be segmented successfully with an average surface distance of $0.13\,\text{mm}$. In contrast to the previously mentioned methods, no differentiation between aneurysm and surrounding vessels is done. However, this information is important e. g., for blood flow simulation or visualization.

In [Cárdenes et al., 2011], the aneurysm neck is detected semi-automatically. A ROI is defined manually on the segmented data set and subsequently, a centerline is computed. The algorithm requires the manual definition of the bifurcation point that divides the aneurysm from the parent vessel. All centerline pixels of the ROI are then either classified as vessel c_v or aneurysm c_a. This assignment is done by computing a surface Voronoi diagram based on a distance transform from the centerline to the surface. Each surface voxel is assigned to the same class as the nearest centerline voxel. Finally, the aneurysm neck is found by iterating over all surface voxels of c_a and searching for the shortest geodesic curve on the surface.

The proposed extraction algorithms rely on user input

Another approach for semi-automatically defining the aneurysm neck was proposed by [Kohout et al., 2013]. The algorithm is similar to [Cárdenes et al., 2011] as the definition is based on a segmented centerline and a user-given splitting point on the centerline. In contrast, the neck is found by computing a fuzzy probabilistic metric taking into account the nearest voxels rather than using a binary metric. The neck is defined as the isosurface where the probability is 0.5 that the surface pixel belongs to the aneurysm class.

Some algorithms, especially blood flow simulations, require the definition of a mesh as input data. The segmented ROI are therefore converted into a geometrical mesh model if needed. This can be done by employing several algorithms such as [Lorensen and Cline, 1987; Lederman et al., 2011a].

Post-processing of the mesh may be required to resolve so-called kissing-vessel artifacts [Tomandl et al., 1999] or to manually include missed vessels. There is currently no algorithm known that solves the problem automatically. Therefore, the mesh has to be processed manually by adequate mesh-manipulating software, e. g., [Cignoni et al., 2008; Schöberl, 1997] to resolve these artifacts. Further information about possible solutions and other model optimizations are discussed in [Mönch et al., 2011].

To summarize, several algorithms have been presented in the area of aneurysm ROI extraction. They can determine relevant vessels, segment the aneurysm sac or find the aneurysm neck. A segmentation is always required as input. The division between aneurysm sac and vessel is commonly used. However, the aneurysm neck that is used as cutting curve cannot clearly be defined. Usually, rules of thumb

have been used to define the size of the aneurysm ROI, e. g., taking two to three times the diameter of the aneurysm [Cárdenes et al., 2011].

3.4 SHAPE CHARACTERIZATION OF ANEURYSMS

The goal of the shape characterization is to compute features on the extracted ROI. These voxel- or geometric-based features aim at characterizing the aneurysm with respect to important clinical questions, e. g., the prediction of rupture or the growth rate. Additionally, hemodynamic features are employed for rupture risk analysis (see Section 3.7).

Several size-based and shape-based features have been proposed to characterize aneurysms (see Table 3.1 for a schematic illustration):

- *Aspect ratio* $r_a = \frac{d_a}{d_n}$, where d_a is the aneurysm size and d_n is the neck width,

- Volume s,

- Maximal radius r_{max},

- the *Writhe number* Wr (cf. Section 4.3.2),

- *Bottleneck factor* $bn = \frac{2r_{max}}{d_n}$,

- *Moment-based geometric invariants* m_g,

- *Moment-based Zernike invariants* m_z,

- *Undulation index* $u = 1 - \frac{s}{s_{CH}}$. where s_{CH} is the volume of the convex hull,

- *Nonsphericity index* $ns = 1 - (18\pi)^{\frac{1}{3}} \frac{s^{\frac{2}{3}}}{a}$, where a is the surface area and

- *Ellipticity index* $e = 1 - (18\pi)^{\frac{1}{3}} \frac{s_{CH}^{\frac{2}{3}}}{a_{CH}}$, where a_{CH} is the surface area of the convex hull.

Moment-based features have been employed to describe and analyze the shape of aneurysms [Millan et al., 2007] and were linked to the rupture risk.

The shape analysis is done based on a smoothed surface description of the aneurysm ROI. Moment theory has been proposed for characterizing 3D shapes. Different orders of moments can be used to describe the shape with arbitrary precision. Order 3 moments encapsulate a very rough representation of the object giving it a very smooth appearance, whereas order 30 moments incorporate detailed information about the morphology. Two different invariants, geometric and Zernike, were used as descriptor and both moments are invariant to translation, scaling and rotation.

The method has been evaluated with segmented ROI stemming from CTA and 3D-RA data sets containing 31 ruptured aneurysms and 24 unruptured aneurysms. Zernike moment invariants performed better in experiments than geometric moment invariants with respect to the robustness of different segmentation methods. Correct rupture prediction of 66 % was found if aspect ratio r_a was used as discrimination function. With order 10 Zernike moments, the correct classification rate was 80 %.

Table 3.1: Schematic illustrations of shape index values, adapted from [Raghavan et al., 2005].

Shape Index	Low	High
Aspect ratio r_a		
Bottleneck factor bn		
Undulation index u		
Nonsphericty index ns		
Ellipticity index e		
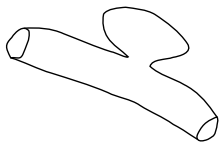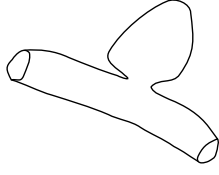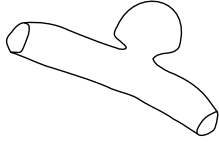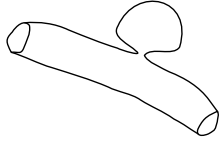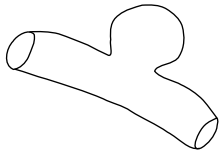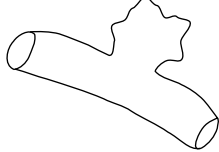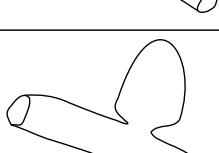
This method is one of the few that employs shape-based features for rupture risk analysis. The approach is interesting because aneurysms are made comparable by their shape using moment feature invariants. This shape description approach could be used as a clustering of aneurysm types.

In [Raghavan et al., 2005], size and shape features were compared on the basis of their power to discriminate between ruptured and unruptured aneurysms in a study of 27 aneurysms from segmented CTA data sets. While size features (volume, maximal diameter and aspect ratio, among others) were not suitable for discrimination, some shape features had a high discriminatory power. The shape features leading to the best discrimination were the undulation index u and the nonsphericity index ns. With ns, it was possible to reach a sensitivity of 87 % while reaching a specificity of 70 %. The accuracy was 79 %. However, it was not tested if a (linear) combination of features leads to better results.

A maximum accuracy of 80 % in rupture prediction can be reached with shape-based analysis

Another study of [Lauric et al., 2011] proposed the Writhe number as discriminant for an aneurysm rupture. 117 saccular aneurysms in segmented 3D-RA data sets were analyzed. In contrast to [Raghavan et al., 2005], the good discrimination power of ns could not be confirmed. The accuracy was only 67 %. The Writhe

number was computed for each point on the aneurysm surface. Its distribution is approximated by histogram smoothing. Then, several statistical measures are computed on the histogram. The histogram of the Writhe number is assumed to have different characteristics for ruptured and non-ruptured aneurysms. The final classification is done by logistic regression with cross validation. By using five features, an accuracy of only 68 % could be reached. It was found that aneurysms having different type (sidewall or bifurcation) distort the measure as they had a high variability between these classes. The accuracy was 87 % for sidewall aneurysms and 71 % for bifurcation aneurysms, respective. While this method reports encouraging results, the reasons for the good performance of the Writhe number in rupture analysis remains an open question.

Further, mostly geometric features such as the aneurysm inclination angle or a Fourier-derived feature have been used for rupture status classification [Dhar et al., 2008; Rohde et al., 2005]. They are not discussed here as they do not reach as good accuracy as the previously discussed methods.

All shape analysis algorithms that aim at discriminating between ruptured and unruptured aneurysms rely on the assumption that aneurysm shape and size do not change upon rupture. This topic is still controversially discussed as some publications support this assumption [Ujiie et al., 1999] while others disapprove [Wiebers et al., 2003]. Thus, the research about this topic has to be reconsidered if this assumption turns out to be incorrect. Only very seldom unruptured aneurysms are included that ruptured shortly after image acquisition.

Despite their use in clinical workflow and clinical studies [Wiebers et al., 2003], size-related features are not suitable for discrimination between ruptured and unruptured aneurysms [Dhar et al., 2008; Raghavan et al., 2005]. Several shape-based features have been proposed that reach at most a an accuracy of about 80 %.

Furthermore, shape characterization can be important in terms of shape comparison between two data sets acquired at different time points. This is the case if unruptured aneurysms are followed-up regularly. Such a shape comparison comprising of an elastic model-based registration of aneurysms was presented [Lederman et al., 2011b]. The model consists of a tetrahedral mesh that was previously created from segmented 3D-RA and CTA volumes. The mesh is then deformed to match the newly acquired data set. As similarity function, a data fidelity term using Level-Sets and a volumetric elastic energy preventing large deformations are combined. The aneurysm growth can then be directly computed based on the mesh deformation.

Aneurysm growth can be measured by registration

3.5 BLOOD FLOW SIMULATION

Blood flow simulations are computed to estimate hemodynamics. These simulations are done using CFD [Chung, 2010]. Hemodynamic features such as blood flow velocity or direction are connected to rupture prediction [Cebral et al., 2005]. A review about hemodynamic analysis of aneurysms can be found in [Jeong and Rhee, 2012; Sforza et al., 2009].

Alternatives to blood flow simulations are direct measurements. PC-MRA data sets have been used also to directly measure the blood flow [Yamashita et al., 2007]. For relatively large aneurysms or large vessels, this works well. However, for small

aneurysms or vessels, the resolution limit (at best 1 mm isotropic voxel size at 7 T) is reached and the flow cannot be represented with high quality [Boussel et al., 2009]. Furthermore, post-processing of the data is required e. g., by registration with a TOF-MRA data set providing high geometric resolution. TCD also can be used to measure parts of the blood flow. However, this technique has major disadvantages as pointed out in Section 2.2.4.

CFD is used to analyze the blood flow

CFD techniques are a subpart of fluid mechanics that use numerical methods and algorithms to analyze fluid flow problems. The Navier-Stokes equations [Batchelor, 2000] have to be solved, this is usually done using either commercial or open-source software. The experiments are done with simplifying assumptions like modeling static geometries, omitting chemical processes and without physical particle interaction. Blood is often modeled as a Newtonian fluid with constant density and viscosity [Radaelli et al., 2008].

An automatic image-based modeling framework for patient specific computational hemodynamics has been presented by [Antiga et al., 2008]. The framework supports all relevant steps for blood flow simulation, i. e., image processing, geometric analysis and mesh generation. Parts of the approach have been implemented in the open source Vascular Modeling Toolkit software [Antiga, 2007].

It is a controversial topic in the biomedical community if CFD, which leaves the geometry static, is sufficient to simulate the patient-specific blood flow. In contrast, Fluid-structure Interaction (FSI) takes the influence of pulsatile blood flow on (flexible) vessels into account as the pulsatile flow behavior could be linked to aneurysm rupture [Costalat et al., 2011]. It was shown that the use of FSI alters hemodynamic features such as Wall Shear Stress (WSS) [Torii et al., 2009]. A major disadvantage of FSI is the large computation time that is at least one order higher compared to CFD computations. Also, higher computational resources are required.

Requirements for simulation are the morphology and boundary conditions

For patient-specific flow simulations, the morphology of the vessel system in the vicinity of the aneurysm has to be determined. Furthermore, inflow and outflow information are required as boundary conditions for an accurate CFD simulation. The geometry has more influence on the CFD result than the boundary conditions [Marzo et al., 2011]. The computation time depends on the number of elements and the available computing power. 20 h were reported for a 13 500 000 element mesh on a standard PC with eight cores [Janiga et al., 2013]. Validation of CFD can be done in vivo by TCD or PC-MRA [Boussel et al., 2009] or in vitro by phantom experiments [Bölke et al., 2007].

3.5.1 *Morphology*

The morphology of the vessels is extracted from angiographic data sets as discussed in the previous Sections 3.1 and 3.3. In [Geers et al., 2011], geometric and hemodynamic variables for the same aneurysms in 3D-RA and CTA were computed. It was found that models built from CTA often had larger aneurysm necks and most of the vessels having diameter < 1 mm could not be successfully reconstructed. The measured features differed 14 % to 44 % by their mean value. Despite these large differences, good agreement was found for qualitative variables that describe the flow field such as the structure of the flow pattern having an agreement $\kappa \geqslant 0.9$.

3.5.2 *Boundary conditions*

Boundary conditions are the second influence factor of blood flow simulations. Blood flow velocity is highly patient-specific as it depends on various parameters such as age, sex, vessel location and vessel characteristics. In a study large variations were shown between arteries: while the left ACI had a mean flow rate $\pm$ standard deviation of $(264 \pm 52)\,\frac{\text{ml}}{\text{min}}$, the left Arteria vertebralis had a mean flow rate of $(96 \pm 38)\,\frac{\text{ml}}{\text{min}}$ [Zhao et al., 2007]. Thus, patient specific boundary conditions have to be modeled for accurate blood flow simulations. Currently, in many algorithms, boundary conditions are applied with uniform or parabolic profile and velocity given by literature such as [Marzo et al., 2011].

Patient-specific boundary conditions ensure realistic simulations

While the outflow boundary condition is commonly assumed with uniform relative pressure 0, the patient-specific input boundary condition is desirable. Thus, only the input boundary condition is regarded in the following.

Patient-specific blood flow can be measured directly by PC-MRA or TCD data sets and indirectly by using 2D-DSA or 3D-RA data sets [Shpilfoygel et al., 2000; Waechter et al., 2008; Hentschke et al., 2011b]. The first modalities are not regarded due to the discussed limitations (cf. Sections 2.2.4 and Section 2.2.3).

In [Waechter et al., 2008], the blood flow waveform and the flow wave are determined from a 3D-RA volume including projections. A model of CA dispersion is estimated from the spatial and temporal CA progression using a pulsatile waveform. Acquisition-related rotation artifacts are reduced using a reliability map. In phantom experiments, relative errors of 5 % to 10 % were determined. The method was validated with two clinical data sets using TCD leading to a relative quantification error of $< 15\,\%$ [Sun et al., 2011]. No standard 3D-RA protocol could be used as the injection flow rate had to be reduced. Furthermore, the method requires a mask scan for background subtraction and requires the catheter to be in the field of view.

In the work of [Hentschke et al., 2011b], flow information from 2D-DSA data sets and morphologic information from 3D-RA data sets are fused to estimate the blood flow velocity. The flow is measured as an integral value at 2D vessel centerline positions. The projective velocity is measured by comparing time-intensity curves on the centerline in 2D-DSA. The vessel centerline is then re-projected to the segmented 3D-RA volume of the same subject using a 2D-3D registration algorithm [Hentschke and Tönnies, 2010] and a ray tracing approach. Thus, true distance information can be recovered. Ambiguities caused by occluding vessels were solved using a graph-based approach. The method was tested with phantom and patient data leading to a small relative quantification error of 11 % to 16 %. In contrast to [Waechter et al., 2008], no changes to clinical angiographic protocols were necessary. Thus, the method is a suitable tool for estimating the patient-specific blood flow by analyzing angiographic images that are routinely acquired clinically.

3.5.3 *Flow-derived features*

Several quantitative and qualitative hemodynamic features have been proposed. The most important ones are:

- Quantitative features

  - The *Wall Shear Stress (WSS)* describes the stress that a fluid causes moving across a solid boundary causes.

  - The *Oscillatory Shear Index (OSI)* measures the change of WSS over time.

  - The *flow velocity* describes the rate and direction of the blood flow.

  - The *inflow concentration* measures the degree of concentration of the flow stream entering the aneurysm.

  - The *turnover time* is the time the blood resides inside the aneurysm (based on the aneurysm neck as border).

- Qualitative features

  - *Flow pattern* is a qualitative feature that describes the flow characteristic, e. g., if the flow is turbulent or straight.

  - The *inflow jet* describes an area with parallel inflow and high speed compared to other parts in the aneurysm.

  - The *impingement zone* is the region on the aneurysm wall where the inflow jet is seen to impact the wall and the jet changes direction. The size of the impingement zone can be derived.

These features are further analyzed with respect to the rupture prediction (cf Section 3.7), to assist the physician in evaluating different treatment options (cf. Section 3.6) or to analyze the vector field as discussed in the following section.

3.5.4 *Analysis of CFD vector fields*

Explorative analysis of CFD may lead to new insights in the hemodynamic analysis for radiologists and biomedical researchers. In [Gasteiger et al., 2012], a computation approach to reliably compute the inflow jet and the impingement zone is presented. The velocity vector field of the CFD is used as input for this method. The inflow jet is defined by three constraints: minimal distance to the aneurysm surface, rapid change in flow direction and strong change of flow speed. These constraints are formalized by a quality function. The upper 5 % quantile of this function is taken as a reasonable isosurface for the inflow jet. The impingement zone is defined subsequently by employing the rapid change of the flow direction criterion. Both features are visualized for explorative analysis (see Section 3.8).

[Kuhn et al., 2011] presented a clustering-based visualization technique to analyze vector fields stemming from flow simulation-derived features. Meaningful regions are emphasized by finding clusters having similar geometric stream properties, e. g., integral curvature.

3.6 VIRTUAL TREATMENT

With respect to the clinical aneurysm management, blood flow simulations are relevant if a change of the geometry occurs either intentionally, e. g., if a stent is inserted.

The goal in virtual treatment is similar to the clinical goal in endovascular treatment: a reduction of blood inflow into the aneurysm to enforce a thrombosis formation. To measure this goal the two hemodynamic features turnover time and the flow velocity are suitable. Different parametrizations can be compared and these leading to the optimal measures should be preferred. However, this approach is chosen in literature rarely as WSS is the most used measure despite the unclear relation to aneurysm rupture. Virtual treatment has the feasibility to support the physician by evaluating quantitatively different possible treatment options.

Virtual treatment can be categorized in three methods:

- virtual stenting,

- virtual coiling and

- thrombosis modeling.

In [Ventikos et al., 2009], a method for each category is presented. The flow properties change after the virtual insertion of a stent, which leads to reduced WSS and also reduced size of the inflow jet. The flow patterns especially depend on the mesh density of the stent. For virtual coiling, it was reported that the velocity profile is changed from the first inserted coil on resulting in a fast decrease of inflow velocity. The packing density measures the volume of the coil with respect to the volume of the whole aneurysm. The desired stagnation of blood flow could be reached in simulation even at small packing densities of 10 %. This is consistent to the clinical experience. Furthermore, the first steps to compute a thrombosis simulation were presented. However, only mechanical properties can be simulated by CFD and biological processes are neglected. To simulate a realistic thrombosis formation, this factor has to be regarded as well.

In [Appanaboyina et al., 2009], it was shown that the stent design, stent positioning and a combination of different stents have a large influence on the hemodynamics in aneurysms. Especially if more than one stent configuration is considered at bifurcations, a virtual stenting is clinically valuable (see Figure 3.4). As quantitative features, the ratio of the aneurysm inflow to the parent flow rate, the velocity in the aneurysm and the WSS were employed. Compared to the pre-treatment values, these feature values mostly improve with the use of a stent. However, the magnitude of improvement depends on the used stent and the geometry. Helical or SILK-stents that are fine-meshed lead to a greater decrease of flow velocity in the aneurysm than Neuroform stents that are wide-meshed.

Virtual stenting has a large potential to assist physicians

The accurate placement of stents in the vessel geometry is challenging. A virtual stenting methodology with the focus of a realistic stent placement was presented in [Janiga et al., 2013]. Stents were positioned for a wall-tight employment using a non-rigid registration based on a free-form deformation. This new approach is conceptually easier than prior approaches, e. g., [Appanaboyina et al., 2009; Larrabide et al., 2012], which rely on a deformable shape model.

Several virtual intracranial stenting challenges have been performed during the past years [Radaelli et al., 2008; Cito, 2011]. Similar to the lung nodule detection challenges [van Ginneken et al., 2010], their aim is to compare different methods using the same evaluation data (morphologic model of aneurysm and vasculature, stent model and boundary condition). As quantitative features, WSS, velocity and

Objective comparison between different blood flow simulations is important

<div style="text-align:center">(a)   (b)   (c)</div>
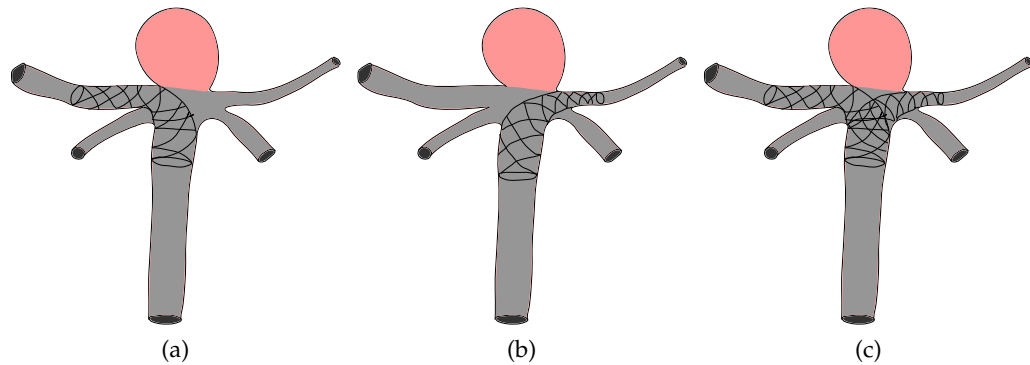
Figure 3.4: Three different configurations for stenting treatment of an aneurysm at the tip of the Arteria basilaris (in red) based on [Janiga et al., 2013]. (a) The stent is placed from the Arteria basilaris to the left ACP, (b) the stent is placed from the Arteria basilaris to the right ACP and (c) treatment with a combined solution.

pressure had to be computed. However, no quantitative comparison could be done as no ground truth was provided. A quantitative comparison, e. g., between CFD and PC-MRA data would be the next step. Evaluation studies using one CFD parametrization have been already done [Gasteiger et al., 2011; Papathanasopoulou et al., 2003].

The effects of packing density to aneurysmal hemodynamics was investigated in [Morales et al., 2011] by virtual coiling. Five different packing densities were tested and each was generated by using three coil configurations, i. e., different arrangements of coils in the aneurysm. CFD was carried out on each variant. Similar to [Ventikos et al., 2009], it was found that the aneurysmal flow velocity decreased with higher packing densities. Even for small packing densities of 12 %, the average flow velocity could be reduced by > 50 %.

Virtual stenting has the largest potential of all virtual treatment methods although stents are employed rather seldom as endovascular aneurysm treatment. However, they are usually employed in complicated cases with relatively high complication rates (cf. Section 2.1.3). The thrombosis model is too simplified to account for suitable results and the virtual coiling cannot model all necessary parameters of the treatment leading to imprecise results. All methods use one quantitative feature to evaluate the treatment effects. However, the treatment decision should be made based on a multi-goal optimization incorporating multiple quantitative features. The configurations leading to the best results may then be further evaluated by medical experts.

3.7 RUPTURE RISK EVALUATION WITH HEMODYNAMIC FEATURES

Some of the previously described features derived from CFD have also been linked with aneurysm rupture.

In [Cebral et al., 2005], CFD of 62 patient-specific aneurysm models has been computed. The relationship between features and rupture status was analyzed. The only significant discriminatory feature that could be found was the impingement jet size. Aneurysms with small jet sizes were more likely to rupture than

aneurysms with a large jet size. Although the database was relatively large, the relatively large amount of some feature classes led to a small sample size per class. Thus, no statistical significance could be found with respect to the rupture status. Similar to [Marzo et al., 2011], it was also reported that small changes of the geometry may lead to large changes of the flow characteristics.

In a subsequent publication by the same authors [Cebral et al., 2011], 210 aneurysm models were used in a CFD simulation. It was observed that ruptured aneurysms were more likely to have complex flow patterns, unstable flow patterns, concentrated inflow and a small impingement zone. All values were significant with $p < 0.018$. Contrary to the prior publication [Cebral et al., 2005], the impingement jet size is classified as either concentrated or diffuse. It is unclear, if the same standards were imposed in both publications. Thus, qualitative features were computed rather than quantitative features.

Hemodynamic features alone are not enough to predict aneurysm rupture. The combination with shape-based features leads to promising results

In a similar publication investigating AComm aneurysms, it was found that the maximum WSS differed significantly[1] as ruptured aneurysms had a higher maximum WSS than unruptured aneurysms [Castro et al., 2009]. In contrast, in another study, no correlation was found [Shojima et al., 2004].

In [Xiang et al., 2011], hemodynamic features in 119 aneurysms have been found as significant discriminant for a rupture. These features were average WSS, maximum WSS, average OSI, number of vortices and relative turnover time. Multivariate logistic regression has been performed and revealed average WSS and average OSI as the only independent significant variables. Together with a morphologic variable, a combined model could be established that predicts the rupture status precisely (Area under Curve (AUC) of 0.89). That means, morphological analysis is as important as hemodynamic analysis to predict the aneurysm rupture.

In conclusion, tendencies were found by analyzing CFD related features with aneurysm rupture, but no statement about rupture prediction can be done with high certainty.

3.8 VISUALIZATION OF ANEURYSMS

The final step of the pipeline and the endpoint for most algorithms is the visualization. The goal is to provide morphological and hemodynamic information to a physician or the biomedical researcher in a comprehensible way. Physicians usually rely on the unaltered two-dimensional visualization of slices of the respective data sets using a center-window approach. As soon as the underlying data are three-dimensional, sophisticated visualization methods can be applied [Preim and Bartz, 2007].

Simple methods such as the Maximum Intensity Projection (MIP) method can be used to visualize a 3D data set (see Figure 3.5a). This technique is popular in the medical community as first overview visualization. More suitable methods that facilitate a three-dimensional impression use opacity and color to display the important parts (see Figures 3.5b and 3.5c). Therefore, a four-dimensional color map (three dimensions for color, one for opacity) has to be created either manually or automatically, e.g., by employing knowledge about the modality. Additional shading can lead to a better perception of depth and vessel topology. A review

Volume visualization is adequate to represent the morphology, but rarely used in clinical practice

---

1 However, p=0.1 is relatively large.
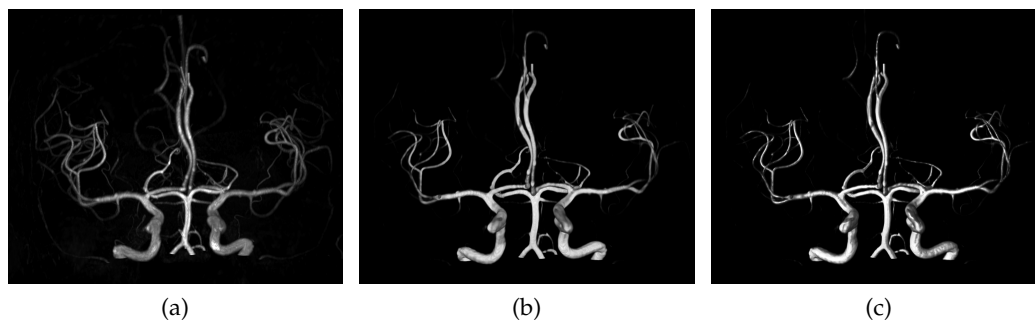
Figure 3.5: Example visualizations of a TOF-MRA data set. (a) Maximum Intensity Projection (MIP), (b) volume visualization with appropriate color transfer function and (c) illuminated volume visualization. Data set courtesy of Oliver Beuing, department of neuroradiology, University Hospital of Magdeburg.

about 3D visualizations of vessels can be found in [Preim and Oeltze, 2008]. The visualization of morphology, i. e., the segmented vasculature, is less challenging if the threshold value is known. The morphology can be directly visualized by employing e. g., Marching Cubes [Lorensen and Cline, 1987].

An overview about flow visualization can be found in [Laramee et al., 2004]. A comprehensive review about visualization of hemodynamics is given in [van Pelt, 2012]. The author proposes a visualization of the blood flow by particle tracing in contrast to the commonly used streamline approach. A special focus is the interactive explorative approach of visualization.

[Gasteiger et al., 2012] propose a volume visualization incorporating anatomical context to analyze the blood flow in the cerebral vasculature (see Figure 3.6). The anatomy is visualized by a smoothed ROI model having a semi-opaque surface and an emphasized aneurysm neck. To visualize the jet stream surface, a color-coding is used with optional surface strips. Also, a fade-out effect of the surface is employed to convey the uncertainty of the jet after touching the impingement zone. A glyph can also be employed to summarize the jet stream. For the depiction of the impingement zone, the quality function is directly used by choosing an adequate isosurface value and a color-coding. Alternatively, impingement zone and the inflow jet can be visualized together. According to the authors, a combination of morphological analysis and hemodynamic analysis is important for evaluating the aneurysmal region.

In [Neugebauer et al., 2009], a map display is proposed to visualize scalar data on aneurysm surfaces. The aneurysm surface is projected onto a cube that is positioned around the aneurysm ROI. Four cube sides are then projected onto a spherical map around the surface visualization of the aneurysm; the background side is projected onto an extruded curve next to the spherical map. In this way, it is possible to display all available scalar data at a time without occluding parts because of the viewpoint. Moreover, the anatomy is visualized which enables the user to establish a connection between the 3D surface visualization and the 2D map projection by choosing a point on either visualization.

[Neugebauer et al., 2011] propose different visualization techniques that aim at displaying the blood flow with anatomy guidance. Slow flow and fast flow visualization enhancement techniques have been integrated by using an adequate
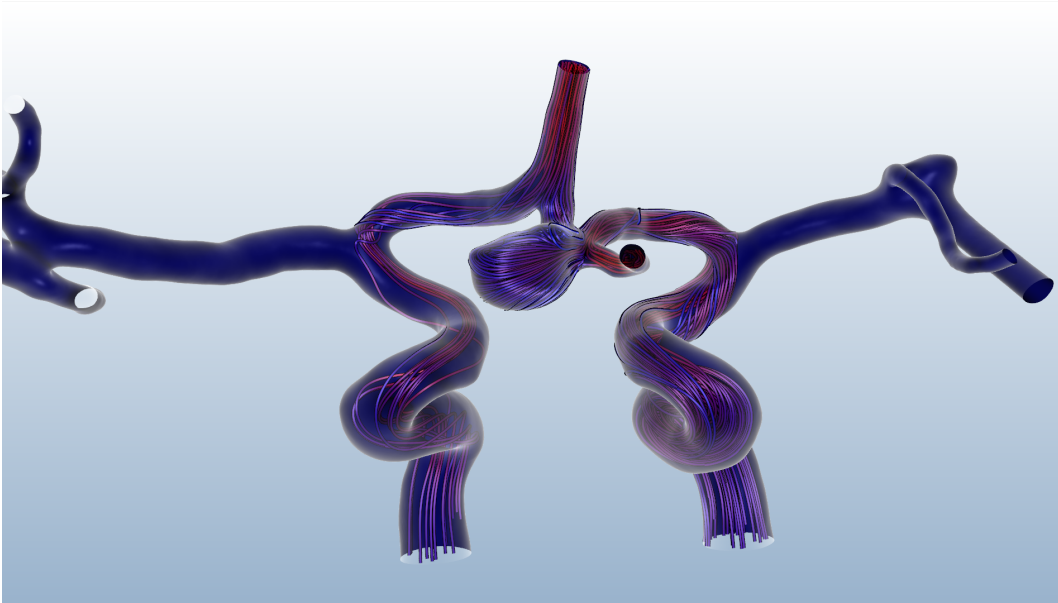
Figure 3.6: Visualization of a blood flow simulation with morphological information using streamlines. The seeds are placed in the aneurysm. Slow flow velocities are encoded red and high flow velocities are encoded purple. Image data courtesy of Oliver Beuing, department of neuroradiology, University Hospital of Magdeburg. The flow simulation was performed by Philipp Berg, institute of Fluid Dynamics and Thermodynamics, University of Magdeburg and the visualization was done by Mathias Neugebauer and Rocco Gasteiger, department of Simulation and Graphics, University of Magdeburg.

color transfer function and streamlines that have been seeded at the aneurysm neck. In contrast to these 3D techniques, 2D isocontour techniques are employed to visualize the velocity in a 2D slice together with the semi-opaque anatomy.

Thus, visualization techniques have been presented that aim at providing morphological and hemodynamic information. Furthermore, these visualizations are enriched by representing suitable features.

3.9 SUMMARY

In this chapter, a potential workflow for a patient-specific computer-aided management of aneurysms has been presented. It includes all important steps for the clinical management whose key points are the detection of aneurysms and the blood-flow simulation (see Table 3.2). An automatic algorithm that indicates potential aneurysms to the physician would have a large impact on the whole aneurysm management. However, such an algorithm has high requirements that are not yet fulfilled by existing methods.

Rupture prediction can be made based on morphological and hemodynamic features of an aneurysm. It was discussed that only both types of features together have the potential to lead to high correct prediction rates. Additionally, also measure of the aneurysm growth should be considered for the rupture prediction.

Virtual stenting of aneurysms can provide additional information for the physician especially in aneurysms containing multiple inflowing or outflowing vessels.

Table 3.2: Overview about the parts in the workflow of computer-aided management of cerebral aneurysms. Clin. pot. = Clinical potential.

Part	Algorithms	Advantages	Disadvantages	Clin. pot.
Segmentation	Lesage et al. [2009]; Bogunović et al. [2011]	Good performance for single modalities	Few multi-modality algorithms, quality depends on resolution, kissing vessel artifacts neglected	Small
Detection	Lauric et al. [2010]; Yang et al. [2011]; Arimura et al. [2006]	Good performance for TOF-MRA	Few multi-modality algorithms, dependence on segmentation	High
Extraction	Neugebauer et al. [2012]; Cárdenes et al. [2011]	Simple algorithms	No clear clinical definition, algorithm rely on user input	Medium
Rupture Prediction (shape)	Millan et al. [2007]; Raghavan et al. [2005]	Fast computation, ~80% correct prediction	Algorithms hardly clinically recognized, no prediction of rupture time	High
Rupture Prediction (hemodynamics)	Cebral et al. [2011]; Xiang et al. [2011]	Relatively good tendencies were found	Algorithms hardly clinically recognized, tools usable by experts only, high computation costs	High
Blood flow simulation	Jeong and Rhee [2012]; Sforza et al. [2009]	Methods are a good approximation of reality	Tools usable by experts only, high computation costs, only usable as preprocessing	Small
Virtual Treatment	Ventikos et al. [2009]; Appanaboyina et al. [2009]	Treatment effects are predictable beforehand, different variants can be evaluated	Tools usable by experts only, good approximation only with virtual stenting	High
Visualization	Gasteiger et al. [2012]; Preim and Oeltze [2008]	Suitable to convey complex information	Radiologists rely on simple 2D slice visualization	Medium

To close the gap between medicine and biomedical research, it is important to convey (possibly research-related) information to the physician by visualization of the aneurysm morphology and features.

Despite the research effort and progress that have been made in the past ten years, only very few methods are regularly used in the clinical workflow. This may be caused by the reservations of physicians against innovative methods, but can be also explained by the lack of feasible solutions that model the whole workflow rather than include only parts of it. Moreover, most tools in this area are expert tools that can only be controlled by biomedical experts. Furthermore, such medical software systems are very complex and a certification requires time, experience and is expensive. In this context, also large-scale validations are required that have only seldom been performed, but are necessary to ensure the quality and generality of an algorithm.

For the future, the potential workflow has to be incorporated into the clinical workflow rather than to only solve academical problems.

STATE OF THE ART

Aneurysm detection can be generalized as a part of a Computer-aided Diagnosis (CAD) algorithm. CAD algorithms are a subset of object detection. Therefore, the following coarse-to-fine structuring approach is chosen for this chapter: first, a short overview about the general topic object detection is given. Different methods to solve the detection problem are discussed. Then, CAD is introduced and applications of object detection algorithms in medical images are presented. Finally, existing approaches to aneurysm detection are thoroughly discussed. Throughout the whole chapter, the focus is placed on the actual topic, object detection in medical images and the methods that are applied for object detection.

It is the goal of this chapter to discuss the relationship between aneurysm detection and related methods. The following questions arise:

- Which methods exist to detect objects in (medical) data sets?

- Which pathologies are similar to cerebral aneurysms in shape, intensity and texture?

- How suitable are existing detection methods to solve the aneurysm detection problem?

4.1 OBJECT DETECTION

Object detection is a part of computer vision and aggregates all methods to find specific objects in images or videos. Despite its complexity, objects are recognized by humans within few milliseconds and even for unknown object instances. However, for computer systems this still poses a large challenge. Although it is an active research topic for 30 years now, it hardly is solved satisfactorily. The more specific the object detection problem is, e. g., the amount of objects is known, the shape of objects is known and the image characteristics are known, the more likely computer vision is able to solve the problem satisfying.

Object detection is relevant in many areas like surveillance, e. g., to detect bags that are set aside, automotive vision, e. g., to detect passengers in front of a car, microscopy, e. g., counting organisms in a microscopic image, scene categorization, e. g., classification of satellite image regions, and in CAD, e. g., to detect organs in medical images [Treiber, 2010].

For decades, psychologists and neuroscientists investigated human vision to understand the visual and cognitive system of humans. Marr proposed a computational approach on multiple processing levels [Marr, 1982]. Another computational approach is proposed by [Poggio et al., 1985]. Several ill-posed problems known as early or low-level vision, such as optical flow and shape from shading, are solved with regularization theory. Theories about human vision point out that edges are salient features of an image. Thus, edge detection algorithms like proposed by Canny or Marr [Canny, 1986; Marr and Hildreth, 1980] can be seen as

low-level vision systems. Biederman postulated a specific theory about human image understanding also known as recognition-by-components [Biederman, 1987].

The basic assumption is that every object is composed of elementary parts called geons. Geons are three-dimensional general shapes, e. g., cylinders or cones. An object is recognized by mentally disassembling it into these viewpoint invariant geons. Further information about the theory of human vision can be found in [Wild, 2005; Bruce et al., 2003].

These theories have their strengths and weaknesses. However, neurological experiments have shown that the human vision is more complex than these theories imply [Dayan and Abbott, 2001]. It is even questionable whether a computer vision system that adapts the human vision may be suitable for object detection.

4.1.1 *Principles*

Object detection is too complex to rely on low-level features only, thus it is classified as high-level computer vision. The goal is to find n objects in m images, where $n, m \in \mathbb{N}$. If a time-dependent image sequence is used ($m \gg 1$), the task is commonly called object tracking. Depending on the specific task, n may be known or unknown and it is even possible that no object is present in the data at all.

There are two general strategies to solve the detection problem: the *bottom-up* approach and the *top-down* approach. Bottom-up is data-based and solves the prob-

lem by combining image-derived features. A top-down approach generalizes the object by defining a model and fitting the model to the data. These two strategies are contrary.

Bottom-up approaches rely on features computed on the image data. The simplest features are the intensities or its derivatives. Scale-invariant features that capture important image information by an abstraction of edges have been proposed and used successfully [Lowe, 2004; Bay et al., 2006]. In contrast, texture features condense texture information in a scalar value [Haralick et al., 1973]. Another important feature is shape, i. e., the object boundaries. If the shape information is coupled with intensity information, it is referred to as appearance. Other features are discussed in [Theodoridis and Koutroumbas, 1999].

A top-down strategy employs a model to generalize the information about the object to be found. This could be, e. g., a geometric polygon-model describing the shape. The challenge is to find a formalization of natural descriptions such as "the object is round in shape, not larger than 5 cm in diameter and usually occurs in the upper right corner of the image". Features such as intensity and texture are used to guide the model during the image data fit. Hence, these features play an important role here as well. Additionally, in a model intrinsic constraints may be employed such as a smooth motion in an image sequence or known acquisition parameters.

The difficulty and complexity of the object search is influenced by the underlying image data and especially its dimensionality. Medical images are two, three or four-dimensional. Two-dimensional images are e. g., X-ray images, three-dimensional images are e. g., CT data sets. If the third dimension is time, it is spoken of a 2D+t dimensionality. This is the case e. g., for 2D-DSA images. It is also possible that images have three dimensions and a time component (3D+t) such as PC-MRA

images. The higher the dimensionality, the more challenging the object detection task is.

4.1.2 *Model-based approaches*

In the remainder of this chapter, only model-based approaches are further discussed as they are the most suitable group for object detection algorithms in presence of additional information.

Top-down techniques for object detection rely on some sort of model that incorporates knowledge of the object properties into the algorithm. Such knowledge can be diverse, such as shape, intensity, location or any other feature describing the object in a general, unique way. These information may also be defined informally ("objects never occur at the border" or "objects are moving in some defined way in an image sequence"), which implies a formalization of object detection for model matching. In the further process, mostly shape is used as a feature and a model represents a shape if not stated otherwise.

The information can be formalized by an energy-minimization scheme:

$$E = \chi(m_\varphi, D) \to \min \tag{4.1}$$

where E is the energy and χ is a similarity function. χ measures the distance of the model m parametrized with parameters $\varphi \in \Phi$ in a parameter space Φ on the underlying data D, usually being an image function or an image-derived feature function. φ can be described using a transformation θ on m. θ may be rigid or elastic (non-rigid). Equation . 4.1 can be solved using various schemes such as gradient-descent, genetic algorithms or simulated annealing. Implicit energy functions produced by e. g., template matching have been used too. The minima can be determined e. g., by clustering methods like Mean shift.

Object detection can be interpreted as an energy-minimizing approach

In case of statistical models, the energy optimization is often interpreted as a Maximum a Posteriori (MAP) estimation.

Instead of choosing a linear categorization, model-based approaches are differentiated with respect to three high level dimensions:

- *Elasticity*
    - *Deformable models* adapt to the data while
    - *rigid templates* keep their shape throughout the fitting process.

- *Division*
    - The model may consist of either *one part* or
    - *multiple parts*.

- *Representation*
    - The model can be *statistical*, trained on a database or
    - created by a domain expert resulting in a *generalized model*.

All detection methods are combinations of representations with respect to different property dimensions. In the following, each dimension is described in detail and methods are presented exemplarily.

4.1.2.1 *Deformable vs. rigid models*

Models can be rigid or deformable. A deformable model adapts to the data while a rigid model, or template, remains unchanged throughout the detection process. Rigid models are computationally less complex, but can represent only small variation with respect to the features. In contrast, deformable models are more suitable for large feature variation; they have higher computational costs, though.

Template matching is one of the most basic techniques that employ rigid models

Template Matching (TM) approaches rely on rigid shape and intensity as generic information. These approaches are used to solve problems like traffic sign detection with predefined feature templates [Gavrila, 1999]. They are also used to detect objects in three-dimensional images like pulmonary nodules in CT images [Lee et al., 2001]. This method is an application of a rather simple template-matching approach using Gaussian distribution information. This has the advantage of rotation-invariance and therefore is computationally suitable. However, objects that largely deviate from the model shape cannot be found.

A similar approach was presented by [Feuerstein et al., 2009] to detect lymph nodes in CT data. The method relies on a *Hessian Eigenvalue Analysis (HEA)* to recognize round shapes. The Hessian matrix is a square matrix of second-order partial derivatives of a function. Details about HEA can be found in Section 4.3.1. Instead of directly searching for profiles having a Gaussian shape by using TM, this is done indirectly by the HEA.

A method to detect objects based on the *Generalized Hough Transform (GHT)* in X-ray images was proposed by [Ruppertshofen et al., 2010]. The GHT extends the Hough transform to allow for detection of arbitrary object shapes by using a rigid template [Ballard, 1981]. A shape model that represents the location of edges is computed by training. The method has problems to find abnormal objects and is not suitable for objects having large shape variance.

An *evolutionary algorithm* employing a deformable model for detection of objects in 3D medical data was proposed by [Heimann et al., 2007]. Initial candidates are found by randomizing pose (translation, rotation, scale) and shape parameters in image space. Shape is represented by a point distribution model that incorporates trained landmark coordinates evaluated by a Principal Component Analysis (PCA) to find the modes of variation. The energy or fitness for each individual candidate is estimated by summing the probabilities of all landmarks. Each candidate is mutated in an iterative manner with a probability proportional to its fitness. After a fixed number of iterations, the candidate having the maximum energy is taken as final solution. The method has limited ability to recognize objects that differ from objects in the training database.

Deformable models adapt to the data and are able to detect objects having flexible shape

A similar approach using Mass-spring Model (MSM) was proposed to localize lymph nodes in CT data sets [Dornheim and Dornheim, 2008]. This approach is computationally expensive showing processing times up to 17 min per data set and thus is unsuitable for object detection. [Engel et al., 2011] propose a hierarchical Finite Element Method (FEM)-based approach that is discussed in the next section. Other possibilities for the implementation of a deformable model include polygonal meshes [Kobbelt et al., 1998] as well as implicit models like Level-Sets [Sethian, 2001] (cf. Section 3.1.3).

Both model representations, rigid templates and deformable models, have their advantages and disadvantages. For aneurysm detection, deformable models are

challenging to parameterize because of their shape variability and because of the possibility of multiple occurrences. It is questionable if rigid templates manage to account for the large shape variance, however their parametrization is easier and their computational complexity is lower.

4.1.2.2 *Single vs. multi-part models*

All of the aforementioned models are single-part models that consist of one connected component. These models do not include a (spatial) dependence of object parts. The search space may be constrained through this additional information to reduce the computational complexity and to exclude impossible instances.

Single part models are suitable for the detection of relatively well-defined objects whereas multi-part models are suitable also for objects having variable representation as additional information. The relationship of each part is defined by their spatial relation. This constrains the possible solutions of Equation 4.1. Furthermore, the detection process does not depend on a single decision to find one object, but on multiple widely independent decisions. This ensures a high robustness.

Multi-part models define relationships between single-part models

Hierarchical models are a subgroup of multi-part models. Their relationship is modeled on several levels. For example, to find a house on a satellite image, first the correct district is searched for, then the representation of the house using only the district boundaries. Thus, a hierarchy is built to reflect the sub-part models rather than only creating relationships among them.

In [Donner et al., 2010], a method was proposed to locate anatomical structures in CT data sets. The objects were found by training a random forest classifier that employed Haar wavelet features on a point-distribution model. The optimal candidate for each object was found by solving a *Markov Random Field (MRF)* that represents the spatial configuration likelihood among objects. MRF are commonly used for constrained energy minimization.

A hierarchical approach to detect different organs in CT volumes was proposed by [Seifert et al., 2009]. The approach operates in three steps. First, salient slices are detected using a previously trained probabilistic boosting-tree with Haar-like features. These slices constrain the subsequent search space as the orientation of the CT data sets is known. Then, body landmarks (e. g., left/right hip, spine) are found by employing a trained probabilistic boosting-tree again. All landmarks are connected in a graph allowing for spatial representation. The final step then includes Marginal Space Learning (MSL) (cf. Section 4.1.2.3). The search space is once again constrained by a priori probability that is given by the found landmarks. This method is a good example for detection where the search space is reduced step-by-step based on statistical information. This yields an implicit hierarchical model that relies on initially found landmarks. This information is passed to the next classifier in a cascade-like approach. The danger is that an initially incorrect assumption leads to wrong detection result as all constraints are hard and a once excluded search space is discarded.

Hierarchical models define relationships of multiple levels between single-part models

A hierarchical FEM-based approach to localize auditory cortical regions was introduced by [Engel et al., 2011]. A cortical mapping is done on MRI data sets to flatten the three-dimensional information to 2D images. A hierarchical model is employed to represent the location and shape of gyri and sulci around the auditory cortex. The top level model enforces the locations of substructures (e. g.,

temporal sulcus, Sylvian fissure). The second level model consists of triangular meshes of these structures. A shape-structure hierarchy is modeled with appearance and pose as driving features. The model is trained with annotated data sets. The search space is constrained by using a cortical atlas. The initial structures are found by employing an evolutionary algorithm with a quality-of-fit function similar to [Heimann et al., 2007]. The method is able to reliably detect objects having a non-discriminatory shape occurring similarly at different positions of the data set by evaluating the structure and position of neighboring of all candidates. The method formalizes constraints by including hierarchical knowledge using a deformable model and an atlas.

A hierarchical multiple-part model could also be suitable for aneurysm detection. The first level would model the head, the second level would model the vessels and the third level would model pathologies like aneurysms. This would also make incorporation of an atlas feasible. In CTA also other objects like the eyes or the skull are included. These could be used for plausibility-checking. Single-part models could be employed by using an appropriate quality-of-fit function in conjunction with an evolutionary algorithm. However, this quality-of-fit function would be challenging to design because of the high disparity among aneurysms.

4.1.2.3 *Statistical vs. physical-based models*

Generally, a model contains the expected distribution of features such as shape and intensity. This modeling step can either be done by a statistical model or by formalizing (expert-given) domain knowledge about the object into a physical-based model. In the latter case, variation is represented via parametrization.

Statistical models rely on learning representative samples that are included into a database. The probability of occurrence of an object o given in a local image region R is $p(o|R)$. On each region, features are computed that are condensed in a feature vector F. The conditional probability of an object to be represented by a feature vector can be computed by using Bayes' rule: $p(o|F) = \frac{p(F|o)p(o)}{p(F)}$ with $p(o)$ being the a priori probability of object o, $p(F)$ being the a priori probability of the feature vector F and $p(F|o)$ the probability density function of the feature vector of object o. Therefore, probability distributions of features have to be estimated. This can be done by learning on an annotated database, i.e., where the position of objects is known. Methods such as kernel density estimation or other histogram approximation methods can be employed.

Statistical models employ training to represent the shape or other features of an object

Classic statistical models are *ASM* [Cootes et al., 1995] and *Active Appearance Model (AAM)* [Cootes et al., 2001]. These models are represented by a point distribution model. Landmark points x_o are given for each object o. These result in an average shape $\bar{x}$. A PCA is computed on the covariance matrix of x_o that yields the principal modes of variation p_m. All valid shapes x can then be described using a limited number (c) of parameters y_m: $x = \bar{x} + \sum_{m=1}^{c} y_m p_m$. The shapes that contribute the most to the overall representation correspond to the highest eigenvalues given by PCA.

Another example of a statistical model was presented by [Viola and Jones, 2001] to detect faces in (non-medical) 2D images based on *Haar wavelet features*. A cascade of weak classifiers similar to AdaBoost is used for classification. In each step of the cascade a simple classifier with a high true-positive rate is used. Through

this approach, a high true-positive rate can be achieved while also the false positives are minimized. Although the method was tested with 2D photographic images, the proposes features were successfully used to detect organs in medical images [Seifert et al., 2009; Donner et al., 2010; Zheng et al., 2009].

Marginal Space Learning (MSL) was proposed for organ detection in (medical) images [Zheng et al., 2009]. The principal idea is to constrain and divide the search space by employing statistical knowledge and then solve the actual detection problem by relatively simple techniques. The search space finding a 3D object in a 3D image is nine-dimensional (three parameters for position, orientation and scaling). Instead of training a discriminative classifier in the nine-dimensional space, a classifier is trained on three three-dimensional sub-spaces. 3D Haar wavelet features and steerable features are used. The ranges of parameter values are either given or trained. Further constraints on the search space are introduced by excluding the image borders and by using the fact that most parameters in the sub-spaces are depending on each other. Again, this is solved by estimating a joint probability density function. This dimensional division approach is relatively elegant accounting for a coarse-to-fine approach of statistical 3D object detection.

In many areas, *atlases* are a method to include statistical or expert-based knowledge. Atlases form a normalized representation of a model that includes the likelihood of object occurrence with respect to the location. Atlases contribute additional information to detect objects in medical images of the head [Nowinski et al., 2011; Talairach and Tournoux, 1988] and other regions such as the liver [Seghers et al., 2007].

Physical-based models are less used than statistical models in object detection algorithms. Examples of physical-based models are the expert-given MSM in [Dornheim and Dornheim, 2008], a simple model of a sphere in [Lee et al., 2001; Feuerstein et al., 2009] and the hierarchical model employed in [Engel et al., 2011].

Physical-based models rely on expert knowledge to define the shape or feature assumptions

Employing a statistical model for aneurysm detection would be challenging as the shape variability as well as the training effort is quite high. Furthermore, the dependence on a representative database should be avoided. Physical-based models that are parametrized by experts are more suitable because a high generality can be ensured. Also, if other features than the shape should be employed in a statistical model, these features would vary among angiographic modalities. It is beneficial to use models that are valid for each modality.

4.1.3 *Summary*

Object detection algorithms commonly incorporate a model to represent shape or other features. The main differences among the models are their ability to change, their number of parts and their creation. Other aspects are the optimization approach and the employed features.

Models can either be deformable or rigid. While rigid models can be used to represent objects with a fixed shape, deformable models adapt to the image data. Deformable models are more often used, but their main disadvantage is the computational complexity, especially in 3D.

Each model-based approach differs by the dimensions elasticity, division and representation

Most models represent the object as one part. In 3D imaging modalities, the information content is high and commonly the aim is to detect multiple objects.

Table 4.1: Overview of the different dimensions in model-based object detection. Dim.=Dimension, Repres.=Representation.

Dim.	Type	Methods	Examples
Elasticity	Rigid	TM, HEA	Lee et al. [2001]; Feuerstein et al. [2009]
	Deformable	ASM, AAM, GHT	Cootes et al. [1995, 2001]; Ruppertshofen et al. [2010]
Division	Single-part	ASM, TM	Cootes et al. [1995]; Lee et al. [2001]
	Multi-part	MRF	Donner et al. [2010]; Seifert et al. [2009]
	Hierarchical	-	Engel et al. [2011]
Repres.	Statistical	ASM, AAM, GHT, MSL	Cootes et al. [1995, 2001]; Zheng et al. [2009]
	Physical-based	MSM, FEM	Dornheim and Dornheim [2008]; Engel et al. [2011]

Therefore, multi-part models enjoy high popularity. Their main idea is to divide the object into different components and use (spatial) relationships among them. Hierarchical models additionally include a hierarchy between subparts.

Models can be created by either statistical or expert-given physical-based approaches. Statistical approaches rely on learning to describe objects by their features, with shape and intensity-based being the most popular ones. All statistical approaches rely on a database. Thus, their performance can vary significantly for unknown objects. In contrast, physical-based models aim at building an object representation by domain knowledge. In Table 4.1, the discussed methods are summarized with respect to all three model dimensions.

Haar-like features are employed in all types of detection algorithms regardless of the data dimension. These features are used commonly in statistical models. Their popularity is also based on their fast computability. Other commonly employed features are shape, intensity, edges, gradients and position.

4.2   COMPUTER-AIDED DIAGNOSIS

In the last section, a methodological overview about object detection was given. In this section, a short summary of algorithms that are used for CAD is given with a focus on applications as cerebral aneurysm detection is a part of CAD. Especially, algorithms that detect pathologies similar to aneurysms are discussed.

Computer-aided Diagnosis (CAD) describes procedures that assist the physician in the interpretation of medical images. Different algorithms are employed to describe a CAD system. The emphasis in CAD is to support the physicians instead of replacing them. A sharp contrast to CAD is automated computer diagnosis, where the goal is to substitute the physician by a machine with appropriate algorithms [Doi, 2005]. However, this concept from the 1960s proved to be a misjudgment as most detection problems are too complex to be solved by an algorithm with

CAD systems assist the physician to find a good diagnosis based on all available information

comparable quality to a human. The performance of the respective algorithms does not have to be comparable to or better than radiologists, but needs to be complementary to them [Doi, 2007].

The purpose of CAD is to serve the physician as a second opinion or to give suggestions. The probability to overlook pathologic regions decreases with the use of CAD [Cupples et al., 2005]. Due to the pressure that physicians are exposed to in today's health care system, CAD is also cost-effective as it may substitute a double-reading[1]. Nevertheless, CAD systems are only able to make suggestions, the final diagnosis is made by the radiologist.

CAD systems can be further classified into three groups [Giger et al., 2008]:

- Computer-aided Detection (CADe) to mark suspicious regions in a data set,

- Computer-aided Diagnosis (CADx) to analyze these regions, e. g., for malignancy or benignancy and

- Computer-aided Quantification (CADq) to quantify the (already known) pathology.

Comprehensive information about CADe and CADx can be found in [Doi, 2005, 2007; van Ginneken et al., 2001]. An overview about CADq can be found in [Giger et al., 2008]. The term CAD is used commonly for CADe and CADx systems in the literature. In this work, the term CAD is used as a synonym for CADe algorithms unless otherwise noted as the initial detection of pathologies is relevant for this thesis.

CAD systems are especially relevant in modern medicine as the amount of medical images has increased due to the availability of high quality and patient-friendly imaging techniques. Most of them are three-dimensional. 2D images, e. g., mammography images, can be interpreted by an experienced radiologist relatively fast (118 s for an information-rich mammography [Tchou et al., 2010]). The interpretation of 3D images is more challenging by reason of their additional information content; hence the reading time also increases. [Kato et al., 1995] reported a mean interpretation time of CT volumes of 343 s and for MRI of 530 s. The reading time also depends on the image size and reason of the image acquisition (e. g., diagnosis with respect to a certain suspicion or therapy). CAD can help the radiologist to reduce the interpretation time especially for 3D image data [Yoshida and Näppi, 2001]. The reading time for a mammography with a CAD system was 19.5 % of the reading time without CAD [Tchou et al., 2010].

CAD is able to shorten reading time of radiologists

4.2.1 *Evaluation measures*

CAD algorithms have to be evaluated to determine their quality and to compare different algorithms. Standard evaluation measures assess the output of the CAD system by comparing it with a given ground truth, i. e., data sets aggregated in a database where the pathologies are labeled by radiologists or domain experts.

---

1 *Reading* refers to the process of interpreting a medical data set by a physician.

Thus, the sensitivity se of an algorithm is equal to the definition given in Section 2.2 and defined as:

$$se = \frac{n_{TP}}{n_{TP} + n_{FN}}, \qquad (4.2)$$

where n_{TP} is the number of True Positives (TPs) (the correctly identified pathologic regions by the CAD system) and n_{FN} is the number of False Negatives (FNs) (the pathologic regions that were not found by the CAD system).

It is important to also measure the average FP amount fp_{DS} for evaluation of a CAD system:

$$fp_{DS} = \frac{n_{FP}}{n_{DS}}. \qquad (4.3)$$

n_{FP} is the number of FPs (the identified pathologic regions by the CAD system that are not pathologic) and n_{DS} is the number of total data sets.

Additionally, the Free Response-operator Characteristic (FROC) curve can be computed to measure the performance of a system by leaving one parameter variable while fixing all other parameters. The curve plots se against fp_{DS}. For a detailed explanation, see Section 6.3.

4.2.2 *Applications*

CAD algorithms have been proposed to detect various pathologies in medical images. These algorithms are employed to detect e.g., cancerous tumor regions in various organs, coronary artery disease or cerebral aneurysms. The majority of algorithms have been presented to find tumors in three organs: lung, breast and

Most CAD systems aim colon [Ye et al., 2009; Cheng, 2003; Yoshida and Näppi, 2007]. All three organs are
at detecting cancerous a major source of today's cancer occurrence. By far the most methods regarding
regions CAD are about detection of breast cancer in mammographies [Suri and Rangayyan, 2006; Tang et al., 2009]. Despite the common use of these methods, the benefit of such a system is still discussed in the medical community. The sensitivity of an expert usually increases by incorporating the system, however also the FP amount increases [Karssemeijer et al., 2009].

In the following sections, example CAD algorithms for different pathologies are presented. First, systems to detect lung nodules are presented. The problem of detecting lung nodules is closely related to cerebral aneurysm detection as they have similar properties. Secondly, two approaches are introduced that have been proposed to detect AAA and to detect retinal microaneurysms. It is analyzed if these types of aneurysms are related to cerebral aneurysms and if the employed algorithms are suitable for cerebral aneurysm detection. Finally, a general scheme for CAD algorithms is derived.

4.2.3 *Methods to detect lung nodules*

A large proportion of CAD algorithms have been developed to detect lung nodules. Nodules in the lung tissue are early indications of lung cancer (see Figure 4.1 for an
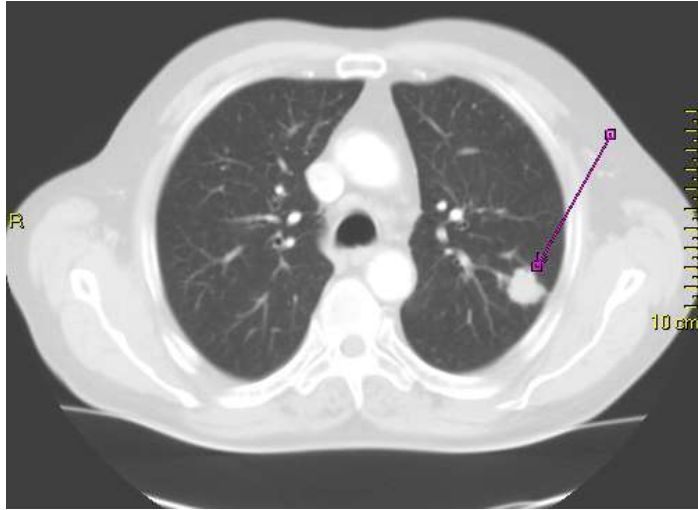
Figure 4.1: Example of a CT data set slice containing a lung nodule, which is denoted by the pink arrow (Author: Lange123, license: CC3.0, source: http://commons.wikimedia.org/wiki/File:Thorax_CT_peripheres_Brronchialcarcinom_li_OF.jpg).

example). Lung nodules are similar to cerebral aneurysms. They can be generally described having a spherical shape and nodules are commonly in the direct vicinity of blood vessels. Both statements are also true for cerebral aneurysms.

Lung nodules and cerebral aneurysms share many features

Many CAD systems to detect lung nodules are proposed [Ye et al., 2009; Li et al., 2003; van Ginneken et al., 2010]. In [Ye et al., 2009] anisotropic diffusion is used as a pre-processing step. The lung region is segmented using a fuzzy thresholding method. Initial candidates are found by evaluating the shape using a *Shape index* value and a *sphericity* value. The Shape index value is based on mean curvatures at a voxel position p:

$$\text{SI}(p) = \frac{1}{2} - \frac{1}{\pi} \arctan \frac{\kappa_1(p) + \kappa_2(p)}{\kappa_1(p) - \kappa_2(p)}, \tag{4.4}$$

where $\kappa_1(p)$ and $\kappa_2(p)$ are primary and secondary principal curvatures at voxel p. The sphericity is based on an analysis of the eigenvalues of the Hessian matrix [Li et al., 2003] to emphasize spherical structures.

Both features aim at finding spherical structures and thus the approach uses a rigid model with parametric domain knowledge. ROI are found by using an adaptive thresholding technique and a combination of a MRF and an expectation-maximization algorithm on maps of both feature values. To reduce the amount of FP, first a Rule-based System (RBS) is applied to remove easily dismissible non-nodule objects and then a Support Vector Machine (SVM) with radial kernel classification is done. Shape and intensity features are used for both classifiers.

Methods to find lung cancer are mostly based on shape information

The method was tested with 54 CT data sets having 118 nodules. A detection rate of 90.2 % is reported at 8.2 fp_{DS}. Problems to detect non-spherical and low-contrast nodules were described.

In [van Ginneken et al., 2010], six algorithms to detect lung nodules were evaluated on the same 55 data sets under the same conditions. The algorithm leading to the best results [Murphy et al., 2009] is similar to [Ye et al., 2009] in its initial ROI

detection. FP removal relies on a k-nearest Neighborhood classifier (kNN). Eight low-level features are used to exclude obvious incorrect ROI by employing a RBS. Finally, 19 high-level features are employed to also classify ambiguous candidates accurately. The study proposes a scoring scheme for CAD algorithms that relies on the FROC analysis (see Section 6.3). Seven predefined FP rates ($2^{-3}, 2^{-2}, \ldots, 2^3$ FP per scan) are used.

Unfortunately, even this environment only allows partial objective evaluation of algorithms. The algorithm leading to the best quality was developed by the organizers of the study and had full access to the test database in advance. The scores were considerably better than those of the other participants. This strengthens the requirement to separate the test and the training data set to objectively evaluate the algorithm on unknown data sets.

Apart from detection algorithm, also algorithms to segment lung nodules in CT data sets have been proposed. The method was additionally tested so segment liver metastases and enlarged lymph-nodes in CT data sets. Thus, it is one of few algorithms that have been practically applied to analyze other organs than they were originally developed for. In [Moltz et al., 2009], an algorithm was proposed that combines a threshold-based approach with a model-based morphological processing (smart opening). The initial position is user-given and is also utilized to estimate the intensity distribution of nodules. According to the found type of the lesion, adaptive thresholds for the segmentation are found. The erosion strength is also set adaptively and finally, an ellipse-fitting is done. Thus, both parametric and statistical information are used to create the model in this approach. The basic algorithm is the same to segment different organs except for its parametrization.

4.2.4 *Methods to detect Abdominal Aortic Aneurysms*

An Abdominal Aortic Aneurysm (AAA) is a localized dilation of the abdominal aorta (see Figure 4.2a). Similar to cerebral aneurysms, a rupture is life-threatening and can lead to death within minutes [Upchurch and Schaub, 2006]. AAA can be roughly compared to fusiform aneurysms by their shape, but their diameter of $> 30\,\mathrm{mm}$ is notably larger than of cerebral aneurysms.

[Dehmeshki et al., 2009] have proposed a segmentation-driven detection algorithm for AAA in CTA volumes. The approach incorporates an extraction of the aortic lumen by threshold-based segmentation. Subsequently, the abdominal section is found by detecting anatomic structures that bound this section (spine and kidneys). The position of the celiac trunk and the iliac junction (see Figure 4.2) are found by a simple threshold segmentation and a bifurcation detection technique on the centerline. Finally, based on the localized position, an ellipsoid fitting algorithm is applied to segment the abdominal aorta. A mask containing several anatomic objects close to the aorta (spine, fat, blood vessels) guides the fitting process; they are used as repulsive forces. The segmented aorta is evaluated quantitatively in terms of maximum diameter, shape irregularity and displacement. Based on these features, aneurysms are detected. The method was tested on 60 CTA images. The sensitivity of the AAA detection is reported to be 98 %. To quantitatively evaluate the segmentation, the mean overlap with a manual expert segmentation
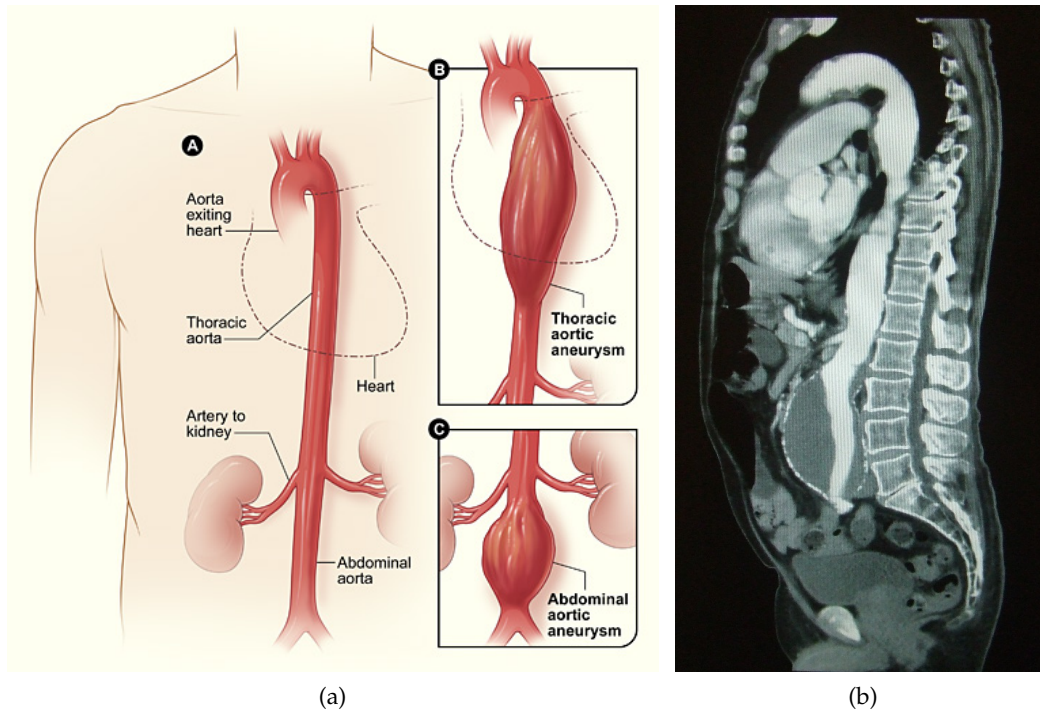
Figure 4.2: (a) Scheme of an abdominal aortic aneurysm. The celiac trunk is seen in the upper part of Section C above the aneurysm. The iliac junction is seen in the lower part of Section C below the aneurysm. (Author: National Institutes of Health, public domain, source: http://commons.wikimedia.org/wiki/File: Aortic_aneurysm.jpg). (b) Sagittal CT slice depicting an AAA. (Author: Glitzy queenoo, public domain, source: http://commons.wikimedia.org/wiki/File: Sagital_aaa.JPG).

has been computed. 95 % of voxels overlap. However, the evaluation is quite unclear and suffers on the imprecise experiment description.

Other CAD algorithms have been presented to segment the AAA in multi-spectral MRI [de Bruijne et al., 2003] based on an user-initialized AAM [Cootes et al., 2001] and in CTA based on a Level-Set formulation [Subasic et al., 2000].

The focus of most approaches in this area is the automatic segmentation and/or quantification. The problem is clearly defined: AAA could only appear on the abdominal part of the aorta, what constraints the location considerably. Furthermore, the aorta is subject to relatively simple segmentation in CTA as it is a large and good distinguishable blood vessel with a high intensity. The detection of AAA heavily relies on the quantification of the aorta and thus on the successful segmentation. Thus, most algorithms are more a CADq algorithm than a CAD algorithm.

In conclusion, the detection of AAA is rather simple compared to the detection of cerebral aneurysms because of their defined location. AAA are comparable to cerebral giant fusiform aneurysms. Thus, the techniques to detect AAA are not applicable for cerebral aneurysm detection of saccular type.

4.2.5 *Methods to detect retinal microaneurysms*

Retinal microaneurysms are visible in 2D digital color fundus photographs of the eye. In these images, they appear as very small, dark and round objects. Microaneurysms have a similar shape compared to cerebral aneurysms; however, the image modality is two-dimensional rather than three-dimensional as in angiographic images. Microaneurysms are related to diabetic retinopathy and can lead to blindness [Niemeijer et al., 2010].

A retinopathy online challenge was organized to objectively evaluate the detection of microaneurysms under realistic clinical assumptions [Niemeijer et al., 2010]. Five different methods were tested with the same objective score as in [van Ginneken et al., 2010]. The score values of all algorithms were similar. An algorithm that involved a template matching in the wavelet domain yield to the best results [Quellec et al., 2008]. The method uses a gaussian model with different standard deviations to characterize the microaneurysms as an object with circular shape. Low and high frequency subbands were ignored. As similarity measure, the coefficients of the wavelet transform of the model are compared against those of the image. A vessel segmentation step is further done to exclude vessels.

Retinal microaneurysms are similar to cerebral aneurysms by its shape, however they are detected in 2D data sets

The method leading to the best results has a sensitivity of 40 % at $1.08\,\mathrm{fp_{DS}}$. These poor results are mainly caused by the realistic experiments, thus leading to the conclusion that such a tool is not yet suitable for screening purposes [Niemeijer et al., 2010].

Another algorithm has been presented by [Hipwell et al., 2000]. A subtraction-based ROI finding is proposed in conjunction with a RBS for classification. The algorithm is tested on 3783 images and reached a sensitivity of 78 % at $0.07\,\mathrm{fp_{DS}}$. However, the method was trained beforehand on a subset of the test database which influences the evaluation beneficially.

One has to bear in mind that the objects of interest, microaneurysms, are rather small, but the images are two-dimensional, have a good SNR and the information density is rather small as many areas with uniform intensity exist. Thus, only the technique to find round shapes can be applied to the cerebral aneurysm detection problem. Otherwise, the two problems, detection of retinal microaneurysms in 2D data sets and detection of cerebral aneurysms in 3D data sets, are too different.

4.2.6 *General approach to CAD*

In almost all CAD algorithms, the workflow is similar and based on a pattern recognition approach. The algorithms commonly consist of four consecutively performed steps:

1. Pre-processing and normalization,

2. Segmentation,

3. ROI detection and

4. Classification of ROI.

The *pre-processing* aims at enhancing the image data through noise reduction techniques and image restoration methods. Furthermore, the image is normalized with respect to the intensity range, the image size and the orientation to create similar conditions for all input images. As pre-processing techniques, linear and non-linear filters are employed, e. g., Gaussian filter and anisotropic diffusion [Tönnies, 2012]. For intensity normalization, simple methods like linear contrast stretching may be used as well as complex histogram-based methods [Bogunović et al., 2008]. Orientation normalization may be reached by using information provided by Digital Imaging and Communications in Medicine (DICOM) header or registration methods [Maes et al., 2003].

The second step, *segmentation*, is done to either remove background structures or to focus on a global structure. This can be, e. g., the lung in the case of a lung nodule detection system [Lee et al., 2010] or the removal of vessels in the case of a retinal microaneurysm detection system [Hipwell et al., 2000]. This step represents a hard constraint as all objects lying outside the search space are not considered anymore. The final exclusion decision should be done as late as possible in the algorithm.

The third step, *ROI detection* is the crucial part of most CADe algorithms. Features are computed that describe the object depending on the used strategy, the object and the image characteristics. Ideally, features f should be highly discriminative, i. e., they should have the form of a generalized Dirac impulse:

The initial ROI detection is the crucial part of every CAD algorithm

$$f(R_i) = \begin{cases} \zeta & \text{if } R_i \text{ is the object of interest,} \\ 0 & \text{otherwise.} \end{cases} \qquad (4.5)$$

R is a region and $\zeta \in \mathbb{R}$ is a scalar feature value.

However, this is not possible due to the complexity and the insufficient generalization and only an approximation of this function is used. This function $\hat{f}$ is an approximated version of f. In practice, many features like shape [Yoshida and Näppi, 2007], intensity [Suzuki et al., 2005], size [Lauric et al., 2010], location [Russakoff and Hasegawa, 2006] and reference to close-by structures [Dehmeshki et al., 2009] are feasible for this step. The actual ROI are defined, e. g., by using a threshold t on the feature image and a clustering method to aggregate pixels. As a high sensitivity is crucial for CADe approaches, usually a large amount of ROI are identified to minimize the chance that a pathology is overlooked [Doi, 2007].

The fourth and last step consists of a *classification*. The aim is to discriminate between true objects and FPs (see Figure 4.3 for an example). The classification can be done either by training or by utilizing expert or empirical domain knowledge.

Several machine learning approaches are used for training, such as kNN classifiers, Artificial Neural Network (ANN) or SVM [Lu and Weng, 2007]. These approaches commonly include feature selection to identify a subset of relevant features [Böröczky et al., 2006]. The quality of statistical methods depends on the quantity and quality of training samples [Lu and Weng, 2007]. The training database is usually rather small, rarely exceeding 100 data sets.

Expert or empirical knowledge is formalized in a Rule-based System (RBS). Simple rules are defined, such as exclusion of the image border or definition of minimal and maximal valid feature values for assignment of ROI to TP or FP. Thus,
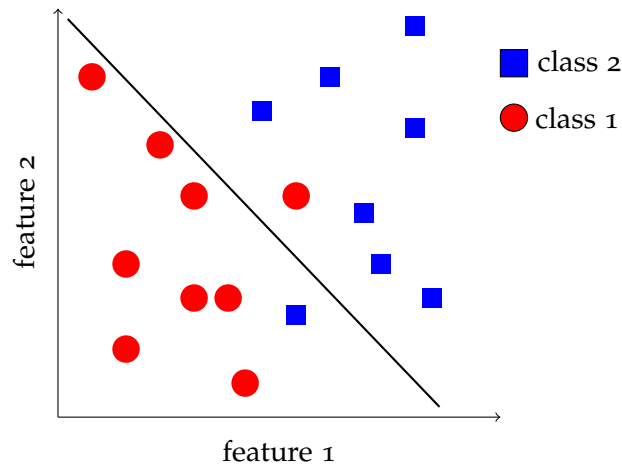
Figure 4.3: Visualization of classification in a two-dimensional feature space. The feature space is divided by a hyperplane into two half spaces (a line in a two-dimensional space). One member of each class is misclassified using this separation line.

RBS are classifiers without training. Examples of Rule-based System (RBS) can be found in [Ye et al., 2009; Feuerstein et al., 2009; Lauric et al., 2010]. An advantage of expert-based models is that they usually can cope better with outliers than statistical methods as a larger variation of the model is permitted. The main disadvantage is the need for an expert that explicitly designs the rules.

Recently, open web databases have been established that cover images of different pathologies, e. g., lung nodules in CT volumes [van Ginneken et al., 2010] and chest radiography images [Shiraishi et al., 2000], digital fundus color photographs of the eye [Niemeijer et al., 2010], mammography images containing cancer [Heath et al., 2000], CT colonoscopy images containing colon cancer [Johnson et al., 2008] and liver tumors in CT volumes [Niessen et al., 2008]. However, at this date, no publicly available database is known that also covers aneurysms in angiographic images. The establishment of public available databases are necessary to objectively compare CAD algorithms as advocated in [van Ginneken et al., 2010; Niemeijer et al., 2010]. The composition of the training data set influences the quality of the algorithm, especially if statistical methods are employed. The more homogeneous a data set is the greater is the risk of an overadaption. Especially if the pathologies itself are heterogeneous as is the case with cerebral aneurysms, a database consisting of a wide range of typical objects is essential.

No publicly available angiography database exists that contains aneurysms

In conjunction with these open databases, grand challenges have been proposed to objectively compare different algorithms on the same database [van Ginneken and Kerkstra, 2013]. A benchmark for the State of the Art in different CAD areas can be established in this way.

4.2.7 *Summary*

In this section, a short introduction about CAD algorithms was given. Example algorithms in three different areas have been presented (see Table 4.2). With re-

Table 4.2: Overview about the different discussed CAD methods. Sim. = similarity to cerebral aneurysms with respect to features, e. g., shape.

Pathology	Method	Data	ROI finding	Sim.
Lung nodules	Ye et al. [2009]; van Ginneken et al. [2010]	CT (3D)	Spherical shape detection, machine learning	High
Abdominal Aortic Aneurysm	Dehmeshki et al. [2009]	CTA (3D)	Segmentation-based feature analysis	Small[a]
Retinal microaneurysms	Niemeijer et al. [2010]; Quellec et al. [2008]	Color photo (2D)	Stochastic modeling of intensity distribution	Medium

[a] High similarity only to fusiform aneurysms.

spect to the model, mostly rigid single-part models are applied. Statistical and parametric models are used in approximately the same extent.

The pathology most similar to cerebral aneurysms, with respect to image processing characteristics, described in the last section is lung nodules. The detection of lung nodules relies on the shape and is mostly solved by a multi-scale filter that emphasizes spherical objects.

The detection of AAA differs to the detection of cerebral aneurysms as their location is clearly defined. Retinal microaneurysms are detected in 2D images. Therefore, the technique of these algorithms is only limited applicable for cerebral aneurysm detection.

The existing approaches are almost always based on the general four-step technique (cf. Section 4.2.6). First, the image data is normalized and then a segmentation is computed to reduce the search space. Subsequently, the initial ROI detection is done based on the primary feature and then the selected regions are classified to reduce FP. It is suitable to use this approach also for a cerebral aneurysm detection algorithm. However, it would be desirable to minimize the dependence on the segmentation and on a statistical database.

4.3 EXISTING APPROACHES TO ANEURYSM DETECTION

Existing approaches to detect cerebral aneurysms are discussed in this section. Most algorithms have been published in the last seven years. The methods can be categorized with respect to their ROI detection approach in five different groups:

1. spherical shape-based analysis,

2. symmetrical shape-based analysis,

3. skeleton analysis,

4. difference image-based technique and

5. a combination of the above techniques.

While the first two categories rely on the shape of aneurysms, the skeleton is the main information carrier in the third category. In the fourth category, a normal artery model is subtracted from the original image resulting in a difference-based approach. A combination of different approaches is used in the last category.

Below, the different approaches are characterized, techniques are outlined and results are given.

4.3.1 *Spherical shape-based analysis*

First, general methods to detect spherical shapes are presented. Then, the existing aneurysm detection approaches are summarized that use such methods.

GENERAL METHODS TO DETECT SPHERICAL SHAPES   Three groups of methods have been employed to find spherical objects in three-dimensional data sets:

- intensity-based methods measuring the local intensity distribution
  - template-matching
  - gradient concentrate feature computation
  - multi-scale filtering with Hessian Eigenvalue Analysis (HEA)
- surface-based methods measuring characteristics of a segmented surface
  - shape index
  - curvedness
  - sphericity
- statistical approaches.

The first intensity-based method is *template-matching*. It is a standard image processing technique to search for a predefined static shape in an image by comparing the shape intensity to intensity in image regions. It is successfully applied to detect spherical pathologies such as lung nodules [Lee et al., 2001]. The *gradient concentrate*, proposed in [Uchiyama et al., 2005] to detect cerebral aneurysms is a similar method. It is based on the gradient intensity magnitude and direction. The third intensity-based method is the *analysis of the Hessian matrix* [Li et al., 2003; Frangi et al., 1998; Sato et al., 1998]. Originally, most of these methods aim at finding vascular structures that are modeled by ellipsoids having a long diameter and a short diameter. In the case of spherical objects, a sphere is used as model.

Surface-based features are the shape index (Equation 4.4), the *curvedness* of a surface [Zhao, 2011] and the *sphericity* Ψ. Ψ is defined as:

$$\Psi = \frac{\pi^{\frac{1}{3}} (6s)^{\frac{2}{3}}}{a}, \tag{4.6}$$

where s is the volume of the ROI and a is the surface area of the ROI. It was used e. g., in [Murphy et al., 2009] to detect lung nodules.

Statistical approaches to find round objects have been presented to detect e. g., breast cancer in 2D mammographies [Tang et al., 2009].

In the following, the Hessian eigenvalue analysis is described in detail as it used a general model. Furthermore, it is used in many CAD methods such as the detection of cerebral aneurysms and lung nodules [Arimura et al., 2006; Li et al., 2003].

The Hessian matrix H of a point p is defined as a matrix of the second order derivatives:

$$H(p) = \begin{bmatrix} f''_{xx} & f''_{xy} & f''_{xz} \\ f''_{yx} & f''_{yy} & f''_{yz} \\ f''_{zx} & f''_{zy} & f''_{zz} \end{bmatrix}, \tag{4.7}$$

where f''_{ij} is the second derivative in direction i and j of p approximated in a discrete image e. g., by differences. Thus, the matrix describes the second order intensity variations of an image. An eigenvalue analysis of $H(p)$, $Eig(H)$, is done to compute the three eigenvalues λ_1, λ_2 and λ_3 with $|\lambda_1| \geqslant |\lambda_2| \geqslant |\lambda_3|$.

Bright spherical objects on a dark background lead to the general property $\lambda_1 \approx \lambda_2 \approx \lambda_3 \ll 0$ [Frangi et al., 1998], i. e., there is a strong magnitude change of intensity in three orthonormal directions in the center of the sphere.

Spherical objects are determined by their eigenvalues that have specific properties

Three different approaches were chosen to compute an estimation for the blobness b [Sato et al., 1998; Frangi et al., 1998; Li et al., 2003]. In [Lesage et al., 2009], further approaches are summarized.

[Sato et al., 1998] proposes

$$b(Eig(H)) = \begin{cases} |\lambda_3| \left(\frac{\lambda_2}{\lambda_3}\right)^{\delta_1} \left(1 + \frac{\lambda_1}{|\lambda_2|}\right)^{\delta_2} & \text{if } \lambda_3 < \lambda_2 < \lambda_1 \leqslant 0. \\ 0 & \text{otherwise.} \end{cases} \tag{4.8}$$

δ_1 and δ_2 control the sharpness of the selectivity for the isotropy of the object with respect to the relation $\frac{\lambda_2}{\lambda_3}$ and $\frac{\lambda_1}{\lambda_2}$, respectively. Common choices for both parameters are 0.5.

[Frangi et al., 1998] proposes

$$b(Eig(H)) = \begin{cases} \left(1 - \exp\left(-\frac{R_A^2}{2\alpha^2}\right)\right) \exp\left(-\frac{R_B^2}{2\beta^2}\right) \exp\left(-\frac{S^2}{2\gamma^2}\right) & \text{if } \lambda_3 < \lambda_2 < \lambda_1 \leqslant 0. \\ 0 & \text{otherwise.} \end{cases}$$

$$\tag{4.9a}$$

$$R_A = \frac{|\lambda_2|}{|\lambda_1|}, \qquad R_B = \frac{|\lambda_3|}{\sqrt{|\lambda_1 \lambda_2|}}, \qquad S = \sqrt{\sum_{k \leqslant 3} \lambda_k^2}. \tag{4.9b}$$

α, β and γ control the sensitivity of the filter to the measures R_A, R_B and S. Common choices are $\alpha = \beta = 0.5$ and $\gamma = 5$.

[Li et al., 2003] proposes

$$b(Eig(H)) = \begin{cases} \frac{|\lambda_3|^2}{|\lambda_1|} & \text{if } \lambda_3 < \lambda_2 < \lambda_1 < 0. \\ 0 & \text{otherwise.} \end{cases} \tag{4.10}$$

Figure 4.4: (a) Example 2D-DSA image. Three different blobness parametrizations are compared: (b) the method by [Sato et al., 1998] with $\delta_2 = 1$ (δ_2 is irrelevant in 2D), (c) the method by [Frangi et al., 1998] with $\alpha = \beta = 0.5$ and $\gamma = 10$ and (d) the method by [Li et al., 2003]. They are all parametrized to find dark circular objects with the same diameter (2 px to 8 px). The first two parametrizations produce rather similar results with large plateau-like intensity peaks while the third parametrization is rather strict producing rapidly sloping maximum peaks.

A visual comparison of all parametrizations is given in Figure 4.4. The conceptually easiest parametrization is the one by [Li et al., 2003] only taking the smallest and the largest eigenvalue into account and using no other parameters.

All these Hessian-based methods employ scale knowledge as the object diameter has to be known. By using scale-space approaches [Lindeberg, 1994], this problem can be circumvented by taking different scales $[r_{min}, r_{max}]$ into account. The image is convolved using a Gaussian kernel having the standard deviation σ. It is reasonable to assume that the following relationship exists: $\sigma_0 = \frac{r}{2}$ as 95 % of the area of the Gaussian function lies within this area [Li et al., 2003]. Thus, the maximum amount of blobness filter response can be measured in the center of the

Scale-space theory is applied to find spherical objects having different diameters

sphere if the smoothing is chosen according to the radius.

The image is then convolved N times between the minimum and maximum scales. $N = 5$ was suggested as sampling for medical imaging applications. Additionally, exponential smoothing scales were proposed by [Li et al., 2003]:

$$\sigma_n = \left(\frac{r_{max}}{r_{min}}\right)^{\frac{1}{N-1}} \sigma_1, \tag{4.11a}$$

$$\sigma_1 = \frac{r_{min}}{4}. \tag{4.11b}$$

The filter response image B_{σ_i} is multiplied at each scale with σ_i^2 to compare the filter responses at the different scales.

The maximum filter value of all scales is taken as the final blobness value [Frangi et al., 1998]:

$$B = \max_{\sigma_i} B(M_{\sigma_i}^\rho), \; i = 1, \dots, N. \tag{4.12}$$

$B(M_{\sigma_i})$ is the image filtered at scale σ_i.

METHODS FOR ANEURYSM DETECTION   Shape-based methods model the appearance of an aneurysm. Although a generalization of aneurysms with respect to the shape is difficult (cf. Section 2.1.2), a spherical shape representation is commonly used as model to search for initial ROI. Popular techniques to find spherical structures are especially the previously discussed techniques that rely on the Hessian eigenvalue analysis.

One of the first methods related to a CAD system for aneurysm detection was presented by [Hayashi et al., 2003]. It relies on the shape index and curvedness measuring the Gaussian curvature of a shape in the image data. Aneurysms do usually not have a smooth surface in contrast to vessels. This basic assumption is utilized in this approach. In a three-dimensional visualization environment, both features are overlaid using a color table. The evaluation was done by two neuroradiologists. In 18 TOF-MRA data sets with 24 aneurysms, they found three aneurysms that were previously not found. Although it is only a feasibility study, it was a pioneer work as similar shape-based features were used in subsequent publications.

Aneurysms commonly have a spherical shape, thus they can be recognized by enhancing spherical structures

A similar method was presented by [Prasetya et al., 2011] for the (manual) detection of aneurysms in CTA images.

The first automatic CAD system to detect aneurysms was developed by [Arimura et al., 2004, 2006]. The algorithm was built for TOF-MRA image data. The scheme involves a detection of ROI by using a sphere-enhancing filter, then a feature extraction of the segmented ROI and finally a removal of FP by a RBS and Linear Discriminant Analysis (LDA).

Initial selection involves two sources: the blobness filter with Li's parametrization [Li et al., 2003] and short branches of the vessel skeleton (see Figures 4.5 and 4.6). Peaks of the filter image are extracted by a multiple gray-value thresholding technique. These peaks and the short branches are then used as initial seed points

(a)   (b)
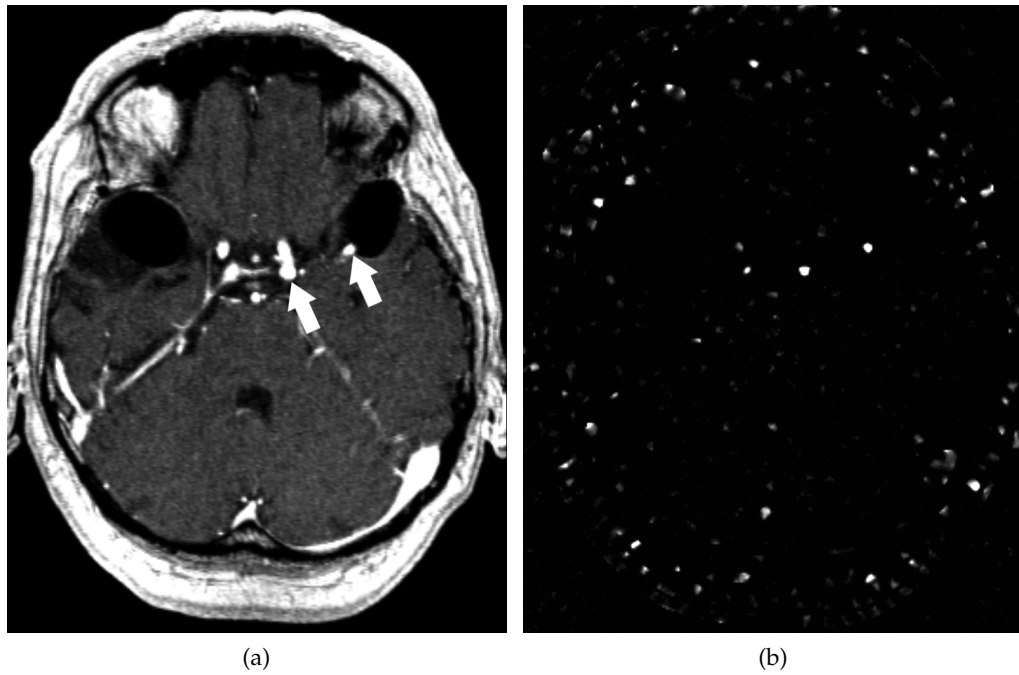
Figure 4.5: Example of the multi-scale filter to enhance blob-like structures on a TOF-MRA slice containing two aneurysms. Li's parametrization is used. The aneurysms are indicated by the white arrows. At their positions in the filtered slice, clear highlighting occurs.

(a)   (b)   (c)   (d)

(e)   (f)   (g)   (h)
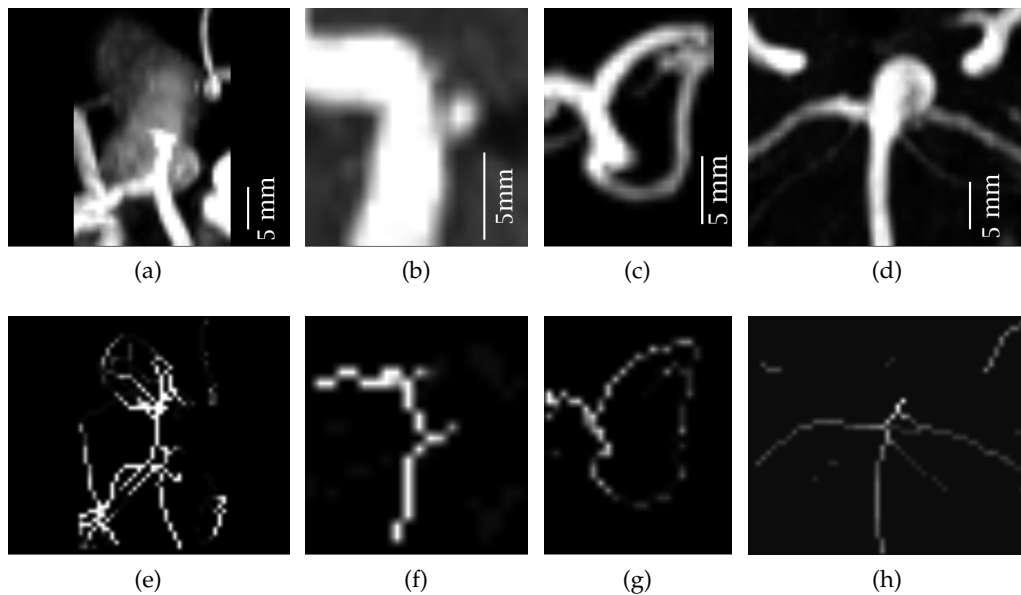
Figure 4.6: The four different aneurysm classes shown by a MIP and their skeleton representation: (a) and (e) large type, (b) and (f) short-branch type, (c) and (g) bifurcation type and (d) and (h) single-vessel type. Depiction is based on [Arimura et al., 2006] with own data. The different images have different scale that is indicated by the bars.

for a region-growing segmentation resulting in initial ROI. Large aneurysms having a spherical shape are enhanced by the multi-scale filter while small aneurysms adjacent to bending vessels are found by the vessel skeleton approach.

Features are computed on each ROI. Different features are computed based on a categorization of each ROI in four different types: large type, bifurcation type, short-branch type and single-vessel type. They are classified according to their diameter and skeleton properties (see Figure 4.6).

Furthermore, a so-called Shape-based Difference Image (SBDI) was computed similar to the difference-image approaches (cf. Section 4.3.4). The SBDI aims at correction for local changes in vessel thickness to suppress normal vessels and leave (small) pathological vessel parts like small aneurysms based on the skeletonized segmented image. Seven features are computed on the SBDI image for single-vessel type and bifurcation type ROI.

Five intensity features have been employed, e. g., average voxel intensity and relative difference in standard deviation of voxel values between inside and outside regions. Eight morphological features have been used, e. g., sphericity and maximum/minimum distance between centroid and surface. Seven SBDI features are computed that are a mixture of shape-based and intensity-based features.

For further removal of FP, a RBS and a consecutive LDA are used. Both classifiers are trained using a test data set. RBS rules are applied that define maximum value ranges $[\hat{f}_{min}, \hat{f}_{max}]$ for every feature with $\hat{f}_{min} = 0.95 \cdot f_{min}$ and $\hat{f}_{max} = 1.05 \cdot f_{max}$, where $\hat{f}_{max}$ is the estimated maximum value and f_{max} is the measured maximum value for true aneurysm ROI in the training database. A LDA is computed on four features chosen by feature selection method as the final FP exclusion step.

For evaluation, a leaving-one-out technique was used. The method was tested on two data sets from different institutions: 115 TOF-MRA data sets including 61 aneurysms (database A) and 63 TOF-MRA data sets including 36 aneurysms (database B). Sensitivity of the algorithm is reported to be 97 % with 3.8 fp$_{DS}$ on database A. The inclusion of the SBDI feature leads to a decrease of 34.5 % of FP at the same sensitivity compared to a previous publication [Arimura et al., 2004]. The robustness of the algorithm was shown on a test with database B. Results were good yielding to a sensitivity of 94 % at 2.3 fp$_{DS}$. Nonetheless, a strong dependence on the training data set was reported, which is always a problem in statistical-based approaches. The authors stated also that the resolution plays an important role for the algorithm.

Another spherical shape-based method was presented by [Uchiyama et al., 2005]. The method is similar to the previous method with respect to the initial ROI finding approach. A simplified single-scale gradient-filter is used to enhance round convex regions in the original image [Kobatake and Murakami, 1996].

Removal of FP was done by an experimentally-found RBS and a Quadratic Discriminant Analysis (QDA) with three features (size, sphericity and mean value of filtered image with respect to the ROI). Details about the RBS were not given. Also, it is unclear why two elimination steps are performed. It can be assumed that most FP that are identified by the RBS are also recognized by the QDA.

False positives are eliminated commonly by using Linear- or Quadratic Discriminant Analysis

The algorithm was tested on 20 TOF-MRA volumes containing 7 aneurysms. A sensitivity of 100 % was reported at 1.85 fp$_{DS}$. The evaluation scenario is invalid

as the statistical-based algorithm is tested on the same data set that it is trained with. Furthermore, the evaluation can give only a very rough estimation of the performance of the algorithm as the database is too small.

An extension to this method was presented in [Uchiyama et al., 2008]. As additional feature, the anatomical location is used, hence vessel regions are identified as described in [Uchiyama et al., 2006]. This algorithm is based on a registration approach. First, a rough initialization is made by maximizing the overlap of vessel regions using only translation. Then, a control-point-based rigid registration is done by a least-square fitting of previously found control points. Thus, a common coordinate system is found for every data set. The normalized position vector $(x\, y\, z)^{\top}$ is used as additional feature in the FP removal stage.

In contrast to the previous algorithm, the RBS scheme is explained in detail. Similar to [Arimura et al., 2006], the minimum and maximum values for each feature are computed and a valid feature range is defined. However, the minimal and maximal values are taken directly without margin what leaves the assumption that the training database was again used for testing. The database contains 100 TOF-MRA data sets with 30 aneurysms. The overall sensitivity was 90 % at 1.5 fp$_{DS}$.

4.3.2 *Symmetrical shape-based analysis*

In this group of methods, the analysis relies on the shape, however without employing curvature-based or spherical-based measures. Instead, a measure is proposed for the symmetry of objects. Only one publication is known applying this method. Although the initial ROI detection strategy is to find short branches of the medial axis, we do not number this publication among the skeleton based group (cf. Section 4.3.3) as the algorithm depends especially on the shape analysis.

This method relies heavily on the surface measure *Writhe number* [Lauric et al., 2010]. This number describes how much a curve twists and coils and is extended to surfaces in the publication. The Writhe number cannot be interpreted intuitively. Generally, the Writhe number is 0 if the surface can be described via a mirror symmetry. A mirror plane exists in cylinders or extruded parabolas that are generalizations of vessels, thus $Wr = 0$ for ideal vessel-like objects. It is assumed that aneurysm ROI are characterized by no or only small and partial symmetries of points on the surface, thus leading to $Wr > 0$. The Writhe number aims at differentiating healthy vessels with clear defined tubular morphology and pathologic vessel objects with unclear and somewhat different morphology. With respect to this idea, this approach is slightly similar to difference-based approaches (cf. Section 4.3.4).

The basic assumption is that aneurysms have shape asymmetries in contrast to vessels

The Writhe number is defined as follows. Given two points p and p' on a (connected) surface, their relationship w is defined by

$$wr(p, p') = \frac{\left[\hat{n}_p, p' - p, \hat{n}'_p\right]}{|\hat{n}_p| \cdot |p' - p| \cdot \left|\hat{n}'_p\right|}, \tag{4.13}$$

where $\hat{n}_p$ is the surface normal at point p, $|p|$ is the norm of the vector p and $[a, b, c]$ is the triple scalar product of vectors a, b and c. It is defined as $[a, b, c] = a \cdot (b \times c)$, where $a \cdot b$ denotes the dot product and $a \times b$ denotes the cross product.

The Writhe number Wr of a point p in a local neighborhood $N(p)$ is given by:

$$Wr(n, N(p)) = \int\limits_{p' \in N(p)} wr(p, p')\, dp'. \tag{4.14}$$

Simplified[2], p' belongs to $N(p)$ and is connected to p. This leads to the following equation in a discrete space:

$$Wr(n, N(p)) = \sum_{p' \in N(p)} wr(p, p'). \tag{4.15}$$

The approach requires a segmented vasculature as input. A medial axis is computed based on the segmentation. Similar to [Arimura et al., 2006], cerebral aneurysms are assumed to be short branches of the medial axis. ROI are extracted based on local neighborhoods of short branches. For each ROI, the Writhe number and the volume are computed. ROI having a non-zero Writhe number and a large size are taken as final candidates.

It is shown that true aneurysms generally have a large volume size and a large Writhe number. No information is provided why this observation is not used as classification criterion.

The method is one of the few tested on multi-modal images [Lauric et al., 2010; Lauric, 2010]. It has been tested on 3D-RA data sets, MRA data sets and CTA data sets. The MRA data sets consist of TOF-MRA data sets and CE-MRA data sets. For each modality, ten data sets were tested. Results of 100 % sensitivity at 0.66 fp_{DS} for 3D-RA, and 5.36 fp_{DS} for CTA are reported [Lauric et al., 2010]. For MRA, 100 % sensitivity at 5.7 fp_{DS} was achieved [Lauric, 2010]. Problems have been reported regarding fusiform aneurysms that are true radially symmetric as the Writhe number is ~ 0 in these cases and no longer useful as discriminatory criterion. As the evaluation database is rather small, no general statement about the quality of the method can be made.

The algorithm by Lauric et al. [2010] was tested with multiple angiographic modalities

The algorithm uses the Writhe number as indication for aneurysms. This number is obviously suitable for the detection task as it evaluates the symmetry of the segmented shape of the vasculature. However, it is a very complex construct what leads possibly to results that are difficult to understand. Also, no prediction can be made when the method leads to good results and when it fails.

The algorithm heavily depends on high quality segmentation as no intensity data or other features are used as information. This is a problem especially in the case of CTA data as high quality segmentation is a challenging task. CTA data required manual pre-processing.

This is the closest approach in literature to define an *aneurysmness measure*[3] as a single feature rather than to combine several features by applying LDA or other feature selection schemes.

---

2 For details, see [Lauric et al., 2010].
3 Analogue to the vesselness measure introduced in [Sato et al., 1998; Frangi et al., 1998].

4.3.3   *Skeleton analysis*

Another approach to aneurysm detection is an analysis of the skeletonized vasculature. The basic assumption is that aneurysms can be characterized by short branches in the vessel tree. This approach was used in several publications [Arimura et al., 2006; Lauric et al., 2010; Hassan et al., 2011; Suniaga et al., 2012]. As already mentioned in Sections 4.3.2 and 4.3.1, the approach by [Lauric et al., 2010] and [Arimura et al., 2006] is categorized in these sections although the ROI detection step is also based on an evaluation of short branches.

The vessel skeleton can be computed from vessel segmentation. Vessel segmentation and centerline detection algorithms have been reviewed in Section 3.1. Their quality depends first and foremost on the image modality and the vessel-background contrast. Vessel segmentation is trivial for 3D-RA data sets, and gets more difficult for CE-MRA, TOF-MRA and CTA data sets.

In [Hassan et al., 2011], a distance-based centerline extraction method was performed on an existing vessel segmentation. By using a modified Dijkstra algorithm, a connected, one voxel wide centerline is extracted. The centerline is then seen as a graph with the vertices being the bifurcation and terminating points and the edges being the blood vessels. The length of each branch l is calculated using a modified Euclidean distance. Additionally, for each voxel of the branch, the radius r_i perpendicular to the branch is computed. An average radius r_{avg} is computed by taking all centerline voxels of a branch into account. Vessels have a relatively constant and slow changing diameter whereas aneurysms usually have a large change in their diameter. A least-squares fitting on the quadratic function $r_{avg} = a + bl + cl^2$ with $a, b, c \in \mathbb{R}$ is done to evaluate the diameter changing characteristic. Branches fulfilling $c > c_t$, where $c_t = 0.2$ is determined experimentally, are counted as aneurysm candidates. No further classification was done.

The basic assumption of skeleton-based algorithms is that aneurysms are characterized by short branches in the vessel tree

The method was tested with 20 data sets containing of CTA and MRA volumes. A sensitivity of 100 % is reported at 0.1 fp_{DS}. The average vessel quantification error was 11.7 %. The evaluation is very short and imprecise. Thus, the quality of the algorithm cannot be judged reliably. A disadvantage is that only one connected component of the segmentation can be analyzed per pass. However, a visible connection of the cerebral vasculature is not necessarily present in all modalities although an actual connection exists. The method does also depend on the quality of the centerline and the segmentation, respectively.

Another algorithm similar to the previous one was recently presented by [Suniaga et al., 2012]. After an automatic segmentation, the centerline is approximated by thinning. Initial ROI are found at terminating points of the skeleton. Several features are computed on these ROI: blobness, vesselness, Förstner filter [Förstner and Gülch, 1987], distance to the next bifurcation and vessel thickness. A SVM was trained as classifier. A leaving-one-out cross validation on 20 TOF-MRA data sets incorporating only saccular aneurysms revealed a sensitivity of 100 % at 3.86 fp_{DS} using a SVM with linear kernel. A radial-basis function kernel SVM led to worse results. FP findings were reported to be located commonly at high surface curvatures and twisting vessels.

The algorithm of Suniaga et al. [2012] employs a classification with SVM

Skeleton-based algorithms completely depend on the centerline of the cerebral vasculature. Thus, the search space is reduced largely. However, the risk to miss

(a)   (b)   (c)
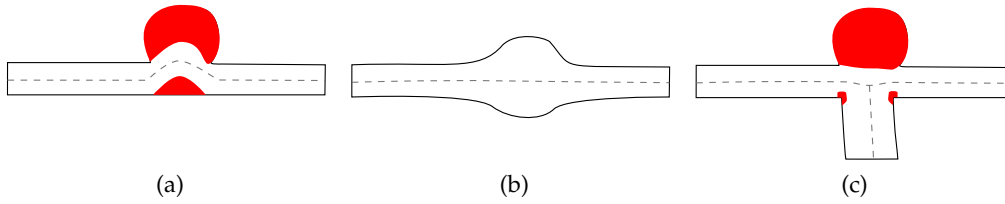
Figure 4.7: Examples of ROI that are found by the algorithm of [Kobashi et al., 2006]. The
vessel centerline is gray and dashed. The red areas denote found ROI. (a)
Sidewall aneurysm, multiple ROI are found. (b) Fusiform aneurysm, no ROI is
found. (c) Bifurcation aneurysm, multiple ROI are found. Drawing adapted
from [Kobashi et al., 2006].

important short centerlines is great. An equilibrium between eliminating short
branches due to noise and retaining short branches have to be found [Bouix et al.,
2005; Antiga et al., 2003]. The choice of the centerline extraction algorithm has
more influence on the results than the actual method. Also, only small aneurysms
can be characterized by short branches, this may not be the case with large aneu-
rysms as the skeleton is quite cluttered there (see Figure 4.6).

4.3.4 *Difference image-based technique*

Difference image-based methods model a healthy vessel volume that is then sub-
tracted from the given volume. Remaining voxels are assumed to be pathologies,
e. g., aneurysms. They are clustered and form initial ROI that are then classified.

The method presented by [Kobashi et al., 2006] employs this strategy to detect
aneurysms in TOF-MRA images. First, a normal artery model is constructed that
consists of a set of tubes and represents the healthy part of the vasculature. The
model is guided by the skeleton of the cerebral vasculature. To extract the cerebral
vasculature, the approach proposed in [Kobashi et al., 2001] is used that is based
on a watershed segmentation and classification with an ANN. Then, short branches
are removed in the skeleton. The vessel radii are estimated by finding the closest
fit of a tube to the data with the given skeleton as basis. The normal artery model
is reconstructed by using the skeleton and the estimated smoothed radii. Subse-
quently, the normal vasculature is subtracted from the segmented vasculature. A
connected component analysis is done to find ROI.

Difference image-based approaches model the healthy vasculature and obtain differences to the original image as initial ROI

For the FP removal step, each ROI is given a score that corresponds to the esti-
mated probability to be a true aneurysm. This is done by kNN. Nine intensity or
shape-based features are computed similar to [Arimura et al., 2006; Hayashi et al.,
2003]. The score is computed by using a slightly modified kNN classifier with $k = 1$.
The score A of a ROI R with respect to a database D is computed by:

$$A(R, D) = \frac{d_{FP}(R, D)}{d_{FP}(R, D) + d_{TP}(R, D)}, \tag{4.16}$$

where d_{FP} is the distance of r to the nearest FP sample of the database and d_{TP} is
the distance to the nearest TP sample in the database. The Euclidean norm is used.
Experiments with the Mahalanobis distance lead to worse results.

The method was tested with phantom and patient data. The phantom experiments revealed that the method is more suitable for detection of saccular aneurysms than for fusiform aneurysms and that aneurysms are rather detected if they are located at a bifurcation than on a straight artery (see Figure 4.7). A clinical evaluation on TOF-MRA image data of 16 patients inhibiting 19 aneurysms was done. A sensitivity of 100 % was reported at 6.4 fp_DS. The evaluation was done with a modified leaving-one-out technique.

The method is similar to skeleton-based approaches (see Section 4.3.3) as characteristics of the vessel skeleton are used. In contrast, this approach is based on employing a tube-fitting algorithm to represent vessels. Interestingly, small skeleton branches are removed as pre-processing. This assumes that aneurysm are always associated with a short skeleton branch. Like other approaches, the segmentation influences the detection. The FP reduction step is statistically based and relies on a kNN classifier with k = 1. This classifier is not very robust as it is prone to outliers in the database. The reason for this is probably the small database. An advantage of this approach is the potential of online-learning by assigning the (re)labeled data directly to the database.

4.3.5 *Hybrid approaches*

Most methods do not depend on one ROI finding strategy solely, but one strategy clearly dominates this step. In contrast to this, [Yang et al., 2011] propose a method where three of the previously mentioned strategies are combined. Initial ROI are found by analyzing the skeleton, by using the difference-based technique and by using the sphere-shaped based technique (see Figure 4.8, cf. Section 4.3.3, Section 4.3.4 and Section 4.3.1). The FP elimination is done by a RBS involving a relatively large amount of features.

The method of Yang et al. [2011] employs a combination of the previously discussed approaches

In a first step, the image data is segmented with a threshold-based method and a subsequent region-growing algorithm similar to [Uchiyama et al., 2005]. Then, all three strategies are employed to find initial ROI. The skeleton-based method extracts short branches, bifurcations, vessels with a local diameter maximum and cyclic short vessel segments similar to [Arimura et al., 2006]. The difference image-based technique is similar to [Kobashi et al., 2006] and a sphere-shaped strategy was employed similar to [Arimura et al., 2006]. A clustering is done to detect multiple findings of the same region.

To reduce the amount of FP, a RBS based sieving technique is applied. Six different intensity and shape-features were extracted dependent on the ROI type. Additionally, the location is used. The rules of the RBS are partly empirically chosen and partly expert-chosen. It is unclear how the expert knowledge is formalized. Finally, a score is assigned to each remaining ROI based on their type. The ROI originated from the skeleton approach are evaluated by a formula involving several features like size of the ROI, radius of the vessel and distance to center of the image. The scores of all other ROI types are assigned only by their distance to the image center.

The evaluation was done with 287 TOF-MRA studies containing 147 aneurysms. No leaving-x-out technique was used for evaluation. As this may be valid at the first glance, this is clearly challenging. Obviously, the RBS was build, at least partially, by statistical methods. A sensitivity of 96 % was reported at 11.6 fp_DS.
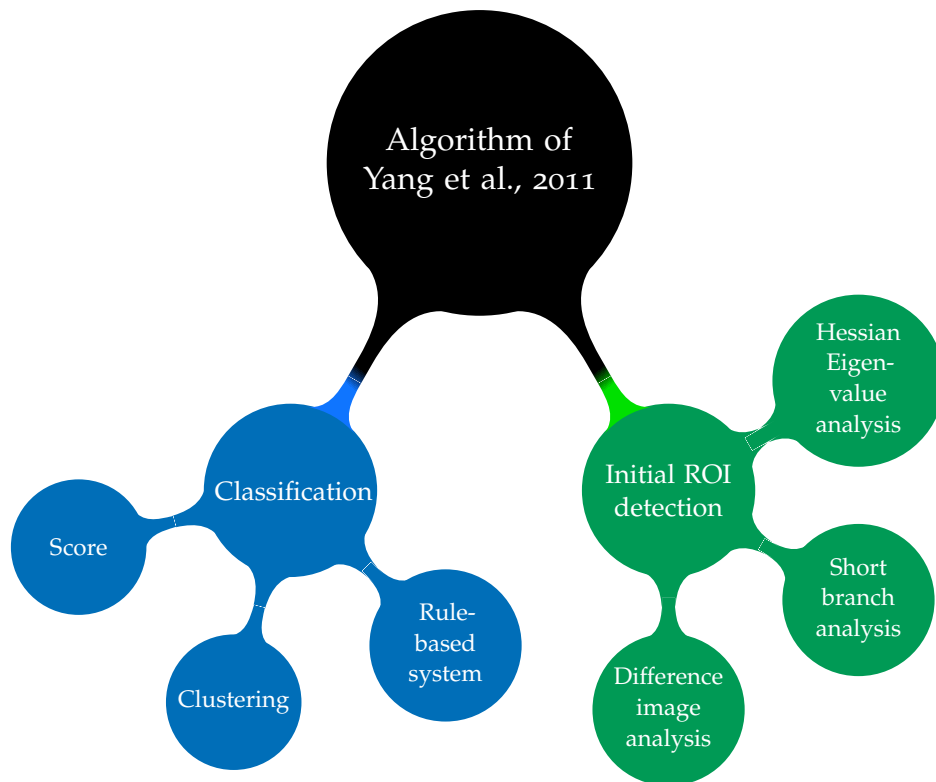
Figure 4.8: Scheme of the algorithm by [Yang et al., 2011].

A further evaluation study on a different data set was done yielding 94.6 % sensitivity at 6.7 fp$_{DS}$ what fortifies the evaluation [Blezek et al., 2010]. However, the evaluation of both publications is not directly comparable as they had a different gold-standard. In the first publication, single reading of 2D-DSA images was used as gold standard and in the latter one double reading of two radiologists was used as gold standard.

The publication of [Yang et al., 2011] represents a mixture of previously presented approaches and is no novelty. The RBS is questionable as it seems rather arbitrary as the rule finding mechanisms are explained by experiments. Thus, the approach is theoretically independent of a database and represents a general model. Practically, the rules are statistically dependent. The strength of the publication is the large image database that contains almost 300 data sets. The main disadvantage of the algorithm is its non-transparency and complexity that could lead to inexplicable results.

4.4 SUMMARY

This section concludes the State of the Art, which gave in a broad-to-narrow manner an overview of the research topic. First, object detection methods in general have been discussed. Then, an introduction to CAD with focus to methodology has been given. Finally, methods to detect cerebral aneurysms have been outlined that are summarized in Table 4.3. Their performance is compared with respect to their FROC in Figure 4.9
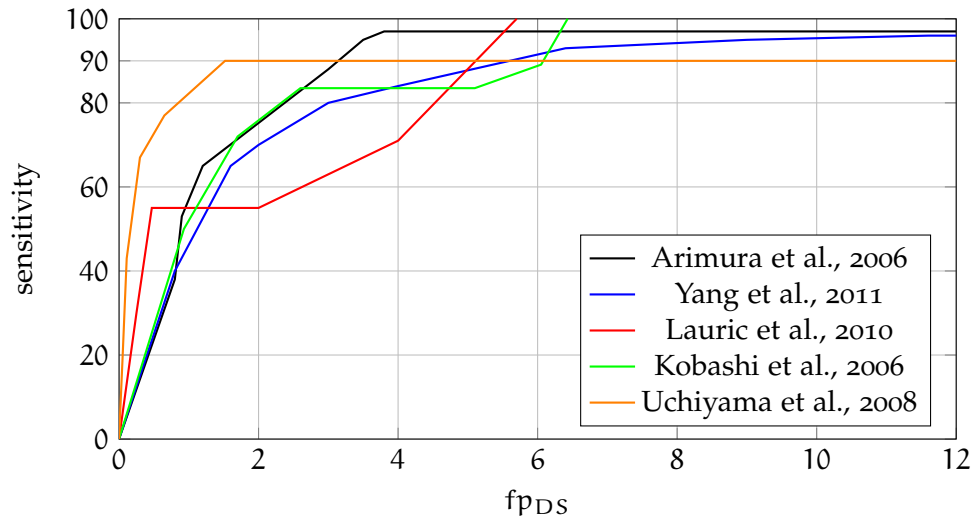
Figure 4.9: FROC for the existing aneurysm detection methods for TOF-MRA [Arimura et al., 2006; Yang et al., 2011; Lauric, 2010; Kobashi et al., 2006; Uchiyama et al., 2008]. For the methods of [Prasetya et al., 2011; Hassan et al., 2011; Suniaga et al., 2012], no FROC or respective values are given. For methods tested with CTA and 3D-RA only one publication [Lauric et al., 2010] provides FROC information, therefore no FROC is given for these modalities.

The three major questions defined in the first paragraph of Chapter 4 can be answered as follows:

- The methods to find initial ROI rely commonly on a search for specific shapes, e. g., by analysis of the Hessian matrix, by an intensity template or by Gaussian mixture modeling. To minimize FP, empirically found rules or machine learning methods such as SVM or LDA are applied.

- Especially, lung nodules are similar to cerebral aneurysms with respect to their shape and their common occurrence at blood vessels.

- The spherical shape-based analysis is the most promising technique to detect cerebral aneurysms. The concept of multiple cascades in FP elimination is suitable because there exist groups of FP that have different feature characteristics with respect to true pathologies.

In summary, five different techniques for the initial detection of ROI exist in aneurysm detection algorithms. These are spherical shape-based methods, symmetrical shape-based objects, skeleton analysis approaches and difference image-based approaches (see Table 4.3). Additionally, hybrid methods have been proposed.

Shape-based methods assume a specific shape of aneurysms (e. g., spherical or non-symmetrical) while skeleton-based methods rely on the specific characteristics of the vascular skeleton in aneurysm regions. Small aneurysms are indeed represented by a short branch in the skeleton, but large and possibly close-to-vessel aneurysms may have no characteristic terminating branch. They rather are characterized by a clot in the skeleton. Difference image-based methods are only partially suitable for initial ROI detection as the definition of a normal artery model is very

challenging and can easily cause erroneous results. Most methods except spherical shape-based methods are not able to detect fusiform aneurysms. Thus, in contrast to the other strategies, spherical shape-based methods are suitable for detecting small and large aneurysms of saccular and fusiform type.

As FP reduction step mostly statistical methods are employed. Several features are computed usually based on intensity and shape of regions. The following classification methods have been used:

- Linear Discriminant Analysis (LDA) or QDA,

- Rule-based System (RBS),

- Support Vector Machine (SVM),

- k-nearest Neighborhood classifier (kNN) and

- Thresholding.

For an overview of the different FP reduction step that are employed in the aneurysm detection algorithms, see Figure 4.3. Most methods use LDA or QDA. These methods employ a combined feature selection and classification and are robust with respect to their parameter settings. Thus, the full potential of State of the Art classifiers is not exploited. One reason for this may be the imbalance that occurs in the database usually. That is, the sample size of aneurysmal ROI compared to that of FP ROI is in the order of 10^1 to 10^3 times smaller. More information about this problem is given in Section 5.9. However, recently a method was proposed that employs a SVM [Suniaga et al., 2012].

The problem of statistical analysis still remains the same independent from the used classifier: it is heavily dependent on the underlying samples, i.e., the test database. Not only the amount of samples plays a role, but also the sample selection. Information about the selection of samples is not provided in any publication. Most databases have only less than 50 true positive samples, which does not allow properly to estimate the feature distribution in a high-dimensional space.

Possible problems related to the classification involve e.g., other ethnicities or other scanning devices than used in the test data. For example, Asians have another body structure than Caucasians, which leads presumably to different feature distributions of aneurysms. Similarly, other acquisition devices lead to different image characteristics changing the appearance of aneurysms. An acquisition-device invariant reduction of ROI has to be found as well as a characterization that is valid on all angiographic modalities.

Most algorithms are only tested on one modality. In a modern clinical environment multiple angiographic modalities are used for aneurysm management (cf. Section 2.2 and 3). It is unlikely that an algorithm that is specifically developed and tested for one modality will also work on another modality. Only two algorithms have been tested on multiple modalities [Lauric et al., 2010; Hassan et al., 2011]. Other algorithms neglect CTA and 3D-RA as major angiographic modalities that are used routinely.

The segmentation of the vasculature is a prerequisite for all discussed aneurysm detection algorithms, even if some parts, such as the blobness filter in [Arimura

Table 4.3: Comparison of the existing aneurysm detection approaches by their techniques. The number behind classification methods is the quantity of used features. For their performance, see Figure 4.9.

Author	Modality	ROI detection	Classification	# data sets
Arimura et al. [2004, 2006]	TOF-MRA	Blob detection and short skeleton branches	RBS + LDA (4)	115
Uchiyama et al. [2005, 2008]	TOF-MRA	Blob detection	RBS + QDA (7)	20/100
Kobashi et al. [2006]	TOF-MRA	Difference image	kNN, k = 1 (9)	16
Lauric et al. [2010]; Lauric [2010]	CTA	Short skeleton branches		10
	3D-RA	and Writhe number	Thresholding (1)	10
	TOF-MRA/CE-MRA			10
Yang et al. [2011]	TOF-MRA	Combination	RBS (6)	287
Hassan et al. [2011]	CTA + MRA	Graph-based	none	20
Suniaga et al. [2012]	TOF-MRA	Short skeleton branches	SVM (5)	20

et al., 2006], work on the original data. This implies not only an additional effort, but also that most algorithm results depend on the quality of the segmentation algorithm.

The algorithms can be compared by means of their FROC curve (see Figure 4.9). However, the evaluation of the algorithms can be questioned with respect to the following points:

- The testing database is too small.

- The testing database contains only images from one acquisition device.

- The testing database contains almost only data sets with aneurysms.

- The evaluation scheme is not described properly.

- The algorithm is trained on the testing database.

The generalization ability can only be tested if the database is large enough and consists of heterogeneous data sets. Otherwise, the algorithm may adapt to the specific characteristics of a scanning device. It is important that the evaluation database contains data sets without aneurysms. If the aneurysm prevalence is almost 100 %, the FP rate may be underestimated and it is not clear how the algorithm will work with images from healthy patients. The evaluation should be described properly and conducted in a valid, transparent way to simulate the behavior of the method on unknown data sets.

Therefore, the following specifications for a valid evaluation are defined:

- The testing database should contain at least 50 data sets per modality.

- The testing database should contain data sets from different devices.

- The testing database should contain an aneurysm prevalence of ~ 50 %.

- The evaluation should be transparent and replicable.

- The evaluation has to be valid (separate training and testing database).

An evaluation scenario of a cerebral aneurysm detection system is specified

The aneurysm prevalence should ideally be realistic, i. e., 3 %. However, it is infeasible to assemble such a large database with enough aneurysms.

In clinical applications, a high sensitivity as well as a low FP rate of a CAD software is crucial. Current algorithms reach a high sensitivity between 90 % and 100 % at fp_{DS} values that depend on the modality. For TOF-MRA, the value is between 1.9 fp_{DS} and 11.2 fp_{DS}, for CTA it is 5.4 fp_{DS} and for 3D-RA, it is 0.7 fp_{DS}. The quality of the different algorithms is not objectively comparable as they depend on their parametrizations and were tested on different databases with different aneurysm characteristics.

Although all authors claim that their CAD system is automatic, they are far away from being used in a clinical environment. Most algorithms depend on user inputs or are very sensitive to parameter changes. Moreover, some algorithms require (manual) pre-processing like vessel segmentation.

METHOD

Different requirements for a clinical aneurysm detection algorithm have been summarized in the Chapters 2 and 3. In this chapter, the own method is described. The algorithm should work without vessel segmentation as this heavily influences the detection process. Although, a large amount of pixels can be excluded (only 0.5 % to 5 % of all pixels are vessel pixels), a vessel segmentation represents a hard constraint. That is, those pixels that are not included in the segmentation are never considered again in the process. Furthermore, the quality of segmentation methods depends on the image quality and therefore, on the modality. The vessel segmentation is replaced by other algorithms, primarily registration to a model data set.

Statistical methods depend on the underlying database. Such a dependence should be avoided. However, it is clear that a complete independence cannot be reached as some assumptions that originate from a statistical database have to be made. The most important requirement is the multi-modality ability of the algorithm for the four relevant modalities as already discussed in Section 2.2.5.

The strategy that is employed for aneurysm detection is based on expert knowledge. In several discussions with neuroradiologists, this knowledge could be identified. The challenge is to formalize the knowledge by deriving features and incorporating constraints. A parametrical model is applied to govern the detection. This model includes modality-given intrinsically information, e. g., the intensity distribution of aneurysms, and extrinsically information given by experts, e. g., the minimal size of aneurysms. Alternatively, a statistical model is employed that is based on training. Both strategies are compared.

5.1 OVERVIEW

An overview of the scheme is given in Figure 5.1. The workflow is derived from the general workflow for CAD algorithms (cf. Section 4.2.7).

The overall scheme was initially presented in [Hentschke et al., 2011a] and then continuously enhanced in [Hentschke et al., 2012a,b].

First, the data sets are normalized to account for different intensity distributions and orientations within the same modalities. The data sets are then processed by a multi-scale sphere-enhancing filter, also called blobness filter, to emphasize possible aneurysm regions. Initial ROI are found by applying a threshold segmentation followed by a Connected Component Analysis (CCA) on the filtered image. Several low-level and high-level features are computed on each ROI. These features are intensity-based, shape-based or location-based. Then, two possible variants are implemented: (I) A RBS excludes ROI based on simple rules that originate either from modality-based knowledge or empirical domain knowledge. An Linear Discriminant Function (LDF) employing either trained weighting or expert-based weighting is used for further FP reduction by projecting the weighted features to
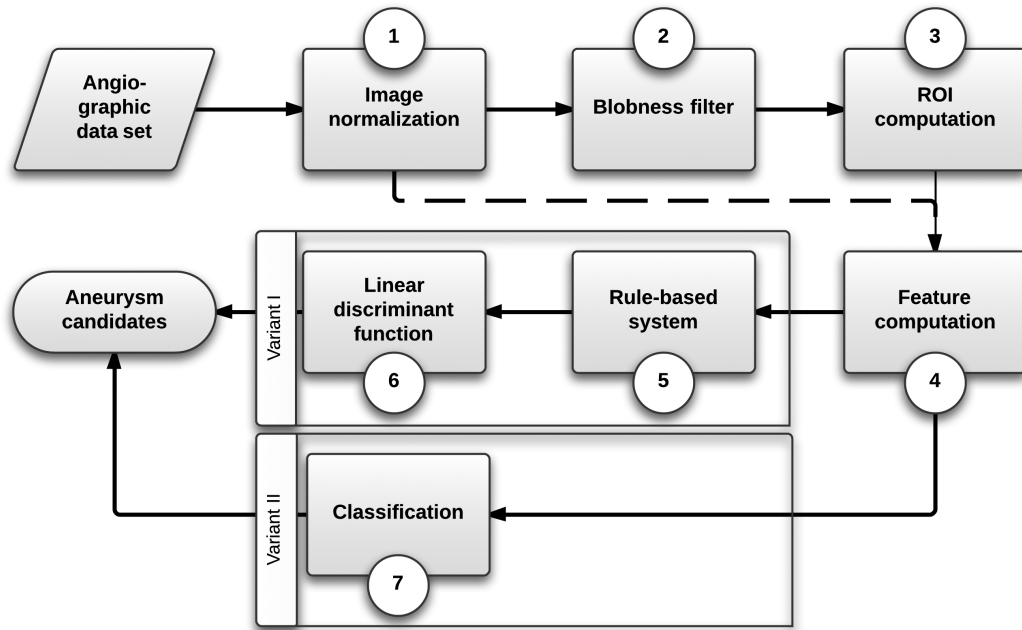
Figure 5.1: The scheme of the proposed algorithm. The dotted line illustrates that features are always computed on the normalized image.

an axis. The ROI that have a certain scalar LDF value above a threshold are determined as final aneurysm candidates. (II) State of the Art classification algorithms are used directly on the features to eliminate FP.

Thus, in variant I an intelligent feature is used in conjunction with a simple classifier. In contrast, in variant II relatively simple features are used, but an intelligent classifier. These are the two principal approaches in pattern recognition [Duda et al., 2000].

A parametrizable system is presented that has a flexible workflow

In order to cope with different modalities, a parametrizable scheme is used that is adapted according to the modality. The major difference between CTA and other modality data sets is that a mask image is created from CTA that only contains intensities of contrast-enhanced blood vessels. The information about known vessel HU in CTA is used (cf. Section 2.2.2). Additionally to vessels, also bone structures are present in this mask.

5.2 ANEURYSM CHARACTERISTICS

Aneurysms can be divided into saccular or fusiform type (cf. Section 2.1.2). The shape of both types differs. A generalization of aneurysms with respect to shape or gray-level distribution is difficult.

Additionally, the feature characteristics differ depending on the modality. The more objects or brain matter are present in the data, the more challenging is the detection task. An optimal data set only contains vessel structures or arteries, respectively. This is the case in 3D-RA. In MRA, vessels are usually emphasized by intensity, however also brain matter is visible in TOF-MRA data. CTA without bone-subtraction is the most challenging modality because of the ambiguous inten-

sity distribution of bone matter and blood vessels that overlap in their HU values. Furthermore, many cerebral structures are visible in the data sets similar to a normal head CT volume. Thus, the level of challenge in CAD algorithms depend on the modality. The same applies for segmentation and detection algorithms.

Interviews with neuroradiologists and a medical literature review have been made to characterize aneurysms with respect to specific features.

The following characteristics have been found:

1. They are located in the direct vicinity of vessels.

2. They are located at specific positions more frequently.

3. Their intensity value is between 150 HU and 375 HU for CTA data sets.

4. They have a diameter of 2 mm to 25 mm.

5. They have a high degree of roundness.

6. They are commonly located medial rather than lateral.

Six general characteristics to describe aneurysms are found

The characteristics 1-4 have a high degree of certainty while 5-6 are only true tendentially (stated by neuroradiologists).

No statement about intensity can be made except for CTA data sets. For CTA data sets, a certain intensity value range can be given as the HU values are normalized [Dammert et al., 2004]. Aneurysms smaller than 2 mm in diameter are usually neglected and aneurysms larger than 25 mm in diameter occur only rarely [Wiebers et al., 2003].

It is not possible to describe aneurysms by only a single characteristic. In this work, the goal is to use the found characteristics that apply for the majority of aneurysms. They have to be weighted as not all characteristics are equally important and are not valid for all aneurysms or modalities.

Computable features from these key characteristics are derived later on (see Section 5.5).

5.3 NORMALIZATION

The image normalization (*step 1*) consists of a linear contrast stretching, an isotropic voxel resampling and orientation normalization. Normalization is important to produce data sets that have similar intensity distributions to minimize the influence of the acquisition device or the used sequence to the algorithm.

The contrast is stretched in the range of $[0; 2048]$ for all 3D-RA and MRA data sets. In CTA, the intensity values have a physical meaning and they are already HU normalized. This has the advantage that the intensity level of contrast-enhanced vessel voxels is known and can be used as a mask for the subsequent filter computation in CTA. Different algorithms could be applied: classic thresholding or double thresholding [Canny, 1986]. The latter is a technique using four thresholds, two upper (t_{u1}, t_{u2}) and two lower thresholds (t_{l1}, t_{l2}). t_{u2} and t_{l1} define the value range where all pixels must be segmented. t_{u1} and t_{l2} define the range where the values have to be segmented only if they are connected to pixels fulfilling the other criterion. The double thresholding represents a more strict constraint

Normalization in CTA involves a mask image consisting of vessel HU

that leads to fewer segmented pixels. Pixels outside the mask are set to an intensity i that is either set to 0 or -2048, the HU value for water or air, respectively. The first one produces within-object gradients and object-background gradients whereas the latter one enhances especially object-background gradients. Further post-processing algorithms as CCA or morphological operators like opening are possible. However, this is not suitable as it bears the danger that aneurysm regions are excluded. Therefore, only the intensity information and no other constraints are used to compute the mask image. The threshold segmentation forms a constraint and represents no vessel segmentation as also other structures are included.

The intensity values of the other methods have only partial meaning. 3D-RA is subtraction based and measures the difference of material density before and after CA administration. Vessels independent of size have the highest intensity values in the data set. MRA measures the relaxation times of hydrogen atoms that are induced through a magnetic field. The intensity values are usually higher for vessels than the background. However, especially in TOF-MRA, also other objects have high intensity values or vessels have a relatively low intensity value due to slow blood flow. Only an approximate mapping between intensity and membership to vessels can be done in these modalities.

Almost all medical data sets have different pixel spacing in the slice than between slices. Thus, the volume of a pixel is $s = ps_p^2 \cdot ps_s$, where ps_p is the pixel spacing or side length of a voxel in mm in the slice (that is the same for both slice directions usually) and ps_s is the pixel spacing of a voxel between slices. As a non-isotropic voxel size is unfavorable for most image processing algorithms, they are resampled by linear interpolation to reach an isotropic voxel size. A subsampling is done within-slices and a supersampling is done between slices what constitutes a compromise with respect to the sampling. Each voxel is assigned a side length of $l = \sqrt{ps_p \cdot ps_s}$ in each dimension. The geometric mean as voxel length is proposed in [Ibáñez et al., 2005]. Typical values for (ps_p, ps_s) are

Resampling is done to ensure pixels of isotropic side length

- 3D-RA: $(0.535, 0.535)$, thus they have already isotropic resolution,

- CE-MRA: $(0.5, 0.98)$,

- TOF-MRA: $(0.43, 0.86)$ and

- CTA: $(0.395, 0.5)$.

Thus, 3D-RA data sets are not resampled. In CTA, the resampling does only change the image content slightly. The largest effect due to resampling was in the MRA modalities as $ps_p \approx 2 ps_s$.

It is required that all data sets have a certain orientation with respect to a patient coordinate system for the computation of a reference coordinate system. The orientation of the volume is normalized so that the $(x/y/z)$ coordinates of the image correspond to left-right direction, to anterior-posterior direction and superior-inferior direction, respectively. This information is taken from the header of the DICOM data set where the direction vectors of all axes are stored. A transformation to the desired coordinate system is then performed.

Figure 5.2: Example of a Maximum Intensity Projection of a CE-MRA image with sagittal slices and the desired region shown.

In contrast to other medical imaging algorithms, where commonly a smoothing filter is applied, the input images are not filtered beforehand. Although noise occurs in angiographic data sets, a linear filter alters the image information which may invalidate certain assumptions about aneurysms and prevent analysis.

The data sets are assumed to have an acquired volume that includes at most the head region from mandible to the top of the head. This was the case for the vast majority of the data sets as the diagnostic or therapeutic questions were always related to the cerebral vasculature or the neck vasculature. However, in few cases of CE-MRA data sets, the acquired volume was very large and reached from the aortic arch to the tip of the head. The desired region is then defined by a manual cropping in one dimension (see Figure 5.2).

Furthermore, the computation of the normalized reference coordinate system can be seen as a part of the normalization process. Details can be found in Section 5.6.

5.4 BLOBNESS FILTERING

The derivation of initial ROI is the most important step in a CAD system. Different techniques used in similar algorithms have been evaluated in Section 4.3. The skeleton-based, difference image-based and symmetrical shape-based methods violate the constraint to be segmentation-free. The spherical shape-based analysis is the most suitable method as its sole assumption is the approximated Gaussian distribution of an aneurysm. A certain degree of roundness can be assumed for the majority of aneurysms and describe saccular and fusiform aneurysms. Thus, this morphological feature is chosen as a necessary condition. Different methods were proposed for detection of spherical objects (see Section 4.3.1).

<table>
<tr><td>(a)</td><td>(b)</td><td>(c)</td></tr>
</table>
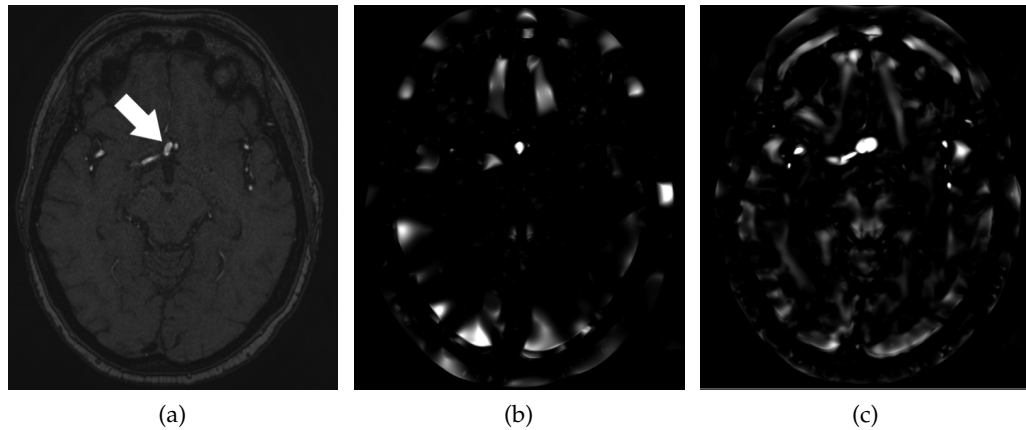
Figure 5.3: (a) Example axial slice of a TOF-MRA data set containing one aneurysm (highlighted by an arrow), (b) the corresponding blobness image and (c) the corresponding vesselness image. Vesselness and blobness values are high for the aneurysmal region.

The HEA method is chosen because of their parametrical property. This method employs a multi-scale filtering and is also known as blobness filter as it enhances blob-like structures. The object diameter has to be known for the computation of the multi-scale filter; however, this information is given. The method does not rely on the exact image intensities. It rather uses the general spherical intensity characteristic as constraint.

Different variants of the method exist. The variants of [Li et al., 2003] and [Frangi et al., 1998] are suitable for the use as initial ROI finding method in *step 2* (see Figure 5.3b for an example of the filter output with Frangi's variant). Li's method was chosen because of its parameter independence, Frangi's method was chosen because of its common use in CAD algorithms [Zhou et al., 2007; Forkert et al., 2011; Wei et al., 2012]. Therefore, the system is configured using either of the two methods. It is tested which variant leads to the best results.

The blobness filtering enhances spherical objects as cerebral aneurysms

The HEA relies on multi-scale information for object size characterization. Objects with a diameter between 2 mm and 10 mm are enhanced. 93 % of aneurysms fall in this range [Vlak et al., 2011]. Larger spherical objects are also found as multiple sub-structures (see Figure 5.4).

Additionally, the vesselness is computed based on Frangi's variant to enhance vessel-like regions [Frangi et al., 1998] (Figure 5.3c). The filter output is used later on as a feature. It is parametrized to enhance vessels having a diameter between 2 mm and 6 mm, which are typical values of the cerebral vasculature [Nowinski et al., 2011]. Smaller vessels are considerably less relevant with respect to aneurysm detection, larger vessels only occur outside a normal cerebral vasculature.

The multi-scale filtered data sets are the basis of the computation of initial ROI. How the actual ROI are derived is the topic of the next section.

(a)   (b)
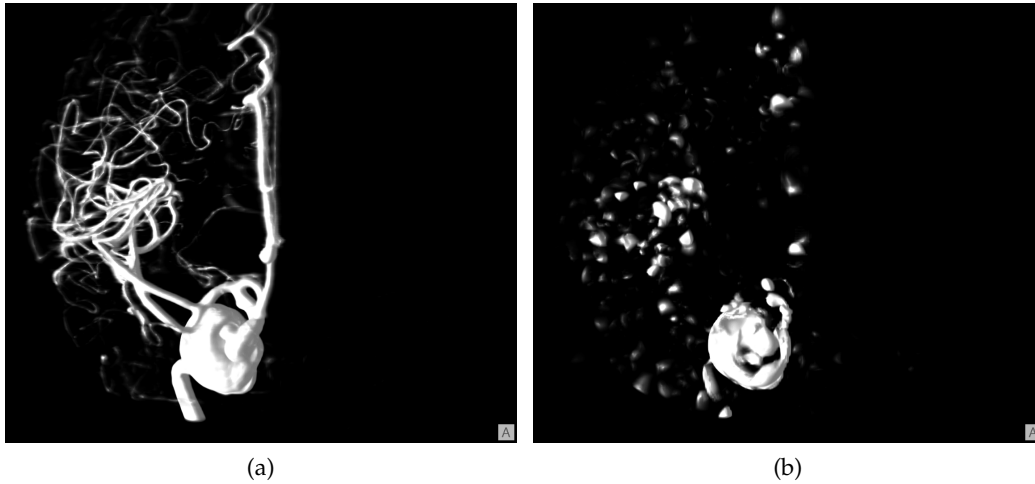
Figure 5.4: (a) 3D-DSA volume rendering of a giant aneurysm with a diameter of 21.3 mm is shown. (b) Volume visualization of a blobness filter of the same image is shown. As the diameter of the aneurysm is larger than the maximum expected radius r_{max}, multiple substructures are found.

5.5 COMPUTATION OF REGIONS OF INTEREST

The goal of *step 3* is to derive ROI from the blobness filtered data set. The highest peaks in the blobness image are found by thresholding segmentation. The threshold $t' = t B_{max}$ was found experimentally for each modality (see Table 5.2 for values and Section 6.4 for robustness experiments). B_{max} is the maximum intensity in the blobness image. t depends on the enhancement amount of the blobness filter that is influenced by the modality characteristics. The lesser the difference in intensities between background and vessels is, the smaller is the enhancement amount on this modality. Thus, for 3D-RA, t has the highest value. This value decreases with MRA and finally CTA has the lowest value.

Initial ROI are found by threshold segmentation and clustering on the blobness image

The segmented volume is then clustered into ROI by a CCA to find connected regions. Components having a volume smaller than s_{min} are excluded. s_{min} is estimated to be the volume of a sphere $s = \frac{4}{3}\pi r^3$ with radius $r = 1$ mm. Also, it slightly depends on the enhancement amount of the blobness filter. Due to the modality characteristic, this was smaller for CTA than for the other modalities since otherwise small aneurysm ROI are excluded erroneously (see Table 5.2). These initially computed ROI form the set of C_0.

The employed threshold segmentation does not contradict the constraint to use no segmentation as it is made on a feature image and not on the original data set. It has the aim to find regions containing spherical objects and not to find vessel pixels.

5.6 FEATURE COMPUTATION

In *step 4*, features are computed for each ROI. Most of these are derived from the defined aneurysm characteristics (cf. Section 5.2).

Table 5.1: Relationship between the characteristics for aneurysms and derived image-based features.

Characteristic	Feature	degree of certainty
Vessel vicinity	v, d_{CoW}	certain
Parent vessel location	p_A	certain
Intensity range (CTA)	i	certain
Intensity range (3D-RA, MRA)	i	unknown
Diameter range	s^a	certain
High degree of roundness	b, Ψ	tendentially
Medial location	d_c	tendentially
Parent vessel location of FP[b]	p_{FP}	-

[a] by indirect measurement in the blobness image.
[b] algorithm-introduced measure, no aneurysm characteristic per se.

18 distinct features are computed on the set of all initial ROI, C_0. The features are computed for each pixel contained in the ROI. The feature values for all pixels are extracted and stored in a feature vector. Statistical measures are then computed on the vector to derive scalar values.

The following features are computed:

- i_{avg}, i_{min}, i_{max}, i_{stddev} : average (avg), minimal (min), maximal (max) and standard deviation (stddev) value of the image intensity,

- b_{avg}, b_{min}, b_{max}, b_{stddev}: average, minimal, maximal and standard deviation blobness values to enhance sphere-like structures,

- v_{avg}, v_{min}, v_{max}, v_{stddev}: average, minimal, maximal and standard deviation vesselness values to enhance vessel-like structures,

- d_c: Euclidean distance of the center of the ROI to the center of the data set (in mm),

- Ψ: sphericity as a second measure of the roundness,

- s: volume of the ROI in mm^3 ($s > s_{min}$),

- d_{CoW}: distance of the ROI to an artery of the Circle of Willis in the reference data set,

- p_A: probability of aneurysm occurrence at the ROI position given by an atlas and

- p_{FP}: probability of FP occurrence at the ROI position given by an atlas.

18 features are computed on the ROI to include intensity-, location- and probability information

Note that i, b and v are vector-based features, the other features are scalar values.

The 18 features form a feature vector $F = (f_1 \cdots f_{18})^T = (i_{avg} \cdots p_{FP})^T$. These features can be divided into low-level and high-level features. While i, d_c and s provide only simple information, the other features are high-level descriptions of

Table 5.2: Parametrization for each step of the workflow and all modalities. The step numbers refer to Figure 5.1. Sec. = Section

Step	Sec.	3D-RA	MRA	CTA
1	5.3	Normalization so that $i = [0, 2048]$		Mask image: $150 \leqslant i_{avg} \leqslant 375$
2	5.4	Parametrization is modality-independent		
3	5.5	$t = 0.25$ $s_{min} = 8\,\text{mm}^3$	$t = (0.2^a / 0.15^b)$ $s_{min} = 8\,\text{mm}^3$	$t = 0.12$ $s_{min} = 5\,\text{mm}^3$
4	5.6	15 features	18 features	
5	5.7	- - -	- $0\,\text{px} \leqslant d_{CoW} < d_{CoWmax}$	$150 \leqslant i_{avg} \leqslant 375$ $d_c < d_{max}$
6	5.8	The LDF depends on a weighting vector W that is computed either by training (W_t / W_{te}) or defined by experts (W_e)		
7	5.9	Parametrization is modality-independent		

[a] for TOF-MRA.
[b] for CE-MRA.

image or object characteristics that incorporate (model-based) knowledge and are realized through sophisticated algorithms. b, v and Ψ were described in Section 5.4, The atlas-based features d_{CoW}, p_A and p_{FP} are presented in the following. These features are not computed in 3D-RA data sets because this modality does only contain one supplying artery per data set. A required model data set could have been constructed by fusing multiple data sets.

Two different normalization methods were used. The first method normalizes each feature with respect to the current data set DS:

$$\min f_i = \min_{DS} f_i, \qquad \max f_i = \max_{DS} f_i. \qquad (5.1)$$

$\min f_i$ and $\max f_i$ are the minimal and maximal feature values.

The second method normalizes each feature with respect to all data sets of the modality M:

$$\min f_i = \min_{\forall DS \in M} f_i, \qquad \max f_i = \max_{\forall DS \in M} f_i. \qquad (5.2)$$

The relationship between characteristics and features are summarized in Table 5.1.

The system shall not require a vessel segmentation as it has been shown to heavily influence the detection quality [Lauric et al., 2010]. Furthermore, for CTA without bone-subtraction, existing vessel segmentation algorithms require a large prototypical training database.

Since inclusion of the vessel information is advantageous nonetheless, it is proposed to replace vessel-segmentation by an atlas-based registration to determine likely vessel locations [Hentschke et al., 2012b]. This produces the d_{CoW} feature. A

model data set of a normal patient is determined manually for all modalities. The model data set has been chosen having a representative head size, a high image quality and occurrence of no or only small aneurysms. A small amount of potential normal data sets have been chosen and initial registration experiments have been made. The candidate data set that proves to result in the best registration quality (evaluated qualitatively) was chosen. Vessels in the reference data set are segmented on each modality. I. e., a vessel segmentation algorithm is applied in a controlled environment only for the four modalities rather than for every data set.

In case of the two MRA modalities, the Circle of Willis arteries are segmented. In both cases, a threshold segmentation was used and a subsequent CCA was applied. The largest x components ($x = [1, 5]$) were taken as initial segmentation and manually edited (especially at ACA locations, where the intensity is rather small). In case of the CTA reference image, a manually segmented CE-MRA data set of the same patient has been manually registered to the CTA data set resulting in an excellent alignment.

The atlas-based features d_{CoW}, p_A and p_{FP} are not computed on the 3D-RA data sets as only a part of the vasculature is seen in each data set which hampers the registration to the reference data set. Furthermore, due to the high vessel intensities, a vessel segmentation is implicitly included and probability information is not necessary.

Then, a distance-transform is applied to the segmented model data sets with a maximum distance of 20 voxels similar to [Chillet et al., 2003]. This represents 8.3 mm for TOF-MRA data sets, 10.7 mm for CE-MRA data sets and 12.1 mm for CTA data sets. All voxels having a larger distance than 20 voxels to the segmented voxels are defined as background with a value < 0. By using a distance transform a fuzzy degree of vessel membership is used rather than applying binary information (vessel/no vessel). This fuzzy degree is necessary as a registration induces alignment errors, i. e., a perfect matching cannot be reached. Furthermore, the vessel topology and morphology is unique for every human, although a general conformity exists. By using a distance transform, a statement can be made if a voxel of a registered data set is inside the vessel ($d = 0$), in the vicinity of a vessel ($d < 20$) or far away from a vessel ($d < 0$ or $d > 20$). Thus, registration errors and the inter-patient vessel variability can be compensated by this technique.

Finally, each data set is automatically registered to the model data set. The goal is to align the vessels of the Circle of Willis in both data sets and then use this information to determine the likelihood of vessels without employing segmentation. A rigid multi-scale registration with normalized cross correlation as similarity metric and a stochastic adaptive gradient-descent as optimizer are used [Klein et al., 2010; Maintz and Viergever, 1998]. The multi-scale approach is able to correct for large initial misplacements. Cross correlation as similarity measure is sufficient because of the intra-modality comparison. With the rigid approach, a good alignment could be found in most cases. Since elastic registration incorporates additional complexity into the problem, this technique was not used.

The distance of a ROI to the nearest vessel of the Circle of Willis arteries, d_{CoW}, can be determined by a lookup in the distance-transformed model data set. A normalized reference system for each modality is defined through the registration.
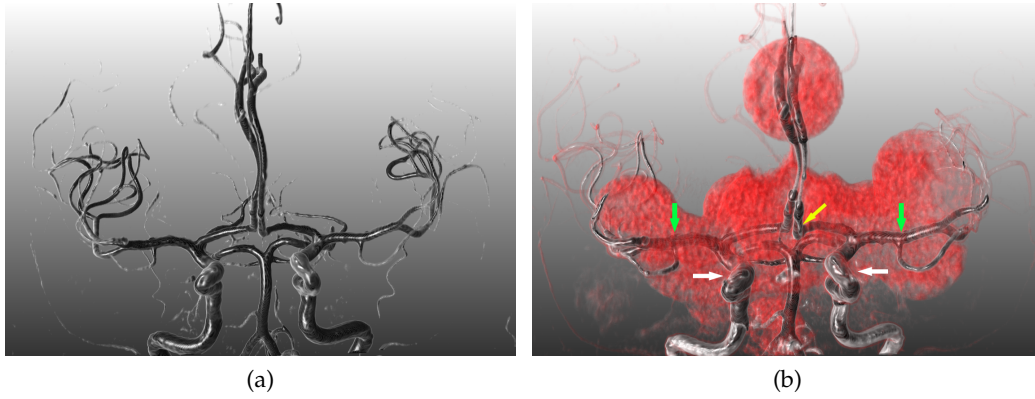
Figure 5.5: (a) Volume visualization of the TOF-MRA reference data set. (b) Visualization of the probability atlas (in red) in conjunction with the reference data set. White arrows denote the left and right cavernous part of the ACI artery, the yellow arrow represents the AComm artery and the green arrows denote the left and right ACM artery.

Additionally to the intra-modality registration an inter-modality registration has been found between the model data sets to be able to align the reference systems of different modalities.

Based on the reference system, an atlas is built that incorporates the occurrence probability of aneurysms with respect to the location. Aneurysm locations are known as they are given by neuroradiologists (see Section 6.2). p_A can be directly derived from the atlas. A similar probabilistic atlas has been proposed for a breast cancer CAD algorithm [Russakoff and Hasegawa, 2006]. A histogram of the occurrences of these locations is built through the use of the normalized reference system. Aneurysm positions from all modalities are used.

An atlas is computed to include aneurysm occurrence information

A 3D Kernel density estimation [Parzen, 1962] is carried out on the histogram data set I_A to compute an estimation of the true location distribution. For this purpose, I_A is filtered with a Gaussian kernel G having a standard deviation σ:

$$\tilde{I}_A \approx I_A * G(\sigma). \tag{5.3}$$

$\sigma = 100$ is set relatively large to ensure a blurring of the positions to account for registration errors and inter-patient vasculature variability.

The final probability p_A is computed by normalization over the whole atlas:

$$p_A(x, y, z) = \frac{\tilde{I}_A(x, y, z)}{\max \tilde{I}_A}, \tag{5.4}$$

where $\max \tilde{I}_A$ is the maximal intensity of $\tilde{I}_A$. Naturally, the value is desired to be high at aneurysm regions and low at positions where an aneurysm is unlikely to occur.

An example of the aneurysm probability atlas can be seen in Figure 5.5b. Locations of high probability are at the AComm, the ACM and the cavernous part of the ACI.

Similarly to p_A the probability p_{FP} is derived by building an atlas of FP ROI for the algorithm. p_{FP} is algorithm induced, not an inherent property of aneurysms. An accumulation of FP ROI was found to be at specific positions, especially around the cavernous ACI with a high curvature (see Section 6.6.3). The same Kernel density estimation as described before is used to construct the atlas. The normalization is done accordingly:

$$p_{FP}(x, y, z) = \frac{\tilde{I}_{FP}(x, y, z)}{\max \tilde{I}_{FP}}. \tag{5.5}$$

The value of p_{FP} is desired to be large for FP ROI. No relationship exists for true aneurysm ROI.

The vessel segmentation is replaced by two algorithms:

- Multi-scale filter enhancing
    - spherical-like structures (blobness filter) and
    - vessel-like structures (vesselness filter)
- registration to a normalized vessel reference system.

The blobness filter is directly used to find initial ROI by threshold-segmentation on the filtered data set. The vesselness filter and the registration are employed to measure the likelihood of the ROI to be located in the direct vicinity to vessels. Thus, the classification of a voxel to vessel or background does not longer rely on one algorithm only. Additionally, no binary assignment, but a fuzzy assignment is done. Whereas vessel segmentation has to be very accurate to ensure good results in a detection algorithm, the employed algorithms allow for deviations from an optimal result with only small changes in the detection algorithm output. Thus, these steps influence the whole detection system lesser than normal (intensity-based) vessel segmentation.

5.7 RULE-BASED SYSTEM

As seen in the workflow of the system in Figures 5.1 and 5.6, two variants have been proposed after feature computation. Both variants serve the further analysis of the ROI and the minimization of the FP amount. In variant I, a RBS and the classification with linear discriminant are employed (see Section 5.7 and Section 5.8). In variant II, State of the Art classification methods are used directly on the features (see Section 5.9). The system is either performed with *steps 5* and *6* (variant I) or with *step 7* (variant II). For an overview about the different variants, see Figure 5.6. The results are compared in Sections 6.5.4 and 6.5.5.

In *step 5*, an RBS is used to exclude ROI from C_0 that are not aneurysms. These ROI are also denoted as FP. This is done by defining expected feature value ranges for three features. If these features lie outside the range, the ROI is labeled as a FP and not transferred to the next set C_1 (see Figure 5.6). This represents a hard constraint. The specific feature value ranges depend on the modality (see Table 5.2). The constraints represent domain knowledge about expected location and intensity of aneurysms.

Feature value ranges are defined to exclude FP
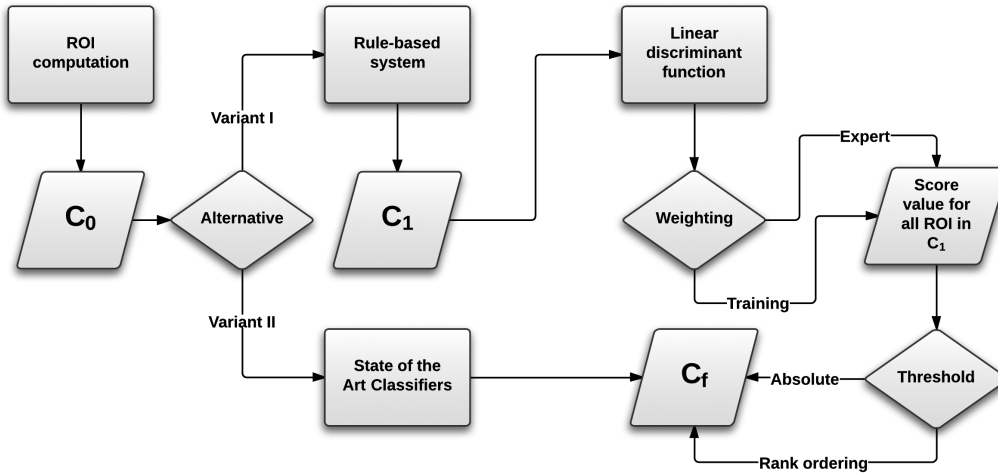
Figure 5.6: Details about the steps 5,6 and 7 that implement the FP elimination are given. The two variants I (employing RBS and LDF) and II (employing only State of the Art classifiers) get their input set of ROI C_0 originating from the ROI computation. In variant I, the RBS is executed resulting in the ROI set C_1 as output. Then, the LDF has to be parametrized with a weighting. This is done by either experts or with training. A score value is determined for each ROI. All ROI are then ordered by their score value. Either an absolute global threshold on the score value on all data sets is applied or a local rang ordering threshold on the rank of the score value for each data set is chosen. This results in the set of final aneurysm candidates C_f. In variant II, only the State of the Art classifiers are executed also resulting in C_f.

The i_{avg} constraint has been chosen according to the known HU value range of enhanced blood vessels in CTA. The constraint of the d_{CoW} value ensures that ROI that are not attached to blood vessels near the Circle of Willis are excluded. This constraint is chosen rather soft to avoid erroneously excluded true aneurysm ROI. The constraint of the d_c value excludes ROI that lie lateral with respect to the image center. The maximum tolerated distance, d_{cmax}, is estimated from the observed values of d_c of true aneurysm ROI:

$$d_{cmax} = \eta \ \max(d_c). \tag{5.6}$$

$\eta \geqslant 1$ is a tolerance factor.

In 3D-RA data sets, an additional constraint is introduced: ROI that are within $5\,\mathrm{px}$ near the image boundary are excluded. This is necessary as the blobness measure can reach extreme high values at the data set boundary. The cropping vessels comply well with the spherical shape and a high filtering answer is the consequence.

This sieving step is important to reduce the computational complexity. Furthermore, if a ROI can be excluded based on simple rules with a probability close to certainty, this has to be exploited as the following classification is easier.

These constraints represent simple classification methods. The aim is to find a good trade-off between exclude as many FP as possible while retaining the true

aneurysms. When in doubt, a less restrictive method is more suitable and a classification can be postponed.

5.8 LINEAR DISCRIMINANT FUNCTION

The set C_1 contains all candidate ROI that are not excluded by the previous step. To compute the set of final aneurysm candidates, C_f, it is desirable to assign a score value to each ROI that describes the probability to be a true aneurysm (see Figure 5.6). All derived features from Section 5.6 are included and combined in the LDF as described in [Hentschke et al., 2012b]. The LDF is then used for final classification in *step 6*. The score value $A(c)$ of a ROI c is defined as:

$$A(c) = \sum_{i=1}^{18} w_i \hat{f}_i(c) + \epsilon. \tag{5.7}$$

A linear discrimination function condenses the characteristic features resulting in a score value for each ROI

with w_i being the weights, $\hat{f}_i(c)$ being all normalized feature values, $c \in C_1$ being a ROI and ϵ being a scalar error term. $\hat{f}_i(c)$ is defined as:

$$\hat{f}_i(c) = \begin{cases} 1 - f_i \bar{(}c) & \text{if } \bar{f} \cong \{d_{\mathrm{CoW}}, d_c, p_{FP}, i_{\min}, b_{\min}, v_{\min}\} \\ f_i \bar{(}c) & \text{otherwise.} \end{cases} \tag{5.8}$$

$$\bar{f}_i(c) = \frac{f_i(c) - \min f_i(c)}{\max f_i(c) - \min f_i(c)}. \tag{5.9}$$

All feature values aim at having a maximal value for aneurysm regions. Therefore, six of them are inverted.

The weighting vector $W = \{w_i\}$, $i = 1, \ldots, 18$ can be parametrized through several techniques. Three techniques are chosen (see Figure 5.6):

- *expert determined weights* (a-priori), denoted as W_e,

The LDF can be either parametrized by expert knowledge or by training

- *weights trained on a database using all features*, denoted as W_t and

- *weights trained on a database using only the expert features*, denoted as W_{te}.

In the first weighting variant, the decision is independent from training. However, as this assumption may not be true, the method is evaluated additionally by the trained weighting and the results are compared. Additionally to train W_t with all features, it is possible to take only the features set to 1 in W_e into account. W_{te} implements an explicit feature selection step. Thus, if the results of W_{te} are better than with W_t, the hypothesis is supported that the features taken in W_e form a relevant subset of all features.

In a final step, all ROI are given a score value $A(c)$ that depends on their features and the chosen weighting. If $\|W\| = 1$ and $\forall f_i \in [0,1]: A(c) \in [0,1]$. The higher the value of $A(c)$, the more likely the ROI is a true aneurysm.

Two different schemes have been used for finding a threshold (see Figure 5.6):

- global threshold A_t or

- rank ordering threshold rk_t based on all A values per data set.

By using the global threshold, all ROI c_i where $A(c_i) > A_t$ are taken as the final aneurysm candidates C_f. A_t depends on the modality.

The threshold rk_t is based on ordering all ROI c_i based on their $A(c)$ value. The ROI having the largest rk_t values are taken as C_f. The advantages and disadvantages of these approaches are evaluated and discussed in Section 6.5.4.

5.8.1 *Expert-based weighting*

In case of the expert chosen features, a weighting vector W_e is built based on the characteristic features defined in Section 5.2. According to Table 5.1, b_{avg} characterizes a high spherical shape whereas v_{avg} and d_{CoW} ensure the proximity of the ROI to vessels. p_A introduces a statistical measure of location occurrence. s incorporates the size of the enhanced and segmented ROI that correlates with the size of the potential aneurysm. d_c integrates the tendency of aneurysms to occur rather medial than lateral. p_{FP} is used as algorithm-induced feature to integrate the probability of FP location.

Even domain experts fail to define an importance for each characteristic feature. Thus, each characteristic feature is taken as equally important for aneurysms. The weights are set equally for all important features. For CTA and the MRA modalities, W_e is defined as follows:

$$w_i = \begin{cases} \frac{1}{7} & \text{if } f_i \in \{s, b_{avg}, v_{avg}, d_c, d_{CoW}, p_A, p_{FP}\} \\ 0 & \text{otherwise.} \end{cases} \tag{5.10}$$

In case of 3D-RA, the reference-system-based features are not computed (cf. Section 5.6), thus they are omitted:

$$w_i = \begin{cases} \frac{1}{4} & \text{if } f_i \in \{s, b_{avg}, v_{avg}, d_c\} \\ 0 & \text{otherwise.} \end{cases} \tag{5.11}$$

ϵ is set to 0 in all modalities.

5.8.2 *Training-based weighting*

The training-based weighting W_t is computed by training a parametrization based on a database with annotated class labels. For each modality, a different data base exists what also leads to a different W_t per modality. The hypothesis is that W_t and W_e have a similar weighting if the characteristic features do truly discriminate true aneurysms and FP ROI.

In matrix form Equation 5.7 can be written as:

$$W_t^T F = L \tag{5.12a}$$

$$W_t = (w_1 \cdots w_{18}, \epsilon), \quad F = \begin{pmatrix} f_1^1 & \cdots & f_1^n \\ \vdots & \ddots & \vdots \\ f_{18}^1 & \cdots & f_{18}^n \\ 1 & \cdots & 1 \end{pmatrix}, \quad L = \begin{pmatrix} l_1 \\ \vdots \\ l_n \end{pmatrix}. \tag{5.12b}$$

where W is the weighting vector, F is the matrix of normalized features containing all ROI, L is the class label vector and n is the number of ROI. $l_i = 1$ is set for true aneurysm ROI while $l_i = 0$ is chosen for FP ROI. ϵ is included as the 19th feature vector.

Linear regression is used as the training-based parametrization algorithm [Witten and Frank, 2000]. By using linear regression, the Mean Square Error (MSE) error is minimized [Duda et al., 2000]:

$$e_{MSE}(W_t) = \sum_{i=1}^{N} (W_t^T F - L)^2 = \|FW_t - C\|^2 \to \min. \tag{5.13}$$

No attribute selection is used and the Akaike criterion for model selection is chosen [Akaike, 1974]. The derived weighting vector is denoted as W_t.

The only difference in computing W_{te} compared to W_t is using a different F matrix. This F matrix consist only of the values of the four (for 3D-RA) or seven (for all other modalities) expert-chosen features.

5.9 CLASSIFICATION

State of the Art classification methods are used in *step 7* to sieve ROI that are no true aneurysms. In variant I the classification is done on the one-dimensional LDF value (see Figure 5.1 and previous section). In contrast, in variant II the computed features are directly used as input for the classification algorithm. Thus, the classification is done in an 18-dimensional space (for CTA and MRA) or 15-dimensional space (for 3D-RA), respectively.

Well-known State of the Art non-linear classification methods are e. g., SVM, Neural Networks and alternating decision tree.

The quality of a classification result depends on several parameters. One of the largest influence factors is the sample size of the underlying classes. Most classification algorithms work best if the sample sizes are equal for each class [Sun et al., 2009].

In this work, each ROI contains one of two classes:

- ROI containing true aneurysms C_{TP} and

- all other ROI C_{FP}.

The samples belonging to C_{TP} and C_{FP} are denoted as $\#C_{TP}$ and $\#C_{FP}$, respectively. As $\#C_{TP} \ll \#C_{FP}$, C_{TP} is the minority class whereas C_{FP} is the majority

class. Imbalance occurs if samples of a class occurs more often (in the order of magnitude) than another class. The between-class ratio μ is defined as

$$\mu = \frac{\#C_{TP}}{\#C_{FP}}. \tag{5.14}$$

Imbalanced class distributions have led to poor results with State of the Art classifiers [Sun et al., 2009]. A distribution is imbalanced if $\mu \leqslant 0.1$. In practical applications, even more drastic ratios occur. Almost all algorithms fail to classify the samples without losing the sensitivity of the minority class [Sun et al., 2009].

Imbalanced class distributions commonly lead to poor classification results

Imbalance occurs in many CAD algorithms [Doi, 2007]. This is due to the aim to avoid missing a pathology what leads to a relatively high amount of ROI containing only few true pathologies. An additional problem is that the absolute amount of $\#C_{TP}$ is usually small. Thus, only a sparse sampling of the $n = 18$ dimensional space is done.

The main problem with imbalanced data in classification is the large sample size of the majority (FP) class. If $\mu = 0.01$ and all samples are classified as the majority class, the overall accuracy is 99 % (see Section 6.3 for the definition of the accuracy). The accuracy is used commonly as measure that is maximized by the classifier. In this case, samples from the minority class would be classified correctly although the accuracy measure is very high. The output of such an algorithm would be useless for CAD purposes.

To overcome the problem of classification of imbalanced data, several approaches have been proposed [He and Garcia, 2009; Sun et al., 2009]. A general data-level strategy is to resample the data to reach an equal sample size of the minority and majority class [Chawla et al., 2002]. This can be done by undersampling the majority class or oversampling the minority class. Another strategy is at the algorithm level by incorporating an appropriate inductive bias into the classification algorithm. This requires deep knowledge and severe modification of the classifier [He and Garcia, 2009]. While resampling strategies are independent of the classifier, this is not the case for algorithm-level approaches. Thus, these approaches can only be used individually. MetaCost, a general strategy independent of the classifier, was proposed to overcome this problem by including misclassification costs [Domingos, 1999].

The problem of classifying imbalanced data can be solved by using misclassification costs or data resampling

Thus, three different strategies are compared:

- the original classifier with the original database (*original*),

- the classifier adapted with misclassification costs and the original database (*MetaCost*) and

- the original classifier with the Synthetic Minority Over-sampling Technique (SMOTE) resampled database (*resampling*).

The classifiers are chosen so that four different classification strategies were covered: Bayesian classification, classification by (non-linear) decision boundaries, tree-based classification and classification by boosting. These State of the Art classifiers are compared:

- *Naive Bayes* [Jain et al., 2000]

- *SVM* [Cortes and Vapnik, 1995] with

  - linear kernel

  - polynomial kernel

  - radial kernel

- *Neural network* [Theodoridis and Koutroumbas, 1999]

- *Alternating decision tree* [Freund and Mason, 1999]

- *Logit Boost* [Friedman et al., 2000]

SVM is parametrized with $c = 10000$ in case of the original classifier and Meta-Cost and with $c = 1$ in case of the resampling. The parametrization was chosen empirically. All other parameters were set to their default values of the used software package Weka [Hall et al., 2009].

MetaCost overcomes the problem of individually adapting classifiers for imbalanced data sets by forming a general cost-sensitive framework for arbitrary classification methods [Domingos, 1999]. A variant of bagging is used as the ensemble method. Multiple bootstrap replicates of the training set are formed and a classifier is trained on all bootstraps. Each class probability is estimated by the votes that it receives from the ensemble. All training samples are relabeled with the estimated optimal class given by Bayes' conditional misclassification risk:

$$R(i|x) = \sum_j P(j|x) C_x(i, j), \qquad (5.15)$$

where $P(j|x)$ is the conditional probability of sample x having class j and C_x is the cost matrix. Then, the classifier is applied once more on the relabeled training data set.

The following cost matrix is used:

$C_x = \begin{pmatrix} 0 & \mu \\ 1 & 0 \end{pmatrix}$, with the first row accounting for TP and the second row accounting for FP. Hence, the cost for misclassifying 1 TP and μ FP are equal.

SMOTE was successfully applied to imbalanced data problems [Chawla et al., 2002]. The algorithm oversamples the original data set by analyzing the similarities in feature space of the minority class. Artificial samples are added into the cluster of C_{TP}. For C_{TP}, the k nearest neighbors in feature space for each sample $x_i \in C_{TP}$ are computed. One neighbor x'_i is randomly chosen and the vector $x_{syn} = x_i + \alpha_r(x'_i - x_i)$ is computed. α_r is a random variable between $[0, 1]$. x_{syn} is added to C_{TP}. Thus, in SMOTE the cluster of the minority class is synthetically condensed. Adaptations and further algorithms based on SMOTE exist [He and Garcia, 2009].

An oversampling percentage of 1000 % with $k = 5$ nearest neighbors is chosen. Additionally to SMOTE, C_{TP} are randomly subsampled to ensure $\mu = 1$.

5.10 GENERALIZATION

Apart from the detection of algorithms, ideas of the proposed system can be employed in other areas.

To use the proposed system to detect specified organs or pathologies the following adaptations have to be done:

- The characteristics of the organ have to be found (e.g., location, shape and other preferably unique characteristics).

- Computable features have to be derived from the characteristics.

- The data sets have to be normalized if they are acquired with different devices.

- A necessary condition has to be found for initial ROI detection. This is commonly the most important characteristic of the pathology.

- Rules to eliminate FP ROI have to be defined based on modality-based knowledge, expert-based knowledge and statistical analysis.

- To rate the remaining ROI, the importance of features or characteristics has to be weighted. This weighting can either be acquired by interviews with experts or by training. Training could also be utilized for the generation of a probability atlas.

The proposed system can be generalized to find other pathologies

Exemplarily, the adaption of the proposed system to work as a detection system for lung nodules is discussed. Most of the characteristics of cerebral aneurysms also apply for lung nodules. An obvious difference is that the pathology occurs in lungs instead of the cerebral vasculature. It has to be assessed if they occur commonly at certain locations or in the vicinity to landmarks. The same features as in the proposed cerebral aneurysm detection system could be used. A normalization of CT data sets is presumably not necessary as the CT modality is already normalized by HU values. To find initial ROI, the blobness filter is suitable as lung nodules commonly have a spherical shape. The parametrization of the RBS would have to be adapted, e.g., by employing intensity information about lung nodules, distance of the lung nodules to the lung wall or the expected size of the lung nodules. An adaption of the LDF would also be necessary. As annotated lung nodule databases are publicly available, a training of the LDF weights is possible. Also the formation of a probability atlas containing enough samples is simplified.

The formalization of characteristics is the main source of intelligence in the system. Characteristics are usually described by vague informal statements. It is commonly difficult for medical experts to formulate their implicit knowledge. Often, they refer to their experience as major source in pathology detection. The transfer of the characteristics to computable features relies on the skills of a computer scientist and cannot be formalized. It is important that the scientist obtains a deep understanding about the pathology by discussion with medical experts, literature review and observation of the clinical workflow.

An expert weighting for an LDF can be acquired by using questionnaires. The medical experts have to decide whether the chosen features describes the pathology well, e.g., by assigning a numeric score. To reach a high generality, a high amount of experts have to fill out the questionnaire. The weighting can be obtained by averaging. Then, the expert-weighted parametrization of the LDF corresponds to a suitable scalar score value.

Furthermore, it may be useful to determine subgroups of the pathology, e. g., small and large pathologies. These groups have varying characteristics and should be treated differently.

The substitution of the segmentation by a registration is advantageous and an important step in the proposed system. This idea can be also be used in other CAD or image-processing areas where a segmentation influences the subsequent algorithms. The binary decision if a voxel consists to a vessel is replaced by a fuzzy degree, e. g., by incorporating a distance transform on a segmented model data set as proposed. The registration also simplifies the creation of a probability atlas by defining a standardized reference system.

6

EVALUATION AND DISCUSSION

In this chapter, the presented method was tested with clinical data sets. The robustness of the parameters and possible variants of each part of the algorithm were evaluated. Thereby, the following major questions had to be answered:

1. What is the best possible performance of the system given the best parametrization?

2. Does the expert-set parametrization of the LDF lead to similar or better results than the trained parametrization?

3. Does the trained parametrization produce similar weighting values than the expert-based parametrization?

4. Are the results computed with the expert-set or trained parametrization comparable to State of the Art classifiers?

First, a short introduction is given about external tools used for implementing the prototype. Then, the evaluation data is presented and the used evaluation measures are introduced.

The experiments are divided into two sections: First, the robustness experiments are presented. Then, the procedural experiments are summarized whereby the different variants of the algorithm are examined. The chapter concludes with a discussion and a comparison to existing algorithms.

As many symbols were used, the referring sections are indicated. Furthermore, a list of all symbols can be found after the table of contents at the beginning of the thesis.

6.1 IMPLEMENTATION

Several software tools and libraries were used to implement a C++ prototype of the described method. The open-source C++ library ITK provides a large variety of image-processing methods [Ibáñez et al., 2005]. Segmentation methods, clustering methods, multi-scale filtering and other methods provided by ITK have been used. The open-source C++ library VTK provides capabilities to visualize (medical) image data [Schroeder et al., 2006]. It has been used to provide informative (volume) visualization. A small C++ wrapper library around the open-source C++ library GDCM [Malaterre, 2008] was used to read DICOM data sets. The library was written by Tom Brosch. To compute the multi-scale blobness filter of Li [Li et al., 2003], a C# implementation written by Fabian Held and Stephan Fensky was used.

Qt is an open-source C++ library providing Graphical User Interface (GUI) functionality and additional methods extending the standard template library of C++ [Blanchette and Summerfield, 2008]. It was employed to build the framework of

Table 6.1: Overview of the four evaluation databases. DS = Data sets, A. = Aneurysms, #Total = Total number, #w/o A. = number of data sets without aneurysms, #< 5 mm = Number of aneurysms smaller than 5 mm, #NIR = number of aneurysms initially not in report. The pixel spacing is given after isotropic resampling.

Modality	DS		A.			Pixel spacing
	#Total	#w/o A.	#Total	# <5 mm	#NIR	
3D-RA	46	6	47	18	2	0.32 mm–0.54 mm
CE-MRA	38	23	19	6	0	0.37 mm–0.91 mm
TOF-MRA	41	18	34	7	0	0.42 mm–0.76 mm
CTA	72	29	59	26	9	0.55 mm–0.79 mm

the prototype and for building the GUI. Furthermore, the commercial software Mevislab [Ritter et al., 2011] and Matlab [Attaway, 2011] have been used for rapid prototyping and creating State of the Art volume visualization for this thesis.

The implementation of the open source data mining software Weka was used for computation of the linear regression and all classification methods [Hall et al., 2009]. The registration was performed with the open-source toolkit elastix [Klein et al., 2010].

6.2   DATA

The proposed system was evaluated on 197 clinical patient data sets which consisted of 46 3D-RA data sets, 38 CE-MRA data sets, 41 TOF-MRA data sets and 72 CTA data sets. These data sets contained a total of 159 cerebral aneurysms. All data sets of the same modality formed a database. An overview of the databases is given in Table 6.1.

The data sets were acquired with different scanners. While the scanning sequences were the same for the majority of CTA and all 3D-RA data sets, different sequences have been used for CE-MRA and TOF-MRA data sets. The majority of data sets were acquired with the SENSE protocol, however the acquisition parameters varied. The scanners had a magnetic field strength of 1 T to 3 T with most data sets acquired at 1.5 T.

Some data sets originated from the same patients, but had different modalities except for some cases. These were 3D-RA data sets where different arteries were contrasted, e. g., the left and right ACI. Although for some patients pre-treatment and post-treatment data sets were available, only the first acquired data set containing the untreated aneurysm(s) was considered.

Overall, 159 unruptured aneurysms were present in the data sets. The size of the aneurysms measured by their largest diameter ranged from 2.0 mm to 54.5 mm. An overview of all aneurysm sizes is given in Figure 6.1. Seven aneurysms were of fusiform type, all other were of saccular type. A distribution of aneurysm sites is given in Figure 2.5.

The effort to collect data sets was high. Access to the clinical database was given, however no access could be granted to the patient record and thus, the diagnosis for each patient was only available by request later on. As data set
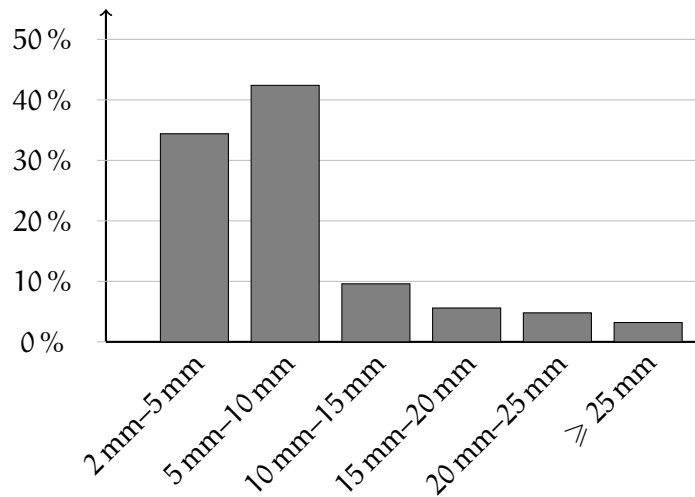
Figure 6.1: Overview of aneurysm sizes in all databases. The bins are divided in 5 mm steps except for the first and the last bin. The first bin covers aneurysms between 2 mm and 5 mm as 2 mm is the minimum defined size of aneurysms. The last bin covers all aneurysms equal to or larger than 25 mm, so-called giant aneurysms.

information, only the modality and the part of the body that was scanned were available. Thus, it was unclear if the data set contains aneurysms. CTA data sets where a subarachnoid hemorrhage was present or images that had a poor image quality (rated as 5 or 6 on a German standard school grade scale by a neuroradiologist) were excluded. Still, some grade 4 data sets were included that were challenging to read even for experienced neuroradiologists. Other artifacts such as image distortions because of clipping or metallic dentures occurred. These and all other data sets were included in the evaluation data bases, no selection was done.

The ground truth consisting of the number and location of aneurysms was given by two experienced neuroradiologists (experience seven and nine years, respectively) who screened the data sets explicitly looking for aneurysms. Additionally, the information was available whether the found aneurysms were listed in the clinical report. Those who were not listed are assumed to be especially hard to find as they were overlooked at least once by a physician. 11 aneurysms were in this group. The quality of the ground truth is comparable to or better than similar aneurysm detection methods. However, it has to be noted that there still is a small chance that aneurysms could be overlooked. This applies especially to small aneurysms in the MRA data sets where the detection rate by physicians is considerably smaller than in the other modalities.

In conclusion, the most data bases fulfill all criteria defined in Section 4.4. For each modality, at least 38 data sets were present. The data sets were acquired with different devices. Approximately 50 % of the data sets contain no aneurysm except for 3D-RA. This was caused by the aneurysm management in the University Hospital Magdeburg (cf. Section 2.3) where 3D-RA data sets are almost only acquired if an aneurysm has already been found. The aneurysm management was also a

reason for the small number of aneurysms in CE-MRA as this modality was used for regular follow-up after treatment.

6.3 MEASURES

The quality of a CAD algorithm can be measured with respect to a given ground truth. All ROI can be classified as one entry in the standard confusion matrix [Jain et al., 2000] (cf. Section 2.2):

- True Positive (TP),

- False Positive (FP),

- True Negative (TN) and

- False Negative (FN)

The sensitivity se given a parametrization is defined as:

$$se = \frac{n_{TP}}{n_{TP} + n_{FN}},$$

(6.1)

where n_{TP} and n_{FN} denotes the amount of TP ROI and FN ROI, respectively. se is computed based on the number of total aneurysms in the data sets. Thus, for reaching $se = 1$ it is required that each aneurysm (TP ROI) is found. If not stated otherwise, TP or FP always denote TP ROI or FP ROI, respectively.

An aneurysm was rated as found and thus belonging to the class TP if a ROI is near the given aneurysm position. Formally defined, it is found if:

$$p_g \in c_i \vee d(c(c_i), p_g) < 2r_g.$$

(6.2)

p_g is the given position of the aneurysm, $c(c_i)$ is the center point of a ROI c_i found by the CAD system, $d(p_1, p_2)$ denotes the Euclidean distance between two points p_1 and p_2 and r_g is the radius of the aneurysm. The found ROI does not have to be centered in the actual aneurysm as a physician notices the aneurysm even if the ROI is located at the aneurysm neck or in the feeding vessel in the vicinity of the aneurysm.

The sensitivity of a system alone is not sufficient for evaluation as the suitability is also expressed by its specificity. It is defined as:

$$sp = \frac{n_{TN}}{n_{TN} + n_{FP}}.$$

(6.3)

n_{FP} is the quantity of FP ROI.

However, in practice, the related amount of FP is of interest to evaluate the algorithm. Therefore, the average FP amount per data set, fp_{DS}, is computed:

$$fp_{DS} = \frac{n_{FP}}{n_{DS}}.$$

(6.4)
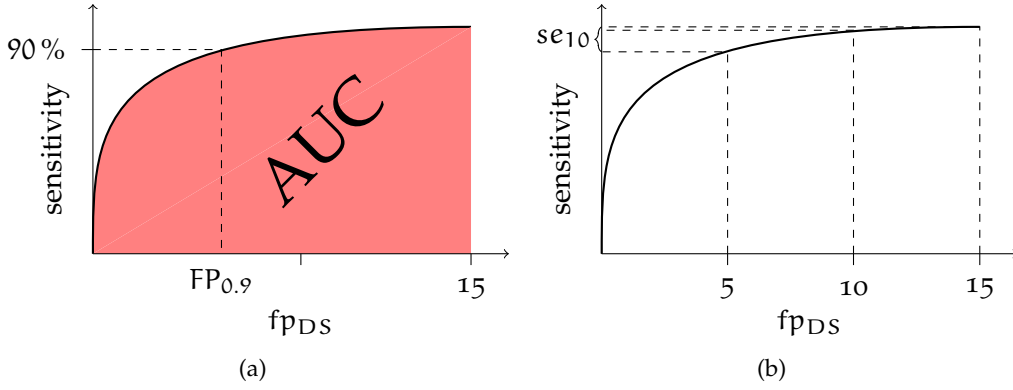
Figure 6.2: (a) The AUC is the area under the FROC curve plotting sensitivity against fp_{DS}. $FP_{0.9}$ is defined as the amount of fp_{DS} at 90 % sensitivity. (b) se_{10} is defined as mean sensitivity at 10 $fp_{DS} \pm 5\,fp_{DS}$ (and sampled every 2.5 fp_{DS}, which is omitted in the scheme for better clarity).

n_{FP} and n_{DS} is the number of data sets. fp_{DS} is normally computed using all data sets of a modality.

Choosing the optimal parameters of a system is a tradeoff between a high sensitivity and a low FP rate. This is condensed in the Free Response-operator Characteristic (FROC) curve by changing a parameter value while leaving all other parameter values fixed and plotting a curve defined by se and fp_{DS} (see Figure 6.2a). Either the global threshold A_t or the rank order threshold rk_t is used as varying parameter. se and fp_{DS} are mutually dependent: $se(fp_{DS})$ or $fp_{DS}(se)$ can be computed. The following evaluation measures are derived from the FROC:

- Area under Curve (AUC) of the FROC (see Figure 6.2a),

- $fp_{0.9}$: the amount of false positive ROI at a sensitivity of 0.9 (see Figure 6.2a),

- se_{10}: the average sensitivity at 10 $fp_{DS} \pm 5\,fp_{DS}$ (see Figure 6.2b).

The AUC of the FROC is defined as:

$$AUC = \frac{1}{\Omega} \int_0^\Omega se \quad d\,fp_{DS}. \tag{6.5}$$

$\Omega > 0$ is the maximum defined fp_{DS} value.

Discretized over all measuring points of the FROC and using the trapezoid rule this leads to:

$$AUC = \frac{1}{2\Omega} \sum_{i=0}^{\Omega-1} (fp_{DS}(i+1) - fp_{DS}(i)) (se(i) + se(i+1)). \tag{6.6}$$

$\Omega = 15$ is chosen for the evaluation of the system as a high sensitivity is reached with this value for all modalities.

AUC is defined in the range of $[0, 1]$ with an optimal value of 1. In this case, each ROI is correctly classified independent of the parametrization.

A high sensitivity is of paramount importance since it is the goal to support physicians by detecting aneurysms. A sensitivity of at least 90 % has to be reached to be suitable for a clinical employment. Thus, $FP_{0.9}$ is defined as:

$$FP_{0.9} = fp_{DS}(0.9). \tag{6.7}$$

That means, the average amount of false positives per data set is computed at 90 % sensitivity. A low $FP_{0.9}$ value is desired for a CAD algorithm.

In a CAD, too many FP are not acceptable since it no longer reduces reading time. Interviews with neuroradiologists have revealed different statements about the maximum amount of FP that could still be tolerated. A fp_{DS} value of 10 is assumed to be the upper bound. Thus, as last evaluation measure the average sensitivity at $10\,fp_{DS} \pm 5\,fp_{DS}$ is used as a score value similar to [van Ginneken et al., 2010]. se_{10} is defined as:

se_{10} is the main evaluation measure

$$se_{10} = \frac{1}{5} \sum_i se(5 + 2.5i), \ i = 0, \dots, 4. \tag{6.8}$$

se_{10} takes values between $[0, 1]$, $se_{10} = 1$ is the optimal value.

As evaluation measures for the classification algorithms, the sensitivity or TP rate (Equation 6.1) and the specificity or TN rate (Equation 6.3) are usually used. Additionally, the accuracy acc is commonly employed:

$$acc = \frac{n_{TP} + n_{TN}}{n_{TP} + n_{FP} + n_{TN} + n_{FN}}. \tag{6.9}$$

However, this assumes the same misclassification costs, i. e., equal costs for misclassifying a true lesion as FP and to misclassify a FP as true lesion. A classifier leading to a simultaneous high sensitivity and specificity is desirable especially for CAD systems as the misclassification costs differ, e. g., it is more costly to erroneously classify a true lesion as no lesion than to classify no lesion as true lesion. The measure G-mean g_m leads to this property [Kubat et al., 1998]:

$$g_m = \sqrt{se \cdot sp}. \tag{6.10}$$

Consequently, it is used as the evaluation measure for the classification algorithms. g_m yields to values between $[0, 1]$ with 1 being the optimal value.

6.4 ROBUSTNESS EXPERIMENTS

Each experiment was performed as a cross-validation to separate training and test data as the system partly depends on statistical measurements. The features p_A, p_{FP}, d_{cmax}, W_t and W_{te} depend on training. For each modality, the data sets were divided into four folds having approximately the same amount of aneurysms and

Table 6.2: Overview about the parameters of the method.

Symbol	Algorithm part	Section
α, β, γ r_{min}, r_{max}, N	Blobness filter	5.4
t, s_{min}	ROI extraction	5.5
d_{CoWmax}, d_{cmax}	RBS	5.7

data sets. The atlas-dependent feature p_A was computed on all data sets of all modalities except the current fold (inter-modality cross-validation). p_{FP} and the threshold d_{cmax} were computed on all data sets of the current modality except the current fold (intra-modality cross-validation). Also, the training of W_t and W_{te} was done by intra-modality cross-validation.

Note: a list of smybols/parameters can be found after the table of contents at the beginning of this thesis

Each experiment resulted in four FROC, one for each fold. The average FROC was computed by the aggregation of the results of all folds. For p_A computation, it was ensured that no data sets of the same patient having a different modality were included in the probability maps. However, this happened only three times.

The goal of the robustness experiments was to test the dependence of the system on its parametrization. In Table 6.2, the relevant parameters are summarized. The testing protocol was the following: only one parameter was varied at a time whereas all other parameters remained fixed. A meaningful value range was determined for each parameter in a pilot experiment on few prototypical randomly chosen data sets. Based on the found value range, a suitable parametrization value sampling was chosen. The experiments were then done either on all databases or only on specific databases. The decision depended on the measured parameter influence in the pilot experiments or expected influence on the results.

Typically, comparative experiments have been done to measure the change of results between different parametrizations or variants. These changes were measured using the introduced evaluation measures. The most important evaluation measure is se_{10}, as it condenses the important characteristics of the FROC in a scalar value. Thus, this measure was used to compare different parametrizations or variants by employing diagrams. Additionally, tables containing all evaluation measures of all experiments can be found in Appendix A.

6.4.1 *Multi-scale filter parametrization*

The first relevant part of the system is the computation of the multi-scale blobness filter described in Section 5.4. This method is the backbone of the whole system as all other parts depend on the filter output. Either Frangi's variant or Li's variant can be used for computation.

As a multi-scale filtering approach was employed, the expected object radii $[r_{min}, r_{max}]$ and the sampling rate N were important parameters for both variants. Larger objects than r_{max} were found as multiple sub-structures (see Figure 5.4). The parameters α, β and γ were used for Frangi's variant only. These parameters
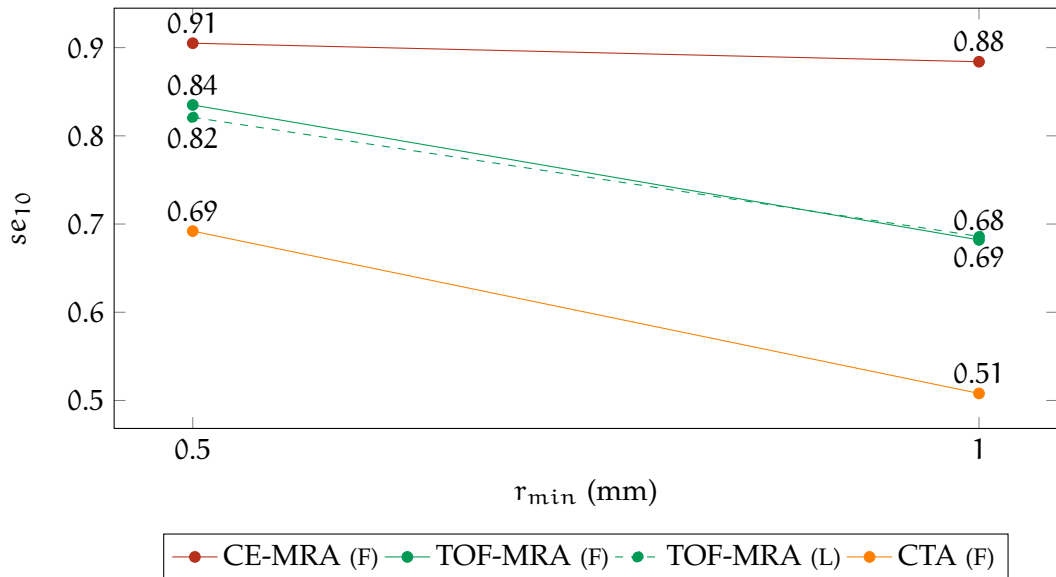
Figure 6.3: The robustness of blobness parameters r_{min} and r_{max} computed with Frangi's method (F) was evaluated. For TOF-MRA, also Li's method (L) was evaluated. $r_{max} = 10\,r_{min}$.

represent coefficients to weight different measures that determine the deviation between object and a Gaussian intensity distribution.

PARAMETRIZATION OF r_{min}, r_{max} AND N   Pilot experiments have been made with eight randomly chosen CE-MRA data sets containing nine aneurysms and Frangi's blobness variant. The expected radii of the aneurysms were parametrized with $[r_{min}, r_{max}] = 2^i \cdot [0.25\,mm, 2.5\,mm]$, $i = 0, \ldots, 3$. N was set to 5. All parametrizations led to the same se_{10} values and similar AUC values with a maximum difference of 3.9 % (see Table A.1).

The second and third multi-scale parametrization with $i = 1$ and $i = 2$ were then chosen for the test with all databases except for the 3D-RA database. For all databases, the parametrization with $[r_{min}, r_{max}] = [0.5\,mm, 5\,mm]$ led to the best results (see Table A.2). The se_{10} value was 2.4 % better for CE-MRA, 22.4 % better for TOF-MRA and 36.2 % better for CTA with respect to the parametrization $[1\,mm, 10\,mm]$. Thus, an expected object diameter of 1 mm to 10 mm led to the best results, as expected. This range represents 77 % of the aneurysms in all evaluation databases.

Optimal diameter ranges were between 1 mm and 10 mm

Regarding the sampling rate N, it was found in a pilot experiment that the default value of N = 5 and N = 6 led to the best results in terms of se_{10} (see Table A.1). N = 5 was used for all remaining experiments due to the smaller computational cost. No further experiments were done as the maximal differences in se_{10} were only 5.3 %.

PARAMETRIZATION OF α, β AND γ The weighting parameters α and β were proposed to be set to 0.5 [Frangi et al., 1998] and were fixed for the evaluation. γ depends on the gray-scale range of the image. Experiments were done with the CE-MRA database with $\gamma = 5$, $\gamma = 10$ and $\gamma = 20$. The last two γ values led to the

same results, while $\gamma = 5$ led to considerable poorer results (see Table A.2). Thus, $\gamma = 10$ was used for further experiments.

COMPARISON OF LI'S BLOBNESS AND FRANGI'S BLOBNESS   Pilot experiments have also been done to evaluate the parameters of Li's blobness variant. This method only requires the parameters $[r_{min}, r_{max}]$ and N. It was assumed that the effects of N are the same as in Frangi's method, thus N was set to the value 5.

In an experiment using seven randomly chosen data sets of all modalities containing 13 aneurysms, $[r_{min}, r_{max}]$ were set to the radii $2^i \cdot [0.25\,mm, 2.5\,mm]$, $i = 0, \ldots, 3$, as before. The parametrization with $[0.5\,mm, 5\,mm]$ and $[1\,mm, 10\,mm]$ led to the best results and was subsequently tested on the TOF-MRA database. Again, the parametrization with $[0.5\,mm, 5\,mm]$ led to better evaluation measurements (see Figure 6.3 and Table A.3). The se_{10} value had improved by 19.7 % in comparison to $[1\,mm, 10\,mm]$. Concerning the comparison to Frangi's variant, the results of Li's variant led to slightly worse evaluation measures. While the se_{10} measure was 1.7 % worse, the AUC value was 3.3 % worse for the radii $[0.5\,mm, 5\,mm]$.

The blobness variant by Frangi performed slightly better

In conclusion, if the best parametrization for both blobness variants was found, they produced similar results. However, Frangi's variant was more robust with respect to the parametrization. Thus, Frangi's method was preferred to enhance spherical structures in this system and used in following experiments.

6.4.2 *ROI extraction parametrization*

The next investigated part is the ROI formation described in Section 5.5. The relevant parameters are the threshold factor t used for the extraction of ROI by clustering all peaks in the blobness image and the minimal size of a ROI, s_{min}. Note that the actual threshold value is $t' = t\,B_{max}$.

PARAMETRIZATION OF t   Experiments have been made with all databases. Values between $t = [0.05, 0.25]$ with $\Delta t = 0.05$ have been tested. In 3D-RA, $t = [0.05, 0.4]$ was tested. The results varied largely per modality (see Figure 6.4 and Table A.4). The best and the worst se_{10} value differed 6.8 % for 3D-RA, 7.6 % for CE-MRA, 25.6 % for TOF-MRA and 11.4 % for CTA. $t = 0.15$ is a good tradeoff between finding the relevant peaks at aneurysmal positions in the blobness image and finding too many peaks related to non-aneurysmal positions. This parametrization led to good results for all databases. However, for each modality, the optimal results were achieved using a specific value for t by optimizing se_{10}:

For optimal results, t has to be set differently for each modality

- For 3D-RA, this was $t = 0.25$ leading to $FP_{0.9} = 2.41$ and $se_{10} = 1.0$.

- For CE-MRA, this was $t = 0.15$ leading to $FP_{0.9} = 9.24$ and $se_{10} = 0.895$.

- For TOF-MRA, this was $t = 0.2$ leading to $FP_{0.9} = 10.34$ and $se_{10} = 0.835$.

- For CTA, this was $t = 0.15$ leading to $FP_{0.9} = 47.47$ and $se_{10} = 0.634$.

PARAMETRIZATION OF s_{min} No formal evaluation has been done with the minimal valid volume of a ROI, s_{min}. This parameter has been estimated based on the
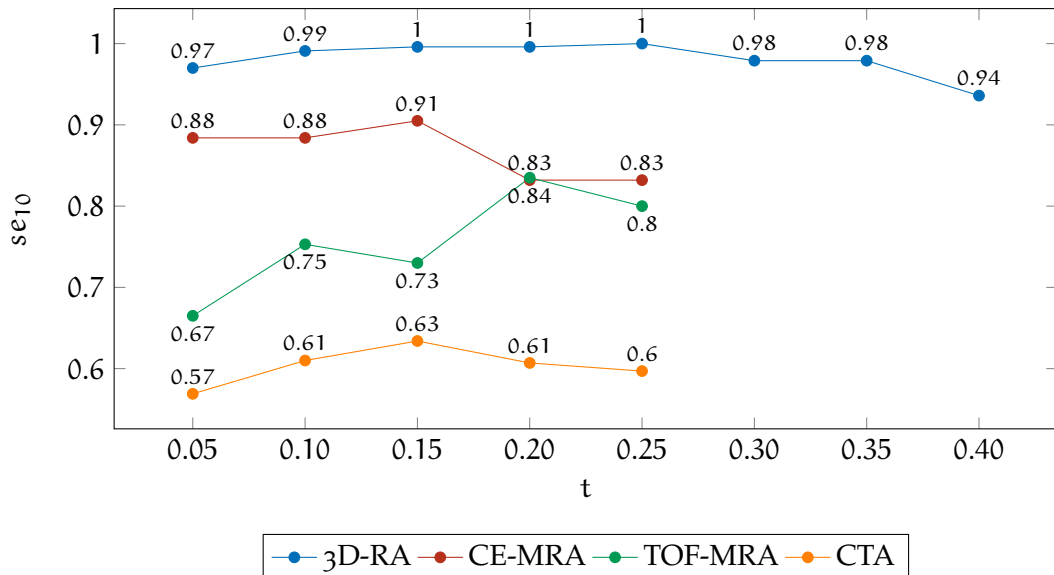
Figure 6.4: The effect of t on the results was studied. t controls the peak extraction from the blobness filtered data set that form the ROI. t was varied between 0.05 and 0.4 for 3D-RA and between 0.05 and 0.25 for all other modalities.

minimal expected diameter of aneurysms, $2\,mm$. Theoretically, this results in a volume $s = 4.19\,mm^3$ for a perfect sphere. As the ROI were not perfectly sphere-shaped and the volume of a pixel differed quite much (between $0.03\,mm^3$ and $0.75\,mm^3$), the value has been chosen slightly larger. For CTA $s_{min} = 5\,mm^3$ was chosen, thus $2r = 2.12\,mm$, for the other modalities $s_{min} = 8\,mm^3$ was chosen, thus $2r = 2.48\,mm$. No aneurysmal ROI has been found in the database that was smaller than these values. As long as $s_{min} < 10\,mm^3$, a different parametrization of s_{min} only led to small changes in the results except for CTA. In CTA $5\,\%$ of the aneurysmal ROI have a volume of $< 10\,mm^3$. This was the case for $< 3\,\%$ only in the other modalities. s_{min} depends on t also: The higher t, the smaller generally was the volume of the ROI.

6.4.3 Rule-based system parametrization

The parametrization of the RBS is important as this step represents a hard constraint. The relevant parameters are the maximal tolerated distance to the next vessel in the model volume, d_{CoWmax}, and the maximal tolerated distance to the center point of the data set, d_{cmax}. The first parameter depends on the registration quality while the second parameter is a statistical measure.

A large value for d_{CoWmax} led to distinctly better results

PARAMETRIZATION OF d_{CoWmax} In this experiment, d_{CoWmax} was assigned the value of $5\,px$, $10\,px$, $15\,px$ and $20\,px$. Experiments have been done on the CTA database as this parameter has a large importance there. The results can be found in Figure 6.5 and in Table A.5. $20\,px$ was the value leading to the best results in terms of all three evaluation measures. The se_{10} measure increased directly proportional to the value of d_{CoWmax}. Thus, the larger the distance to the vessels were, the less was the probability that a ROI was erroneously excluded. Therefore,

d_{CoWmax} was set to 20 px for all modalities. This is the maximal value as the distance transform has been computed with a maximum distance of 20 px.

PARAMETRIZATION OF η η represents a tolerance factor accounting for inter-fold variations. $d_{cmax} = \eta \max(d_c)$ was computed for each cross-validation fold with $\max(d_c)$ denoting the maximum value of d_c for TP ROI on all data sets of a database except these that were in the current fold. η was parametrized with 1.05, 1.1, 1.15 and 1.2 to estimate a suitable d_{cmax} value.

The experiments are summarized in Figure 6.6 and in Table A.6. The parameter η did only have a minor influence on the results as the se_{10} measure varied between 0.4 % and 3.7 % if the best and the worst results were taken into account. The best results have been achieved with $\eta = 1.05$ in case of CE-MRA and CTA. For TOF-MRA, η had to be set between 1.15 and 1.2 to ensure the inclusion of all true aneurysm ROI. A too low value for η has the risk that a true aneurysm ROI is excluded. Therefore, higher values for η were preferred. Further experiments between the parametrization $\eta = 1.15$ and $\eta = 1.2$ revealed that 1.17 was a suitable value for all modalities to minimize the risk of eliminating a TP ROI at the cost of including more FP ROI.

η is robust to changes, but a higher value is preferred to provide a safety margin

6.4.4 *Summary*

t was the most important analyzed parameter as it heavily influenced the results of the system. This parameter had to be determined carefully for each modality. A default value that produced good results for all modalities has been found. In all further experiments, t was fixed at the optimal value to estimate the best results. Frangi's variant of blobness produced slightly better results than Li's variant. A minimal expected object radius of 1 mm and a maximal object radius of 10 mm led to the best results. The other blobness filter parameters were relatively robust.

The RBS parameters had to be carefully set as they could lead to the elimination of true aneurysm ROI. A good parametrization has been found by setting $d_{CoWmax} = 20$ px and $\eta = 1.17$ for each modality. Both parameters were set rather conservatively. This led to an optimal sensitivity, but also to a higher amount of FP ROI.

6.5 PROCEDURAL EXPERIMENTS

Every part of the system workflow influences the results. For most parts, different variants have been proposed and it was tested which one led to the best result. If no variants have been proposed, the relevance of the parts was evaluated by comparing the results obtained with and without the specific algorithm step.

Both experiment types are referred to as procedural[1] experiments. An overview about the relevant steps covered by experiments is given in Table 6.3. The different blobness variants have already been tested in Section 6.4.1, all other variants are tested below.

---

1 *procedural*: of or pertaining to a procedure or procedures (according to www.dictionary.com).
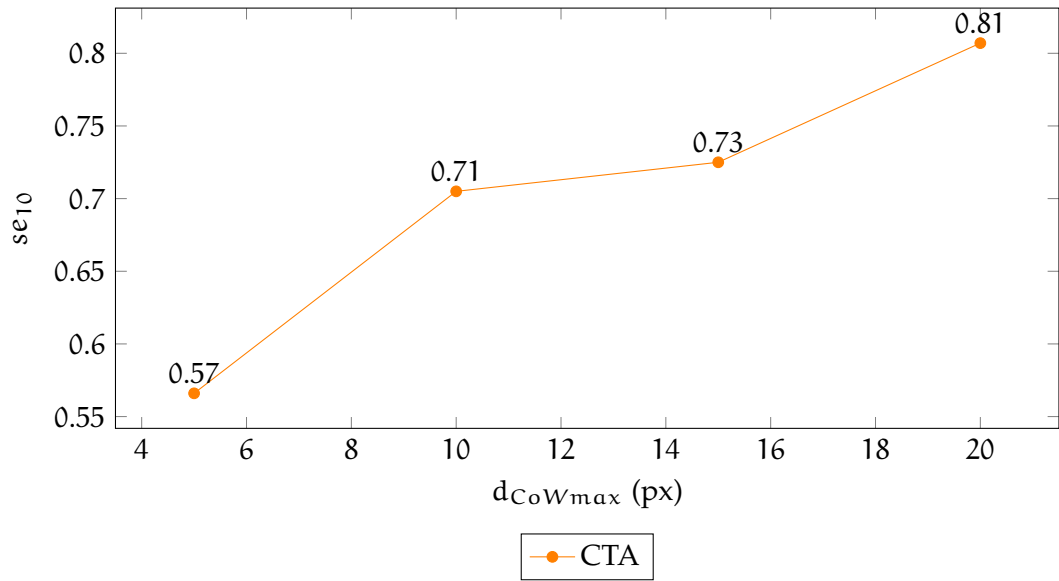
Figure 6.5: The robustness of d_{CoWmax}, the maximal distance to the nearest vessel, was evaluated. The rank order scheme was chosen.
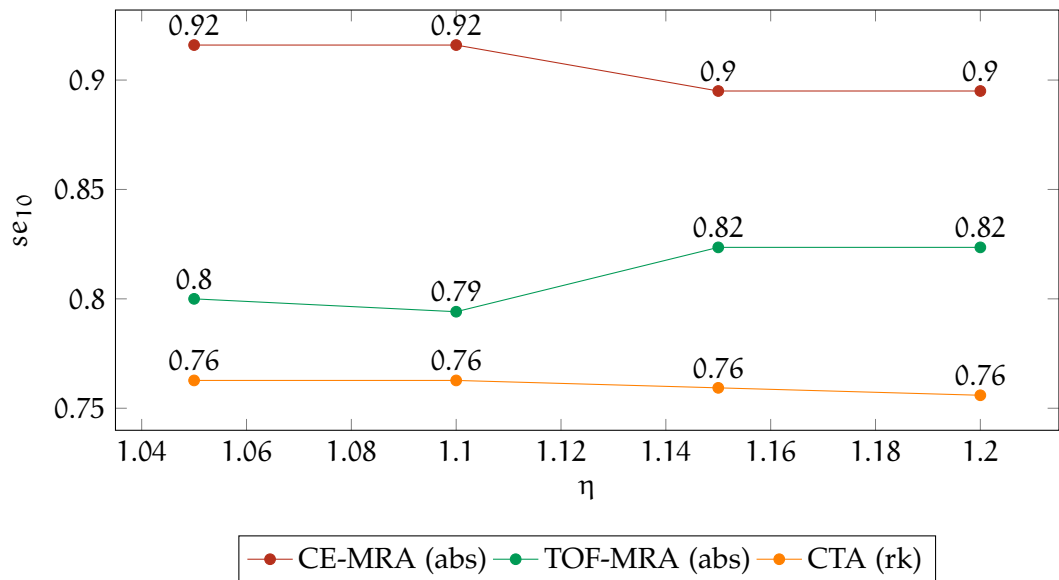
Figure 6.6: The robustness of the η, directly related to d_{cmax} (maximal distance to the center of the image of a ROI), was evaluated.

Table 6.3: Overview about relevant steps that were tested in procedural experiments. V = Variant, S = Skip step.

Step	Variants	Section
CTA mask image	Thresholding, Double Thresholding (V)	5.3
Blobness variant	Frangi, Li (V)	5.4
Registration quality	Omit registration-based parameters (S)	5.6
Feature normalization	Local, global (V)	5.6
Relevance of RBS	Omit RBS (S)	5.7
Single features as threshold for classification	s, b_{avg}, b_{max}, Ψ (V)	5.8
Influence of LDF weighting	W_e, W_t, W_{te} (V)	5.8
Different ordering scheme	A_t, rk_t (V)	5.8
Classification	State of the Art classifiers (V)	5.9

6.5.1 *CTA mask computation*

As first procedural experiment, the mask computation of CTA was evaluated. The mask ensures that the blobness computation is only done on relevant blood vessel intensities (cf. Section 5.3). Three options have been tested: no masking, normal thresholding and double thresholding. The normal thresholding has been tested with two outside values, 0 and -2048. The double thresholding has been tested with masking (the value of the segmented pixels remains unchanged while the others were set to the value 0) and without masking (binary segmentation).

A masking of CTA data sets was important. In experiments without a mask, the number of ROI approximately tripled. The general problem was that extremely high blobness values emerged at skull bones that distorted the whole multiscale-filtered image. As the ROI extraction step depends on the maximal blobness, most relevant ROI at vessel positions were either not regarded or too many ROI were included.

The produced segmentations with thresholding and double thresholding were similar. The amount of segmented pixels was only $18\,\%$ less with double thresholding compared to normal thresholding. This value was expected higher as the double thresholding algorithm includes more information compared to a simple thresholding algorithm.

In a pilot experiment, the unmasked double thresholding led to better results than the masked double thresholding and was used afterwards. Surprisingly, the double thresholding led to worse evaluation results than simple thresholding (see Figure 6.7 and Table A.7). The value of se_{10} decreased by $40.1\,\%$ and $35.9\,\%$ in comparison to normal thresholding with $-2048\,\mathrm{HU}$ and $0\,\mathrm{HU}$ outside value, respectively. The vessel masking of the double thresholding was more precise. However, many (artificial) boundaries were introduced that led to a larger amount of ROI in comparison to the normal thresholding.

The thresholding variant with an outside value of $-2048\,\mathrm{HU}$ led to better results than the variant using $0\,\mathrm{HU}$ as outside value. The se_{10} value increased by $3.1\,\%$. This was due to the effect of the higher gradients at the boundaries between ves-

Normal thresholding performed better than double thresholding for CTA mask computation
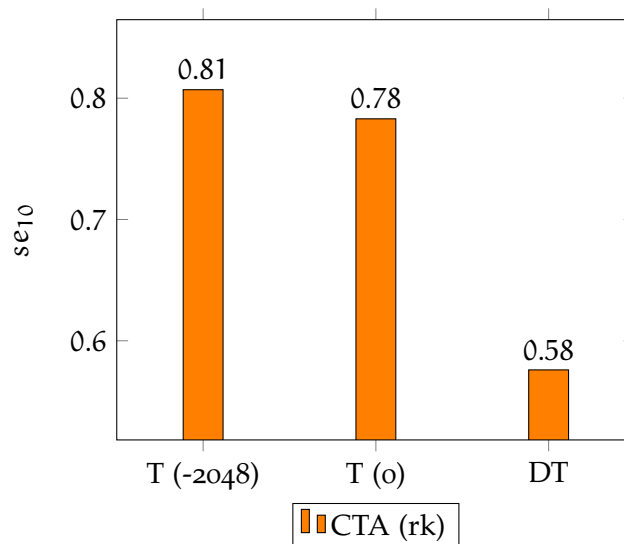
Figure 6.7: Influence of the CTA Mask image parametrization on the system. In contrast to thresholding, where t has been set to the value of 0.12, the experiments with DT were done with t = 0.07. The results achieved with t = 0.12 and DT were worse. T (-2048) = thresholding with -2048 HU, T (0) = thresholding with 0 HU, DT = double thresholding without masking.

sels and background in CTA. They were more important than the within-object boundaries as they contributed to the differentiation between vessels and other objects.

6.5.2 *Registration features*

The registration-based features are important to discriminate between vessel ROI and non-vessel ROI (d_{CoW}). Additionally, the probability features p_A, p_{FP} are incorporated into the LDF. These features depend on the registration quality. The registration led to suitable results even if it was only approximate. Possible registration errors and the inter-patient vessel variability are compensated by several mechanisms. Thus, the registration-based features are valid even in the case of minor registration errors.

Due to the lack of ground truth as in most registration problems [Maintz and Viergever, 1998; Aylward et al., 2003], the registration quality could be measured by using appropriate methods such as comparing the distance between fiducial markers at the same morphological (vessel) locations in the model image and the original data set. Also other methods have been proposed [van de Kraats et al., 2005]. However, a formal evaluation of the registration quality was relinquished.

Instead, an indirect evaluation of the impact of these features was done by omitting them in the computation of A. The results of this experiment are summarized in Figure 6.8 and Table A.8. The evaluation measures deteriorated if the three registration-based features were weighted with 0 in experiments on all databases. The deterioration measured by se_{10} was 16.1 % for CE-MRA, 6.8 % for TOF-MRA and 22.1 % for CTA. No experiments have been done with the 3D-RA database as none of the registration-based features was computed there (see Section 5.6).

The system performed worse without registration-based features

6.5.3 *Rule-based system*

The RBS eliminates ROI by defining valid feature value ranges. This step is important because otherwise irrelevant ROI are included in the final aneurysm candidates. This was confirmed in the experiments with and without the RBS (see Figure 6.9 and Table A.11). The largest effect was present in the CTA database due to the impact of the intensity constraint. The se_{10} value deteriorated by 56.3 %. For the TOF-MRA database, the se_{10} value deteriorated by 44.3 % and for CE-MRA, the value deteriorates by 38.3 %. In the 3D-RA database, only few ROI were excluded as the initial ROI computation already contained almost only relevant ROI. The se_{10} value did not change and the AUC value deteriorated by 1.3 %.

The rule-based system is important to exclude false positive ROI

Thus, the RBS is an important part of the system as irrelevant ROI were discarded.

6.5.4 *Linear discriminant function*

After the completion of the RBS, the remaining ROI are further evaluated on basis of a score value A. Two thresholding methods were tested to define the final aneurysm candidates on A (cf. Section 5.8). The absolute threshold A_t is computed on all data sets, while the rank order threshold rk_t is computed per data set. The ROI having the rk_t largest A values are defined as final candidates.

THRESHOLDING OF THE SCORING VALUE A The effect of both methods on the different modalities is summarized in Figure 6.10 and Table A.11. In 3D-RA, both methods produced equal se_{10} values, only a difference in the $FP_{0.9}$ measure was present (25.2 % in favor of the absolute scheme). For CE-MRA, the difference in se_{10} was 4.9 % in favor of the absolute scheme. For TOF-MRA there was no difference in terms of se_{10}, however the other two values were slightly better by employing the absolute threshold (4.1 % for AUC and $FP_{0.9}$). For the CTA data base, the rank ordering led to considerably better results (see Figure 6.19b). The se_{10} value differed by 16.6 %.

Rank order thresholding led to better results for CTA while absolute thresholding led to better results in all other modalities

It is desirable to combine the absolute and the rank order scheme. This can be done as follows: first, all ROI fulfilling the criterion $A(c_i) < A_t$ are excluded. Then, the rank order thresholding is done with rk_t as the varying parameter. This led to good results in all modalities and can be seen as a compromise for the two schemes (see Figures 6.18 and 6.19). A drawback is the resulting two-dimensional optimization function.

LDF PARAMETRIZATION: W_e, W_t AND W_{te} An important aspect is if the expert parametrization and the trained parametrization led to comparable results. W_e represents the expert weighting while W_t denotes the trained weighting using all features. W_{te} is the trained weighting computed by regarding the features of W_e. W_t and W_{te} are computed using linear regression.

The results are summarized in Figure 6.11 and Table A.10. Compared to W_e, the parametrization W_t resulted in worse evaluation measure values in almost every database. In 3D-RA the difference in se_{10} was 4.5 %, in CE-MRA the difference was 1.1 %, in TOF-MRA the value differed by 25.6 % and in CTA the value differed by 14 %. Thus, a good generality has been achieved with the trained parametrization

The expert parametrization led to better results for all modalities compared to the trained parametrization
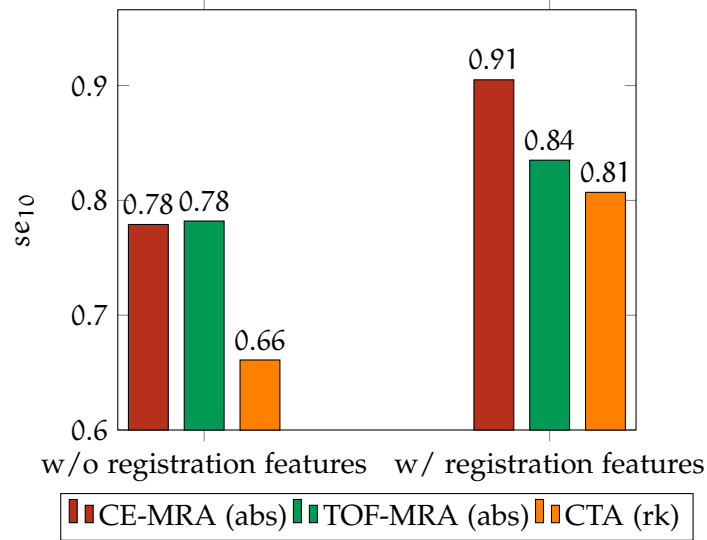
Figure 6.8: Results that were achieved by omitting registration-based features p_A, p_{FP} and d_{CoW} (w/o registration features). Results achieved with these features (w/ registration features) are shown for comparison.
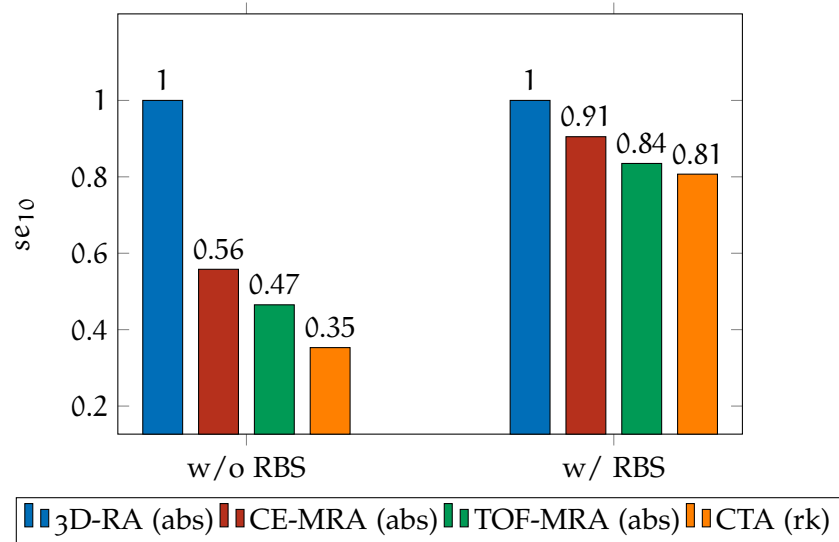
Figure 6.9: Results that were achieved without excluding ROI by the RBS (w/o RBS). Results achieved with the RBS are shown for comparison (w/ RBS).
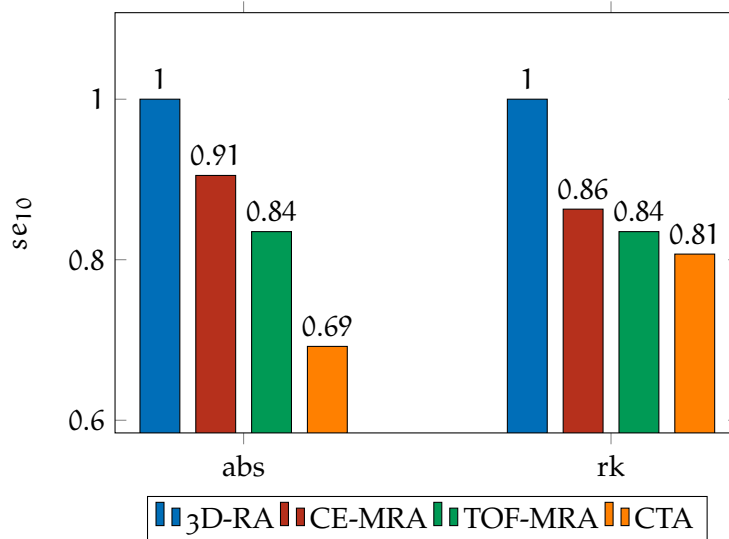
Figure 6.10: Results that were achieved with the absolute threshold (abs) and the rank order threshold (rk).

only for 3D-RA and CE-MRA. The small amount of training data sets (75 % of data sets for each database as a four-fold cross-validation was done) influenced the results in favor of the static expert parametrization.

The relevance of the expert-chosen weighting can be indirectly measured by comparing the results using the parametrization W_t and W_{te}. If the features are relevant, the evaluation measures computed with W_{te} should improve in comparison with W_t. This was clearly the case for all modalities except 3D-RA (see Figure 6.11 and Table A.10). In 3D-RA the differences between the evaluation measure values were only marginal (no difference in terms of se_{10} and 1 % in terms of AUC). For CE-MRA the difference in terms of se_{10} was 1.1 %, for TOF-MRA the improvement was 15 % and for CTA the value increased by 5.4 % compared to the results computed with W_t parametrization.

The results with W_e parametrization led to better measurements than with W_{te} parametrization except for CE-MRA. The improvement in terms of se_{10} was 4.4 % for 3D-RA, 9.2 % for TOF-MRA and 27.3 % for CTA. For CE-MRA, the se_{10} value was the same. Thus, even if a feature selection was done, the generalization of the expert-based parametrization could not be achieved using the trained parametrization.

To test the influence of the cross-validation, the experiments with parametrization W_t and W_{te} were repeated without cross-validation, thus using all data sets of a database for training. The improvements for W_t were between 2.3 % and 14.3 % and for W_{te} the improvement was between 1.3 % and 14.3 % in terms of se_{10} (see the error bars in Figure 6.11 and the average FROC curve of CTA in Figure 6.13). This was the estimation of the upper boundary of results that can be achieved with linear discrimination. The evaluation measures of W_e and W_{te} converge if a training on all datasets is done.

Expert-based feature selection improved the results

It is also possible to compute W_t on all modalities rather than only on one modality. The chance is that additional training samples lead to a better discrimination model. The risk is that the data sets of different modalities are too heterogeneous
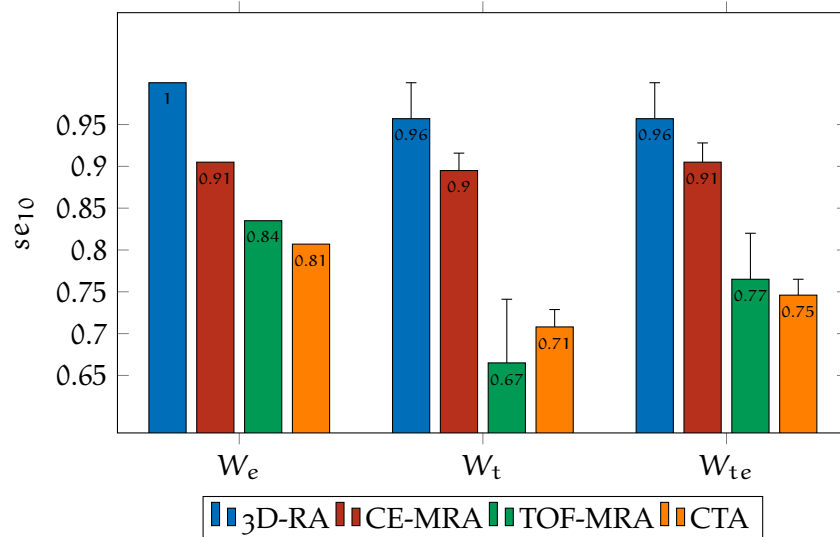
Figure 6.11: Experiments with the LDF and parametrization with W_e, W_t and with W_{te}. The error bars show how the values improved if no cross-validation was done (all data sets of the same modality were used for training).

and that the ROI characteristics of the two classes cannot be generalized with respect to their features. The 3D-RA database was not considered in the computation as its image characteristics are too different and as only one supplying vessel is shown per data set.

The results are summarized in Figure 6.12 and Table A.9. The measures deteriorated compared to the training over one modality for CE-MRA by 8.3 % and for CTA by 9.5 %. For TOF-MRA, however, the results improved by 6.9 %. This means that the in-modality heterogeneity of TOF-MRA (between folds) was larger than the heterogeneity across all modalities. For the other modalities the assumption holds true that the characteristics of the modalities were too different to be well-generalized in a common training.

An interesting question is which features were the most relevant with respect to their statistical discrimination power computed in W_t. The trained weighting values in W_t are shown in Table 6.4 (computed per modality). The weighting values differed quite heavily per modality and also per fold. For the 3D-RA database the volume s statistically was the most relevant feature for discrimination. For the CE-MRA database, it was the standard deviation of the blobness values, b_{stddev}. For TOF-MRA, it was the standard deviation of the vesselness, v_{stddev}, and for CTA, it was the aneurysm probability, p_A.

SINGLE FEATURES AS SCORING VALUE   The LDF value $A(c_i)$ consists of the combination of four or seven weighted feature values. To demonstrate the superiority of this combination over the use of single feature values as score, experiments have been performed (similar to [Hentschke et al., 2012a]). The LDF was parametrized with a weighting factor 1 for the tested feature and 0 for all other features. As threshold A_t, all absolute values of the respective feature were iterated and a FROC was computed. In a pilot experiment, only four features led to good results: s, b_{avg}, b_{max} and Ψ. These were subsequently tested as score values for
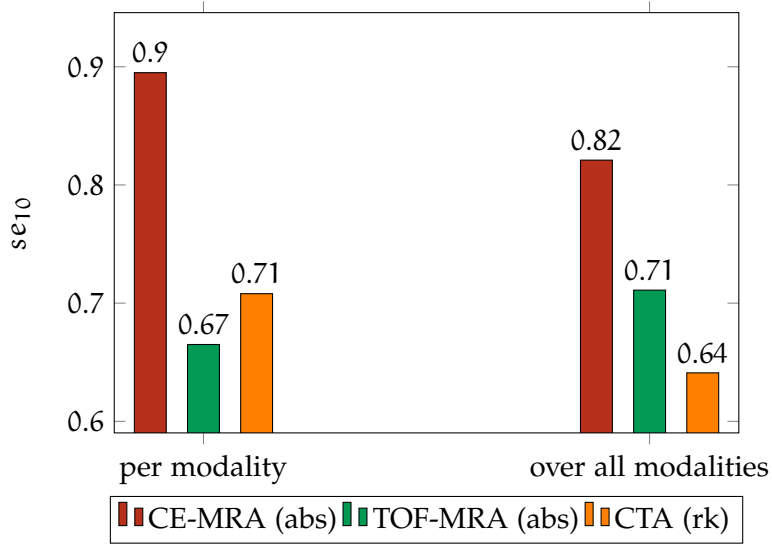
Figure 6.12: Results with W_t trained across all modalities. For comparison, the results achieved with W_t trained across one modality is shown.
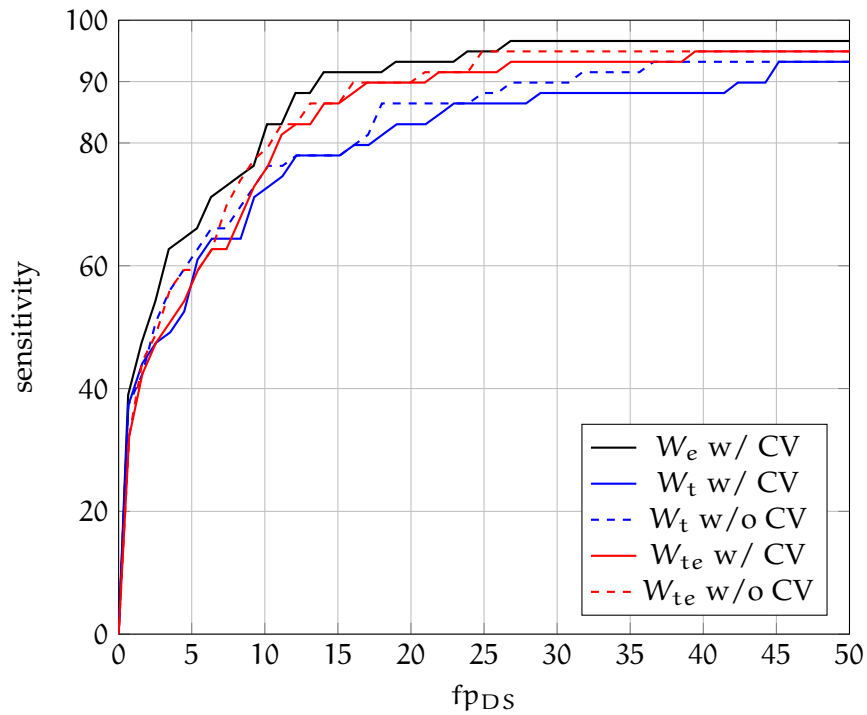
Figure 6.13: Average FROC for CTA database reached with rank ordering scheme and different LDF weighting parametrization with cross-validation (w/ CV) and without cross-validation (w/o CV).

Table 6.4: Normalized weight values for the trained parametrization W_t. Mod.: Modality, opt: optimal value computed on all folds, ϵ: the error term in linear regression. The maximum absolute value for each column is printed bold. The entry "–" means that these features were omitted for training.

Mod.	3D-RA					CE-MRA					TOF-MRA					CTA				
Fold	1	2	3	4	opt	1	2	3	4	opt	1	2	3	4	opt	1	2	3	4	opt
s	0.53	**0.66**	**0.47**	0.37	**0.53**	0.12	0.13	0.20	0.13	0.09	0.04	0.11	-0.07	0.12	0.05	0.32	0.37	**0.47**	0.29	0.36
ψ	–	–	–	–	–	0.15	0.31	0.18	0.23	0.12	0.10	0.13	0.10	0.14	0.13	0.04	0.01	0.03	0.01	0.03
i_{avg}	-0.20	-0.23	-0.32	-0.29	-0.29	0.09	-0.02	-0.07	-0.25	-0.18	-0.10	-0.21	-0.12	-0.06	-0.12	0.02	0.01	0.10	0.00	0.04
i_{min}	-0.04	-0.12	-0.03	-0.11	-0.08	0.00	0.16	0.02	0.27	0.18	0.24	0.06	0.20	0.02	0.12	-0.31	-0.31	-0.32	-0.21	-0.29
i_{max}	-0.08	-0.08	0.08	-0.11	-0.05	0.04	0.15	-0.04	-0.02	0.07	-0.10	-0.23	-0.09	-0.09	-0.13	-0.03	0.01	0.00	0.01	-0.01
i_{stddev}	0.01	0.05	-0.15	-0.05	-0.04	0.05	-0.22	0.02	-0.16	-0.13	-0.06	0.04	-0.20	0.05	-0.04	0.26	0.26	0.22	0.14	0.23
b_{avg}	-0.16	0.25	0.17	0.26	0.17	-0.37	-0.34	-0.58	-0.23	-0.27	0.33	0.25	0.40	0.40	0.36	0.30	0.31	0.25	0.45	0.33
b_{min}	0.19	0.09	0.19	0.16	0.17	-0.04	-0.10	-0.05	-0.06	0.02	0.04	0.00	0.09	0.05	0.05	0.04	0.03	0.03	0.04	0.04
b_{max}	**0.61**	-0.11	0.41	0.36	0.35	-0.21	0.03	0.19	-0.02	-0.11	-0.12	-0.29	-0.20	-0.24	-0.21	-0.39	-0.31	-0.39	-0.29	-0.36
b_{stddev}	-0.10	0.19	0.15	-0.26	-0.06	**0.75**	**0.58**	**0.64**	**0.66**	**0.70**	-0.12	0.23	-0.01	-0.11	-0.02	0.17	0.07	0.17	-0.12	0.09
v_{avg}	-0.06	-0.03	-0.13	-0.07	-0.09	0.03	0.19	0.00	0.10	0.15	0.29	0.36	0.30	0.21	0.31	0.20	0.25	0.20	0.19	0.21
v_{min}	-0.24	-0.19	-0.29	-0.24	-0.25	0.01	0.02	-0.11	-0.03	-0.07	0.16	0.17	0.12	0.12	0.15	0.04	0.09	0.01	0.06	0.05
v_{max}	0.11	0.24	0.21	0.32	0.27	-0.09	-0.04	-0.12	-0.03	-0.11	0.18	0.18	0.27	0.33	0.25	0.01	0.15	0.11	0.18	0.13
v_{stddev}	-0.35	-0.48	-0.44	**-0.45**	-0.48	-0.18	-0.29	-0.08	-0.28	-0.14	**-0.55**	**-0.47**	**-0.45**	**-0.51**	**-0.53**	-0.13	-0.27	-0.22	-0.27	-0.23
d_{CoW}	–	–	–	–	–	0.13	0.02	0.13	0.14	0.13	0.22	0.04	0.10	0.07	0.11	0.01	-0.02	0.02	-0.01	0.00
d_c	0.07	-0.03	0.11	0.07	0.05	-0.08	0.01	0.03	-0.14	-0.04	0.02	0.23	0.08	0.20	0.14	0.10	0.06	0.07	-0.01	0.05
p_A	–	–	–	–	–	0.20	0.25	0.14	0.23	0.24	-0.08	-0.01	-0.09	0.07	-0.03	**0.53**	**0.51**	0.42	**0.61**	**0.53**
p_{FP}	–	–	–	–	–	0.19	0.21	0.21	0.25	0.27	0.22	0.22	0.24	0.16	0.21	0.11	0.05	0.10	0.04	0.08
ϵ	0.18	0.23	0.18	0.29	0.25	-0.27	-0.32	-0.17	-0.20	-0.33	-0.47	-0.40	-0.46	-0.46	-0.47	-0.30	-0.27	-0.28	-0.18	-0.26
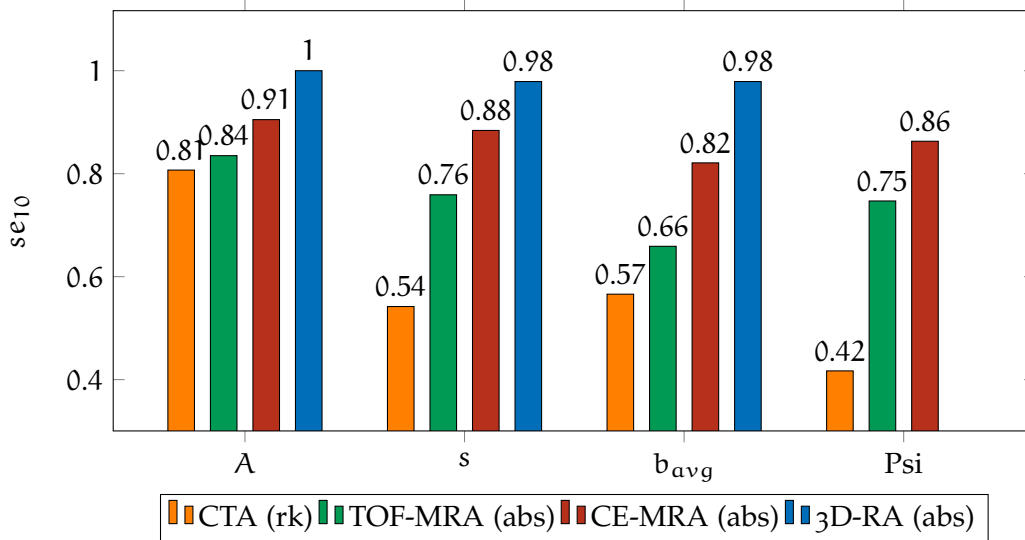
Figure 6.14: Experiments with single features as score values. The results were computed with the ordering scheme leading to the optimal quality. A is the score value for aneurysms, s is the volume of the ROI, b_{avg} is the average blobness value and Ψ is the sphericity value. Ψ was not computed for 3D-RA due to technical restrictions. Psi = Ψ.

all databases. The results are summarized in Figure 6.14 and Table A.12. The best results achieved with single features as score were still worse than the A value computed with the W_e parametrization for all modalities. The best single feature was s for 3D-RA, CE-MRA and TOF-MRA and b_{avg} for CTA. The difference in terms of se_{10} to the results with A was 2.1 % for 3D-RA, 2.4 % for CE-MRA, 10 % for TOF-MRA and 42.6 % for CTA. Thus, the largest effects of the feature combination were seen in the TOF-MRA and the CTA database.

The combined feature A led to superior results compared to other single features

Furthermore, the same experiment was done with the locally normalized features instead of the globally normalized features. The value was normalized by the maximum value of the feature in the data set (see Section 5.6). By locally normalizing the feature values the probability density functions of the classes TP and FP change. More importantly, the overlap of both distributions changes. A small overlap is desirable as the classes can be differentiated based on feature value threshold. The probability density functions are directly associated with the FROC: Each point on the curve represents a classification threshold value. Thus, the AUC values computed with locally normalized feature values were compared to the non-normalized feature values. If the AUC measure value increases, the local normalization reduces the overlap of both probability density functions. For the majority of features, this was the case (see Figure 6.15 and Table A.13). The normalization has only a small effect for 3D-RA and CE-MRA data sets while for TOF-MRA and CTA data sets, the effect was larger. Thus, the use of local normalization is suitable as it led to quality improvements in the proposed system.

Figure 6.15: Experiments with feature normalization. The difference between the AUC computed with local normalization (AUC_l) and the AUC computed wit global normalization (AUC_g) is given for selected features. A is the score value for aneurysms, s is the volume of the ROI, b_{avg} is the average blobness value and Ψ is the sphericity value. Ψ was not computed for 3D-RA due to technical restrictions. Psi = Ψ.

6.5.5 *Classification*

The LDF can be replaced by State of the Art classification algorithms (cf. Section 5.9). While a LDF uses a linear decision boundary, classification algorithms also allows for non-linear decision boundaries. The experiments have been done in the same test environment as the experiments with LDF. All features were locally normalized. A four-fold cross-validation was employed. The data basis was the ROI set C_0, i. e., the results of the system without applying the RBS. Experiments with applied RBS resulting in the ROI set C_1 led to worse results. This was due to the smaller amount of samples (ROI) in C_1 with respect to C_0.

The amounts of samples were:

- For 3D-RA 267 and 305 in C_1 and C_0, respectively,

- for CE-MRA 700 and 2587 in C_1 and C_0, respectively,

- for TOF-MRA 657 and 2565 in C_1 and C_0, respectively and

- for CTA 40 613 and 8106 in C_1 and C_0, respectively.

All experiments have been done with five classifiers (*Naive Bayes*, *SVM*, *Neural Network*, *ADTree* and *LogitBoost*) and three different parametrizations:

- Neither the data, nor the classifier was altered (*original*).

- The data was resampled (*resampling*).

- The classifier was evaluated incorporating misclassification costs (*MetaCost*).

For details about the classifiers, their parametrization and selection, see Section 5.9. A scatterplot of the features b_{avg} and v_{avg} can be found in Table 6.6. Further feature scatterplots can be found in Figure A.15 and Figure A.16. As the main evaluation measure, G-mean g_m was used (see Section 6.3).

The results are summarized in Figure 6.16, Figure 6.17 and Table A.14. The original classifiers without adaptations did not allow a good discrimination between true aneurysm ROI and FP ROI. The naive Bayes classifier led to the best results with an average g_m of 0.78 and an average se of 0.68. However, this quality was still too poor for the use in a CAD algorithm.

The resampling parametrization and MetaCost were able to classify the imbalanced data leading to good results

The results of all algorithms improved in terms of g_m if the database was resampled or if the algorithm accounted for misclassification costs by using Meta-Cost. The resampling method performed slightly better on average, the average g_m value of all databases was 0.82 compared to 0.70 with MetaCost. However, for three modalities, the best results of a single classifier were achieved with the MetaCost adaptation.

A disadvantage of MetaCost is that misclassification costs have to be provided. These were estimated by the between-class ratio µ. The resampling algorithm was less dependent on its parametrization and should therefore be preferred. The best results of one classifier averaged over all modalities have been achieved with the combination of LogitBoost and MetaCost.

Comparison of the classifier results and the results with the linear discriminant function is only indirectly possible

As no robustness evaluation with respect to the relevant parameters has been done, no FROC could be computed, but only a point on the FROC curve. Based on this point, a quality can be given as se and fp_{DS} values are defined. As the classification algorithms were trained on the ROI set C_0, they were also evaluated on this set. In this set, a very small amount of aneurysms were not included because they have not been found during the initial ROI finding step. For LogicBoost a sensitivity of 77 % in 3D-RA at 0.85 fp_{DS} could be reached. For CE-MRA the sensitivity was 95 % at 8.9 fp_{DS} and for TOF-MRA 79 % sensitivity has been reached at 10.7 fp_{DS}. In case of CTA the sensitivity was 90 % at 44.2 fp_{DS}. Except for 3D-RA these results are within the FROC curve of the results achieved with W_e LDF parametrization (see Figures 6.18 and 6.19). Thus, the use of a classification method instead of applying the LDF led to better results only in the case of 3D-RA. The results with LogicBoost were better compared to the results computed with W_t parametrized LDF. Thus, the non-linear classifier is superior to the linear discriminant function.

Note that the results were affected by the cross-validation and by the relatively small amount of folds. Because of computational complexity and reduction of evaluation effort, four folds were chosen. Also, this represents a rather realistic evaluation as the system was tested on a relatively large amount of unknown data sets.

6.5.6 *Summary*

Regarding the procedural experiments, the ordering scheme in the final classification step has a large influence on the results. While the rank order scheme produced distinctly better results for the CTA database, the absolute thresholding produced slightly better results in the other databases. The difference was 16.6 % in terms of the se_{10} value for CTA and 4.9 % for CE-MRA. The se_{10} values were
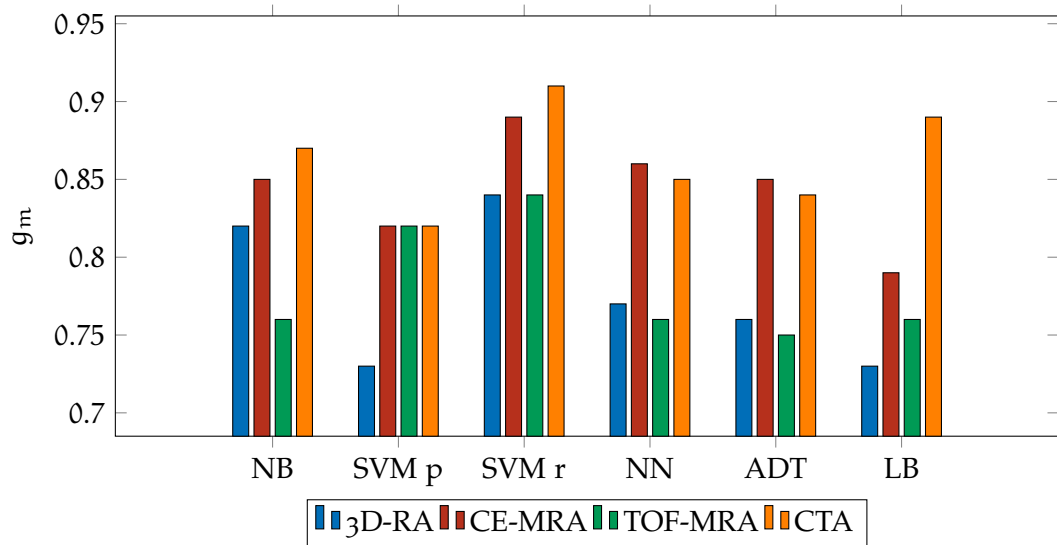
Figure 6.16: Experiments with the tested State of the Art classifiers and resampling. NB = Naive Bayes, SVM p = SVM with polynomial kernel, SVM r = SVM with radial kernel, NN = Neuronal network, LB = LogitBoost.
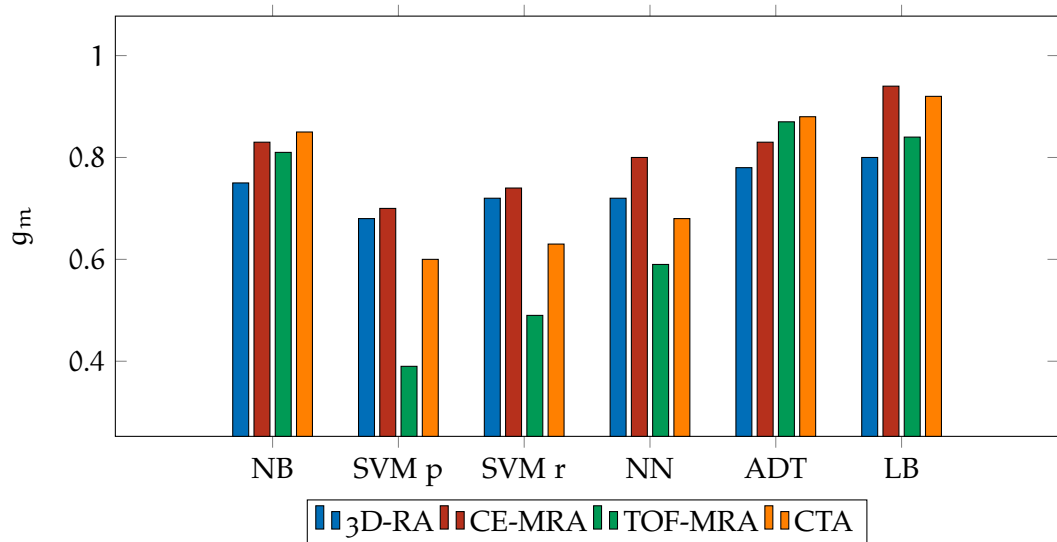
Figure 6.17: Experiments with the tested State of the Art classifiers and MetaCost. NB = Naive Bayes, SVM p = SVM with polynomial kernel, SVM r = SVM with radial kernel, NN = Neuronal network, LB = LogitBoost.

Table 6.5: The optimal evaluation measurements computed with the weighting W_e. The values correspond to the FROC in Figures 6.18 and 6.19. The best evaluation measure values for each modality are printed bold.

Ordering	Database	AUC	$FP_{0.9}$	se_{10}
abs	3D-RA	**0.927**	**2.41**	**1**
rk	3D-RA	**0.927**	3.22	**1**
combined	3D-RA	**0.927**	**2.41**	**1**
abs	CE-MRA	**0.786**	9.08	**0.905**
rk	CE-MRA	0.735	11.39	0.863
combined	CE-MRA	0.764	**8.24**	0.895
abs	TOF-MRA	**0.689**	10.34	**0.835**
rk	TOF-MRA	0.662	10.78	**0.835**
combined	TOF-MRA	0.668	**10.1**	**0.835**
abs	CTA	0.608	48.53	0.692
rk	CTA	0.637	14.03	**0.807**
combined	CTA	**0.688**	**13.93**	**0.807**

equal for TOF-MRA and 3D-RA, however the other evaluation measures showed better results. A combined scheme can be computed leading to good results in all modalities. It resulted in the best values for $FP_{0.9}$ in all modalities and in the best values for se_{10} in all modalities except for CE-MRA, where it was only 1.1 % worse.

It was shown that the registration-based features led to an improvement of the system quality. The se_{10} measurement deteriorated between 6.8 % and 22.1 % without the use of these features. The use of the expert feature weighting W_e led to similar or better results than the trained weighting W_t for all modalities except CE-MRA, especially because of the small amount of folds in the cross-validation. The improvements were between -3.4 %² and 9.2 %. Additionally, no non-linear classifiers were found that produced better results for all modalities except for 3D-RA.

6.6 DISCUSSION

In Figures 6.18 and 6.19, the FROC of the system using the optimal parametrization is shown. Note that the average FROC was computed because of the cross-validation evaluation. The respective evaluation measures for each database are summarized in Table 6.5. They are directly related to the grade of complexity that the modality poses for aneurysm detection. The best measure values have been achieved on the 3D-RA database. On the CE-MRA database, the results were slightly worse. Because of the heterogeneity of the data sets, the proposed algorithm performs worse in TOF-MRA than in CE-MRA. Although the task was

---

2 For CE-MRA, the parametrization with W_e led to worse evaluation values than the parametrization with W_t.

challenging, the results for the CTA database have almost reached the quality of the TOF-MRA database. For all modalities a good sensitivity was achieved at a reasonable amount of FP.

The four key questions can be answered as follows:

1. The results reaching the maximal sensitivity for the four modalities were (cf. Section 6.5.4):

   - 3D-RA: 100 % sensitivity at 3.7 fp_{DS},
   - CE-MRA: 95 % sensitivity at 8.2 fp_{DS},
   - TOF-MRA: 94 % sensitivity at 10.9 fp_{DS} and
   - CTA: 95 % sensitivity at 22.8 fp_{DS}.

2. The expert-set parametrization W_e of the LDF led to comparable or better results for all modalities than the trained parametrization W_t (cf. Section 6.5.4).

3. The trained weighting vector values in W_t were similar to the expert-based weighting vector values in W_e for TOF-MRA and CTA. For 3D-RA and CE-MRA the similarity was small (cf. Section 6.5.4).

4. The results achieved with the expert-set parametrization W_e were comparable or better to the chosen State of the Art classifiers. The results computed with the classifiers led to better evaluation measures than the parametrization with W_t (cf. Section 6.5.5).

For the MRA modalities > 90 % sensitivity was reached while having around 10 fp_{DS}. For the 3D-RA modality, even > 95 % sensitivity has been reached at 3 fp_{DS}. These values are within the initially defined target. For CTA data sets > 90 % sensitivity has been reached at 14 fp_{DS}. However, compared to the other modalities, this is a good result considering the challenges of CTA data sets.

The detection method had an average runtime of 4 min 20 s per data set on a standard quad-core PC. The runtime on CTA was higher than on MRA and 3D-RA as it mainly depends on the image size. The major amount of time was required to compute the multi-scale filter and the registration (combined 94 % of the time). The runtime may be easily reduced, e. g., by using parallelization and hardware acceleration.

6.6.1 *Detection of small and overlooked aneurysms*

The sensitivity to detect small aneurysms is good

The size of aneurysms influences the detection rate by neuroradiologists [Wardlaw and White, 2000]. Smaller aneurysms tend to be overlooked more easily than larger aneurysms, although the position described by their feeding vessel plays an important role as well [Wardlaw and White, 2000; White et al., 2000]. The sensitivity to detect small aneurysms having a diameter of < 5 mm was 95 % (56/59) in the proposed system measured across all modalities. The FROC for small aneurysms is given in Figure 6.20 for each modality. For 3D-RA and TOF-MRA, the results with data sets containing small aneurysms were better than the results on all data sets. On CTA, the evaluation measures were slightly worse and on CE-MRA, they were
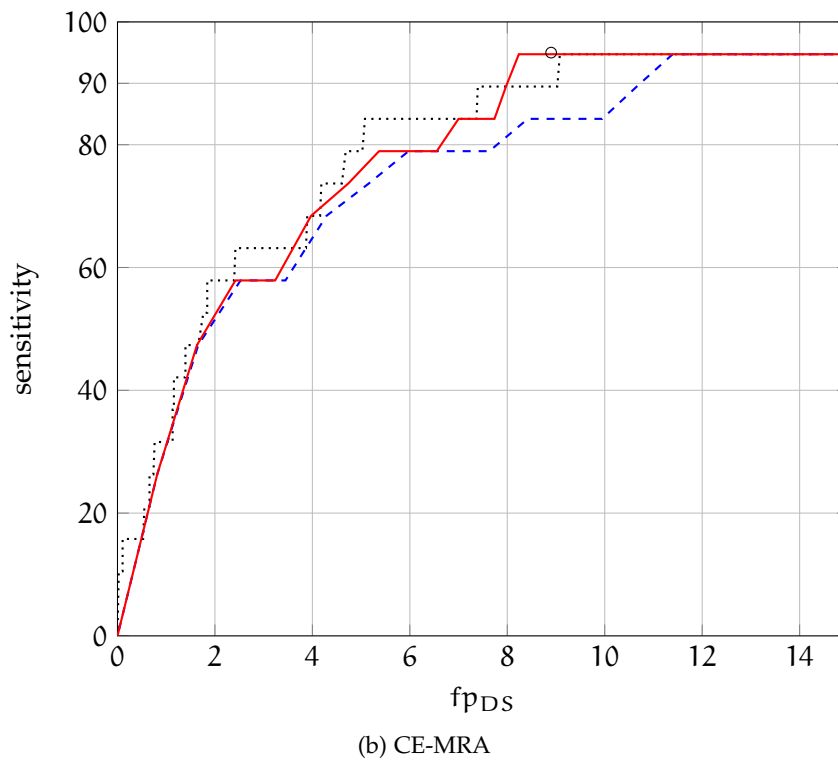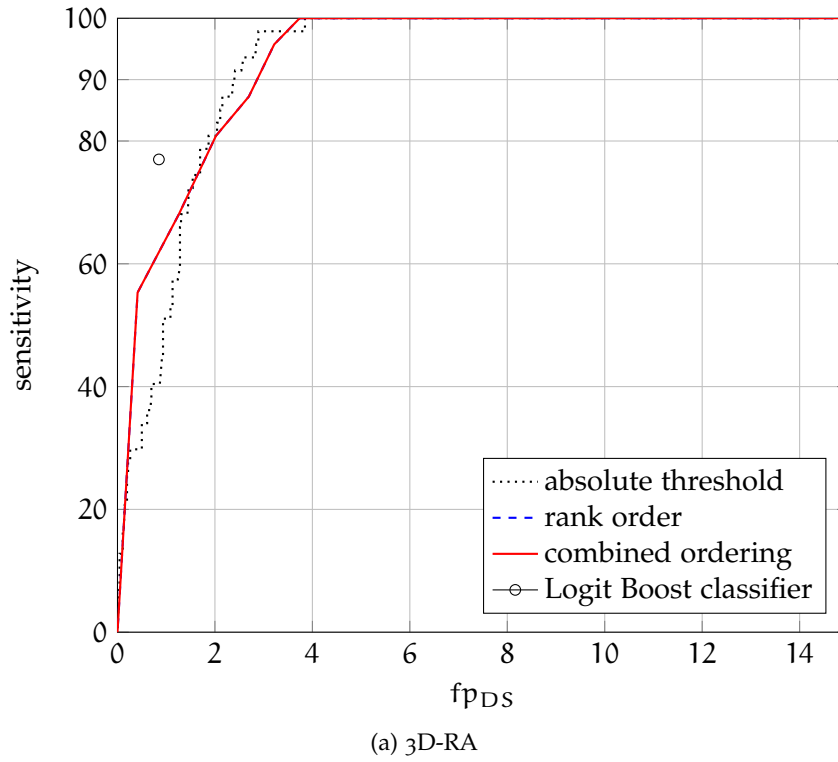
(a) 3D-RA

(b) CE-MRA

Figure 6.18: The average FROC for the three different ordering schemes for (a) 3D-RA and (b) CE-MRA using the W_e parametrization. In (a), the rank order and the combined ordering scheme produce identical results. Additionally, the performance with the best classifier, LogitBoost, is shown as a black circle.
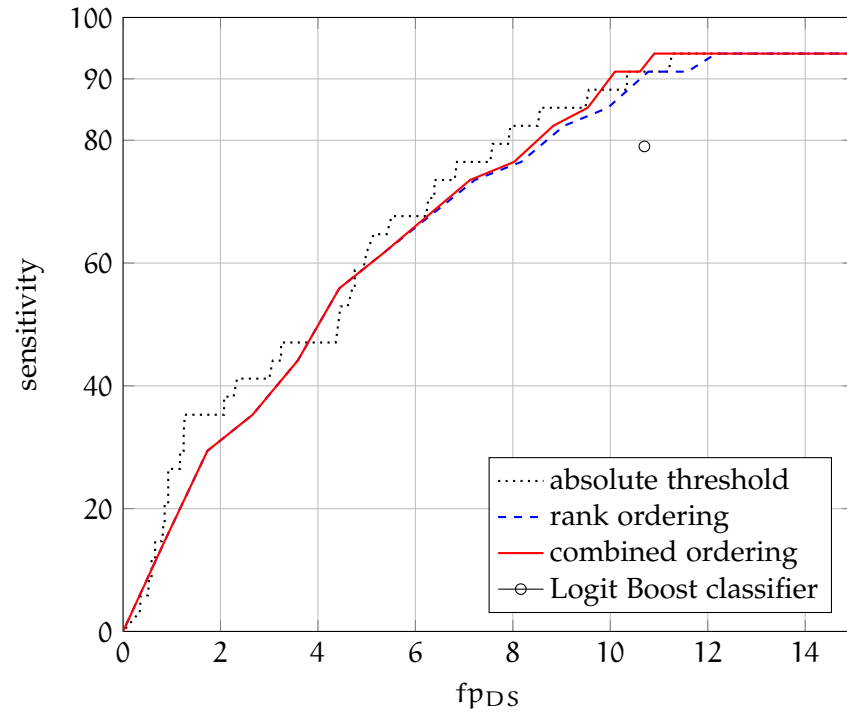
(a) TOF-MRA
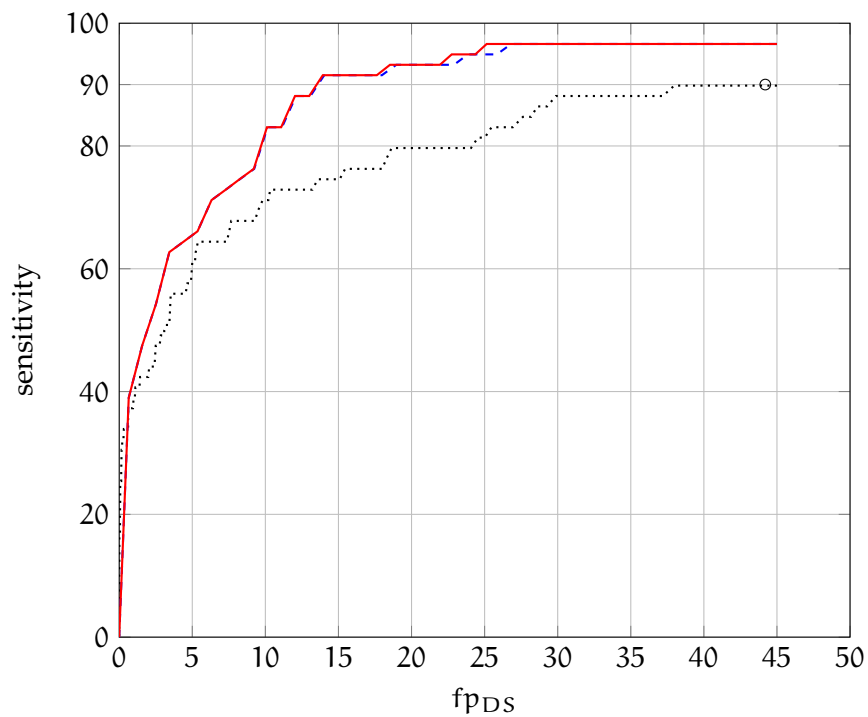
(b) CTA

Figure 6.19: The average FROC for the three different ordering schemes for (a) TOF-MRA
and (b) CTA using the W_e parametrization. In (b), the rank order and the
combined ordering scheme produce almost identical results. Additionally, the
performance with the best classifier, LogitBoost, is shown as a black circle.
Note that the x-axis in (b) is differently scaled than in the other FROC curves.

Table 6.6: Scatterplot for the features b_{avg} and v_{avg} with respect to the classes TP and FP and for all modalities.
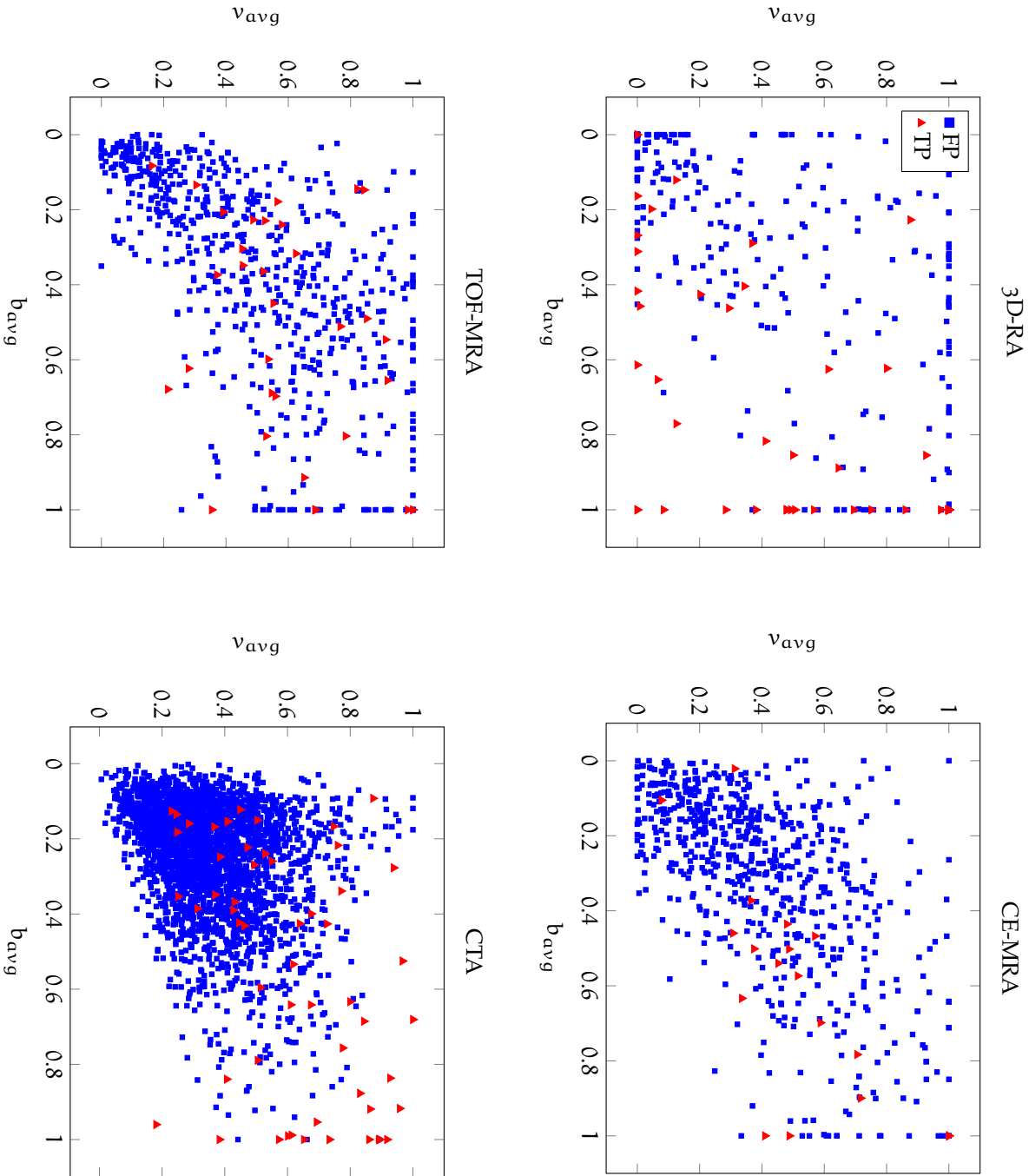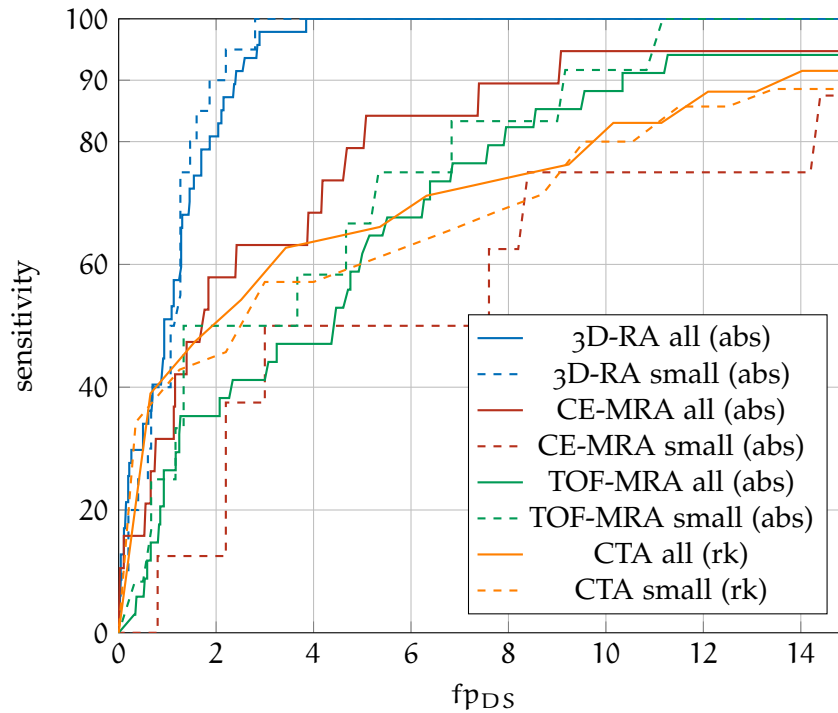
Figure 6.20: The average FROC for the all databases for small aneurysms (diameter $< 5\,\text{mm}$) using the W_e parametrization is shown. The FROC on all data sets are shown for comparison.

distinctly worse. More CE-MRA data sets containing small aneurysms have to be tested to evaluate this result further.

The system detected 82 % of aneurysms (9/11) that were not detected by at least one radiologist who was responsible for the clinical report. Thus, the proposed

The proposed system is able to detect aneurysms that were overlooked by physicians

system is able to reveal previously overlooked aneurysms.

All fusiform aneurysms in the data sets have been found. These were quite large[3] in size (8.6 mm to 54.4 mm).

6.6.2 *Relationship between A and aneurysm features*

The scalar value of $A(c_i)$ may be correlated to aneurysm features such as size or parent vessel location. Therefore, the feature vectors were compared using the

The value of A is related to the vessel location

correlation coefficient[4]. The correlation was high for the CE-MRA database with W_e (0.62) and low with all other databases (0.24 for 3D-RA, 0.04 for TOF-MRA and 0.03 for CTA). Thus, a high A value does usually not imply a large aneurysm size.

The parent vessel location influenced the score value $A(c_i)$ with parametrization W_e. ROI belonging to AComm aneurysms generally had high A values for 3D-RA, CE-MRA and CTA data sets. Almost all aneurysms at this location had a round and regular shape and did fulfill all defined criteria quite well despite that they

---

3 This is related to the definition of the size as the largest lumen diameter. For fusiform aneurysms, the diameter perpendicular to the vessel centerline is more relevant. It is 5.0 mm to 18.8 mm.

4 Two vectors, F_a and A_a, were compared. $F_a = (f_{a1}, \ldots, f_{an})$ denotes the features values $f_{ai}, i = 1, \ldots, n$ of all aneurysm ROI. $A_a = (A(c_1), \ldots, A(c_n))$ represents the A values of the corresponding aneurysm ROI.

had a small size of approximately 5 mm in average. ROI belonging to aneurysms at the ACM had small values in all modalities. The reason might be that the ACM is rather laterally located and that the aneurysms are commonly small. Thus, the defined aneurysm criteria were not fulfilled well and the A value was rather low. Also ROI belonging to aneurysms at ACI locations had usually quite high A values.

6.6.3   *Analysis of FP and FN*

In the next paragraphs, FP ROI and FN ROI are analyzed in detail per modality. The analysis was done at two system parametrizations φ_1 and φ_2. A parametrization may be specified by defining a point on the FROC curve. Either the point having the maximal sensitivity was taken, denoted by φ_1, or the point at $3\,\text{fp}_{DS}$, denoted by φ_2. FN ROI was analyzed with both parametrizations, while FP ROI were only analyzed at φ_2. For the analysis with φ_1 all data sets were taken into account, while for φ_2 only between 4 and 15 randomly chosen data sets were employed.

FN ANALYSIS   The proposed algorithm was able to detect 96.8 % of aneurysms (154/159) overall at parametrization φ_1. Only five aneurysms were never found, i. e., they were FN. The proposed algorithm detected all aneurysms in 3D-RA. One aneurysm was missed in CE-MRA, two aneurysms were missed in TOF-MRA and in CTA, respectively.

In CE-MRA, no ROI was found at the aneurysm position because of a blobness value smaller than the threshold value defined by t. The two missed aneurysms in TOF-MRA were poorly enhanced in the blobness image and thus were also below the threshold. Both aneurysms were small (size of 3.3 mm and 5.2 mm) and were in the direct vicinity of large tortuous vessels. This usually complicates the detection, since these structures also had a high blobness value. In the CTA database, all but one aneurysms were included before the RBS was executed. This aneurysm originated from a data set that contained abnormal high HU values. Some vessels such as the Arteria basilaris had a HU value of >500 in this data set. Consequently, neither the vessel nor the aneurysm at this position were included in the initial mask image that covered values between 150 HU and 375 HU. The RBS excluded another aneurysm in CTA, as the d_{CoW} value for the aneurysmal ROI was erroneously assigned to the background. The registration failed to align this data set to the reference data set. This was the only example in which the registration led to erroneously exclusions of true aneurysm ROI.

Analysis of aneurysms that were not detected by the proposed algorithm

Naturally, more FN occurred at parametrization φ_2 as the sensitivity was considerably smaller than with φ_1. Only one aneurysm could not be found in the selection of 3D-RA data sets. It was quite large, 18.5 mm, but had an ellipsoid shape with a rather irregular surface. Thus, the blobness and the vesselness were low compared with other ROI. Aneurysms were not detected in the selection of CE-MRA at lateral positions, commonly at the ACM and if they were small. In the set of TOF-MRA data sets, the missed aneurysms were excluded especially because of their small volume, small blobness value or small aneurysm probability occurrence value. This led to a low A value and the ROI were excluded. In the CTA selection, no clear grouping of TN could be done as the aneurysms had different sizes, locations and properties.

FP ANALYSIS   Below, FP are analyzed with parametrization φ_2 and the selected example data sets. One example of a 3D-RA data set can be found in Figure 6.21. FP occurred most notably at bifurcations and at the ACI where the vessel had lot of twists and a high curvature. Furthermore, the ACI is located centrally in the data set. Therefore, the aneurysm criteria formulated in Section 5.8 were fulfilled as a high blobness value, a high vesselness value and a medial position were present in these ROI.

The selected CE-MRA data sets had similar behavior than the 3D-RA data sets. An example is shown in Figure 6.22. FP occurred at similar locations.

False positive ROI commonly occurred at bifurcations and tortuous vessel segments

Also, in the selection of TOF-MRA data sets a frequent appearance of FP at ACI locations with a high curvature could be observed (an example is shown in Figure 6.23). However, FP appeared less frequently at bifurcation positions.

The most challenging modality for aneurysm detection was CTA. This was proven by the analysis (see Figure 6.24 for an example data set). The analysis of FP ROI in CTA led to the following insights:

- 32 % of FP were located in bony structures or at the border from bone to other matter.

- 50 % of FP were located at vessels of the Circle of Willis.
    - location at bifurcations
        * 19 % of vessel FP were located at bifurcations.
    - location at vessels
        * 30 % of vessel FP were located at ACI locations, especially at locations having a high tortuosity.
        * 30 % of vessel FP were located at the posterior circulation.
        * 21 % of vessel FP were located at the ACM.
        * 12 % of vessel FP were located at the ACA and AComm locations.
        * 7 % of vessel FP were located at other Circle of Willis locations.

- 18 % of FP were located elsewhere (including vessels outside the Circle of Willis)

The amount of FP that were at the posterior circulation was too high as aneurysms occur only relatively seldom at this location (about 16 %) compared to the anterior circulation. Remarkably, only 10 % of FP occurred outside the Circle of Willis and simultaneously were not within bone. Thus, the RBS system eliminated the majority of irrelevant ROI. The FP characteristics in CTA were different than in the other modalities. More FP occurred at bifurcations and less FP occur at tortuous vessel locations.

32 % of FP in CTA have been found in bony structures. With the broader employment of dual-energy CT devices, these FP would vanish. The system then would achieve the same quality in CTA and TOF-MRA (approximately a $FP_{0.9}$ value of 10 fp_{DS}).

Thus, two large groups of FP were found across all modalities: bifurcations and tortuous vessel locations, mostly at the ACI. For CTA, FP at bony structures form a

| | A (rk) | | |
	W_e	W_t	W_{te}
🔴	**0.76 (1)**	**0.42 (2)**	**0.48 (2)**
🟠	0.52 (2)	0.07 (8)	0.23 (6)
🟡	0.49 (3)	0.69 (1)	0.53 (1)
🟢	0.47 (4)	0.23 (6)	0.16 (8)
⚪	0.39 (5)	0.33 (4)	0.33 (5)
🔵	0.36 (6)	0.27 (5)	0.34 (4)
🔵	0.36 (7)	0.39 (3)	0.39 (3)

(a)   (b)
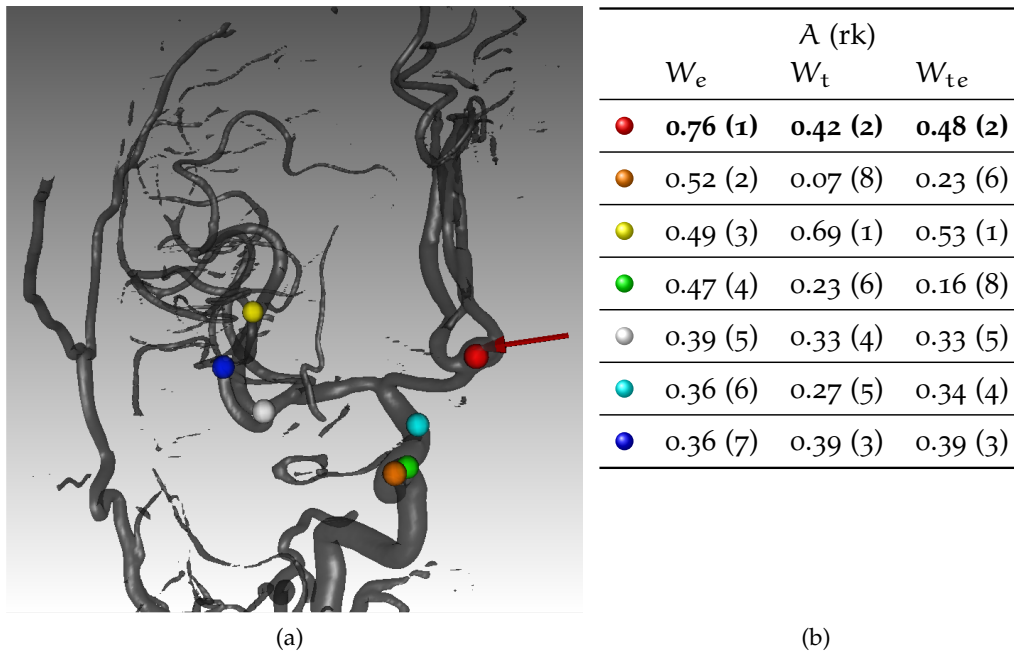
Figure 6.21: (a) Result of the proposed system on an exemplary 3D-RA data set with CA injection in the right ACI. The ROI centers are marked as colored spheres. The aneurysm position is indicated by a red arrow. (b) The values for each corresponding ROI (differentiated by the color of the spheres) for A and rk are given for each ROI and each weighting. TP are printed bold.

| | A (rk) | | |
	W_e	W_t	W_{te}
🔴	0.61 (1)	0.16 (3)	0.12 (1)
🟠	0.59 (2)	0.17 (2)	0.11 (2)
🟡	0.59 (3)	0.10 (8)	0.07 (6)
🟢	0.57 (4)	0.15 (4)	0.09 (3)
FN	*0.56 (5)*	*0.17 (1)*	*0.07 (5)*

(a)   (b)
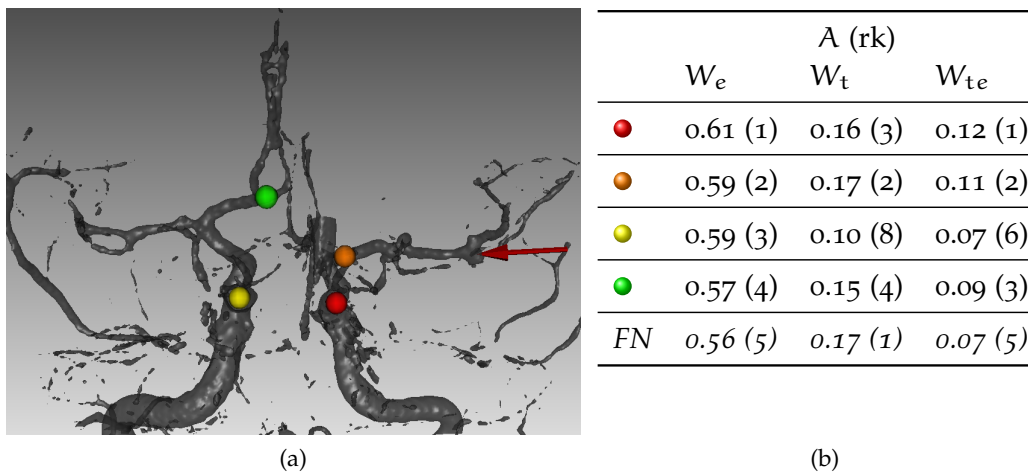
Figure 6.22: (a) Result of the proposed system on an exemplary CE-MRA data set. The ROI centers are marked as colored spheres. The aneurysm position is indicated by a red arrow. (b) The corresponding values for A and rk are given for each ROI and each weighting. FN are printed italic.

| | A (rk) | | |
	W_e	W_t	W_{te}
🔴	0.72 (1)	-0.05 (12)	0.10 (2)
🟠	0.65 (2)	0 (8)	0.06 (10)
🟡	**0.61 (3)**	**0.08 (3)**	**0.10 (3)**
🟢	0.60 (4)	-0.09 (16)	0.11 (1)
⚪	0.59 (5)	-0.04 (7)	0.05 (12)
🔵	0.56 (6)	-0.04 (11)	0.08 (4)

(a) (b)
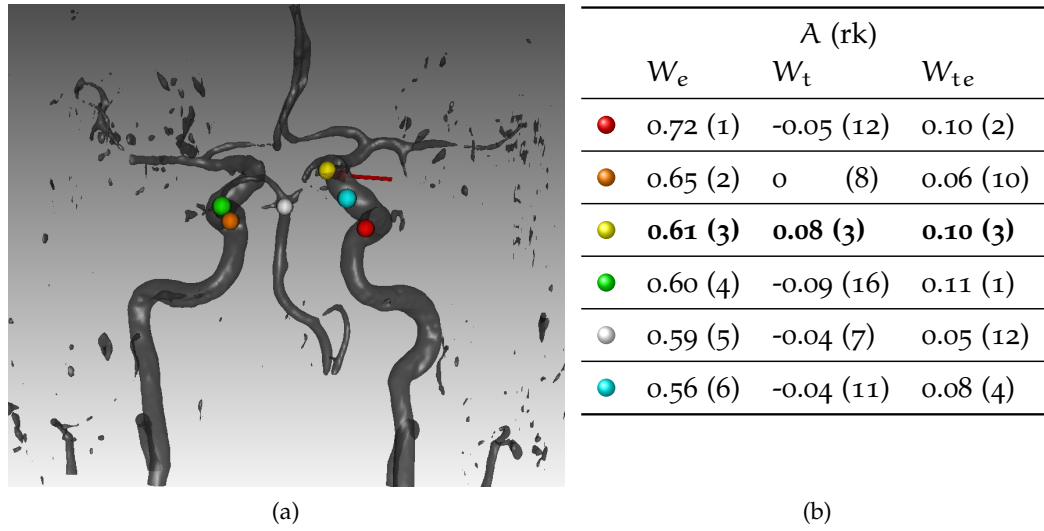
Figure 6.23: (a) Result of the proposed system on an exemplary TOF-MRA data set. The ROI centers are marked as colored spheres. The aneurysm position is indicated by a red arrow. (b) The corresponding values for A and rk are given for each ROI and each weighting. TP are printed bold.

| | A (rk) | | |
	W_e	W_t	W_{te}
🔴	0.62 (1)	0.06 (30)	0.05 (26)
🟠	0.62 (2)	0.06 (24)	0.05 (22)
🟡	**0.61 (3)**	**0.15 (1)**	**0.07 (10)**
FN	*0.55 (13)*	*0.1 (4)*	*0.04 (41)*

(a) (b)
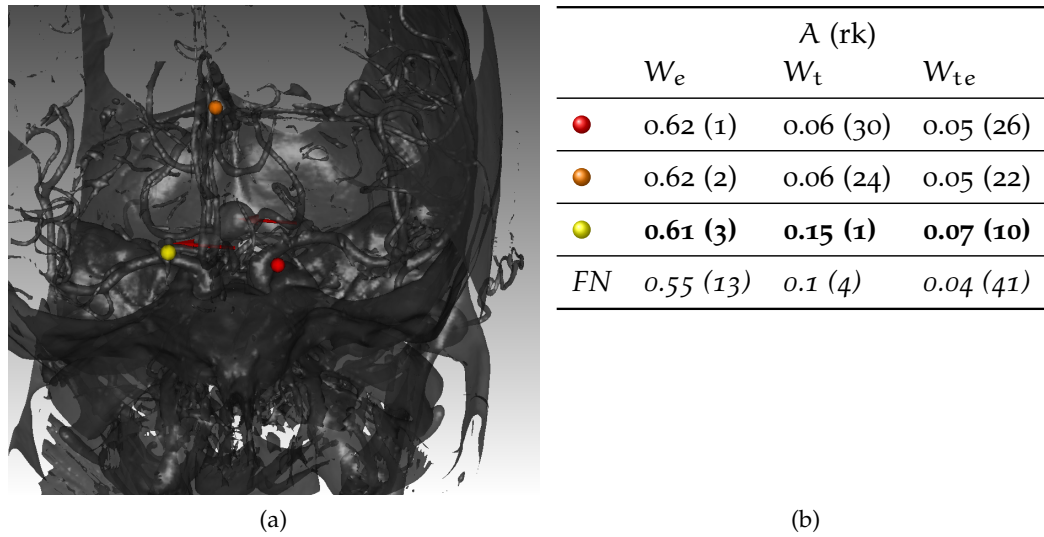
Figure 6.24: (a) Result of the proposed system on an exemplary CTA data set. The data set is cropped on the borders to visualize vessels inside the skull. The ROI centers are marked as colored spheres. The aneurysm positions are indicated by a red arrow. (b) The corresponding values for A and rk are given for each ROI and each weighting. TP are printed bold, FN are printed italic.

third group which fail to differentiate between vessels and bone by the HU value. Thus, these FP comply well with the defined aneurysm characteristics.

Another interesting observation was that FP commonly occur at similar positions at both sides of the vascular system, especially for MRA data sets. The vascular system of healthy people is symmetric, as a sagittal mirror axis can be found at the middle of the head. Thus, if a ROI is found by the proposed system at the first bifurcation of the left ACM, this is commonly also the case for the right ACM. This is especially the case for the tortuous segment of the left and right ACI. In the example visualizations (Figures 6.22 and 6.23) however the symmetry is not observable, as only the ROI having the highest A values are shown.

If the HU window for contrast-enhanced vessels of a CTA data set is not in the predefined range, this leads to undetected aneurysms. However, this only occurred once in our database. Also, as the HU values are standardized and absolute, this is a technical calibration problem of the scanner and the CA injection and is no limitation of the proposed system.

The intensity overlap between vessels and bone is the largest problem in CTA data sets. This problem is solved hardware-sided by dual-energy CT devices [Kalender, 2011].

6.6.4 *Unusual results*

The different performance of the absolute thresholding and rank order thresholding in CTA needs reflection (see Figure 6.10). With all other modalities the differences of both ordering schemes were negligible. There are different explanations for this phenomenon. In CTA the number of ROI per data set was larger and also has a higher variability than in other modalities. In CTA data sets the average amount of ROI in the set C_1 was 113 ± 56, for TOF-MRA it was 16 ± 6. Thus, the A values have a higher variability per data set than in the other modalities. A related explanation might be that the feature distributions have a higher variance per data set. Thus, a rank ordering leads to an implicit normalization of the feature values and consequently also the A values. However, no large differences were observable between the different modalities in the feature distributions visualized by scatterplots in Tables 6.6, A.15 and A.16.

The experiments have shown that the expert parametrization with W_e led to similar or better results than the trained parametrization with W_t (see Figure 6.11). This is unusual as W_e is a static parametrization, while W_t is a dynamic parametrization and relies on data observation. One possible explanation is the *curse of dimensionality* [Houle et al., 2010]. W_t was trained in an 18-dimensional feature space. Only a sparse sampling of the feature distributions can be done as the number of training samples is too small. Feature selection could solve this problem. Indeed, the results with the W_{te} parametrization were similar in comparison to the W_e parametrization, especially if one considers the influence of the cross-validation (see Figure 6.11).

It is difficult to compare the performance of the tested State of the Art classifiers to the results with the LDF. The classifiers were not tested independently of the parametrization and thus, no FROC could be determined. Instead, the default setting of Weka was used for each classifier. Although small tests revealed that this

parametrization is relatively robust, further tests have to be done for a conclusive statement. With the default parametrization, LogitBoost was the classifier leading to the best performance. Compared with the FROC curve using the LDF and the trained parametrization W_t, the performance was slightly better for 3D-RA and CE-MRA and equal for TOF-MRA and CTA (see Section 6.5.5). Thus, the potential of non-linear classifiers was shown and is at least similar to the quality of the linear discriminant function.

The performance of the TOF-MRA database differed largely with respect to the other databases. Especially compared to the related CE-MRA database, the performance was distinctly worse. The reason might be the large differences between folds. The folds were constructed randomized, but by chance one fold contained many data sets acquired with a different device than in the other folds. Thus, the image characteristics changed significantly and also the feature distributions for TP and FP were different. In experiments on all data sets, the quality with the trained parametrization W_t increased considerably. The results acquired with the parametrizations W_e and W_{te} were approximately the same if one considers the large influence of the cross-validation (see Figure 6.11).

6.7 COMPARISON WITH EXISTING METHODS

The comparison with other methods is no trivial task as one compares apples with oranges. The proposed method has another focus than the existing methods. The major differences are that the proposed method:

- does not require explicit vessel segmentation,

- is multi-modality capable,

- has only a small dependence on a database and

- was evaluated on a database containing more samples than all other methods except for [Yang et al., 2011].

Compared to other algorithms that are specialized for TOF-MRA, the proposed method has a smaller AUC value[5]. However, it reaches similar results as [Yang et al., 2011] for the relevant sensitivity range of $> 90\%$ (see Figure 6.25). Two other methods [Arimura et al., 2006; Uchiyama et al., 2008] present better results than the proposed method.

The only other algorithm that is able to process data sets of multiple modalities was evaluated with only ten data sets for each modality [Lauric et al., 2010]. Therefore, a comparison has to be drawn very carefully. For 3D-RA 100% sensitivity at 0.7 fp_{DS} was reported and for MRA 100% sensitivity at 5.7 fp_{DS} was achieved. For CTA 100% sensitivity at 5.4 fp_{DS} has been reported. Thus, the method of [Lauric et al., 2010] achieves better results than the proposed method. However, the method requires a manual bone-removal for CTA data sets and a segmentation of the data sets.

---

5 The AUC of other algorithms is computed based on the FROC that is given in the respective publications.
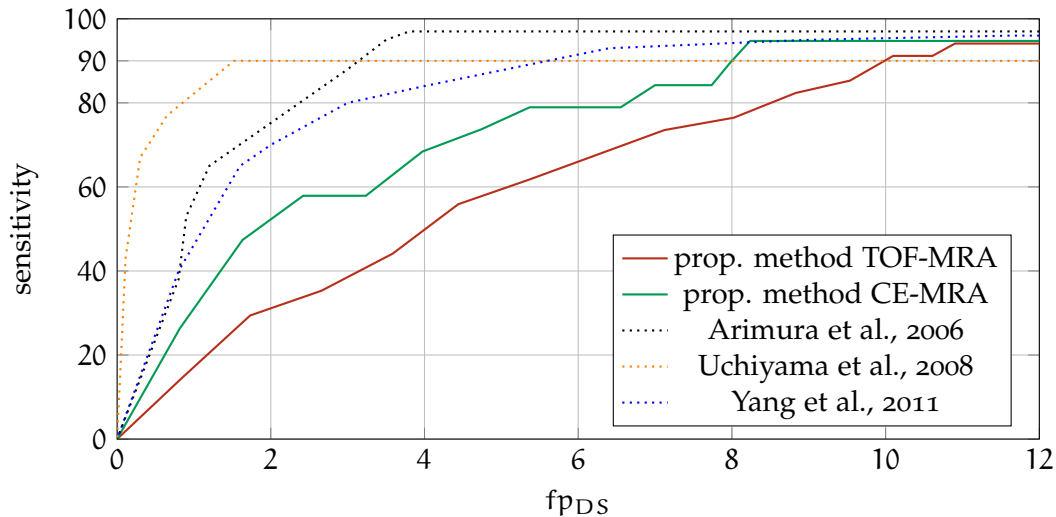
Figure 6.25: FROC for the proposed method compared with the existing aneurysm detection methods for TOF-MRA and CE-MRA ([Arimura et al., 2006], [Uchiyama et al., 2008] and [Yang et al., 2011]). Only methods that were tested with an adequate amount of testing data sets were included.

Despite the fact that other methods achieved better results for single modalities, the proposed method has its value besides the multi-modality ability. It is able to find saccular and fusiform aneurysms. All other methods except for [Yang et al., 2011] have problems detecting fusiform aneurysms.

Also, the sensitivity with respect to small aneurysms is convincing in the proposed system. In comparison to [Yang et al., 2011], where 91 % of small aneurysms were found, the proposed system is able to detect 95 % of small aneurysms. The only constraint of our method with respect to the data sets is that the acquired volume should include at least the Circle of Willis and at most an area of the whole head.

A major disadvantage of existing methods is that they require a fairly large amount of (manual) pre-processing. A manual bone removal for CTA data sets is required in [Lauric et al., 2010], vessel segmentation is required in all existing methods (cf. Section 4.3) and skeleton-based approaches require additionally the skeleton, where bifurcation points and endpoints have to be labeled [Arimura et al., 2006; Lauric et al., 2010; Hassan et al., 2011; Suniaga et al., 2012].

In contrast, the proposed method relies on no segmentation and needs no bone-removal. The only constraint is that the data sets have an acquired volume that includes at least the Circle of Willis and at most the whole head.

SUMMARY AND FUTURE WORK

A system for cerebral aneurysm detection in multi-modality angiographic data sets was presented in this thesis. The system is able to process data sets of four angiographic types, 3D-RA, CE-MRA, TOF-MRA and CTA. These modalities are heterogeneous with respect to the image and aneurysm characteristics. The goal to implement a system that does not depend on vessel segmentation and that does not require user interaction was reached.

The workflow of the system is parametrizable to work with all four modalities. First, initial regions of interest are found by enhancing sphere-like structures using a multi-scale filtering approach. Low-level and high-level features are computed on the regions of interest. These are intensity-based features, shape-based features and location-based features that evaluate the location with respect to a normalized coordinate system. For the latter, a registration to a model data set is performed and a probability atlas is constructed. These methods are able to replace vessel segmentation information.

Two algorithms are used subsequently to eliminate false positives: a rule-based system and a classification method. The rule-based system operates based on modality characteristics and empirically-found rules. As classification method either a linear discriminant function or non-linear state-of-the-art classifiers were employed. The linear discriminant function can be parametrized either by medical experts or by training.

The system was thoroughly evaluated on 197 clinical patient data sets containing all four previously mentioned modalities. All data sets of a modality form an evaluation database. The ground truth consisting of number and position of aneurysms were given by experienced neuroradiologists.

In the evaluation, it was found that the expert parametrization lead to slightly better results for most modalities than the trained parametrization. Thus, it was shown that the dependence of a method on a training database can be reduced by incorporating expert knowledge. For all modalities except CTA, more than 90 % of aneurysms could be detected with an average amount of false positives per data set below 11. Thus, the initially defined quality goal could be achieved for these modalities. The average amount of false positives was 2.41 for 3D-RA, 9.07 for CE-MRA and 10.3 for TOF-MRA. In case of CTA, this quality is reached with 14.03 false positives per data set on average.

The following contributions were made in the thesis. A thorough State of the Art in aneurysm detection is given. The existing approaches are presented and their quality is evaluated. No survey publication about this topic exists yet. Additionally, existing computer-aided methods for aneurysm management are summarized and the effects on the clinical workflow are shown. Their aim is to assist radiologists in treatment decision by providing a reliable scanning for aneurysms, a rupture risk estimation and a quantitative comparison of different treatment options.

The proposed system is the first one published that is designed and tested for more than two types of angiographic data sets. It includes a parametrizable workflow that accounts for the different image and aneurysm characteristics. The system is either parametrized by experts or by learning, making it adaptable to particular requirements.

The system has a modular design; each part can be substituted without affecting the functionality. This was important as several variants for algorithm parts exist. The variants are compared with respect to their performance in the evaluation. The modular approach also simplifies future extensions of the system.

CAD systems commonly rely on segmentation methods to define the object of interest. In the proposed approach, the segmentation has been replaced by multi-scale filtering and registration. The advantage is that these techniques do not need to be perfectly accurate to achieve good results in contrast to the segmentation. Small changes in the input do not lead to largely different results of the detection system.

By defining a standardized vessel reference system for each modality, a probability atlas can be created. The atlas determines the aneurysm occurrence probability for each vessel location. The mapping of the data sets to the reference system is done by registration. The system makes use of the probability atlas as aneurysms mostly occur at certain locations.

7.1 FUTURE WORK

Future improvements of the proposed CAD system are possible and are briefly outlined in this section.

The quality of a CAD system should be evaluated on a large database, preferably incorporating a large amount of heterogeneous data sets. The database in the present thesis is already quite large. However, by evaluating the proposed system on a broad database containing images from multiple scanner types and hospitals, the quality of the system could be measured more precisely. Furthermore, the quality and validity of the probability atlas increases with the amount of data sets containing aneurysms in the database. Also the image resolution could have an influence on the quality of the system. This has to be evaluated systematically.

The benefit of the probability atlas depends on the quality of the registration. The quality can be further improved by using non-rigid registration methods or by employing specific registration methods that were successfully tested in vessel applications [Chillet et al., 2003; Bullitt et al., 2005].

In the current state, the system is parametrized either by an expert or by training. An alternative would be a hybrid approach. The amount of influence of each part could depend on the sample size in the database. The larger the database, the greater could the influence of the trained parametrization be weighted. If no or only few data sets are available for training, the expert parametrization could be emphasized.

The majority of false positives occur at bifurcations and tortuous vessel segments. Thus, the system could be improved by eliminating these types of false positives. Algorithms to detect bifurcation have been proposed and could be employed that

rely on centerline detection [Zhang et al., 2005] and standard moments [Fotin et al., 2010].

Especially for CTA data sets, the amount of false positives should be reduced for the use in a clinical environment. A further preprocessing of the data sets is required to reliably reduce the initial amount of false positives in CTA. For this purpose, CTA masking could employ additional features like vesselness to suppress other irrelevant structures. However, the effect of data sets acquired with dual energy CT scanners has to be investigated. A smaller amount of false positives is likely.

An information that could be suitable for false-positive reduction in MRA and CTA is the symmetry of the vessel system. ROI emerge commonly at symmetrical locations having similar feature values. Symmetrical ROI that have similar feature vectors could be removed. Symmetrical aneurysms occur, however, it is very unlikely that their feature values resemble.

The major property of the proposed system is the ability to process data sets of four different modalities. This ability could be further exploited if multiple data sets of the same patient having different modalities acquired within a short time interval are available. The result of each data set could be mapped to a common reference vessel system for all modalities. Then, ROI at similar positions could be joined and the remaining ROI form a common result. Depending on the quality of a data set, modality characteristics and A values of each ROI, the results for each modality could be joined to create a common result.

To show the improvements of a CAD system, it is necessary to test the algorithm in a clinical environment with unknown cases. A reader study with and without the CAD system is required to measure how the detection rate of radiologists is affected using the proposed system. In this context, not only the output of such a system, the location of aneurysm candidates, but also their visualization is important and both aspects have to be regarded.

In conclusion, the large potential of CAD systems in cerebral aneurysm management was shown. A step towards better patient-specific diagnosis and treatment of cerebral aneurysms has been made.

A

APPENDIX

The last part of this thesis is the appendix. All evaluation measures for all experiments are listed in the following tables. See Section 6.4 and Section 6.5 for the description of the respective experiments.

The best measure for each database and measure is printed bold. The value "-" in the $FP_{0.9}$ column means that no sensitivity of 90 % or more was reached.

Table A.1: Pilot experiment to the robustness of blobness parameters computed with Frangi's method on a subset of the CE-MRA database.

Parameter	Value	AUC	$FP_{0.9}$	s_{10}
$[r_{min}, r_{max}]$	[0.25 mm, 2.5 mm]	0.778	-	**0.867**
$[r_{min}, r_{max}]$	[0.5 mm, 5 mm]	0.761	-	**0.867**
$[r_{min}, r_{max}]$	[1 mm, 10 mm]	0.788	-	**0.867**
$[r_{min}, r_{max}]$	[2 mm, 20 mm]	**0.792**	-	**0.867**
N	3	0.764	-	0.844
N	5	0.805	-	**0.889**
N	6	**0.812**	-	**0.889**
N	8	0.757	-	0.844

Table A.2: The robustness of blobness parameters computed with Frangi's method are evaluated.

Parameter	Value	Database	AUC	$FP_{0.9}$	s_{10}
$[r_{min}, r_{max}]$	[0.5 mm, 5 mm]	CE-MRA	**0.786**	**9.08**	**0.905**
$[r_{min}, r_{max}]$	[1 mm, 10 mm]	CE-MRA	0.775	-	0.884
$[r_{min}, r_{max}]$	[0.5 mm, 5 mm]	TOF-MRA	**0.689**	**10.34**	**0.835**
$[r_{min}, r_{max}]$	[1 mm, 10 mm]	TOF-MRA	0.573	-	0.682
$[r_{min}, r_{max}]$	[0.5 mm, 5 mm]	CTA	**0.608**	**48.53**	**0.692**
$[r_{min}, r_{max}]$	[1 mm, 10 mm]	CTA	0.456	-	0.508
γ	5	CE-MRA	0.727	-	0.842
γ	10	CE-MRA	**0.775**	**9.58**	**0.895**
γ	20	CE-MRA	**0.775**	**9.58**	**0.895**

Table A.3: The robustness of blobness parameters computed with Li's method are evaluated.

Parameter	Value	Database	AUC	$FP_{0.9}$	s_{10}
$[r_{min}, r_{max}]$	[0.5 mm, 5 mm]	TOF-MRA	**0.666**	-	**0.821**
$[r_{min}, r_{max}]$	[1 mm, 10 mm]	TOF-MRA	0.570	-	0.686

Table A.4: The robustness of the blobness peak extraction depending on the threshold parameter t is evaluated.

Parameter	Value	Database	AUC	$FP_{0.9}$	s_{10}
t	5	3D-RA	0.887	3.63	0.970
t	10	3D-RA	0.908	4.00	0.991
t	15	3D-RA	0.907	3.11	0.996
t	20	3D-RA	0.914	2.70	0.996
t	25	3D-RA	**0.927**	2.41	**1.000**
t	30	3D-RA	0.907	2.96	0.979
t	35	3D-RA	0.923	2.30	0.979
t	40	3D-RA	0.896	**2.07**	0.936
t	5	CE-MRA	0.773	10.21	0.884
t	10	CE-MRA	0.767	9.24	0.884
t	15	CE-MRA	**0.786**	9.08	**0.905**
t	20	CE-MRA	0.739	-	0.832
t	25	CE-MRA	0.764	-	0.832
t	5	TOF-MRA	0.564	33.46	0.665
t	10	TOF-MRA	0.612	20.10	0.753
t	15	TOF-MRA	0.595	14.68	0.730
t	20	TOF-MRA	**0.689**	**10.34**	**0.835**
t	25	TOF-MRA	0.661	-	0.8
t	5	CTA	0.493	95.43	0.569
t	10	CTA	0.532	57.00	0.610
t	15	CTA	**0.559**	**47.47**	**0.634**
t	20	CTA	0.553	-	0.607
t	25	CTA	0.536	-	0.597

Table A.5: The robustness of the d_{CoWmax}, maximal distance to the nearest vessel, is evaluated. The rank ordering ordering scheme is chosen.

Parameter	Value	Database	AUC	$FP_{0.9}$	s_{10}
d_{CoWmax}	5	CTA	0.495	-	0.566
d_{CoWmax}	10	CTA	0.607	31.57	0.705
d_{CoWmax}	15	CTA	0.573	22.04	0.725
d_{CoWmax}	20	CTA	**0.637**	**14.03**	**0.807**

Table A.6: The robustness of the a, directly related to d_{cmax}, maximal distance to the center of the image of a ROI, is evaluated.

Parameter	Value	Database	Ordering	AUC	$FP_{0.9}$	s_{10}
a	1.05	CE-MRA	abs	**0.801**	**8.18**	**0.916**
a	1.1	CE-MRA	abs	0.795	8.68	**0.916**
a	1.15	CE-MRA	abs	0.786	9.45	0.895
a	1.17	CE-MRA	abs	0.786	9.08	0.905
a	1.2	CE-MRA	abs	0.779	9.92	0.895
a	1.05	CE-MRA	rk	0.733	11.29	0.863
a	1.1	CE-MRA	rk	0.728	11.53	0.853
a	1.15	CE-MRA	rk	0.727	11.61	0.853
a	1.17	CE-MRA	rk	0.735	11.39	0.863
a	1.2	CE-MRA	rk	0.728	11.62	0.853

Table A.7: Three different mask computation variants for CTA data sets have been tested.

Variant	Ordering	Parameter	AUC	$FP_{0.9}$	s_{10}
Thresholding	abs	-2048 outside value	0.608	48.53	0.692
Thresholding	rk	-2048 outside value	**0.637**	**14.03**	**0.807**
Thresholding	abs	0 outside value	0.554	61.03	0.614
Thresholding	rk	0 outside value	0.622	26.83	0.783
Double thresholding[a]	abs	unmasked	0.460	-	0.502
Double thresholding[a]	rk	unmasked	0.470	-	0.576

[a] In contrast to the other experiments, where t = 0.12 has been set, these experiments were done with t = 0.07. The results achieved with t = 0.12 were worse.

Table A.8: Results that were achieved by omitting p_A, p_{FP} and d_{CoW}. Results achieved with these features are shown for comparison. Additionally, the results are given with the two ordering schemes.

Variant	Ordering	Database	AUC	$FP_{0.9}$	s_{10}
with features	abs	CE-MRA	**0.786**	**9.08**	**0.905**
with features	rk	CE-MRA	0.735	11.39	0.863
without features	abs	CE-MRA	0.673	15.89	0.779
without features	rk	CE-MRA	0.642	16.92	0.789
with features	abs	TOF-MRA	**0.689**	**10.34**	**0.835**
with features	rk	TOF-MRA	0.662	10.78	0.835
without features	abs	TOF-MRA	0.639	12.98	0.782
without features	rk	TOF-MRA	0.634	13.35	0.8
with features	abs	CTA	0.608	48.53	0.692
with features	rk	CTA	**0.637**	**14.03**	**0.807**
without features	abs	CTA	0.446	69.58	0.488
without features	rk	CTA	0.541	45.88	0.661

Table A.9: W_t trained across all modalities.

Variant	Ordering	Database	AUC	$FP_{0.9}$	s_{10}
across all modalities	abs	CE-MRA	0.730	16.50	0.821
across all modalities	rk	CE-MRA	0.681	13.84	0.800
across one modality	abs	CE-MRA	0.789	10.56	0.895
across one modality	rk	CE-MRA	0.776	9.89	0.905
across all modalities	abs	TOF-MRA	0.557	12.95	0.712
across all modalities	rk	TOF-MRA	0.556	13.95	0.724
across one modality	abs	TOF-MRA	0.543	10.55	0.665
across one modality	rk	TOF-MRA	0.568	13.93	0.718
across all modalities	abs	CTA	0.441	62.51	0.525
across all modalities	rk	CTA	0.499	36.54	0.641
across one modality	abs	CTA	0.466	68.21	0.532
across one modality	rk	CTA	0.565	45.17	0.708

Table A.10: Experiments where the the LDF is parametrized with W_e, W_t and with W_{te}.

Variant	Ordering	Database	AUC	$FP_{0.9}$	s_{10}
W_e	abs	3D-RA	0.927	**2.41**	**1**
W_e	rk	3D-RA	**0.927**	3.22	**1**
W_t	abs	3D-RA	0.896	3.52	0.957
W_t	rk	3D-RA	0.887	3.93	0.957
W_{te}	abs	3D-RA	0.887	3.65	0.957
W_{te}	rk	3D-RA	0.886	3.93	0.957
W_e	abs	CE-MRA	0.786	9.08	0.905
W_e	rk	CE-MRA	0.735	11.39	0.863
W_t	abs	CE-MRA	0.789	10.56	0.895
W_t	rk	CE-MRA	0.776	9.89	0.905
W_{te}	abs	CE-MRA	0.814	11.13	0.905
W_{te}	rk	CE-MRA	**0.816**	**5.92**	**0.937**
W_e	abs	TOF-MRA	**0.689**	**10.34**	**0.835**
W_e	rk	TOF-MRA	0.662	10.78	**0.835**
W_t	abs	TOF-MRA	0.543	10.55	0.665
W_t	rk	TOF-MRA	0.568	13.93	0.718
W_{te}	abs	TOF-MRA	0.62	11.13	0.765
W_{te}	rk	TOF-MRA	0.638	12.18	0.824
W_e	abs	CTA	0.608	48.53	0.692
W_e	rk	CTA	**0.637**	**14.03**	**0.807**
W_t	abs	CTA	0.466	68.21	0.532
W_t	rk	CTA	0.565	45.17	0.708
W_{te}	abs	CTA	0.548	55.19	0.634
W_{te}	rk	CTA	0.576	21.92	0.746

Table A.11: Results that were achieved by omitting the RBS. Results achieved with the RBS are shown for comparison. Additionally, the results are given with the two ordering schemes.

Variant	Ordering	Database	AUC	$FP_{0.9}$	s_{10}
with RBS	abs	3D-RA	0.927	**2.41**	**1**
with RBS	rk	3D-RA	**0.927**	3.22	**1**
without RBS	abs	3D-RA	0.915	2.87	**1**
without RBS	rk	3D-RA	0.916	3.5	**1**
with RBS	abs	CE-MRA	**0.786**	**9.08**	**0.905**
with RBS	rk	CE-MRA	0.735	11.39	0.863
without RBS	abs	CE-MRA	0.450	34.45	0.558
without RBS	rk	CE-MRA	0.528	24.79	0.695
with RBS	abs	TOF-MRA	**0.689**	**10.34**	**0.835**
with RBS	rk	TOF-MRA	0.662	10.78	**0.835**
without RBS	abs	TOF-MRA	0.398	46.68	0.465
without RBS	rk	TOF-MRA	0.365	48.17	0.471
with RBS	abs	CTA	0.608	48.53	0.692
with RBS	rk	CTA	**0.637**	**14.03**	**0.807**
without RBS	abs	CTA	0.291	324.91	0.332
without RBS	rk	CTA	0.288	162.28	0.353

Table A.12: Experiments with single features as score values. The results are computed with the ordering schemes leading to the optimal quality.

Feature	Ordering	Database	AUC	$FP_{0.9}$	s_{10}
A	abs	3D-RA	0.927	2.41	**1**
s	abs	3D-RA	**0.932**	**1.83**	0.979
b_{avg}	abs	3D-RA	0.867	3.54	0.979
b_{max}	abs	3D-RA	0.880	3.28	0.979
A	abs	CE-MRA	**0.786**	**9.08**	**0.905**
s	abs	CE-MRA	0.735	12.21	0.884
b_{avg}	abs	CE-MRA	0.658	12.11	0.821
b_{max}	abs	CE-MRA	0.732	11.34	0.863
Ψ	abs	CE-MRA	0.753	14.45	0.863
A	abs	TOF-MRA	**0.689**	**10.34**	**0.835**
s	abs	TOF-MRA	0.456	13.07	0.759
b_{avg}	abs	TOF-MRA	0.509	14.37	0.659
b_{max}	abs	TOF-MRA	0.523	13.44	0.682
Ψ	abs	TOF-MRA	0.617	14.29	0.747
A	rk	CTA	**0.637**	**14.03**	**0.807**
s	rk	CTA	0.412	43.14	0.542
b_{avg}	rk	CTA	0.440	49.49	0.566
b_{max}	rk	CTA	0.412	43.14	0.542
Ψ	rk	CTA	0.312	66.49	0.417

Table A.13: Experiments with normalized single features as score values.

Feature	Ordering	Database	AUC	FP$_{0.9}$	s$_{10}$
A	abs	3D-RA	**0.927**	**2.41**	**1**
s	abs	3D-RA	0.920	3.32	0.979
b_{avg}	abs	3D-RA	0.914	3.04	0.979
b_{max}	abs	3D-RA	0.915	3.28	0.979
A	abs	CE-MRA	**0.786**	**9.08**	**0.905**
s	abs	CE-MRA	0.655	13.71	0.800
b_{avg}	abs	CE-MRA	0.730	16.92	0.853
b_{max}	abs	CE-MRA	0.730	16.92	0.853
Ψ	abs	CE-MRA	0.767	14.82	0.874
A	abs	TOF-MRA	**0.689**	**10.34**	**0.835**
s	abs	TOF-MRA	0.545	14.85	0.694
b_{avg}	abs	TOF-MRA	0.614	14.78	0.735
b_{max}	abs	TOF-MRA	0.636	11.80	0.788
Ψ	abs	TOF-MRA	0.595	11.54	0.765
A	abs	CTA	**0.608**	**48.53**	**0.692**
s	abs	CTA	0.389	94.90	0.468
b_{avg}	abs	CTA	0.332	74.32	0.400
b_{max}	abs	CTA	0.426	73.72	0.468
Ψ	abs	CTA	0.388	71.67	0.444

Table A.14: Experiments with the tested classification algorithms. The best results for each modality are printed bold.

Algorithm	Database	Original		Resampling		MetaCost	
		r_{TP}	g_m	r_{TP}	g_m	r_{TP}	g_m
Naive Bayes	3D-RA	0.70	0.77	0.83	0.82	0.74	0.75
SVM linear	3D-RA	0.55	0.72	0.79	0.81	0.64	0.75
SVM polynomial	3D-RA	0.47	0.65	0.62	0.73	0.53	0.68
SVM radial	3D-RA	0.43	0.63	**0.85**	**0.84**	0.60	0.72
Neural Network	3D-RA	0.53	0.69	0.81	0.77	0.60	0.72
ADtree	3D-RA	0.51	0.69	0.77	0.76	0.74	0.78
LogitBoost	3D-RA	0.43	0.63	0.74	0.73	0.77	0.80
Naive Bayes	CE-MRA	0.61	0.74	0.83	0.85	0.94	0.83
SVM linear	CE-MRA	0.11	0.33	0.89	0.89	0.39	0.62
SVM polynomial	CE-MRA	0.28	0.52	0.78	0.82	0.50	0.70
SVM radial	CE-MRA	0.33	0.58	0.89	0.89	0.56	0.74
Neural Network	CE-MRA	0.28	0.53	0.78	0.86	0.67	0.80
ADtree	CE-MRA	0.06	0.24	0.78	0.85	0.78	0.83
LogitBoost	CE-MRA	0.06	0.24	0.67	0.79	**1.00**	**0.94**
Naive Bayes	TOF-MRA	0.59	0.72	0.69	0.76	0.84	0.81
SVM linear	TOF-MRA	0	0	0.84	0.83	0	0
SVM polynomial	TOF-MRA	0.09	0.30	0.88	0.82	0.16	0.39
SVM radial	TOF-MRA	0.09	0.30	0.91	0.84	0.25	0.49
Neural Network	TOF-MRA	0.09	0.30	0.63	0.76	0.38	0.59
ADtree	TOF-MRA	0	0	0.63	0.75	**0.94**	**0.87**
LogitBoost	TOF-MRA	0	0	0.66	0.76	0.84	0.84
Naive Bayes	CTA	0.83	0.89	0.83	0.87	0.86	0.85
SVM linear	CTA	0.05	0.23	0.88	0.91	0.14	0.37
SVM polynomial	CTA	0.28	0.53	0.71	0.82	0.36	0.60
SVM radial	CTA	0.28	0.53	0.90	0.91	0.40	0.63
Neural Network	CTA	0.26	0.51	0.76	0.85	0.47	0.68
ADtree	CTA	0.05	0.23	0.74	0.84	0.90	0.88
LogitBoost	CTA	0.07	0.26	0.83	0.89	**0.91**	**0.92**

Table A.15: Scatterplot for the features b_{avg} and s with respect to the classes TP and FP and for all modalities.
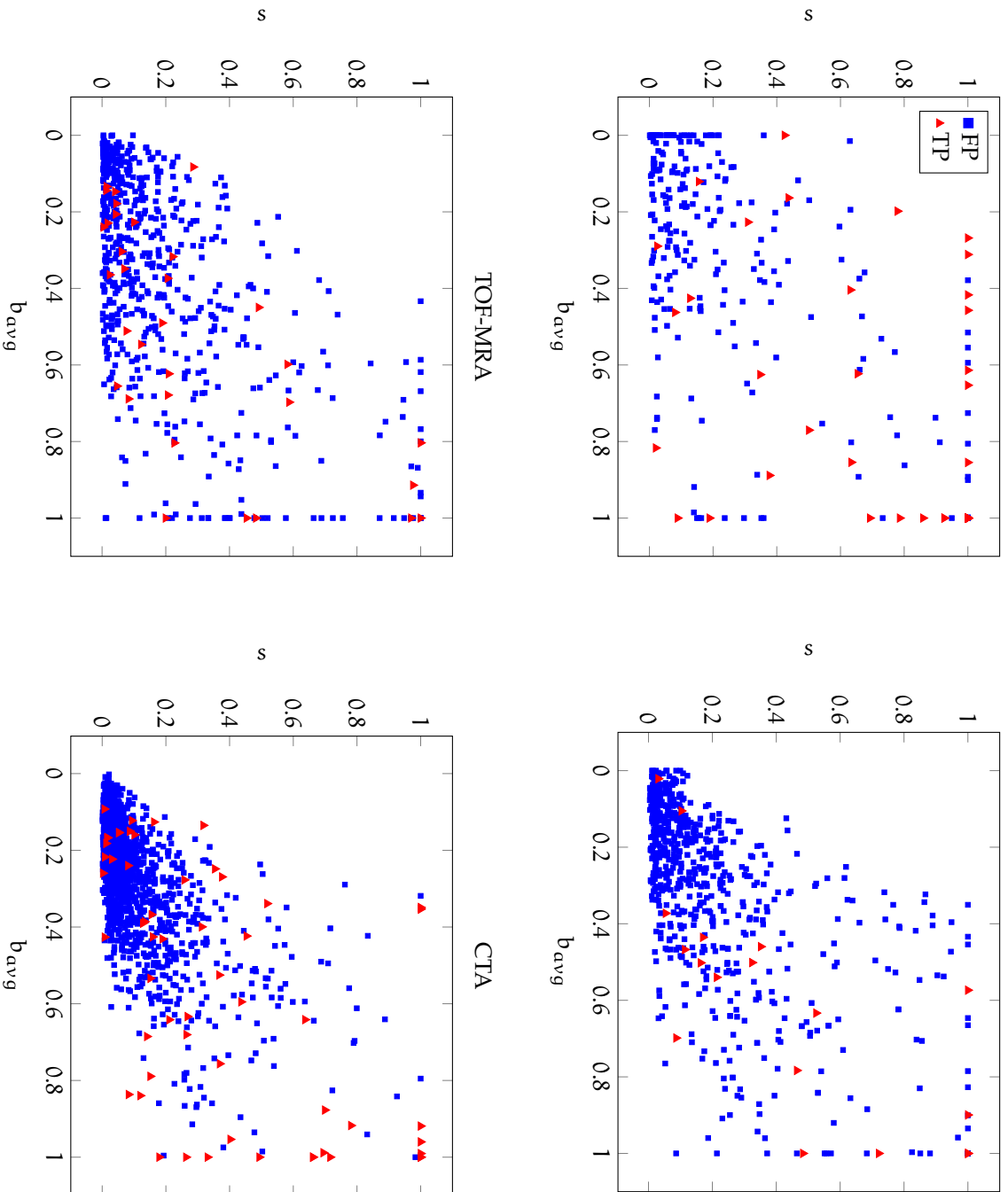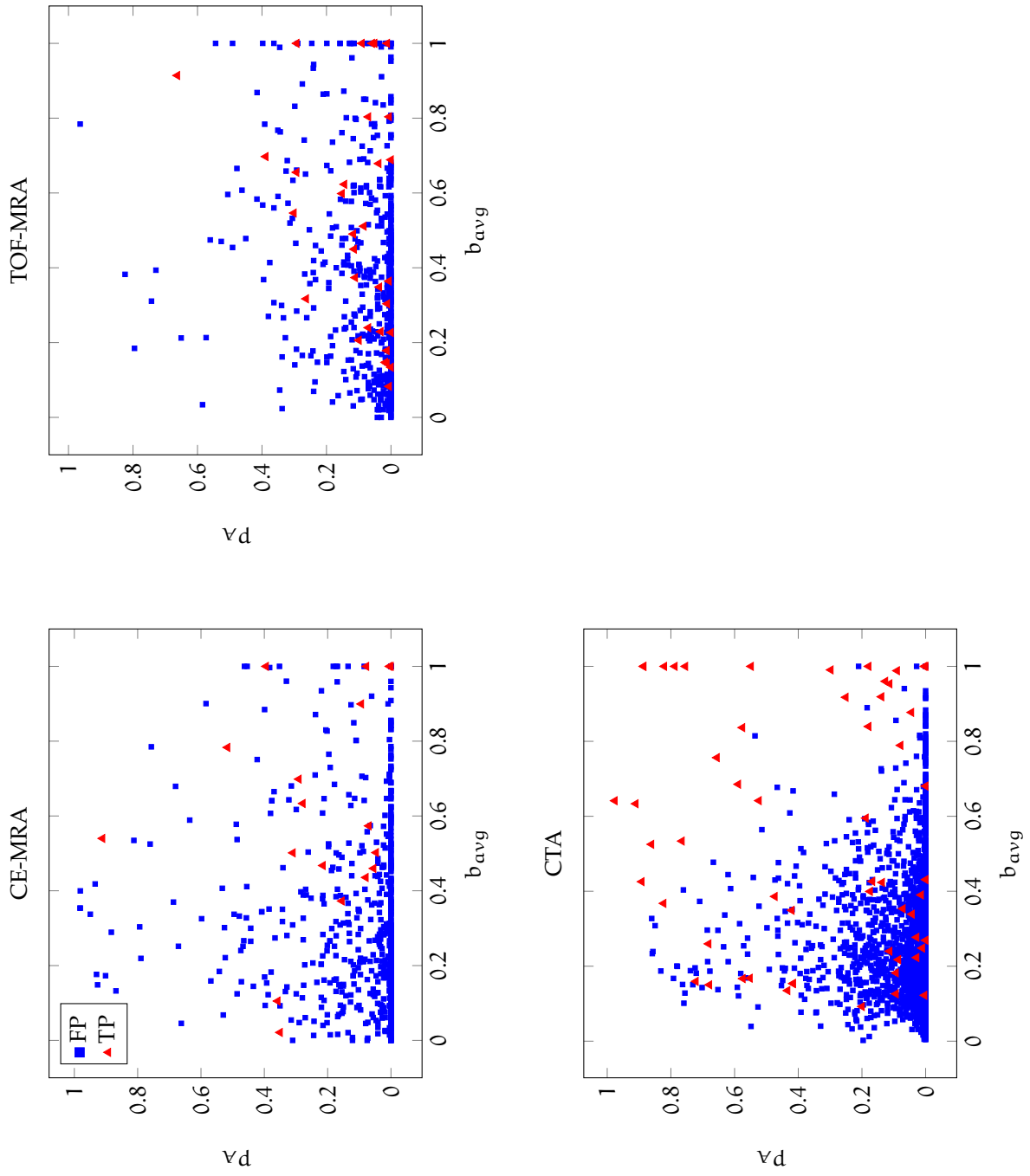
Table A.16: Scatterplot for the features b_{avg} and p_A with respect to the classes TP and FP and for all modalities.

H. Akaike. A new look at the statistical model identification. *IEEE Transactions on Automatic Control*, 19(6):716–723, 1974. (Cited on page 98.)

L. Antiga. Vascular Modeling Toolkit, 2007. URL http://www.vmtk.org. (Cited on page 38.)

L. Antiga, B. Ene-Iordache, and A. Remuzzi. Centerline computation and geometric analysis of branching tubular surfaces with application to blood vessel modeling. In *Winter School of Computer Graphics*, pages 1–3, Plzen, Czeck Republic, 2003. (Cited on page 75.)

L. Antiga, M. Piccinelli, L. Botti, B. Ene-Iordache, A. Remuzzi, and D. Steinman. An image-based modeling framework for patient-specific computational hemodynamics. *Medical & biological engineering & computing*, 46(11):1097–112, November 2008. (Cited on pages 28 und 38.)

R. Anxionnat, S. Bracard, X. Ducrocq, Y. Trousset, L. Launay, E. Kerrien, M. Braun, R. Vaillant, F. Scomazzoni, A. Lebedinsky, and L. Picard. Intracranial Aneurysms: Clinical Value of 3D Digital Subtraction Angiography in the Therapeutic Decision and Endovascular Treatment. *Radiology*, 218(3):799, March 2001. (Cited on page 16.)

S. Appanaboyina, F. Mut, R. Löhner, C. Putman, and J. Cebral. Simulation of intracranial aneurysm stenting: Techniques and challenges. *Computer Methods in Applied Mechanics and Engineering*, 198(45-46):3567–3582, 2009. (Cited on pages 41 und 46.)

H. Arimura, Q. Li, Y. Korogi, T. Hirai, and H. Abe. Automated computerized scheme for detection of unruptured intracranial aneurysms in three-dimensional magnetic resonance angiography. *Academic radiology*, 11(10):1093–1104, 2004. (Cited on pages 69, 71 und 80.)

H. Arimura, Q. Li, Y. Korogi, T. Hirai, S. Katsuragawa, Y. Yamashita, K. Tsuchiya, and K. Doi. Computerized detection of intracranial aneurysms for three-dimensional MR angiography: Feature extraction of small protrusions based on a shape-based difference imaging technique. *Medical Physics*, 33(2):394, 2006. (Cited on pages xiii, 1, 46, 67, 69, 70, 72, 73, 74, 75, 76, 78, 79, 80, 138 und 139.)

S. Attaway. *Matlab, Second Edition: A Practical Introduction to Programming and Problem Solving*. Butterworth-Heinemann, Waltham, MA, 2nd edition, 2011. (Cited on page 104.)

J. I. Ausman, F. G. Diaz, B. Sadasivan, M. Gonzeles-Portillo, G. M. Malik, and C. E. Deopujari. Giant intracranial aneurysm surgery: the role of microvascular reconstruction. *Surgical neurology*, 34(1):8–15, July 1990. (Cited on page 12.)

S. Aylward and E. Bullitt. Initialization, noise, singularities, and scale in height ridge traversal for tubular object centerline extraction. *IEEE Transactions on Medical Imaging*, 21(2):61, 2002. (Cited on page 28.)

S. Aylward, J. Jomier, S. Weeks, and E. Bullitt. Registration and analysis of vascular images. *International Journal of Computer Vision*, 55(2):123–138, 2003. (Cited on page 116.)

S. Aylward, E. Bullitt, S. Pizer, and D. Eberly. Intensity ridge and widths for tubular object segmentation and description. In *Mathematical Methods in Biomedical Image Analysis*, pages 131–138, 1996. (Cited on page 27.)

M. Backens and B. Schmitz. Unenhanced MR Angiography. In G. Schneider, M. R. Prince, J. F. M. Meaney, and V. B. Ho, editors, *Magnetic Resonance Angiography*, chapter I.1, pages 3–22. Springer, Milan, 2005. (Cited on page 19.)

D. H. Ballard. Generalizing the hough transform to detect arbitrary shapes. *Pattern Recognition*, 13(2):111–122, 1981. (Cited on page 52.)

G. K. Batchelor. *An Introduction to Fluid Dynamics*. Cambridge University Press, 2000. (Cited on page 38.)

H. Bay, T. Tuytelaars, and L. V. Gool. Surf: Speeded up robust features. In *Computer Vision*, 2006. (Cited on page 50.)

J. Beck, S. Rohde, J. Berkefeld, V. Seifert, and A. Raabe. Size and location of ruptured and unruptured intracranial aneurysms measured by 3-dimensional rotational angiography. *Surgical neurology*, 65(1):18–25, 2006. (Cited on page 8.)

S. Behrens. Automatic level set based cerebral vessel segmentation and bone removal in CT angiography data sets. In *DAGM-OAGM*, Graz, 2012. (Cited on page 29.)

I. Biederman. Recognition-by-components: a theory of human image understanding. *Psychological review*, 94(2):115–47, April 1987. (Cited on page 50.)

J. Blanchette and M. Summerfield. *C++ GUI Programming with Qt 4*. Prentice Hall, Upper Saddle River, NJ, 2nd edition, 2008. (Cited on page 103.)

D. Blezek, W. Brinjikji, X. Yang, D. F. Kallmes, and B. J. Erickson. Evaluation of an automated intracranial aneurysm detection system on a clinical cohort. In *Computer Assisted Radiology and Surgery*, page 217, Geneva, 2010. Springer. (Cited on page 77.)

H. Bogunović, A. G. Radaelli, M. De Craene, D. Delgado, and A. F. Frangi. Image intensity standardization in 3D rotational angiography and its application to vascular segmentation. In *SPIE Medical Imaging*, pages 6914–1–8, 2008. (Cited on pages 32 und 63.)

H. Bogunović, J. M. Pozo, M. C. Villa-Uriol, C. B. L. M. Majoie, R. van den Berg, H. a. F. Gratama van Andel, J. M. Macho, J. Blasco, L. S. Román, and A. F. Frangi. Automated segmentation of cerebral vasculature with aneurysms in 3DRA and TOF-MRA using geodesic active regions: an evaluation study. *Medical physics*, 38(1):210–22, January 2011. (Cited on pages 32 und 46.)

T. Bölke, S. Seshadhri, O. Gurvit, R. Bade, B. Preim, G. Janiga, M. Skalej, S. Serowy, and G. Rose. Phantom based flow analysis by means of dynamic angiography, CFD and laser-doppler-velocimetry. In *IEEE Nuclear Science Symposium*, pages 3440–3445, Honolulu, 2007. Ieee. (Cited on page 38.)

L. Böröczky, L. Zhao, and K. P. Lee. Feature subset selection for improving the performance of false positive reduction in lung nodule CAD. *IEEE transactions on information technology in biomedicine*, 10(3):504–11, July 2006. (Cited on page 63.)

S. Bouix, K. Siddiqi, and A. Tannenbaum. Flux driven automatic centerline extraction. *Medical Image Analysis*, 9(3):209–221, 2005. (Cited on pages 27, 28 und 75.)

L. Boussel, V. Rayz, A. Martin, G. Acevedo-Bolton, M. T. Lawton, R. Higashida, W. S. Smith, W. L. Young, and D. Saloner. Phase-contrast magnetic resonance imaging measurements in intracranial aneurysms in vivo of flow patterns, velocity fields, and wall shear stress: comparison with computational fluid dynamics. *Magnetic resonance in medicine*, 61(2): 409–17, February 2009. (Cited on page 38.)

R. R. Bridcut, E. Murphy, a. Workman, P. Flynn, and R. J. Winder. Patient dose from 3D rotational neurovascular studies. *The British journal of radiology*, 80(953):362–6, May 2007. (Cited on pages 16 und 23.)

V. Bruce, P. R. Green, and M. A. Georgeson. *Visual Perception: Physiology, Psychology and Ecology*. Psychology Press, New York, 4th edition, 2003. (Cited on page 50.)

E. Bullitt, K. E. Muller, I. Jung, W. Lin, and S. Aylward. Analyzing attributes of vessel populations. *Medical image analysis*, 9(1):39–49, February 2005. (Cited on page 142.)

S. Bundesamt. Todesursachen in Deutschland. Technical report, Statistisches Bundesamt, Wiesbaden, 2012. (Cited on page 3.)

J. V. Byrne, M. Bashiri, a. Pasco, and J. H. Morris. A novel flexible endovascular stent for use in small and tortuous vessels. *Neuroradiology*, 42(1):56–61, January 2000. (Cited on page 11.)

J. V. Byrne, R. Beltechi, J. A. Yarnold, J. Birks, and M. Kamran. Early experience in the treatment of intra-cranial aneurysms by endovascular flow diversion: a multicentre prospective study. *PloS one*, 5(9):e12492, January 2010. (Cited on page 12.)

J. Canny. A computational approach to edge detection. *IEEE transactions on pattern analysis and machine intelligence*, 8(6):679–98, June 1986. (Cited on pages 49 und 85.)

R. Cárdenes, J. Pozo, H. Bogunovic, I. Larrabide, and A. Frangi. Automatic Aneurysm Neck Detection Using Surface Voronoi Diagrams. *IEEE transactions on medical imaging*, 30(10):1863–1876, 2011. (Cited on pages 34, 35 und 46.)

M. Castro, C. Putman, M. Sheridan, and J. Cebral. Hemodynamic patterns of anterior communicating artery aneurysms: a possible association with rupture. *American Journal of Neuroradiology*, 30(2):297, 2009. (Cited on page 43.)

J. R. Cebral, F. Mut, J. Weir, and C. M. Putman. Association of hemodynamic characteristics and cerebral aneurysm rupture. *American Journal of Neuroradiology*, 32(2):264–70, February 2011. (Cited on pages 43 und 46.)

J. Cebral, M. Castro, J. Burgess, R. Pergolizzi, M. Sheridan, and C. Putman. Characterization of cerebral aneurysms for assessing risk of rupture by using patient-specific computational hemodynamics models. *American Journal of Neuroradiology*, 26(10):2550, November 2005. (Cited on pages 10, 37, 42 und 43.)

T. F. Chan and L. a. Vese. Active contours without edges. *IEEE transactions on image processing*, 10(2):266–77, January 2001. (Cited on page 29.)

N. Chawla, K. Bowyer, and L. Hall. SMOTE: synthetic minority over-sampling technique. *Journal Of Artificial Intelligence Research*, 16:341–378, 2002. (Cited on pages 99 und 100.)

H. Cheng. Computer-aided detection and classification of microcalcifications in mammograms: a survey. *Pattern Recognition*, 36(12):2967–2991, December 2003. (Cited on page 58.)

D. Chillet, J. Jomier, D. Cool, and S. Aylward. Vascular atlas formation using a vessel-to-image affine registration method. In *Medical Image Computing and Computer-Assisted Intervention (MICCAI)*, pages 335–342, Montreal, 2003. Springer. (Cited on pages 92 und 142.)

A. C. S. Chung, J. A. Noble, and P. Summers. Fusing speed and phase information for vascular segmentation of phase contrast MR angiograms. *Medical image analysis*, 6(2):109–28, June 2002. (Cited on page 27.)

T. Chung. *Computational Fluid Dynamics*. Cambridge University Press, 2nd edition, 2010. (Cited on page 37.)

P. Cignoni, M. Corsini, and G. Ranzuglia. Meshlab: an open-source 3D mesh processing system. *Ercim news*, 73:45–46, 2008. (Cited on page 34.)

S. Cito. Virtual Intracranial Stenting Challenge 2011, 2011. URL http://www.cistib.upf.edu/visc11/. (Cited on page 41.)

M. Clarke. Systematic review of reviews of risk factors for intracranial aneurysms. *Neuroradiology*, 50(8):653–64, August 2008. (Cited on page 10.)

T. Cootes, C. Taylor, D. Cooper, and J. Graham. Active shape models-their training and application. *Computer Vision and Image Understanding*, 61(1):38–59, 1995. (Cited on pages 54 und 56.)

T. Cootes, G. Edwards, and C. Taylor. Active appearance models. *IEEE Transactions on Pattern Analysis and Machine Intelligence*, 23(6):681–685, June 2001. (Cited on pages 54, 56 und 61.)

A. Cordebar, S. Bracard, S. Kremer, E. Schmitt, R. Anxionnat, A. Martin-Bertaux, and L. Picard. Contrast-enhanced transcranial Doppler sonography in the follow-up of intracranial aneurysms after endovascular treatment. *Neuroradiology*, 46(11):940–6, November 2004. (Cited on pages 21 und 22.)

C. Cortes and V. Vapnik. Support-vector networks. *Machine Learning*, 20(3):273–297, September 1995. (Cited on page 100.)

V. Costalat, M. Sanchez, D. Ambard, L. Thines, N. Lonjon, F. Nicoud, H. Brunel, J. P. Lejeune, H. Dufour, P. Bouillot, J. P. Lhaldky, K. Kouri, F. Segnarbieux, C. a. Maurage, K. Lobotesis, M. C. Villa-Uriol, C. Zhang, a. F. Frangi, G. Mercier, a. Bonafé, L. Sarry, and F. Jourdan. Biomechanical wall properties of human intracranial aneurysms resected following surgical clipping (IRRAs Project). *Journal of biomechanics*, 44(15):2685–91, October 2011. (Cited on page 38.)

T. E. Cupples, J. E. Cunningham, and J. C. Reynolds. Impact of computer-aided detection in a regional screening mammography program. *American journal of roentgenology*, 185 (4):944–50, October 2005. (Cited on page 57.)

S. Dammert, T. Krings, W. Moller-Hartmann, E. Ueffing, F. J. Hans, K. Willmes, M. Mull, and a. Thron. Detection of intracranial aneurysms with multislice CT: comparison with conventional angiography. *Neuroradiology*, 46(6):427–34, June 2004. (Cited on page 85.)

P. Dayan and L. Abbott. *Theoretical neuroscience - Computational and Mathematical Modeling of Neural Systems*. The MIT Press, Cambridge, Massachusetts, 2001. (Cited on page 50.)

M. de Bruijne, B. Ginneken, L. L. Bartels, M. M. Laan, M. Bruijne, J. Blankensteijn, W. Niessen, and M. Viergever. Automated segmentation of abdominal aortic aneurysms in multi-spectral MR images. In *Medical Image Computing and Computer Assisted Intervention (MICCAI)*, pages 538–545, Montreal, 2003. Springer. (Cited on pages 27 und 61.)

J. Dehmeshki, H. Amin, M. Ebadian-Dehkordi, A. Jouannic, and S. Qanadli. Automatic detection, segmentation and quantification of of Abdominal Aortic Aneurysm using Computed Tomography Angiography. In *Medical Image Understanding and Analysis (MIUA)*, Kingston upon Thames, 2009. (Cited on pages 60, 63 und 65.)

S. Dhar, M. Tremmel, J. Mocco, and M. Kim. Morphology parameters for intracranial aneurysm rupture risk assessment. *Neurosurgery*, 63(2):185–197, 2008. (Cited on page 37.)

K. Doi. Current status and future potential of computer-aided diagnosis in medical imaging. *The British journal of radiology*, 78 Spec No:3–19, 2005. (Cited on pages 56 und 57.)

K. Doi. Computer-aided diagnosis in medical imaging: historical review, current status and future potential. *Computerized medical imaging and graphics*, 31(4-5):198, 2007. (Cited on pages 13, 57, 63 und 99.)

P. Domingos. Meta Cost: a general method for making classifiers cost-sensitive. In *Conference on Knowledge Discovery and Data Mining*, pages 155–164, San Diego, 1999. (Cited on pages 99 und 100.)

R. Donner, E. Birngruber, H. Steiner, H. Bischof, and G. Langs. Localization of 3D anatomical structures using random forests and discrete optimization. In *MICCAI Workshop - Medical Computer Vision. Recognition Techniques and Applications in Medical Imaging*, pages 86–95, Beijing, China, 2010. (Cited on pages 53, 55 und 56.)

L. Dornheim and J. Dornheim. Automatische Detektion von Lymphknoten in CT-datensätzen des Halses. In *Bildverarbeitung für die Medizin 2008*, pages 308–312, Berlin, 2008. Springer. (Cited on pages 52, 55 und 56.)

R. O. Duda, P. E. Hart, and D. G. Stork. *Pattern Classification*. Wiley, 2nd edition, 2000. (Cited on pages 84 und 98.)

C. L. Dumoulin, S. P. Souza, M. F. Walker, and W. Wagle. Three-dimensional phase contrast angiography. *Magnetic Resonance in Medicine*, 9(1):139–149, January 1989. (Cited on page 20.)

J. A. Edlow, A. M. Malek, and C. S. Ogilvy. Aneurysmal subarachnoid hemorrhage: update for emergency physicians. *Journal of Emergency Medicine*, 34(3):237–51, April 2008. (Cited on pages 8 und 32.)

K. Engel, K. D. Tönnies, and A. Brechmann. Part-based localisation and segmentation of landmark-related auditory cortical regions. *Pattern Recognition*, 44(9):2017–2033, September 2011. (Cited on pages 52, 53, 55 und 56.)

S. P. Ferns, P. T. Nieuwkerk, W. J. J. van Rooij, G. J. E. Rinkel, and C. B. L. M. Majoie. Long-term MRA follow-up after coiling of intracranial aneurysms: impact on mood and anxiety. *Neuroradiology*, 53(5):343–8, May 2011. (Cited on pages 9 und 12.)

M. Feuerstein, D. Deguchi, T. Kitasaka, S. Iwano, K. Imaizumi, Y. Hasegawa, Y. Suenaga, and K. Mori. Automatic mediastinal lymph node detection in chest CT. In *SPIE Medical Imaging*, pages 72600V–1–8, Orlando, 2009. Spie. (Cited on pages 52, 55, 56 und 64.)

J. B. Fiebach, P. D. Schellinger, A. Gass, T. Kucinski, M. Siebler, A. Villringer, P. Olkers, J. G. Hirsch, S. Heiland, P. Wilde, O. Jansen, J. Röther, W. Hacke, and K. Sartor. Stroke magnetic resonance imaging is accurate in hyperacute intracerebral hemorrhage: a multicenter study on the validity of stroke imaging. *Stroke*, 35(2):502–6, February 2004. (Cited on page 13.)

J. Fiehler. Nicht rupturierte intrakranielle Aneurysmen: wann suchen, wann behandeln? *RöFo - Fortschritte auf dem Gebiet der Röntgenstrahlen und der bildgebenden Verfahren*, 184(2): 97–104, 2012. (Cited on pages 3, 6, 9, 10, 12 und 13.)

A. Firouzian, R. Manniesing, Z. H. Flach, R. Risselada, F. van Kooten, M. C. J. M. Sturkenboom, A. van der Lugt, and W. J. Niessen. Intracranial aneurysm segmentation in 3D CT angiography: Method and quantitative validation with and without prior noise filtering. *European journal of radiology*, 79(2):299–304, August 2011. (Cited on page 34.)

N. D. Forkert, A. Schmidt-Richberg, J. Ehrhardt, J. Fiehler, H. Handels, and D. Säring. Vesselness-geführte Level-Set Segmentierung von zerebralen Gefäßen. In H. Handels, J. Ehrhardt, T. M. Deserno, H.-P. Meinzer, and T. Tolxdorff, editors, *Bildverarbeitung für die Medizin*, Informatik aktuell, pages 8–12, Lübeck, 2011. Springer Berlin Heidelberg. (Cited on pages 27, 29 und 88.)

W. Förstner and E. Gülch. A fast operator for detection and precise location of distinct points, corners and centres of circular features. In *ISPRS Intercommission Workshop*, pages 281–305, Interlaken, 1987. (Cited on page 74.)

S. V. Fotin, A. P. Reeves, A. M. Biancardi, D. F. Yankelevitz, and C. I. Henschke. Standard moments based vessel bifurcation filter for computer-aided detection of pulmonary nodules. In *SPIE Medical Imaging*, pages 762413–1–10, 2010. (Cited on page 143.)

F. Fraioli, C. Catalano, A. Napoli, M. Francone, F. Venditti, M. Danti, F. Pediconi, and R. Passariello. Low-dose multidetector-row CT angiography of the infra-renal aorta and lower extremity vessels: image quality and diagnostic accuracy in comparison with standard DSA. *European radiology*, 16(1):137–46, January 2006. (Cited on page 16.)

A. F. Frangi. @neurIST, 2007. URL http://www.aneurist.org. (Cited on page 25.)

A. F. Frangi, W. J. Niessen, K. L. Vincken, and M. A. Viergever. Multiscale vessel enhancement filtering. In *Medical Image Computing and Computer-Assisted Intervention*, pages 130–137, Cambridge, 1998. (Cited on pages 27, 66, 67, 68, 69, 73, 88 und 110.)

Y. Freund and L. Mason. The alternating decision tree learning algorithm. In *Machine Learning International Workshop*, pages 124–133, 1999. (Cited on page 100.)

J. Friedman, T. Hastie, and R. Tibshirani. Additive logistic regression: a statistical view of boosting. *The Annals of Statistics*, 28(2):337–407, 2000. (Cited on page 100.)

B. Furlow. Radiation dose in computed tomography. *Radiologic technology*, 81(5):437–50, 2010. (Cited on pages 16 und 23.)

R. A. Gabriel, H. Kim, S. Sidney, C. E. McCulloch, V. Singh, S. C. Johnston, N. U. Ko, A. S. Achrol, J. G. Zaroff, and W. L. Young. Ten-year detection rate of brain arteriovenous malformations in a large, multiethnic, defined population. *Stroke*, 41(1):21–6, January 2010. (Cited on pages 1, 6 und 10.)

R. Gasteiger, G. Janiga, and D. Stucht. Vergleich zwischen 7 Tesla 4D PC-MRI-Flussmessung und CFD-Simulation. In *Bildverarbeitung für die Medizin*, pages 304–308, Lübeck, 2011. (Cited on page 42.)

R. Gasteiger, D. J. Lehmann, R. van Pelt, G. Janiga, O. Beuing, A. Vilanova, H. Theisel, and B. Preim. Automatic Detection and Visualization of Qualitative Hemodynamic Characteristics in Cerebral Aneurysms. *IEEE Transactions on Visualization and Computer Graphics*, 18(12):2178–2187, December 2012. (Cited on pages 40, 44 und 46.)

D. Gavrila. Traffic sign recognition revisited. In *DAGM symposium fur Musterekennung*, pages 86–93, Bonn, 1999. (Cited on page 52.)

A. J. Geers, I. Larrabide, A. G. Radaelli, H. Bogunovic, M. Kim, H. A. F. Gratama van Andel, C. B. Majoie, E. VanBavel, and A. F. Frangi. Patient-specific computational hemodynamics of intracranial aneurysms from 3D rotational angiography and CT angiography: an in vivo reproducibility study. *American journal of neuroradiology*, 32(3):581–6, March 2011. (Cited on page 38.)

G. F. Gibbs, J. Huston, M. a. Bernstein, S. J. Riederer, and R. D. Brown. 3.0-Tesla MR angiography of intracranial aneurysms: comparison of time-of-flight and contrast-enhanced techniques. *Journal of magnetic resonance imaging*, 21(2):97–102, February 2005. (Cited on page 21.)

M. L. Giger, H.-P. Chan, and J. Boone. Anniversary Paper: History and status of CAD and quantitative image analysis: The role of Medical Physics and AAPM. *Medical Physics*, 35 (12):5799, 2008. (Cited on page 57.)

D. L. Gillespie, J. L. Villavicencio, C. Gallagher, A. Chang, J. K. Hamelink, L. a. Fiala, S. D. O'Donnell, M. R. Jackson, E. Pikoulis, and N. M. Rich. Presentation and management of venous aneurysms. *Journal of vascular surgery*, 26(5):845–52, November 1997. (Cited on page 3.)

G. Guglielmi, F. Viñuela, G. Duckwiler, J. Dion, P. Lylyk, a. Berenstein, C. Strother, V. Graves, V. Halbach, and D. Nichols. Endovascular treatment of posterior circulation aneurysms by electrothrombosis using electrically detachable coils. *Journal of neurosurgery*, 77(4):515–24, October 1992. (Cited on page 11.)

H. Hahn, M. Wenzel, O. Konrad-Verse, and H. Peitgen. A minimally-interactive watershed algorithm designed for efficient CTA bone removal. In *Computer Vision Approaches to Medical Image Analysis*, pages 178–189. Springer, 2006. (Cited on page 18.)

M. Hall, E. Frank, G. Holmes, and B. Pfahringer. The WEKA data mining software: an update. *ACM SIGKDD Explorations Newsletter*, 11(1):10–18, 2009. (Cited on pages 100 und 104.)

R. M. Haralick, K. Shanmugam, and I. Dinstein. Textural features for image classification. *Systems, Man and Cybernetics*, 3(6):610–621, 1973. (Cited on page 50.)

S. Hassan, F. Hétroy, F. Faure, and O. Palombi. Automatic localization and quantification of intracranial aneurysms. In *International Conference on Computer Analysis of Images and Patterns*, pages 554–562, Seville, 2011. (Cited on pages 74, 78, 79, 80 und 139.)

N. Hayashi, Y. Masutani, T. Masumoto, H. Mori, A. Kunimatsu, O. Abe, S. Aoki, K. Ohtomo, N. Takano, and K. Matsumoto. Feasibility of a curvature-based enhanced display system for detecting cerebral aneurysms in MR angiography. *Magnetic resonance in medical sciences*, 2(1):29–36, April 2003. (Cited on pages 69 und 75.)

H. He and E. Garcia. Learning from imbalanced data. *IEEE Transactions on Knowledge and Data Engineering*, 21(9):1263–1284, 2009. (Cited on pages 99 und 100.)

M. Heath, K. Bowyer, D. Kopans, R. Moore, and P. Kegelmeyer Jr. The digital database for screening mammography. In M. J. Yaffe, editor, *International Workshop on Digital Mammography*, pages 212–218, Toronto, 2000. (Cited on page 64.)

T. Heimann, S. Münzing, H.-P. Meinzer, and I. Wolf. A shape-guided deformable model with evolutionary algorithm initialization for 3D soft tissue segmentation. In *Information processing in medical imaging*, pages 1–12, Kerkrade, January 2007. Springer. (Cited on pages 52 und 54.)

A. Helgadottir, G. Thorleifsson, K. P. Magnusson, S. Grétarsdottir, V. Steinthorsdottir, and Others. The same sequence variant on 9p21 associates with myocardial infarction, abdominal aortic aneurysm and intracranial aneurysm. *Nature genetics*, 40(2):217–24, February 2008. (Cited on page 6.)

C. M. Hentschke and K. D. Tönnies. Automatic 2D-3D Registration of Cerebral DSA Data Sets. In *Bildverarbeitung für die Medizin*, pages 162–166, Aachen, 2010. (Cited on page 39.)

C. M. Hentschke, O. Beuing, R. Nickl, and K. D. Tönnies. Automatic Cerebral Aneurysm Detection in Multimodal Angiographic Images. In *IEEE Medical Imaging Conference*, pages 3116–3120, Valencia, 2011a. (Cited on page 83.)

C. M. Hentschke, S. Serowy, G. Janiga, G. Rose, and K. D. Tönnies. Estimating blood flow velocity in angiographic image data. In *SPIE Medical Imaging*, pages 7964–1–8, Orlando, 2011b. (Cited on page 39.)

C. M. Hentschke, O. Beuing, R. Nickl, and K. D. Tönnies. Detection of cerebral aneurysms in MRA, CTA and 3D-RA data sets. In *SPIE Medical Imaging*, pages 8315I–1–8, San Diego, 2012a. (Cited on pages 83 und 120.)

C. M. Hentschke, K. D. Tönnies, O. Beuing, and R. Nickl. A new feature for automatic aneurysm detection. In *IEEE International Symposium on Biomedical Imaging*, pages 800–803, Barcelona, 2012b. (Cited on pages 83, 91 und 96.)

M. Hernandez and A. F. Frangi. Non-parametric geodesic active regions: method and evaluation for cerebral aneurysms segmentation in 3DRA and CTA. *Medical image analysis*, 11(3):224–41, June 2007. (Cited on page 32.)

J. H. Hipwell, F. Strachan, J. A. Olson, K. C. McHardy, P. F. Sharp, and J. V. Forrester. Automated detection of microaneurysms in digital red-free photographs: a diabetic retinopathy screening tool. *Diabetic Medicine*, 17(8):588–594, August 2000. (Cited on pages 62 und 63.)

T. Hirai, Y. Korogi, H. Arimura, S. Katsuragawa, M. Kitajima, M. Yamura, Y. Yamashita, and K. Doi. Intracranial aneurysms at MR angiography: effect of computer-aided diagnosis on radiologists' detection performance. *Radiology*, 237(2):605–10, November 2005. (Cited on page 23.)

Y. Hiratsuka, H. Miki, I. Kiriyama, K. Kikuchi, S. Takahashi, I. Matsubara, K. Sadamoto, and T. Mochizuki. Diagnosis of unruptured intracranial aneurysms: 3T MR angiography versus 64-channel multi-detector row CT angiography. *Magnetic resonance in medical sciences*, 7(4):169–78, January 2008. (Cited on pages 21 und 23.)

A. T. Hirsch, Z. J. Haskal, N. R. Hertzer, C. W. Bakal, M. a. Creager, J. L. Halperin, L. F. Hiratzka, W. R. C. Murphy, J. W. Olin, J. B. Puschett, K. a. Rosenfield, and Others. ACC/AHA 2005 Practice Guidelines for the management of patients with peripheral arterial disease (lower extremity, renal, mesenteric, and abdominal aortic). *Circulation*, 113(11):e463–654, March 2006. (Cited on page 3.)

V. B. Ho, W. R. Corse, and J. H. Maki. Contrast-Enhanced MRA: Theory and Technical Optimization. In G. Schneider, M. R. Prince, J. F. M. Meaney, and V. B. Ho, editors, *Magnetic Resonance Angiography*, chapter I.2, pages 23–42. Springer, Milan, 2005. (Cited on page 18.)

R. M. Hoogeveen. MRA of Brain Vessels. In S. O. Schoenberg, O. Dietrich, and M. F. Reiser, editors, *Parallel Imaging in clinical MR Applications*, pages 285–290. Springer, 2007. (Cited on page 19.)

M. E. Houle, H.-P. Kriegel, P. Kröger, E. Schubert, and A. Zimek. Can shared-neighbor distances defeat the curse of dimensionality? In *Scientific and Statistical Database Management*, pages 482–500, Heidelberg, 2010. Springer. (Cited on page 137.)

S. Hwang, H. Kwak, Y. Han, and G. Chung. Detection of intracranial aneurysms using three-dimensional multidetector-row CT angiography: Is bone subtraction necessary? *European Journal of Radiology*, pages 1–6, February 2010. (Cited on page 17.)

L. Ibáñez, W. Schroeder, L. Ng, and J. Cates. *The ITK Software Guide*. Kitware Inc., 2nd edition, 2005. (Cited on pages 86 und 103.)

F. Ikawa, M. Sumida, T. Uozumi, S. Kuwabara, K. Kiya, K. Kurisu, K. Arita, and H. Satoh. Comparison of three-dimensional phase-contrast magnetic resonance angiography with three-dimensional time-of-flight magnetic resonance angiography in cerebral aneurysms. *Surgical neurology*, 42(4):287–92, October 1994. (Cited on pages 21 und 23.)

T. Inagawa. Surgical treatment of multiple intracranial aneurysms. *Acta neurochirurgica*, 108(1-2):22–9, January 1991. (Cited on pages 4 und 5.)

T. Inagawa. Incidence and risk factors for multiple intracranial saccular aneurysms in patients with subarachnoid hemorrhage in Izumo City, Japan. *Acta neurochirurgica*, 151 (12):1623–30, December 2009. (Cited on page 5.)

A. K. Jain, R. P. Duin, and J. Mao. Statistical pattern recognition: a review. *IEEE Transactions on Pattern Analysis and Machine Intelligence*, 22(1):4–37, 2000. (Cited on pages 100 und 106.)

G. Janiga, C. Rössl, S. Seshadhri, and M. Skalej. Overview of the virtual intracranial stenting challenge 2010. In *microCAD*, pages 45–50, Miskolc, Hungary, 2011. (Cited on page 25.)

G. Janiga, C. Rössl, M. Skalej, and D. Thévenin. Realistic virtual intracranial stenting and computational fluid dynamics for treatment analysis. *Journal of biomechanics*, 46(1):7–12, October 2013. (Cited on pages 25, 38, 41 und 42.)

W. Jeong and K. Rhee. Hemodynamics of Cerebral Aneurysms: Computational Analyses of Aneurysm Progress and Treatment. *Computational and Mathematical Methods in Medicine*, 2012:1–11, 2012. (Cited on pages 37 und 46.)

C. Johnson, M. Chen, A. Toledano, J. Heiken, A. Dachman, M. Kuo, C. Menias, B. Siewert, J. Cheema, R. Obregon, J. Fidler, P. Zimmerman, K. Horton, K. Coakley, R. Iyer, A. Hara, R. H. Jr., G. Casola, J. Yee, B. A. Herman, L. Burgart, and P. Limburg. Accuracy of CT colonography for detection of large adenomas and cancers. *New England Journal of Medicine*, 359(12):1207–1217, 2008. (Cited on page 64.)

S. Juvela, K. Poussa, and M. Porras. Factors Affecting Formation and Growth of Intracranial Aneurysms: A Long-Term Follow-Up Study. *Stroke*, 32(2):485–491, 2001. (Cited on page 6.)

S. Kakeda, Y. Korogi, H. Arimura, T. Hirai, S. Katsuragawa, T. Aoki, and K. Doi. Diagnostic accuracy and reading time to detect intracranial aneurysms on MR angiography using a computer-aided diagnosis system. *American journal of roentgenology*, 190(2):459–65, 2008. (Cited on page 23.)

W. Kalender. *Computed Tomography: Fundamentals, System Technology, Image Quality, Applications*. John Wiley & Sons, 3rd edition, 2011. (Cited on pages 16 und 137.)

D. F. Kallmes and H. J. Cloft. The use of hydrocoil for parent artery occlusion. *American journal of neuroradiology*, 25(8):1409–10, September 2004. (Cited on page 11.)

E. Z. Kapsalaki, C. D. Rountas, and K. N. Fountas. The Role of 3 Tesla MRA in the Detection of Intracranial Aneurysms. *International journal of vascular medicine*, 2012, January 2012. (Cited on page 21.)

N. Karssemeijer, A. M. Bluekens, D. Beijerinck, J. J. Deurenberg, M. Beekman, R. Visser, R. van Engen, A. Bartels-Kortland, and M. J. Broeders. Results 5 Years after Introduction of Digital Mammography in a Population. *Radiology*, 253(2):353–358, 2009. (Cited on page 58.)

M. Kass, A. Witkin, and D. Terzopoulos. Snakes: Active contour models. *International journal of computer vision*, 1(4):321–331, January 1988. (Cited on page 28.)

H. Kato, G. Kubota, K. Kojima, N. Hayashi, E. Nishihara, H. Kura, and M. Aizawa. Preliminary time-flow study: comparison of interpretation times between PACS workstations and films. *Computerized Medical Imaging and Graphics*, 19(3):261–265, 1995. (Cited on page 57.)

T. J. Kaufmann, J. Huston, H. J. Cloft, J. Mandrekar, L. Gray, M. a. Bernstein, J. L. Atkinson, and D. F. Kallmes. A prospective trial of 3T and 1.5T time-of-flight and contrast-enhanced MR angiography in the follow-up of coiled intracranial aneurysms. *American journal of neuroradiology*, 31(5):912–8, May 2010. (Cited on page 21.)

C. Kirbas and F. Quek. A review of vessel extraction techniques and algorithms. *ACM Computing Surveys*, 36(2):81–121, 2004. (Cited on page 26.)

S. Klein, M. Staring, K. Murphy, M. A. Viergever, and J. P. Pluim. Elastix: a Toolbox for Intensity-Based Medical Image Registration. *IEEE transactions on medical imaging*, 29(1): 196–205, January 2010. (Cited on pages 92 und 104.)

S. Kobashi, N. Kamiura, Y. Hata, and F. Miyawaki. Volume-quantization-based neural network approach to 3D MR angiography image segmentation. *Image and Vision Computing*, 19:185–193, 2001. (Cited on page 75.)

S. Kobashi, K. Kondo, and Y. Hata. Computer-aided diagnosis of intracranial aneurysms in MRA images with case-based reasoning. *Transactions on Information and Systems*, 89 (1):340–350, 2006. (Cited on pages xiii, 75, 76, 78 und 80.)

H. Kobatake and M. Murakami. Adaptive filter to detect rounded convex regions: Iris filter. In *International Conference on Pattern Recognition*, pages 340–344, Vienna, 1996. IEEE Computer Society Press. (Cited on page 71.)

L. Kobbelt, S. Campagna, J. Vorsatz, and H.-P. Seidel. Interactive multi-resolution modeling on arbitrary meshes. In *conference on Computer graphics and interactive techniques*, pages 105–114, Orlando, 1998. (Cited on page 52.)

J. Kohout, A. Chiarini, G. J. Clapworthy, and G. Klajnšek. Aneurysm identification by analysis of the blood-vessel skeleton. *Computer methods and programs in biomedicine*, 109 (1):32–47, January 2013. (Cited on page 34.)

T. Koller, G. Gerig, G. Skékely, and D. Dettwiler. Multiscale detection of curvilinear structures in 2-D and 3-D image data. In *International Conference on Computer Vision*, pages 864–869, Boston, 1995. (Cited on page 27.)

S. Kostopoulos, D. Glotsos, G. Kagadis, D. A., A. Spyridonos, I. Kalatzis, M. Karamessini, T. Petsas, D. Cavouras, and G. Nikiforidis. A hybrid pixel-based classification method for blood vessel segmentation and aneurysm detection on CTA. *Computers & Graphics*, 31(3):493–500, 2007. (Cited on page 29.)

M. Kubat, R. Holte, and S. Matwin. Machine learning for the detection of oil spills in satellite radar images. *Machine learning*, 30(2-3):195–215, 1998. (Cited on page 108.)

A. Kuhn, D. J. Lehmann, R. Gasteiger, M. Neugebauer, B. Preim, and H. Theisel. A Clustering-based Visualization Technique to Emphasize Meaningful Regions of Vector Fields. In *Vision, Modeling, and Visualization (VMV)*, Berlin, 2011. (Cited on page 40.)

R. S. Laramee, H. Hauser, H. Doleisch, B. Vrolijk, F. H. Post, and D. Weiskopf. The State of the Art in Flow Visualization: Dense and Texture-Based Techniques. *Computer Graphics Forum*, 22(2):203–221, 2004. (Cited on page 44.)

I. Larrabide, M. Kim, L. Augsburger, M. C. Villa-Uriol, D. Rüfenacht, and A. F. Frangi. Fast virtual deployment of self-expandable stents: method and in vitro evaluation for intracranial aneurysmal stenting. *Medical image analysis*, 16(3):721–30, April 2012. (Cited on page 41.)

A. Lauric. *Automated Detection and Classification of Intracranial Aneurysms based on 3D Surface Analysis*. PhD thesis, Tufts, 2010. (Cited on pages 73, 78 und 80.)

A. Lauric, E. L. Miller, S. Frisken, and A. M. Malek. Automated detection of intracranial aneurysms based on parent vessel 3D analysis. *Medical Image Analysis*, 14(2):149–159, 2010. (Cited on pages 29, 46, 63, 64, 72, 73, 74, 78, 79, 80, 91, 138 und 139.)

A. Lauric, E. L. Miller, M. I. Baharoglu, and A. M. Malek. 3D Shape Analysis of Intracranial Aneurysms Using the Writhe Number as a Discriminant for Rupture. *Annals of biomedical engineering*, 39(5):1457–1469, January 2011. (Cited on pages 10 und 36.)

M. W. K. Law and A. C. S. Chung. Efficient implementation for spherical flux computation and its application to vascular segmentation. *IEEE transactions on image processing*, 18(3): 596–612, March 2009. (Cited on page 27.)

C. Lederman, A. Joshi, I. Dinov, and L. Vese. The generation of tetrahedral mesh models for neuroanatomical MRI. *NeuroImage*, 55(1):153–164, 2011a. (Cited on page 34.)

C. Lederman, L. Vese, and A. Chien. Registration for 3D morphological comparison of brain aneurysm growth. *Advances in Visual Computing*, pages 392–399, 2011b. (Cited on page 37.)

S. L. A. Lee, A. Z. Kouzani, and E. J. Hu. Automated detection of lung nodules in computed tomography images: a review. *Machine Vision and Applications*, 23(11):151–163, May 2010. (Cited on page 63.)

Y. Lee, T. Hara, H. Fujita, S. Itoh, and T. Ishigaki. Automated detection of pulmonary nodules in helical CT images based on an improved template-matching technique. *IEEE transactions on medical imaging*, 20(7):595–604, July 2001. (Cited on pages 52, 55, 56 und 66.)

D. Lesage, E. D. Angelini, I. Bloch, and G. Funka-Lea. A review of 3D vessel lumen segmentation techniques: models, features and extraction schemes. *Medical image analysis*, 13(6):819–45, December 2009. (Cited on pages 26, 27, 46 und 67.)

J. Lewin, G. Laub, and R. Hausmann. Three-dimensional time-of-flight MR angiography: applications in the abdomen and thorax. *Radiology*, 179(1):261–264, 1991. (Cited on page 18.)

H. Li, L. Yan, M.-H. Li, Y.-D. Li, H.-Q. Tan, B.-X. Gu, and W. Wang. Evaluation of intracranial aneurysms with high-resolution MR angiography using single-artery highlighting technique: correlation with digital subtraction angiography. *La Radiologia medica*, August 2012. (Cited on page 21.)

M.-H. Li, Y.-D. Li, H.-Q. Tan, B.-X. Gu, Y.-C. Chen, W. Wang, S.-W. Chen, and D.-J. Hu. Contrast-free MRA at 3.0 T for the detection of intracranial aneurysms. *Neurology*, 77(7): 667–76, August 2011. (Cited on page 21.)

Q. Li, S. Sone, and K. Doi. Selective enhancement filters for nodules, vessels, and airway walls in two-and three-dimensional CT scans. *Medical Physics*, 30(8):2040, 2003. (Cited on pages 27, 59, 66, 67, 68, 69, 88 und 103.)

T. Lindeberg. Scale-space theory: A basic tool for analyzing structures at different scales. *Journal of applied statistics*, 21(1-2):225–270, 1994. (Cited on page 68.)

W. Lorensen and H. Cline. Marching cubes: A high resolution 3D surface construction algorithm. *ACM SIGGRAPH Computer Graphics*, 1(4):163–169, 1987. (Cited on pages 32, 34 und 44.)

D. G. Lowe. Distinctive Image Features from Scale-Invariant Keypoints. *International Journal of Computer Vision*, 60(2):91–110, November 2004. (Cited on page 50.)

D. Lu and Q. Weng. A survey of image classification methods and techniques for improving classification performance. *International Journal of Remote Sensing*, 28(5):823–870, January 2007. (Cited on page 63.)

F. Maes, D. Vandermeulen, and P. Suetens. Medical Image Registration Using Mutual Information. *Proceedings of the IEEE*, 91(10):1699–1722, 2003. (Cited on page 63.)

J. Maintz and M. Viergever. A survey of medical image registration. *Medical image analysis*, 2(1):1–36, March 1998. (Cited on pages 92 und 116.)

M. Malaterre. GDCM Reference Manual. Technical report, –, Lyon, 2008. URL http://gdcm.sourceforge.net/gdcm.pdf. (Cited on page 103.)

S. Mandai, K. Kinugasa, and T. Ohmoto. Direct thrombosis of aneurysms with cellulose acetate polymer. *Journal of neurosurgery*, 77(10):497–500, 1992. (Cited on page 12.)

R. Manniesing, B. Velthuis, M. Van Leeuwen, I. Van der Schaaf, P. Van Laar, and W. Niessen. Level set based cerebral vasculature segmentation and diameter quantification in CT angiography. *Medical Image Analysis*, 10(2):200–214, 2006. (Cited on pages 27, 28 und 29.)

M. Markl, F. P. Chan, M. T. Alley, K. L. Wedding, M. T. Draney, C. J. Elkins, D. W. Parker, R. Wicker, C. a. Taylor, R. J. Herfkens, and N. J. Pelc. Time-resolved three-dimensional phase-contrast MRI. *Journal of magnetic resonance imaging*, 17(4):499–506, April 2003. (Cited on page 20.)

D. Marr and E. Hildreth. Theory of edge detection. *Proceedings of the Royal Society of London. Series B, Containing papers of a Biological character. Royal Society (Great Britain)*, 207(1167): 187–217, February 1980. (Cited on page 49.)

D. Marr. *A computational investigation into the human representation and processing of visual information*. Freeman, New York, 1982. (Cited on page 49.)

A. Marzo, P. Singh, I. Larrabide, A. Radaelli, S. Coley, M. Gwilliam, I. D. Wilkinson, P. Lawford, P. Reymond, U. Patel, A. Frangi, and D. R. Hose. Computational hemodynamics in cerebral aneurysms: the effects of modeled versus measured boundary conditions. *Annals of biomedical engineering*, 39(2):884–96, February 2011. (Cited on pages 38, 39 und 43.)

T. McInerney and D. Terzopoulos. Topology adaptive deformable surfaces for medical image volume segmentation. *IEEE transactions on medical imaging*, 18(10):840–50, October 1999. (Cited on page 28.)

J. Menke, J. Larsen, and K. Kallenberg. Diagnosing cerebral aneurysms by computed tomographic angiography: meta-analysis. *Annals of neurology*, 69(4):646–54, April 2011. (Cited on pages 17 und 23.)

A. Militzer and F. Vega-Higuera. Probabilistic boosting trees for automatic bone removal from CT angiography images. In *SPIE Medical Imaging*, volume 7259, pages 7259–1–8, Orlando, 2009. (Cited on pages 18 und 29.)

R. Millan, L. Dempere-Marco, J. Pozo, J. Cebral, and A. Frangi. Morphological characterization of intracranial aneurysms using 3-D moment invariants. *IEEE transactions on Medical Imaging*, 26(9):1270, 2007. (Cited on pages 34, 35 und 46.)

J. H. Moltz, L. Bornemann, J.-M. Kuhnigk, V. Dicken, E. Peitgen, S. Meier, H. Bolte, M. Fabel, H.-C. Bauknecht, M. Hittinger, A. Kieß ling, M. Pusken, and H.-O. Peitgen. Advanced Segmentation Techniques for Lung Nodules, Liver Metastases, and Enlarged Lymph Nodes in CT Scans. *IEEE Journal of Selected Topics in Signal Processing*, 3(1):122–134, February 2009. (Cited on page 60.)

A. Molyneux, R. Kerr, L. Yu, M. Clarke, M. Sneade, J. Yarnold, P. Sandercock, and Others. International subarachnoid aneurysm trial (ISAT) of neurosurgical clipping versus endovascular coiling in 2143 patients with ruptured intracranial aneurysms: a randomised comparison of effects on survival, dependency, seizures, rebleeding, subgroups, and . *The Lancet*, 366(9488):809–817, 2005. (Cited on page 12.)

T. Mönch, R. Gasteiger, G. Janiga, H. Theisel, and B. Preim. Context-aware mesh smoothing for biomedical applications. *Computers & Graphics*, 35(4):755–767, August 2011. (Cited on page 34.)

C. Mönninghoff, S. Maderwald, J. M. Theysohn, O. Kraff, S. C. Ladd, M. E. Ladd, M. Forsting, H. H. Quick, and I. Wanke. Evaluation of intracranial aneurysms with 7 T versus 1.5 T time-of-flight MR angiography - initial experience. *RöFo: Fortschritte auf dem Gebiete der Röntgenstrahlen und der Nuklearmedizin*, 181(1):16–23, January 2009. (Cited on page 21.)

H. Morales, M. Kim, E. Vivas, M. C. Villa-Uriol, I. Larrabide, T. Sola, L. Guimaraens, and A. F. Frangi. How Do Coil Configuration and Packing Density Influence Intra-Aneurysmal Hemodynamics? *American Journal of Neuroradiology*, 32:1935–1941, 2011. (Cited on page 42.)

K. Murphy, B. van Ginneken, a. M. R. Schilham, B. J. de Hoop, H. a. Gietema, and M. Prokop. A large-scale evaluation of automatic pulmonary nodule detection in chest CT using local image features and k-nearest-neighbour classification. *Medical image analysis*, 13(5):757–70, October 2009. (Cited on pages 59 und 66.)

K. Nael and J. Villablanca. Contrast-enhanced MR angiography at 3T in the evaluation of intracranial aneurysms: a comparison with time-of-flight MR angiography. *American Journal of Neuroradiology*, 27(10):2118–2121, 2006. (Cited on page 21.)

M. Neugebauer, V. Diehl, M. Skalej, and B. Preim. Geometric Reconstruction of the Ostium of Cerebral Aneurysms. In *Visualization, Modeling and Vision*, pages 307–314, Siegen, 2010. (Cited on pages 4 und 33.)

M. Neugebauer, K. Lawonn, O. Beuing, and B. Preim. Automatic Generation from of Anatomic Characteristics from cerebral Aneurysm Surface Models. *International journal of computer assisted radiology and surgery*, 8(2):279–89, 2012. (Cited on pages 33 und 46.)

M. Neugebauer, R. Gasteiger, O. Beuing, V. Diehl, M. Skalej, and B. Preim. Combining Map Displays and 3D Visualizations for the Analysis of Scalar Data on Cerebral Aneurysm Surfaces. In *Computer Graphics Forum*, pages 1041–1050, 2009. (Cited on page 44.)

M. Neugebauer, G. Janiga, O. Beuing, M. Skalej, and B. Preim. Anatomy-Guided Multi-Level Exploration of Blood Flow in Cerebral Aneurysms. *Computer Graphics Forum*, 30 (3):1041–1050, June 2011. (Cited on page 44.)

M. Niemeijer, B. van Ginneken, M. J. Cree, A. Mizutani, G. Quellec, C. I. Sanchez, B. Zhang, R. Hornero, M. Lamard, C. Muramatsu, X. Wu, G. Cazuguel, J. You, A. Mayo, Q. Li, Y. Hatanaka, B. Cochener, C. Roux, F. Karray, M. Garcia, H. Fujita, and M. D. Abramoff. Retinopathy online challenge: automatic detection of microaneurysms in digital color fundus photographs. *IEEE transactions on medical imaging*, 29(1):185–95, January 2010. (Cited on pages 62, 64 und 65.)

W. Niessen, T. van Walsum, C. Metz, M. Schaap, M. Styner, S. K. Warfield, X. Deng, T. Heimann, and B. van Ginneken. Liver Tumor Segmentation 08, 2008. URL http://lts08.bigr.nl/index.php. (Cited on page 64.)

W. L. Nowinski, B. C. Chua, Y. Marchenko, F. Puspitsari, I. Volkau, and M. V. Knopp. Three-dimensional reference and stereotactic atlas of human cerebrovasculature from 7 Tesla. *NeuroImage*, 55(3):986–998, January 2011. (Cited on pages 55 und 88.)

M. Okahara. Diagnostic Accuracy of Magnetic Resonance Angiography for Cerebral Aneurysms in Correlation With 3D-Digital Subtraction Angiographic Images: A Study of 133 Aneurysms. *Stroke*, 33(7):1803–1808, July 2002. (Cited on page 23.)

S. Osher. Level Set Methods: An Overview and Some Recent Results. *Journal of Computational Physics*, 169(2):463–502, May 2001. (Cited on page 28.)

N. Otsu. A threshold selection method from gray-level histograms. *Automatica*, 20(1):62–66, 1975. (Cited on page 29.)

P. Papathanasopoulou, S. Zhao, U. Köhler, M. B. Robertson, Q. Long, P. Hoskins, X. Y. Xu, and I. Marshall. MRI measurement of time-resolved wall shear stress vectors in a carotid bifurcation model, and comparison with CFD predictions. *Journal of magnetic resonance imaging*, 17(2):153–62, March 2003. (Cited on page 42.)

S.-H. Park, M.-B. Yim, C.-Y. Lee, E. Kim, and E.-I. Son. Intracranial Fusiform Aneurysms: It's Pathogenesis, Clinical Characteristics and Managements. *Journal of Korean Neurosurgical Society*, 44(3):116–23, September 2008. (Cited on page 8.)

E. Parzen. On estimation of a probability density function and mode. *The annals of mathematical statistics*, 33(3):1065–1076, 1962. (Cited on page 93.)

N. Passat, C. Ronse, J. Baruthio, J.-P. Armspach, C. Maillot, and C. Jahn. Region-growing segmentation of brain vessels: an atlas-based automatic approach. *Journal of magnetic resonance imaging*, 21(6):715–25, June 2005. (Cited on pages 27 und 28.)

Philips. Higher expectations, lower dose, 2012. URL http://www.healthcare.philips.com/gb_en/products/ct/products/iDose/index.wpd. (Cited on page 17.)

L. Pierot. Flow diverter stents in the treatment of intracranial aneurysms: Where are we? *Journal of neuroradiology. Journal de neuroradiologie*, 38(1):40–6, March 2011. (Cited on page 11.)

M. Piotin, R. Blanc, L. Spelle, C. Mounayer, R. Piantino, P. J. Schmidt, and J. Moret. Stent-assisted coiling of intracranial aneurysms: clinical and angiographic results in 216 consecutive aneurysms. *Stroke*, 41(1):110–5, January 2010. (Cited on page 11.)

T. Poggio, V. Torre, and C. Koch. Computational vision and regularization theory. *Nature*, 317(6035):314–319, 1985. (Cited on page 49.)

H. Prasetya, T. Mengko, O. Santoso, and H. Zakaria. Detection method of cerebral aneurysm based on curvature analysis from 3D medical images. In *Instrumentation, Communications, Information Technology, and Biomedical Engineering (ICICI-BME)*, pages 141–144, 2011. (Cited on pages 69 und 78.)

B. Preim and D. Bartz. *Visualization in Medicine. Theory, Algorithms, and Applications*. Morgan Kaufmann, 1st edition, 2007. (Cited on page 43.)

B. Preim and S. Oeltze. 3D visualization of vasculature: an overview. In L. Linsen, H. Hagen, and B. Hamann, editors, *Visualization in medicine and life sciences*, pages 1–20. Springer, 2008. (Cited on pages 44 und 46.)

F. K. Quek and C. Kirbas. Vessel extraction in medical images by wave-propagation and traceback. *IEEE transactions on medical imaging*, 20(2):117–31, February 2001. (Cited on page 28.)

G. Quellec, M. Lamard, P. M. P. Josselin, G. Cazuguel, B. Cochener, and C. Roux. Optimal wavelet transform for the detection of microaneurysms in retina photographs. *IEEE Transactions on Medical Imaging*, 27(9):1230–1241, 2008. (Cited on pages 62 und 65.)

A. G. Radaelli, L. Augsburger, J. R. Cebral, M. Ohta, D. Rüfenacht, R. Balossino, G. Benndorf, D. R. Hose, A. Marzo, R. Metcalfe, P. Mortier, F. Mut, P. Reymond, L. Socci, B. Verhegghe, and A. F. Frangi. Reproducibility of haemodynamical simulations in a subject-specific stented aneurysm model–a report on the Virtual Intracranial Stenting Challenge 2007. *Journal of biomechanics*, 41(10):2069–81, July 2008. (Cited on pages 38 und 41.)

M. Raghavan, B. Ma, and R. Harbaugh. Quantified aneurysm shape and rupture risk. *Journal of neurosurgery*, 5(2):13–22, 2005. (Cited on pages 36, 37 und 46.)

J. Raymond, F. Guillemi, F. Proust, A. J. Molyneux, A. J. Fox, J. Claiborne, J. Meder, R. I, and F. Guillemin. Unruptured Intracranial Aneurysms. A Critical Review of the International Study of Unruptured Intracranial Aneurysms (ISUIA) and of Appropriate Methods to Address the Clinical Problem. *Interventional Neuroradiology*, 14(1):85–96, 2008. (Cited on page 9.)

J. Raymond, T. E. Darsaut, and A. J. Molyneux. A trial on unruptured intracranial aneurysms (the TEAM trial): results, lessons from a failure and the necessity for clinical care trials. *Trials*, 12(1):64, January 2011. (Cited on page 9.)

G. J. E. Rinkel. Intracranial aneurysm screening: indications and advice for practice. *Lancet neurology*, 4(2):122–8, February 2005. (Cited on pages 12 und 13.)

G. Rinkel, M. Djibuti, A. Algra, and J. Van Gijn. Prevalence and risk of rupture of intracranial aneurysms: a systematic review. *Stroke*, 29(1):251–256, 1998. (Cited on page 9.)

F. Ritter, T. Boskamp, A. Homeyer, H. Laue, M. Schwier, F. Link, and H.-O. Peitgen. Medical Image Analysis: A visual approach. *IEEE Pulse*, 2(6):60–70, 2011. (Cited on page 104.)

S. Rohde, K. Lahmann, J. Beck, R. Nafe, B. Yan, A. Raabe, and J. Berkefeld. Fourier analysis of intracranial aneurysms: towards an objective and quantitative evaluation of the shape of aneurysms. *Neuroradiology*, 47(2):121–6, February 2005. (Cited on page 37.)

H. Ruppertshofen, C. Lorenz, S. Schmidt, P. Beyerlein, Z. Salah, G. Rose, and H. Schramm. Discriminative Generalized Hough transform for localization of joints in the lower extremities. *Computer Science - Research and Development*, 26(1-2):97–105, October 2010. (Cited on pages 52 und 56.)

D. B. Russakoff and A. Hasegawa. Generation and application of a probabilistic breast cancer atlas. In *Medical Image Computing and Computer-Assisted Intervention*, pages 454–461, Copenhagen, January 2006. (Cited on pages 63 und 93.)

P. K. Saha, J. K. Udupa, and D. Odhner. Scale-Based Fuzzy Connected Image Segmentation: Theory, Algorithms, and Validation. *Computer Vision and Image Understanding*, 77(2):145–174, February 2000. (Cited on page 29.)

Y. Sato, S. Nakajima, N. Shiraga, H. Atsumi, S. Yoshida, T. Koller, G. Gerig, and R. Kikinis. Three-dimensional multi-scale line filter for segmentation and visualization of curvilinear structures in medical images. *Medical image analysis*, 2(2):143–68, June 1998. (Cited on pages 27, 66, 67, 68 und 73.)

H. Scherl, J. Hornegger, M. Prümmer, and M. Lell. Semi-automatic level-set based segmentation and stenosis quantification of the internal carotid artery in 3D CTA data sets. *Medical image analysis*, 11(1):21–34, February 2007. (Cited on page 29.)

J. Schöberl. NETGEN An advancing front 2D/3D-mesh generator based on abstract rules. *Computing and visualization in science*, 1(1):41–52, 1997. (Cited on page 34.)

W. Schroeder, K. Martin, and B. Lorensen. *The Visualization Toolkit - An Object-Oriented Approach To 3D Graphics*. Kitware Inc., 4th edition, 2006. (Cited on page 103.)

K. E. Schwab, P. Gailloud, and G. Wyse. Limitations of magnetic resonance imaging and magnetic resonance angiography. *Magnetic Resonance Imaging*, 63(1):29–35, 2008. (Cited on page 21.)

D. Seghers, P. Slagmolen, Y. Lambelin, J. Hermans, D. Loeckx, F. Maes, and P. Suetens. Landmark based liver segmentation using local shape and local intensity models. In B. v. G. T. Heimann, M. Styner, editor, *MICCAI Workshop on 3D Segmentation in the Clinic*, pages 135–142, Brisbane, 2007. (Cited on page 55.)

S. Seifert, A. Barbu, S. K. Zhou, D. Liu, J. Feulner, M. Huber, M. Suehling, A. Cavallaro, and D. Comaniciu. Hierarchical parsing and semantic navigation of full body CT data. In J. P. W. Pluim and B. M. Dawant, editors, *SPIE Medical Imaging*, volume 7259, pages 7259–1–8, February 2009. (Cited on pages 53, 55 und 56.)

J. Sethian. Evolution, Implementation, and Application of Level Set and Fast Marching Methods for Advancing Fronts. *Journal of Computational Physics*, 169(2):503–555, May 2001. (Cited on pages 28 und 52.)

D. Sforza, C. Putman, and J. Cebral. Hemodynamics of cerebral aneurysms. *Annual review of fluid mechanics*, 41:91–107, 2009. (Cited on pages 37 und 46.)

W.-Y. Shi, Y.-D. Li, M.-H. Li, B.-X. Gu, S.-W. Chen, W. Wang, B.-L. Zhang, and M. Li. 3D rotational angiography with volume rendering: the utility in the detection of intracranial aneurysms. *Neurology India*, 58(6):908–13, 2011. (Cited on page 16.)

J. Shiraishi, S. Katsuragawa, J. Ikezoe, T. Matsumoto, T. Kobayashi, K.-i. Komatsu, M. Matsui7, H. Fujita, Y. Kodera, and K. Doi. Image Database for Chest Radiographs With and Without a Lung Nodule Receiver Operating Characteristic Analysis of Radiologists' Detection of Pulmonary Nodules. *American journal of neuroradiology*, 174:71–74, 2000. (Cited on page 64.)

M. Shojima, M. Oshima, K. Takagi, R. Torii, M. Hayakawa, K. Katada, A. Morita, and T. Kirino. Magnitude and role of wall shear stress on cerebral aneurysm: computational fluid dynamic study of 20 middle cerebral artery aneurysms. *Stroke*, 35(11):2500–5, November 2004. (Cited on pages 33 und 43.)

S. D. Shpilfoygel, R. A. Close, D. J. Valentino, and G. R. Duckwiler. X-ray videodensitometric methods for blood flow and velocity measurement: A critical review of literature. *Medical Physics*, 27:2008, 2000. (Cited on page 39.)

Siemens. Fast care means care that fits, 2012. URL http://www.medical.siemens.com/webapp/wcs/stores/servlet/LandingPage~q%_catalogId~e_-1~a_catTree~e_~a_langId~e_-1~a_pageId~e_142941~a_storeId~e_10001.htm. (Cited on page 17.)

R. Solomon, M. Fink, and J. Pile-Spellman. Surgical management of unruptured intracranial aneurysms. *Journal of Neurosurgery: Pediatrics*, 80(3):1227–34, June 1994. (Cited on page 11.)

M. Sonobe, T. Yamazaki, M. Yonekura, and H. Kikuchi. Small unruptured intracranial aneurysm verification study: SUAVe study, Japan. *Stroke*, 41(9):1969–77, September 2010. (Cited on page 9.)

S. M. Stivaros, J. N. Harris, W. Adams, and A. Jackson. Does black blood MRA have a role in the assessment of intracerebral aneurysms? *European radiology*, 19(1):184–92, January 2009. (Cited on pages 19 und 21.)

M. Straka, A. LaCruz, and L. Dimitrov. Bone segmentation in CT-angiography data using a probabilistic atlas. In *Vision, Modeling, and Visualization (VMV)*, pages 505–512, München, 2003. (Cited on page 29.)

J. I. Suarez, R. W. Tarr, and W. R. Selman. Aneurysmal subarachnoid hemorrhage. *The New England journal of medicine*, 354(4):387–96, January 2006. (Cited on page 9.)

M. Subasic, S. Loncaric, and E. Sorantin. 3-D image analysis of abdominal aortic aneurysm. *Studies in health technology and informatics*, 77:1195–1200, 2000. (Cited on page 61.)

T. Sugahara, C. Wijmenga, K. Nakashima, S. Hamatake, S. Honda, and M. Takahashi. Comparison of 2D and 3D digital subtraction angiography in evaluation of intracranial aneurysms. *American journal of neuroradiology*, 23(9):1545–52, October 2002. (Cited on page 14.)

Q. Sun, A. Groth, M. Bertram, O. Brina, V. M. Pereira, and T. Aach. A comprehensive validation of patient-specific CFD simulations of cerebral aneurysm flow with virtual angiography. In *SPIE Medical Imaging*, pages 79642–1–8, Orlando, 2011. (Cited on page 39.)

Y. Sun, A. K. C. Wong, and M. S. Kamel. Classification of Imbalanced Data: a Review. *Intern. Journal of Pattern Recogn. and Artif. Intell.*, 23(04):687, 2009. (Cited on pages 98 und 99.)

S. Suniaga, R. Werner, A. Kemmling, M. Groth, J. Fiehler, and N. D. Forkert. Computer-Aided Detection of Aneurysms in 3D Time-of-Flight MRA Datasets. In *MICCAI Workshop on Machine Learning in Medical Imaging*, pages 63–69, Nice, 2012. (Cited on pages 74, 78, 79, 80 und 139.)

J. S. Suri and R. M. Rangayyan. *Recent Advances in Breast Imaging, Mammography, And Computer-Aided Diagnosis of Breast cancer*. SPIE Press, 2006. (Cited on page 58.)

J. S. Suri, K. Liu, L. Reden, and S. Laxminarayan. A review on MR vascular image processing algorithms: acquisition and prefiltering: part I. *IEEE transactions on information technology in biomedicine*, 6(4):324–37, December 2002a. (Cited on pages 14, 18, 19 und 20.)

J. S. Suri, K. Liu, L. Reden, and S. Laxminarayan. A review on MR vascular image processing: skeleton versus nonskeleton approaches: part II. *IEEE transactions on information technology in biomedicine*, 6(4):338–50, December 2002b. (Cited on pages 26 und 27.)

K. Suzuki, J. Shiraishi, H. Abe, H. MacMahon, and K. Doi. False-positive reduction in computer-aided diagnostic scheme for detecting nodules in chest radiographs by means of massive training artificial neural network. *Academic radiology*, 12(2):191–201, February 2005. (Cited on page 63.)

J. Talairach and P. Tournoux. *Co-Planar Stereotaxic Atlas of the Human Brain*. Thieme, New York, 1 edition, 1988. (Cited on page 55.)

J. Tang, R. Rangayyan, J. Xu, I. El Naqa, and Y. Yang. Computer-aided detection and diagnosis of breast cancer with mammography: Recent advances. *IEEE transactions on information technology in biomedicine*, 13(2):236–251, 2009. (Cited on pages 13, 58 und 66.)

P. M. Tchou, T. M. Haygood, E. N. Atkinson, T. W. Stephens, P. L. Davis, E. M. Arribas, W. R. Geiser, and G. J. Whitman. Interpretation Time of Computer- aided Detection at Screening. *Radiology*, 257(1):40–46, 2010. (Cited on page 57.)

C. Teng, Z. Li, and M. Liao. Detection of cerebral aneurysms: Multislice CT angiography compared with DSA. *Chinese Journal of Interventional Imaging and Therapy*, 3(4):270–273, 2006. (Cited on page 17.)

S. Theodoridis and K. Koutroumbas. *Pattern recognition*. Academic Press, San Diego, 1999. (Cited on pages 50 und 100.)

D. Thévenin. MoBeStAn: Modellierung und Beeinflussung von Strömungen in Aneurysmen, 2008. URL http://www.uni-magdeburg.de/isut/LSS/mobestan_home.html. (Cited on page 25.)

B. F. Tomandl, P. Hastreiter, K. Eberhardt, C. Rezk-Salama, C. Nimsky, and M. Buchfelde. The kissing vessel-artifact: a problem occurring in the visualization of intracranial aneurysms using volume rendering and virtual endoscopy. *Radiology*, 213:311, 1999. (Cited on pages 28 und 34.)

B. F. Tomandl, T. Hammen, E. Klotz, H. Ditt, B. Stemper, and M. Lell. Bone-subtraction CT angiography for the evaluation of intracranial aneurysms. *American journal of neuroradiology*, 27(1):55–9, January 2006. (Cited on page 17.)

K. D. Tönnies. *Guide to Medical Image Analysis: Methods and Algorithms Advances in Computer Vision and Pattern Recognition*. Springer, 2012. (Cited on page 63.)

R. Torii, M. Oshima, T. Kobayashi, K. Takagi, and T. E. Tezduyar. Fluid-structure interaction modeling of blood flow and cerebral aneurysm: Significance of artery and aneurysm shapes. *Computer Methods in Applied Mechanics and Engineering*, 198(45-46):3613–3621, September 2009. (Cited on page 38.)

M. A. Treiber. *Geometroc Correspondence-based Methods*. Advances in Pattern Recognition. Springer London, London, 2010. (Cited on page 49.)

J. Trzasko, C. Haider, E. A. Borisch, N. G. Campeau, J. F. Glockner, S. J. Riederer, and A. Manduca. Sparse-CAPR: highly accelerated 4D CE-MRA with parallel imaging and nonconvex compressive sensing. *Magnetic Resonance in Medicine*, 66(4):1019–1032, 2011. (Cited on page 21.)

R. P. R. Tummala, M. K. Baskaya, R. C. R. Heros, and M. Bas Kaya. Contemporary management of incidental intracranial aneurysms. *Neurosurgical Focus*, 18(1):1–7, January 2005. (Cited on pages 6 und 10.)

Y. Uchiyama, H. Ando, R. Yokoyama, T. Hara, H. Fujita, and T. Iwama. Computer-aided diagnosis scheme for detection of unruptured intracranial aneurysms in MR angiography. In *IEEE Conference of Engineering in Medicine and Biology Society*, pages 3031–3034, Shanghai, 2005. (Cited on pages 66, 71, 76 und 80.)

Y. Uchiyama, M. Yamauchi, H. Ando, and R. Automated classification of cerebral arteries in MRA images and its application to maximum intensity projection. In *Engineering in Medicine and Biology Society*, pages 4865–4868, New York City, 2006. (Cited on pages 26 und 72.)

Y. Uchiyama, X. Gao, T. Hara, H. Fujita, H. Ando, H. Yamakawa, T. Asano, H. Kato, T. Iwama, M. Kanematsu, and H. Hoshi. Computerized detection of unruptured aneurysms in MRA images: reduction of false positives using anatomical location features. In *SPIE Medical Imaging*, volume 6915, pages 69151–1–8, San Diego, 2008. Spie. (Cited on pages 72, 78, 80, 138 und 139.)

Y. Uchiyama, T. Asano, T. Hara, H. Fujita, Y. Kinosada, T. Asano, H. Kato, M. Kanematsu, H. Hoshi, and T. Iwama. Performance evaluation of an automatic segmentation method of cerebral arteries in MRA images by use of a large image database. *Proceedings of SPIE*, 7260:72602J–72602J–7, 2009. (Cited on page 29.)

J. K. Udupa and S. Samarasekera. Fuzzy connectedness and object definition: theory, algorithms, and applications in image segmentation. *Graphical Models and Image Processing*, 58(3):246–261, 1996. (Cited on page 28.)

H. Ujiie, H. Tachibana, O. Hiramatsu, A. L. Hazel, T. Matsumoto, Y. Ogasawara, H. Nakajima, T. Hori, K. Takakura, and F. Kajiya. Effects of Size and Shape (Aspect Ratio) on the Hemodynamics of Saccular Aneurysms: A Possible Index for Surgical Treatment of Intracranial Aneurysms. *Neurosurgery*, 45(1):119, 1999. (Cited on page 37.)

G. R. Upchurch and T. a. Schaub. Abdominal aortic aneurysm. *American family physician*, 73(7):1198–204, April 2006. (Cited on pages 3 und 60.)

E. B. van de Kraats, G. P. Penney, D. Tomazevic, T. van Walsum, and W. J. Niessen. Standardized evaluation methodology for 2-D-3-D registration. *Transactions on medical Imaging*, 24(9):1177–1189, 2005. (Cited on page 116.)

J. van Gijn, R. S. Kerr, and G. J. E. Rinkel. Subarachnoid haemorrhage. *Lancet*, 369(9558): 306–18, January 2007. (Cited on page 9.)

B. van Ginneken, B. M. ter Haar Romeny, and M. a. Viergever. Computer-aided diagnosis in chest radiography: a survey. *IEEE transactions on medical imaging*, 20(12):1228–41, December 2001. (Cited on page 57.)

B. van Ginneken and S. Kerkstra. Grand Challenges in Medical Image Analysis, 2013. URL `http://www.grand-challenge.org/`. (Cited on page 64.)

B. van Ginneken, S. G. Armato, B. de Hoop, S. van Amelsvoort-van de Vorst, and Others. Comparing and combining algorithms for computer-aided detection of pulmonary nodules in computed tomography scans: The ANODE09 study. *Medical image analysis*, 14(6): 707–22, December 2010. (Cited on pages 41, 59, 62, 64, 65 und 108.)

R. van Pelt. *Real-time Illustrative Visualization of Cardiovascular Hemodynamics*. PhD thesis, Technical University of Eindhoven, 2012. (Cited on page 44.)

W. J. van Rooij and M. Sluzewski. Procedural morbidity and mortality of elective coil treatment of unruptured intracranial aneurysms. *American journal of neuroradiology*, 27 (8):1678–80, September 2006. (Cited on page 8.)

W. J. van Rooij, M. E. Sprengers, a. N. de Gast, J. P. P. Peluso, and M. Sluzewski. 3D rotational angiography: the new gold standard in the detection of additional intracranial aneurysms. *American journal of neuroradiology*, 29(5):976–9, May 2008. (Cited on page 16.)

M. Van Straten, H. Venema, C. Majoie, L. Ciancibello, and K. Subramanyan. Automatic bone removal in CT angiography. *MEDICAMUNDI*, 49(1):5, 2005. (Cited on page 18.)

Y. Ventikos, E. C. Holland, T. J. Bowker, P. N. Watton, N. M. P. Kakalis, M. Megahed, F. Zhu, P. E. Summers, and J. V. Byrne. Risk evaluation and interventional planning for cerebral aneurysms: computational models for growth, coiling and thrombosis. *The British journal of radiology*, 82(1):62–71, 2009. (Cited on pages 41, 42 und 46.)

M. C. Villa-Uriol, I. Larrabide, J. M. Pozo, M. Kim, O. Camara, M. De Craene, C. Zhang, a. J. Geers, H. Morales, H. Bogunović, R. Cardenes, and a. F. Frangi. Toward integrated management of cerebral aneurysms. *Philosophical Transactions of the Royal Society A: Mathematical, Physical and Engineering Sciences*, 368(1921):2961–82, June 2010. (Cited on page 25.)

M. C. Villa-Uriol, G. Berti, D. R. Hose, a. Marzo, a. Chiarini, J. Penrose, J. Pozo, J. G. Schmidt, P. Singh, R. Lycett, I. Larrabide, and a. F. Frangi. @neurIST complex information processing toolchain for the integrated management of cerebral aneurysms. *Interface focus*, 1(3):308–19, June 2011. (Cited on page 25.)

P. Viola and M. Jones. Rapid object detection using a boosted cascade of simple features. In *Computer Vision and Pattern Recognition*, volume 1, pages 511–518, Kauai, 2001. (Cited on page 54.)

M. H. Vlak, A. Algra, R. Brandenburg, and G. J. Rinkel. Prevalence of unruptured intracranial aneurysms, with emphasis on sex, age, comorbidity, country, and time period: a systematic review and meta-analysis. *Lancet Neurology*, 10(7):626–636, 2011. (Cited on pages 5, 6, 8, 9 und 88.)

I. Waechter, J. Bredno, R. Hermans, J. Weese, D. C. Barratt, and D. J. Hawkes. Model-based blood flow quantification from rotational angiography. *Medical image analysis*, 12 (5):586–602, 2008. (Cited on page 39.)

I. Wanke and M. Forsting. Intracranial Aneurysms. In M. Forsting, editor, *Intracranial Vascular Malformations and Aneurysms*, chapter 5, pages 167–283. Springer-Verlag, Heidelberg, 2nd edition, 2008. (Cited on pages 1, 3, 5, 13, 14, 16, 18, 21 und 22.)

J. M. Wardlaw and P. M. White. The detection and management of unruptured intracranial aneurysms. *Brain*, 123(2):205–21, February 2000. (Cited on pages 12, 17, 21, 23 und 128.)

Z. Wei, J. Yao, S. Wang, J. Liu, and R. M. Summers. Computer-aided marginal artery detection on computed tomographic colonography. In *SPIE Medical Imaging*, pages 8315–1–8, San Diego, 2012. (Cited on page 88.)

M. Weiger, K. P. Pruessmann, A. Kassner, G. Roditi, T. Lawton, A. Reid, and P. Boesiger. Contrast-enhanced 3D MRA using SENSE. *Journal of magnetic resonance imaging*, 12(5): 671–7, November 2000. (Cited on page 18.)

M. J. H. Wermer, I. C. van der Schaaf, A. Algra, and G. J. E. Rinkel. Risk of rupture of unruptured intracranial aneurysms in relation to patient and aneurysm characteristics: an updated meta-analysis. *Stroke*, 38(4):1404–10, April 2007. (Cited on pages 9 und 10.)

M. J. H. Wermer, H. Koffijberg, and I. C. van der Schaaf. Effectiveness and costs of screening for aneurysms every 5 years after subarachnoid hemorrhage. *Neurology*, 70(22): 2053–62, May 2008. (Cited on page 12.)

S. Wesarg and E. Firle. Segmentation of vessels: the corkscrew algorithm. In *SPIE Medical Imaging*, volume 5370, pages 5370–1–10, San Diego, 2004. (Cited on page 29.)

P. M. White, J. M. Wardlaw, E. Teasdale, S. Sloss, J. Cannon, and V. Easton. Power transcranial Doppler ultrasound in the detection of intracranial aneurysms. *Stroke*, 32(6):1291–7, June 2001. (Cited on pages 22 und 23.)

P. M. White, J. M. Wardlaw, and V. Easton. Can noninvasive imaging accurately depict intracranial aneurysms? A systematic review. *Radiology*, 217(2):361–70, November 2000. (Cited on pages 17, 21, 22, 23 und 128.)

D. O. Wiebers, J. P. Whisnant, J. Huston, I. Meissner, R. D. Brown, D. G. Piepgras, G. S. Forbes, K. Thielen, D. Nichols, W. M. O'Fallon, J. Peacock, L. Jaeger, N. F. Kassell, G. L. Kongable-Beckman, and J. C. Torner. Unruptured intracranial aneurysms: natural history, clinical outcome, and risks of surgical and endovascular treatment. *Lancet*, 362 (9378):103–10, July 2003. (Cited on pages 8, 9, 37 und 85.)

D. Wiebers. Unruptured intracranial aneurysms: natural history and clinical management. Update on the international study of unruptured intracranial aneurysms. *Neuroimaging Clinics of North America*, 16(3):383, 2006. (Cited on page 6.)

F. Wild. Outline of a Computational Theory of Human Vision. In *KI 2005 Workshop - Mixed-reality as a challenge to image understanding and artificial intelligence*, page 55, Koblenz, 2005. (Cited on page 50.)

O. Wink, W. J. Niessen, and M. a. Viergever. Fast delineation and visualization of vessels in 3-D angiographic images. *IEEE transactions on medical imaging*, 19(4):337–46, April 2000. (Cited on page 28.)

O. Wink, W. J. Niessen, and M. A. Viergever. Multiscale vessel tracking. *IEEE transactions on medical imaging*, 23(1):130–133, 2004. (Cited on page 28.)

I. H. Witten and E. Frank. *Data mining: practical machine learning tools and techniques with Java implementations*. Kaufman, San Francisco, 3rd edition, 2000. (Cited on page 98.)

J. Xiang, S. K. Natarajan, M. Tremmel, D. Ma, J. Mocco, L. N. Hopkins, A. Siddiqui, E. I. Levy, and H. Meng. Hemodynamic-morphologic discriminants for intracranial aneurysm rupture. *Stroke*, 42(1):144–152, 2011. (Cited on pages 43 und 46.)

S. Yamashita, H. Isoda, M. Hirano, H. Takeda, S. Inagawa, Y. Takehara, M. T. Alley, M. Markl, N. J. Pelc, and H. Sakahara. Visualization of hemodynamics in intracranial arteries using time-resolved three-dimensional phase-contrast MRI. *Journal of magnetic resonance imaging*, 25(3):473–8, March 2007. (Cited on page 37.)

X. Yang, D. J. Blezek, L. T. Cheng, W. J. Ryan, D. F. Kallmes, and B. J. Erickson. Computer-Aided Detection of Intracranial Aneurysms in MR Angiography. *Journal of Digital Imaging*, 24(1):86–95, 2011. (Cited on pages xiii, 1, 46, 76, 77, 78, 80, 138 und 139.)

X. Ye, X. Lin, J. Dehmeshki, G. Slabaugh, and G. Beddoe. Shape Based Computer Aided Detection of Lung Nodules in Thoracic CT Image. *IEEE Transactions on Biomedical Engineering*, 56(7):1810–1820, 2009. (Cited on pages 58, 59, 64 und 65.)

H. Yoshida and J. Näppi. Three-dimensional computer-aided diagnosis scheme for detection of colonic polyps. *IEEE transactions on medical imaging*, 20(12):1261–74, December 2001. (Cited on page 57.)

H. Yoshida and J. Näppi. CAD in CT colonography without and with oral contrast agents: progress and challenges. *Computerized medical imaging and graphics*, 31(4-5):267–84, 2007. (Cited on pages 58 und 63.)

G. W. Zack, W. E. Rogers, and S. a. Latt. Automatic measurement of sister chromatid exchange frequency. *Journal of Histochemistry & Cytochemistry*, 25(7):741–753, July 1977. (Cited on page 29.)

B. Zhang, X. Wu, J. You, Q. Li, and F. Karray. Detection of microaneurysms using multi-scale correlation coefficients. *Pattern Recognition*, 43(6):2237–2248, June 2010a. (Cited on page 18.)

L. Zhang, B. Chapman, D. Parker, J. Roberts, J. Guo, P. Vemuri, S. Moon, and F. Noo. Automatic detection of three-dimensional vascular tree centerlines and bifurcations in high-resolution magnetic resonance angiography. *Investigative Radiology*, 40(10):661–671, 2005. (Cited on page 143.)

L. Zhang, Y.-Z. Wang, and J. Lei. Diagnostic value of CT angiography and MR angiography for intracranial aneurysms: A Metaanalysis. *Chinese Journal of Cerebrovascular Diseases*, 9 (9):466–471, 2012. (Cited on page 21.)

L.-J. Zhang, S.-Y. Wu, J.-B. Niu, Z.-L. Zhang, H. Z. Wang, Y.-E. Zhao, X. Chai, C.-S. Zhou, and G.-M. Lu. Dual-energy CT angiography in the evaluation of intracranial aneurysms: image quality, radiation dose, and comparison with 3D rotational digital subtraction angiography. *American journal of roentgenology*, 194(1):23–30, January 2010b. (Cited on page 18.)

L. Zhao. *Curvature Lines for Lesion Detection and Visualization in CT Colonography*. PhD thesis, TU Delft, 2011. (Cited on page 66.)

M. Zhao, S. Amin-Hanjani, S. Ruland, a. P. Curcio, L. Ostergren, and F. T. Charbel. Regional cerebral blood flow using quantitative MR angiography. *American journal of neuroradiology*, 28(8):1470–3, September 2007. (Cited on page 39.)

Y. Zheng, B. Georgescu, H. Ling, S. K. Zhou, M. Scheuering, and D. Comaniciu. Constrained marginal space learning for efficient 3d anatomical structure detection in medical images. In *Computer Vision and Pattern Recognition*, pages 194–201, Miami Beach, June 2009. (Cited on pages 55 und 56.)

C. S. Zhou, S. Luo, M. Wang, and G. M. Lu. Digital Subtraction CT Angiography for Detection of Intracranial Aneurysms : Comparison with Three-dimensional Digital Subtraction Angiography. *Radiology*, 262(2):605–612, 2012. (Cited on page 18.)

C. Zhou, H. Chan, and B. Sahiner. Automatic multiscale enhancement and segmentation of pulmonary vessels in CT pulmonary angiography images for CAD applications. *Medical Physics*, 34(12):4567–4577, 2007. (Cited on page 88.)